SEISMIC RESIDUAL CAPACITY OF REINFORCED CONCRETE FRAMES

ALBERTO CUEVAS

A thesis submitted in partial fulfilment of the requirements for the Degree
of Doctor of Philosophy in Earthquake Engineering
at the University of Canterbury
Christchurch, New Zealand
October 2018

To my mom

ABSTRACT

One of the most controversial issues highlighted by the 2010-2011 Christchurch earthquake series and more recently the 2016 Kaikoura earthquake, has been the evident difficulty and lack of knowledge and guidelines for: a) evaluation of the residual capacity damaged buildings to sustain future aftershocks; b) selection and implementation of a series of reliable repairing techniques to bring back the structure to a condition substantially the same as prior to the earthquake; and c) predicting the cost (or cost-effectiveness) of such repair intervention, when compared to fully replacement costs while accounting for potential aftershocks in the near future.

As a result of such complexity and uncertainty (i.e., risk), in combination with the possibility (unique in New Zealand when compared to most of the seismic-prone countries) to rely on financial support from the insurance companies, many modern buildings, in a number exceeding typical expectations from past experiences at an international level, have ended up being demolished. This has resulted in additional time and indirect losses prior to the full reconstruction, as well as in an increase in uncertainty on the actual relocation of the investment.

This research project provides the main end-users and stakeholders (practitioner engineers, owners, local and government authorities, insurers, and regulatory agencies) with comprehensive evidence-based information to assess the residual capacity of damage reinforced concrete buildings, and to evaluate the feasibility of repairing techniques, in order to support their delicate decision-making process of repair vs. demolition or replacement.

Literature review on effectiveness of epoxy injection repairs, as well as experimental tests on full-scale beam-column joints shows that repaired specimens have a reduced initial stiffness compared with the undamaged specimen, with no apparent strength reduction, sometimes exhibiting higher displacement ductility capacities. Although the bond between the steel and concrete is only partially restored, it still allows the repaired specimen to dissipate at least the same amount of hysteretic energy. Experimental tests on buildings subjected to earthquake

loading demonstrate that even for severe damage levels, the ability of the epoxy injection to restore the initial stiffness of the structure is significant.

Literature review on damage assessment and repair guidelines suggests that there is consensus within the international community that concrete elements with cracks less than 0.2 mm wide only require cosmetic repairs; epoxy injection repairs of cracks less and 2.0 mm wide and concrete patching of spalled cover concrete (i.e., minor to moderate damage) is an appropiate repair strategy; and for severe damaged components (e.g., cracks greater than 2.0 mm wide, crushing of the concrete core, buckling of the longitudinal reinforcement) local replacement of steel and/or concrete in addition to epoxy crack injection is more appropriate.

In terms of expected cracking patterns, non-linear finite element investigations on well-designed reinforced concrete beam-to-column joints, have shown that lower number of cracks but with wider openings are expected to occur for larger compressive concrete strength, f'_c, and lower reinforcement content, ρ_s. It was also observed that the tensile concrete strength, f_t, strongly affects the expected cracking pattern in the beam-column joints, the latter being more uniformly distributed for lower f_t values. Strain rate effects do not seem to play an important role on the cracking pattern. However, small variations in the cracking pattern were observed for low reinforcement content as it approaches to the minimum required as per NZS 3101:2006.

Simple equations are proposed in this research project to relate the maximum and residual crack widths with the steel strain at peak displacement, with or without axial load.

A literature review on fracture of reinforcing steel due to low-cycle fatigue, including recent research using steel manufactured per New Zealand standards is also presented. Experimental results describing the influence of the cyclic effect on the ultimate strain capacity of the steel are also discussed, and preliminary equations to account for that effect are proposed.

A literature review on the current practice to assess the seismic residual capacity of structures is also presented. The various factors affecting the residual fatigue life at a component level (i.e., plastic hinge) of well-designed reinforced concrete frames are discussed, and equations to quantify each of them are proposed, as well as a methodology to incorporate them into a full displacement-based procedure for pre-earthquake and post-earthquake seismic assessment.

Keywords: epoxy repairing techniques, strain-rate, material characteristics, residual crack widths, low-cycle fatigue, residual strain capacity, plastic hinge, loss of stiffness.

ACKNOWLEDGEMENTS

I would like to thank my supervisor Professor Stefano Pampanin for the opportunity given, for all the great support not only on academic matters but also during the life circumstances experienced over these years. To Professor Josko Ozbolt for the many helpful sessions and feedback on finite element modelling. To Umut Akguzel and Akanshu Sharma for sharing with me their knowledge on MASA.

To the CNRE technical staff, in particular to Mosese Fifita, John Maley, and Alan Thirlwell for all their help and hard work during the experimental campaign. Special thanks to Giuseppe Loporcaro and Amir Malek, and to all my friends at the University of Canterbury.

To all my family for supporting me unconditionally. To my wife Natalia, for giving me all her love, spirituality, support and for keeping me motivated when I needed the most. To God who after all could not have made this whole experience more rewarding.

TABLE OF CONTENTS

Page

LIST OF FIGURES

Page

LIST OF TABLES

Page

1 INTRODUCTION

1.1 Research motivation

One of the most controversial issues highlighted by the 2010-2011 Christchurch earthquake series and more recently the 2016 Kaikoura earthquake, has been the evident difficulty and lack of knowledge and guidelines for: a) evaluation of the residual capacity damaged buildings to sustain future aftershocks; b) selection and implementation of a series of reliable repairing techniques to bring back the structure to a condition substantially the same as prior to the earthquake; and c) predicting the cost (or cost-effectiveness) of such repair intervention, when compared to fully replacement costs while accounting for potential aftershocks in the near future.

As a result of such complexity and uncertainty (i.e., risk), in combination with the possibility (unique in New Zealand when compared to most of the seismic-prone countries) to rely on financial support from the insurance companies, many modern buildings, in a number exceeding typical expectations from past experience at an international level, have ended up being demolished. This has resulted in additional time and indirect losses prior to the full reconstruction, as well as in an increase in uncertainty on the actual relocation of the investment.

This research project provides Engineers, Insurers, Territorial (Local or Government) Authorities, Owners, Developers and Investors with a set of technical guidelines based on sound experimental and numerical evidences that can strongly support the decision-making process of repair vs. demolition or replacement which, considering its overall socio-economic impact, ultimately affects from the beginning the shaping of the future of an earthquake-damaged city (e.g., Christchurch) as well as the country as a whole.

It is believed that less uncertainty on the definition of reparability solutions and costs vs. replacement costs will allow more targeted premiums to be provided by insurers and thus,

overall, a way forward with confirmation of investments and financial support needed for the rebuild of the city.

The question that this project aimed at answering has been proven to be a serious obstacle in the first phase of recovery/rebuild of Christchurch. Consultant engineers had to deal with a problem for which the answer was not yet available within the international community in the form of a simple document and, more importantly, based on robust evidences.

Moving forward, it has been clear that a missing link in the past research at international level is the lack of incorporation in the design of new structures as well as in the strengthening retrofit phase of considerations based on the cost-feasibility of the actual post-earthquake reparability. The findings of this research project help in understanding and evaluating from a socio-economic stand point what would the impact of an earthquake on the newly designed structure be. This could lead to a design/retrofit approach that better respects the principles of performance-based design, targeting reparability after a design level event. Similarly, the wider communication of the reparability vs. irreparability threshold could lead to the adoption and wider spread of more recently developed higher performance seismic-resisting technology, capable of providing a limited (if not ideally negligible) level of damage, both structural and non-structural, under a major event. Ultimately this is the highest goal of earthquake engineering.

Thus, the outcomes of this project and benefits in implementing and disseminating the achieved know-how could significantly affect also the regulations in terms of seismic risk acceptance and reduction for the whole country.

1.2 Scope and Research objectives

The main objective of this research project is to provide the main end-users and stakeholders (practitioner engineers, owners, local and government authorities, insurers, and regulatory agencies) with comprehensive evidence-based information to assess the residual capacity of damaged reinforced concrete frame buildings, and to evaluate the feasibility of repairing techniques, in order to support their delicate decision-making process of repair vs. demolition or replacement.

The key objectives of this research are:

1. Fully understand what residual capacity in structural members is (at a local level), and how it is affected by factors such as low-cycle fatigue, bond deterioration, strain-ageing, strain hardening, and material properties;

2. Implement, calibrate and validate analytical tools for modelling and assessment of residual capacity of those structural members where inelastic action is observed or expected (i.e., at the plastic hinge);
3. Understand how the hysteretic behaviour of the structural members deteriorates after a real earthquake (in terms of strength, stiffness and energy dissipation), as well as how it is improved up to a certain level after implementing a repairing technique;
4. Gain a better understanding on the seismic performance of damaged reinforced concrete frame buildings after an earthquake, its residual capacity and how it improves after being repaired; and
5. Propose a methodology to account for the residual capacity in either the design of new buildings and assessment process of existing ones.

1.3 Research methodology

The research project comprises numerical, experimental and analytical investigations, building on current best engineering practice and guidelines, and closely referring to the damage observations in reinforced concrete buildings in Christchurch as case study.
Figure 1-1 shows an overview of the methodology. Each of the numerical, experimental and analytical investigations are sub-divided into two main phases.

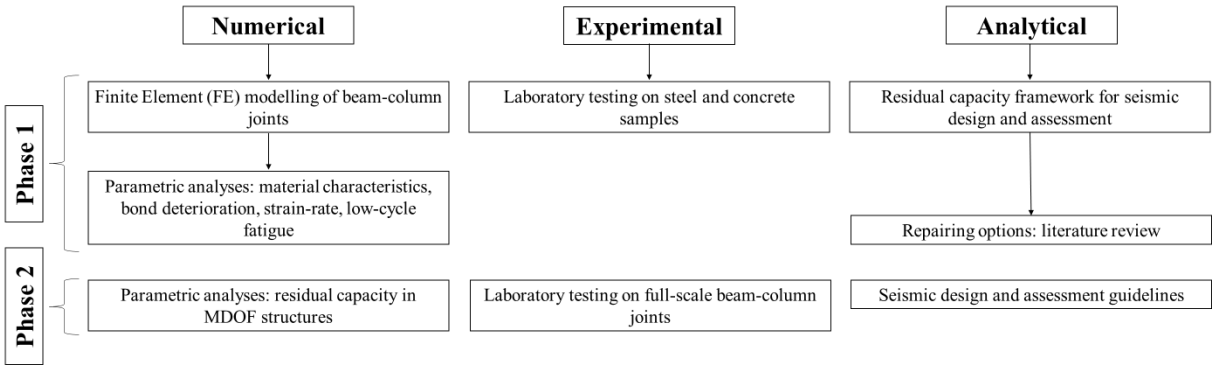

Figure 1-1. Flowchart of the research methodology for seismic residual capacity of buildings.

In Phase 1, parametric analyses are performed through Non-linear Finite element (*FE*) simulations on capacity designed beam-column joints from previous experimental research projects, aiming at understanding quantitatively and qualitatively (i.e., different cracking patterns) the effect on the residual capacity of the plastic hinge of variations in parameters like yield and tensile strength of the steel, reinforcement content, concrete strength and bond deterioration; with and without considering the velocity of loading (strain-rate). The study is

further extended and the results used to implement and calibrate a procedure to account for residual strain capacity of plastic hinges, which is a key component of the proposed framework to account for the seismic residual capacity in plastic hinges.
Destructive tests on steel and concrete from real specimens (i.e., those beam-column joints extracted from the PWC building and to be tested in the Laboratory in Phase 2) are performed to calibrate the numerical model of the beam-column joints.
The effectiveness of epoxy injection techniques is reviewed and summarized, and consequently implemented in full-scale specimens tested in the laboratory.
In Phase 2, experimental tests on well-designed full-scale beam-column joints extracted from a real building are be performed in order to estimate the hysteretic behaviour (strength and stiffness deterioration, pinching effect) of damaged (post-earthquake) and repaired plastic hinges.
A framework to account for residual capacity for seismic design and assessment of plastic hinges is proposed and further expanded to be used in multi-degree-of-freedom systems.

1.4 Thesis outline

Chapter 2 presents a summary of previous research done on effectiveness of epoxy injection techniques, probably one of most used to repair damage structures following the 2010-2011 Christchurch earthquakes. Special attention is given to experimental tests performed using capacity designed specimens. Experimental tests looking at bond strength between the concrete, steel and the epoxy resin are also discussed, as well as tests on simply supported beams and beams under double bending actions. Previous research on shear walls repaired with epoxy resins is also included for completeness.
The chapter also summarises assessment and repair guidelines currently available in the literature, emphasizing on the criteria to determine appropriate repair strategies depending on the type and severity of the observed damage.
Chapter 3 describes the experimental program performed on three “modern designed” beam-column joints extracted from a 1980s multi-storey reinforced concrete frame building, while Chapter 4 describes the global response of the specimens tested prior to and after the epoxy repairs. Special attention is given to the cracking pattern, crack widths, and failure mechanism. The chapter also shows comparison of the hysteretic behaviour and energy dissipation and stiffness, aiming at evaluating the effectiveness of the epoxy repairs in the cyclic performance of beam-column joints. Maximum, residual, and Res/Max crack width

ratios are also presented. Lastly, the nonlinear finite element modelling of the specimen is presented, along with preliminary results of a parametric study on plastic hinge relocation details.

Chapter 5 presents the results of an experimental and numerical *FE* investigation on a modern (i.e., relatively well-designed according to post-1970s seismic codes) reinforced concrete beam-to-column joint, targeting at identifying and understanding qualitatively and quantitatively the influence of various parameters on the cracking pattern and nonlinear behaviour of reinforced concrete plastic hinges, at various limit states.

Chapter 6 presents a numerical *FE* investigation aiming at gaining a better understanding on how the maximum and residual crack widths, and steel strain at peak displacement are related, once the onset of nonlinearity has been exceeded.

Chapter 7 presents a literature review on fracture of reinforcing steel due to low-cycle fatigue, including recent research using steel manufactured per New Zealand standards. Experimental results describing the influence of the cyclic effect on the ultimate strain capacity of the steel are discussed, and preliminary equations to account for that effect are proposed.

Chapter 8 presents a review of the current know-how on seismic residual capacity, describes the various factors affecting the residual fatigue life at a component (i.e., plastic hinge) level, and how they can be quantified and incorporated into a full displacement-based seismic assessment procedure.

Chapter 9 includes concluding remarks and recommendations for future research.

2 EFFECTIVENESS OF EPOXY INJECTION TECHNIQUES: LITERATURE REVIEW

2.1 Introduction

This chapter presents a summary of previous research done on effectiveness of epoxy injection techniques. This technique is probably one of most used to repair earthquake-damaged structures, such after the 2010-2011 Christchurch earthquakes sequence in New Zealand.

Special attention is given to experimental tests performed using specimens designed according to modern codes, in which the inelastic behaviour is expected to occur at the beam-ends, and very little or no damage is expected in the columns and joint. Experimental tests looking at bond strength between the concrete, steel and the epoxy resin are also discussed, as well as tests on simply supported beams and beams under double bending actions. Previous research on shear walls repaired with epoxy resins is also included for completeness.

The second part of the chapter summarises assessment and repair guidelines available in the literature, which outline some criteria to determine the appropriate repair strategy depending on the type and severity of the observed damage.

2.2 Literature review

2.2.1 Bond tests and tests on reinforced concrete beams

Bertero et al (1972) studied the strain-rate effects and the effectiveness of epoxy injection techniques on simply supported doubly reinforced concrete beams. The motivation of the study was the fact that "*the larger the ductility designed into the earthquake, the greater the damage it can suffer in an earthquake without collapsing*". In other words, greater cracks may be expected in modern or ductile design compared to older buildings, without implying that the building is prone to collapse. They tested six beams under a four-point loading condition,

inducing a zone of constant bending moment in the central third of the beams. Two beams (prototype 3 and 4) were subjected to a load just enough to induce some yielding in the longitudinal reinforcement; the beams were repaired by epoxy injection and retested again following the same loading regime. The load was gradually increased until reaching failure. Cracks wider than 0.127 mm were observed in the central third of the prototype beams, which eventually were epoxy injected. There was no indication of fractured bars at any stage of the tests. The damage observed in the repaired specimens was similar to the one observed in the prototype beams, for the same loading history.

In the repaired specimens, the cracks did not form at their original locations. As the loading history was gradually increased, significant diagonal cracking developed outside the central third, which eventually resulted in a shear failure of the beams. No spalling of the concrete cover was observed. Figure 2-1 shows the load-displacement curves of the prototype and repaired specimens.

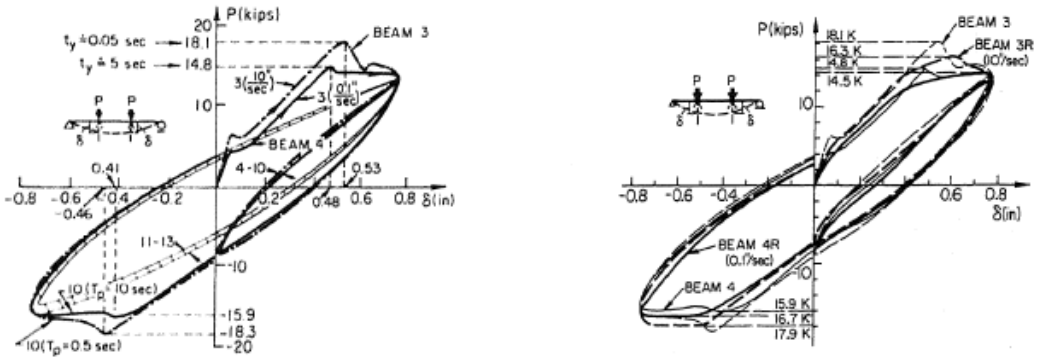

Figure 2-1. Load-displacement curves of prototype specimens 3 and 4 (left), comparison of the load-displacement curves of the prototype specimens with the epoxy-repaired specimens 3R and 4R (right) (Bertero et al, 1972).

The initial stiffness of the repaired specimens was found to be lower than that of the prototype specimens. They attributed this effect to the fact that not all cracks were repaired. The repaired specimens did not show a definite cracking and yielding point, potentially due to the loss of bond between the longitudinal reinforcement and surrounding concrete. However, the repaired specimens developed maximum strengths slightly higher than the prototype specimens. By inspecting the hysteresis loops in Figure 2-1, it can be concluded that the energy absorption and dissipation characteristics of the repaired specimens were slightly reduced.

Celebi and Penzien (1973) tested four epoxy repaired specimens (beams 5, 7, 9, and 10) that were previously tested as part of another research. Each specimen consisted of two half-

beams, one at each side of a central column stub. They stated that "*whenever possible and feasible, practice has been to repair buildings to restore them to their normal serviceability, strength and aesthetics. One important method of repairing which is commonly used is the epoxy injection method*".

The epoxy resin used to repair the specimens was a low-viscosity resin of 3.0-3.5 hr gel time, with tension and compression strengths of 47.6 MPa and 67.9 MPa (at seven days and 24 hr, respectively). The curing time of the specimens after the repairs was seven days.

The prototype specimens were subjected to 20 pre-yield reversed cycles, and 20 cycles at and above the yield point. After the epoxy repairs, the specimens were subjected to a quasi-static cyclic loading with incremental displacement amplitudes, applying 4 cycles at each displacement amplitude. The specimen 5 had a shear span ratio (*a/d*) of 5.1, whilst specimens 7, 9 and 10 had a shear span ratio of 3.70 and different volumetric shear reinforcement ratios.

The damage of prototype 5 (i.e., prior to the repairs) consisted of beam hinging adjacent to the column stub. The damage after the repairs spread out and shifted away from the repaired portion. The most critical cracks in the prototype specimen did not open-up after they were repaired, however new cracks opened-up adjacent to the repaired ones. Figure 2-2 shows the load-displacement curves of specimen 5 before and after the repairs. It is evident that the repaired specimen became stronger and stiffer than the prototype one. No maximum and residual cracks are reported, and there is no indication of fractured bars at any stage of the test of specimen 5.

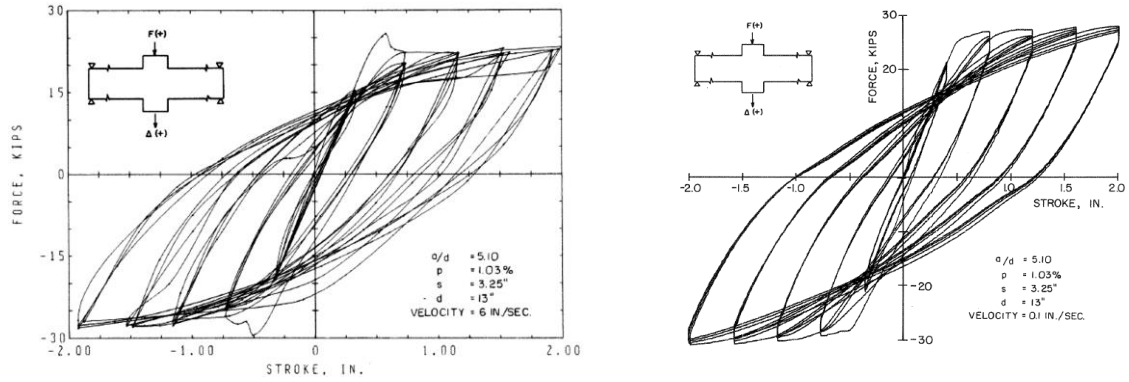

Figure 2-2. Load-displacement curves of beam 5 before (left) and after repairs (right) (Celebi and Penzien, 1973).

Regarding the specimens 7, 9 and 10 (i.e., beams with shorter shear span ratio), the test in the repaired specimens had to stopped because one of the bottom bars fractured within the stub region, in addition to crushing of the concrete cover. They attributed the fracture of the

bottom bar to exhaustion of the elongation and bond capacity of the bar. Figure 2-3 shows the load-displacement curves of beam specimen 7 before and after the repairs.

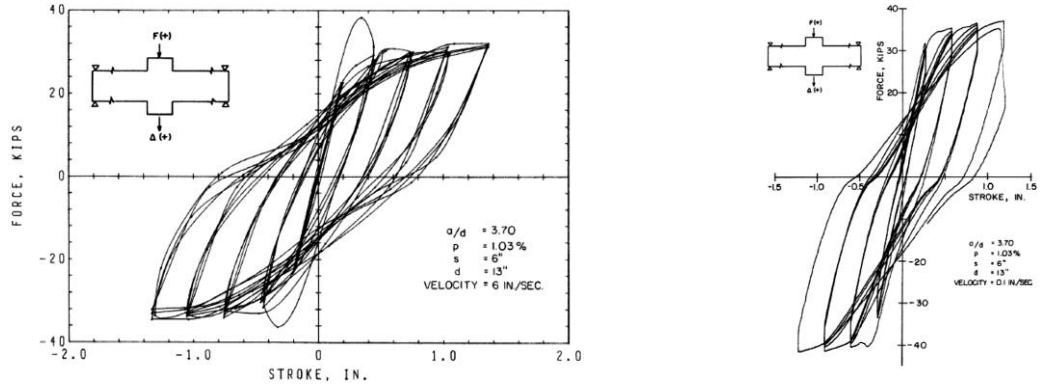

Figure 2-3. Load-displacement curves of beam 7 before (left) and after repairs (right) (Celebi and Penzien, 1973).

They concluded that "*both strength and stiffness of the beams when repaired are increased as much as 18-25%...however, this increase in strength is accompanied by a corresponding decrease in ductility*". It is interesting to note that the decrease in ductility (due to the fractured bar) occurred in the case of beams with short shear span ratios. As seen in Figure 2-2, specimen 5 (with a shear span ratio of 5.1) did not show any reduction of its displacement capacity. They couldn't detect any significant difference in the energy absorption characteristics between the prototype and repaired specimens.

They did raise the concern of residual deformations that may exist in repaired beams of damaged buildings. In fact, they attribute the fractured bar in specimens 7, 9, and 10 to residual deformations.

Regarding the restoration of aesthetics, they concluded that "*in all the beams repaired, it can be stated that the surface finish due to grinding after the epoxy injection was quite satisfactory*".

Chung (1981) performed tests on nine pull-out specimens and on two simply supported reinforced concrete beams subjected to a four-point loading, with the objective of getting a better understanding on the effectiveness of the epoxy injection to restore the bond between the steel and the concrete. Excessive splitting of the concrete in the pull-out specimens was prevented with steel helix as transverse reinforcement. Bond failure in the reinforced concrete beams was ensured by debonding the bars at both beam ends, and adjacent to notches located at 300 mm from the beam support (approximately where the two-point loads were applied). The pull-out specimens were subjected to tensile forces until reaching the maximum bar capacity. The bar slip was measured at the free end of the specimen. In the case of the

reinforced concrete beams, the load was increased gradually until the beam failed in shear at the support. No maximum and residual cracks are reported, and there is no indication of fractured bars at any stage of the tests. The bar slip was measured at each bar end.
Both the pull-out tests and beams were repaired with epoxy resins, cured at ambient temperature for seven days, and retested again until failure. Figure 2-4 shows the bond-slip results of the prototype and repaired specimens.

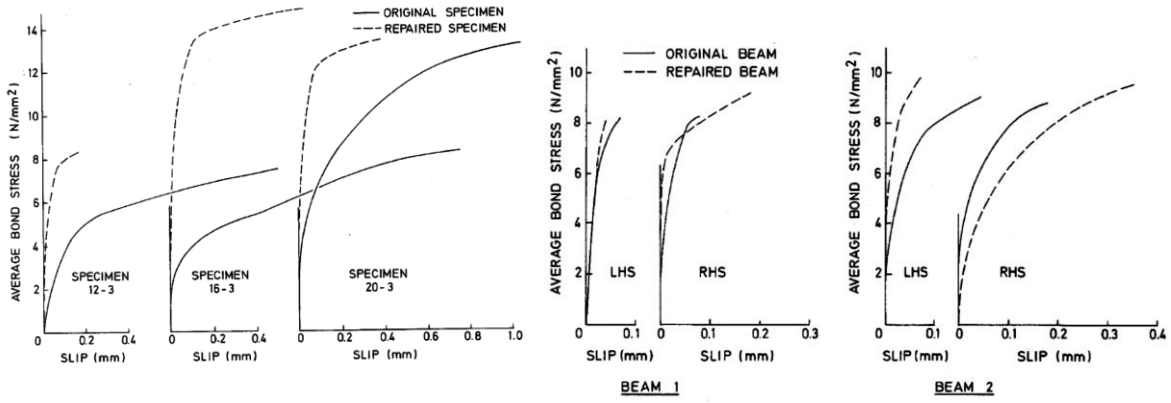

Figure 2-4. Development of bond-slip in pull-out (left) and beam specimens (right) (Chung, 1981).

Regarding the pull-out specimens, it is evident that the initial slope of the bond-slip curves of the repaired specimens is steeper (i.e., stiffer) at low slip values, but flatten out at higher ones. In other words, the bars in the repaired specimens sustained the same load and transmit it to the surrounding concrete by the epoxy resin, with much less slip than in the prototype specimens. Even though the epoxy resin appears to not have penetrated more than one-half of the embedded bar length, the bond stresses measured in the repaired specimens at the initiation of the slipping, at an advance state of slipping and at complete failure, were higher than the ones measured in the prototype specimens.
Regarding the beam tests, the repaired specimen 1 failed at the same location as the prototype but at greater load. A new diagonal crack was developed 25 mm away from the repaired crack. The repaired specimen 2 failed at the other beam-end (but at the same load) compared to the prototype. As observed in the pull-out tests, the initial slope of the bond-slip curves of the repaired specimens was steeper (i.e., stiffer) at low slip values, which means that the repaired specimens were also able to resist the same load as the prototypes with much less slip. The bond stresses in the repaired specimens at the initiation of slipping and at complete failure were not lower than the measured ones in the prototype specimen.
Based on the limited amount of tests, Chung (1981) concluded that although the full length of bar where the bond deteriorated is not fully covered with epoxy, the above results are good

signs of the effectiveness of the epoxy injection repairs in restoring the bond, and stated that "*flexural tests on reinforced concrete beams have shown that the repair process not only eliminates the unsightly appearance of wide cracks but also restores the flexural strength and stiffness of the damaged member. Push-off tests, both static and dynamic, have further indicated that concrete-to-concrete joints can regain their shear strength after being repaired by epoxy injection*".

Mansur and Ong (1985) tested six reinforced concrete beams with rectangular openings and compared the results of the prototype specimens with the repaired ones. The specimens were tested under a three-point loading condition until failure. The prototype beams developed numerous cracks as well as concrete crushing at the four corners of the openings. There was evidence of residual deformations after the load was removed, which was corrected prior to commencing the repair works. The loose concrete was removed and replaced with an epoxy mortar. The cracks were subsequently repaired by epoxy injection.

The repaired specimens were retested again following the same loading scheme. They observed that the development of cracks at the four critical corners was delayed due to the presence of the epoxy mortar. The new cracks formed in the old concrete adjacent to the epoxy mortar, however the observed cracking pattern in the prototype and repaired specimen were very similar.

In terms of maximum crack widths, the repaired beams exhibited larger crack widths at initial loading stages and smaller crack widths as the load increased, compared to the prototype specimens. In general, the maximum crack widths at service load were smaller for the repaired specimens than for the prototype ones.

The stiffness of the repaired specimens was lower, evidenced by more deflections at the same load level, potentially due to the existence of hairline cracks that were not repaired. The mode of failure of the repaired specimens was similar to the prototype ones, although the repaired specimens failed at a much higher load (between 7.2% and 18% higher). The reasons of the gain of strength included the high-strength epoxy mortar at the critical sections, strain hardening of the steel, increase of concrete strength between the two sets of experiments, and an apparent reduction of the effective length of the opening. The latter appeared to be the principal contributor.

Ozaka and Suzuki (1986) tested one-third scale and one-half scale beam specimens with different shear span (*a/d*) ratios and reinforcement content under different loading regimes. The specimens consisted of half beam and a column stub. The load was applied at the beam

end (i.e., at the theoretical location of the inflection point). They injected cracks wider than 0.2 mm at the surface of some of the specimens and retested them again. The cracks in the repaired specimen formed close to the repaired cracks. They observed that the initial (secant) stiffness of the repaired specimens was less compared to the prototype specimens (about 50% of the prototype's stiffness, at a load of about 20% of the yield load). No significant differences were observed between the prototype and repaired specimens with respect to the yield load, yield displacement, ultimate load, ultimate displacement, and maximum displacement, although the displacement ductility values were higher for the repaired specimens compared to the prototype ones. Based on the results, they concluded that "*even a member that had practically failed, if properly repaired injecting epoxy resin, will be roughly the same or slightly better in capacity and deformability. Therefore, it can be said that it is amply safe to use the original values for estimating yielding load and capacity, or ductility of a member after repair*".

Tasai (1988) investigated the reasons of the increase of the flexural strength in beam specimens failed in flexure that were subsequently repaired with epoxy injection. Some specimens were subjected to monotonic loading (test series *A* and *B*), and some others to cyclically reverse loading (test series *C*). All the beam specimens were half-scale. Test series *A* consisted of a column stub with two half beams, one at each side. The two beam ends were simply supported, and an axial load was applied at the column stub. Test series *B* consisted of simply supported beams subjected to a four-point loading. Test series *C* consisted of a beam subjected to double-curvature. In addition to epoxy injection, some specimens were also repaired with epoxy mortar to replace the crushed or spalled concrete. The tensile strength of the epoxy resin and epoxy mortar was 33.3 MPa and 28.4 MPa, respectively. No maximum and residual cracks are reported, and there was no indication of fractured bars at any stage of the tests.

Tasai observed an increase in the yield strength (between 3% and 8%) after repairing the specimens with epoxy injection for both monotonic and cyclic loading tests (series *A* and *C*), effect attributable to strain hardening and strain-ageing effects. He also observed a shift in the location of yielding after the specimen was repaired with epoxy. The reason for that could be the increase in the steel strength due to strain-ageing at those locations that yielded previously.

Regarding the beam specimens repaired with epoxy mortar over one-fifth of the section from the bottom (test series *B*), he observed that their ultimate moment capacity exceeded the

capacity of the prototype specimens. Tasai concluded that "*the epoxy mortar filling can carry a significant tensile force to increase the flexural resistance of the new repaired section*". Basunbul et al (1990) tested the ability of four different repair methods on reinforced concrete beams: epoxy injection, ferrocement, steel-plate bonding, and a combined method epoxy injection and ferrocement. Only the results of the specimens repaired with epoxy injection are discussed herein.

Nine small-scale reinforced concrete beams with shear span ratios (*a/d*) of 3.33 were subjected to a four-point monotonic loading. Three different damage states were studied: 10 and 15 mm central deflection, and failure. Only cracks greater than 0.3 mm wide were epoxy injected. The repaired specimens were cured for 7 days at room temperature and consequently retested to failure. Figure 2-5 shows the load versus deflection and load versus crack width curves, whilst Table 2-1 shows the summary of the test results of the prototype and the epoxy-repaired beams.

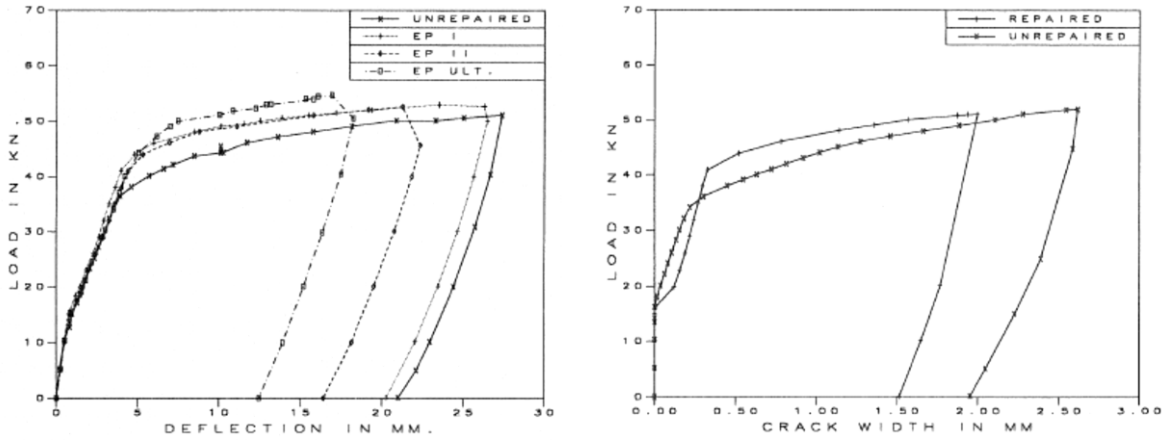

Figure 2-5. Load-deflection curves (left) and load-crack widths (right) of prototype and epoxy-repaired specimens (Basunbul et al, 1990).

Table 2-1. Summary of test results of the prototype (original) and epoxy-repaired specimens (Basunbul et al, 1990).

Damage level	P_{cr} (kN)		P_u (kN)		Δ_u (mm)		Ductility (kN-mm)	
	Original	Repaired	Original	Repaired	Original	Repaired	Original	Repaired
10 mm	14.07	17.62	-	52.82	-	25.32	-	1017.57
15 mm	15.29	17.52	-	52.80	-	22.08	-	851.47
Failure	13.97	17.94	51.38	52.23	27.4	16.02	1036.28	566.05

As it can be seen in the previous table, although the ultimate capacity of the epoxy-repaired specimens showed no increase whatsoever, the cracking load increased between 15% and 28%. On the other hand, the ultimate deflection of the epoxy-repaired specimens decreased between 8% and 42% (i.e., the more damage prior to repairs, the more reduction in the

ultimate deflection). In terms of ductility (defined as the area under the load-deflection curve), the epoxy-repaired specimens exhibited a decrease between 2% and 45% (i.e., the more damage prior to repairs, the more ductility degradation).

Table 2-2 shows the summary of the number of cracks and crack widths observed in the prototype and epoxy-repaired beams. Overall, both the prototype and epoxy repaired beams behaved in a similar manner.

Table 2-2. Cracking behaviour of the prototype and epoxy-repaired beams (Basunbul et al, 1990).

Damage Levels	Prototype beam			Repaired beam		
	No. of cracks	Maximum width (mm)	Max. width at SLS (mm)	No. of cracks	Maximum width (mm)	Max. width at SLS (mm)
10 mm	5	0.70	0.20	4	2.17	0.20
15 mm	6	1.10	0.23	5	2.00	0.20
Failure	6	2.50	0.23	4	2.67	0.20

Tasai (1992) investigated the effectiveness of epoxy injection in restoring bond, testing a reinforced concrete beam subjected to double curvature under an antisymmetric reverse loading with no axial load until splitting bond failure was observed. The specimen was repaired by injecting with low-viscosity epoxy resin through the splitting cracks and retested again following the same loading protocol. Figure 2-6 shows the cracking patterns and load-deflection curves of the prototype and epoxy-repaired specimens.

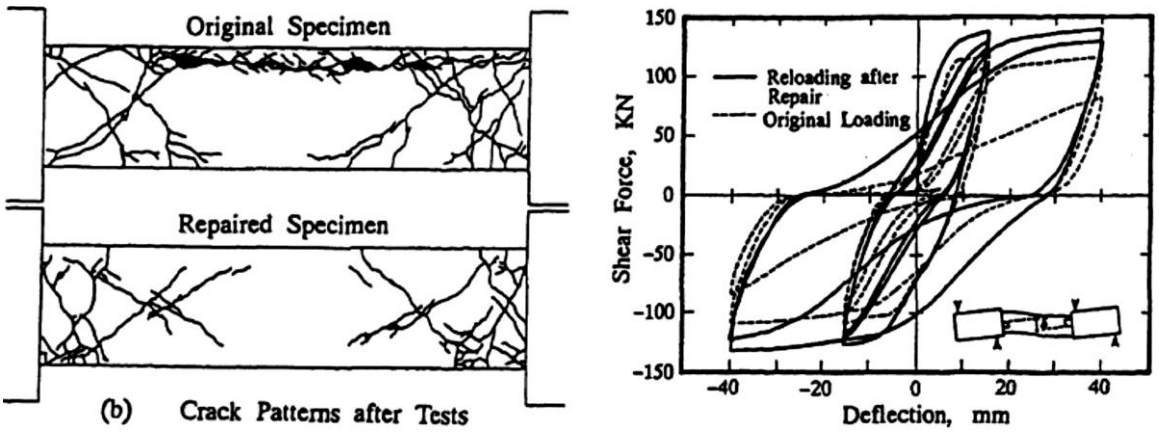

Figure 2-6. Cracking patterns (left) and load-deflection curves (right) of the prototype and epoxy-repaired specimen (Tasai, 1992).

From the previous figure it can be observed that the epoxy-repaired specimen failed in a flexure manner. The epoxy resin was effective in preventing the splitting bond failure to occur observed in the prototype specimen. The above becomes more evident by comparing the

cyclic behaviour of both specimens (Figure 2-6). The strength and stiffness of the epoxy-repaired did not deteriorate as in the prototytpe specimen.

Tasai, in order to investigate the effectiveness of the epoxy resin to restore bond, also performed three pull-out tests with and without transverse reinforcement. Figure 2-7 shows the cracking patterns and bond-slip curves obtained from the tests. While the prototype specimens failed in splitting bond, the epoxy-repaired specimens failed in shear. The bond-slip stiffness was not fully restored by the epoxy, but the bond stress doubled due to the adhesive strength of the epoxy resin injected around the bars.

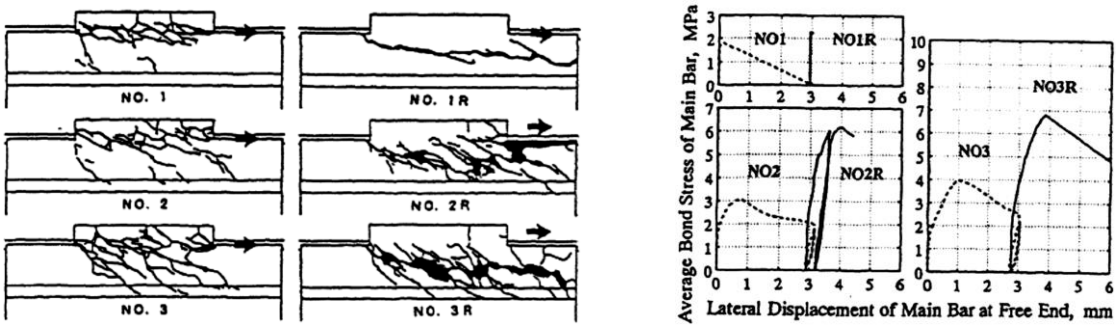

Figure 2-7. Cracking patterns (left) and bond-slip curves (right) obtained from the pull-out tests (Tasai, 1992).

Kunieda et al (2001) tested unreinforced concrete notched beams subjected to monotonic loading under a four-point loading condition, aiming at investigating the effect of the roughness surface on the bond properties between the epoxy resins and concrete. The fractured surface after the test was repaired with epoxy injection and retested again. The results were compared with those obtained using control (uncracked) specimens and specimens with smooth surfaces epoxied together. They observed that the flexural strength, fracture energy and ductility of the repaired specimens exceeded those from smooth and uncracked specimens.

They also tested a reinforced concrete beam under a four-point loading condition subjected to monotonic loading until reaching a curvature ϕ of 1.5×10^{-4} rad/mm, the cracks between 0.2 mm and 0.8 mm were epoxy-injected and the specimen was retested again. Figure 2-8 shows the moment-curvature and cracking pattern of the prototype and epoxy-repaired specimen. The initial stiffness of the repaired specimen was lower than the prototype one due to the existence of narrow cracks that could not be injected. In terms of cracking pattern, the unrepaired cracks opened-up and new ones developed adjacent to the repaired cracks.

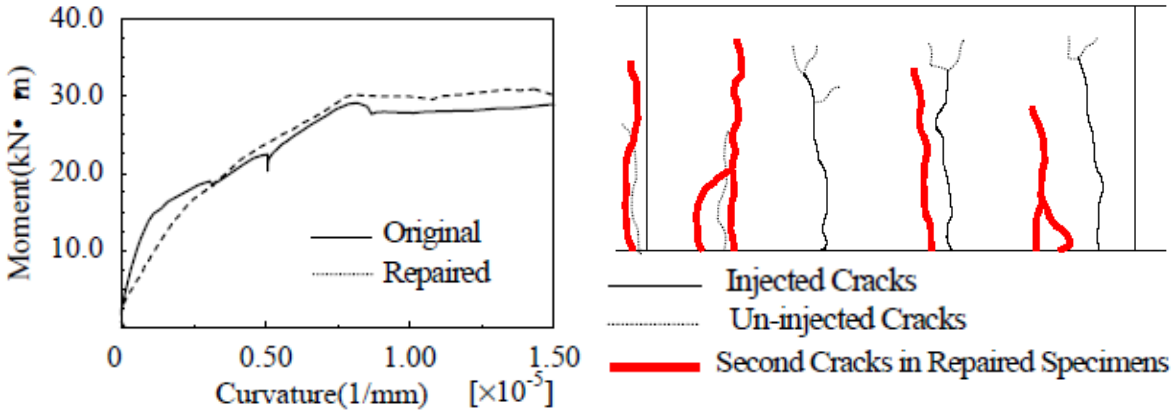

Figure 2-8. Moment-curvature (left) and cracking pattern (right) of prototype and epoxy-repaired specimens (Kunieda et al, 2001).

Ahmad et al (2013) also tested reinforced concrete beams subjected to monotonic loading under a four-point loading condition. The specimens were loaded until cracks 1 mm wide were observed. The load was removed, and the cracks were repaired with a low viscosity epoxy (Type I, Grade 1, Class B+C as per ASTM C881-78), let cured and retested again up to failure. They observed that in the repaired specimens, 33% more deflection and 49% more load compared to the prototype specimens was required in order to develop cracks 1 mm wide. In addition, the repaired specimens exhibited the same or slightly higher initial stiffness. The energy absorption, estimated as the area under the load-deflection curve, was also higher for the repaired specimen.

2.2.2 Reinforced concrete beam-column joints

Karayanis et al (1998) tested seventeen exterior beam-column joints, approximately half-scale, to investigate the efficiency of epoxy repairs with reference to the joint shear reinforcement. Only the results of joints with stirrups and detailed such that strong-column/weak-beam mechanism prevails (which corresponds to specimens with X-type reinforcement within the joint), are described herein. The specimens were tested cyclically, repaired and retested following the same loading protocol. The first loading cycle corresponded to 1.2 to 1.5 times the yield displacement. The following loading cycles were gradually increased at a rate of 2.5 mm/cycle, until the lateral capacity of the specimen decreased to approximately 40% of the yield load level, which was considered as failure. The specimens were repaired with a low-viscosity resin of 2-3 poises and 40 min pot life, with tension and compression strengths of 60.8 MPa and 92.2 MPa. They observed that the repaired specimens resisted more full loading cycles of gradually increasing displacement without significant loss of strength, as well as equal or higher maximum loading cycles (i.e.,

greater displacement ductility capacity) to those of the prototype specimen. Table 2-3 shows comparative values between the repaired and prototype specimens. In the table, the stiffness ratios are estimated using tangent stiffness at 80% of the cycle peak load, and the mean values correspond to the average of the first 10 loading cycles. It is observed that the initial stiffness (at the 1st cycle) of the repaired specimens is higher compared to the prototype ones, and although it degrades more rapidly during the following loading cycles, on average the stiffness of the repaired and the prototype specimens is very similar. They concluded that "*the loading stiffness of the repaired joints was restored satisfactorily achieving similar stiffness levels to the virgin joints*".

Regarding the energy dissipation characteristics of the repaired specimens, it decreased during the 1st loading cycle, potentially due to the fact that most likely not all the cracks were epoxied. However, more energy was dissipated in the repaired specimens during subsequent loading cycles. In fact, and as mentioned before, the repaired specimens resisted more loading cycles without significant loss of strength, contributing to the increase in the energy dissipation. Also, the hysteresis loops of the repaired specimens showed a less pinched (i.e., fatter) behaviour (see Figure 2-9).

Table 2-3. Response ratios (repaired upon prototype) of tested beam-column joints with stirrups in the joint and strong-column/weak-beam behaviour (Karayannis et al, 1998).

Joint Code	Failure cycle	Load ratio				Stiffness ratio				Energy ratio			
		Cycles			Mean	Cycles			Mean	Cycles			Mean
	r/i	*1st*	*3rd*	*10th*	*value*	*1st*	*3rd*	*10th*	*value*	*1st*	*3rd*	*10th*	*value*
JX2b	22/32	1.21	1.23	1.30	1.24	1.29	1.04	0.99	1.05	0.70	1.60	2.27	1.94
JX1	29/32	1.32	1.38	1.43	1.40	1.65	1.41	0.75	1.05	0.79	1.51	2.49	2.12
JX1b	25/24	1.09	1.12	1.32	1.19	1.33	1.25	0.76	1.00	0.64	1.64	2.32	1.94

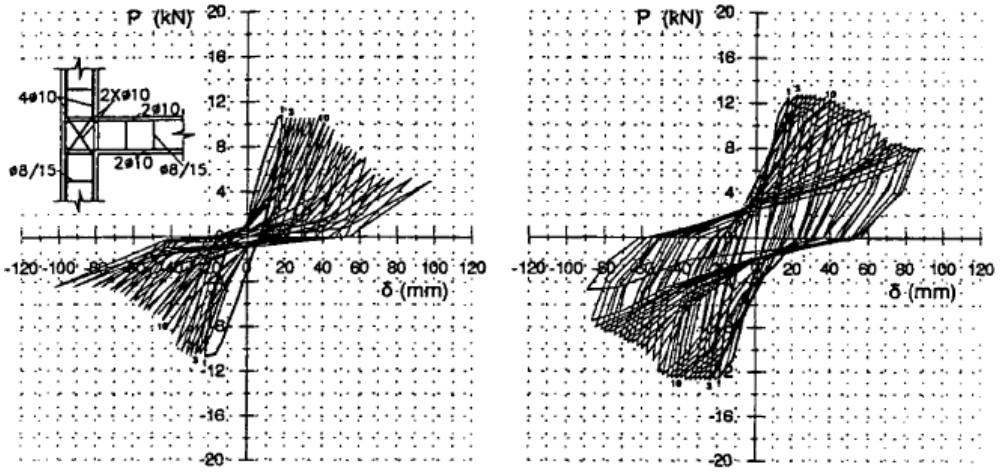

Figure 2-9. Hysteretic behaviour of joint JX2b, prototype (left) and repaired (right) specimens (Karayannis et al, 1998).

The failure mode of the prototype specimens was characterised by hairline cracking at the joint region and at beam-ends during the first two or three loading cycles, followed by localised damage at the beam-end during subsequent loading cycles, until a distinct plastic hinge was developed.

The failure mode of the repaired specimens was characterised by cracks developing at the beam-end adjacent to the repaired part. The cracks increased and became wider during subsequent loading cycles, until the concrete at the beam-end adjacent to the repaired part was "*seriously fragmented and disorganised*". Therefore, the epoxy repairs "*strengthened*" the joint so that no damage was observed during the test, potentially due to the higher tensile and compressive strength of the epoxy compared to the concrete strength.

No maximum and residual cracks are reported, and there is no indication of fractured bars at any stage of the tests. They concluded that "*the examined repair technique either improves the failure behaviour of the beam-column joint or, in the worst case, it does not change the failure characteristics of the virgin joint*".

French et al (1990) conducted two different tests to investigate the effectiveness of epoxy injection techniques to repair moderate earthquake damaged internal beam-column joints. The ratio of the column moment capacities to the beam moment capacities was 1.8, ensuring a strong-column/weak-beam mechanism. The specimens were first subjected to reverse cyclic loading to replicate moderate earthquake damage, repaired and subjected again to the same cyclic load regime. They applied two different epoxy techniques namely pressure injection and vacuum impregnation.

The cracks were repaired with a low viscosity epoxy with 2.4 poise and 80 min pot-life. They chose this epoxy between three different types because it offered the best overall characteristics for both pressure injection and vacuum impregnation techniques.

The loading protocol consisted of lateral cyclic displacements with displacement ductilities varying from +1.0/-0.5 to +4.0/-4.0, with a theoretical yield displacement estimated as 25.4 mm.

As shown in Figure 2-10(a), the repaired specimens RPI and RVI (*P* stands for pressure injection, whilst *V* stands for vacuum impregnation) achieved 89% and 85% of the stiffness of the respective prototype specimen, after the first cycle of loading. However, by comparing the initial stiffness of the repaired specimen with the one of the damaged specimen prior to repairs, is clear that the initial stiffness of the repaired specimens increased 3 and 2.5 times. Figure 2-10b shows energy dissipation ratios; it is evident how the repaired specimens can

dissipate between 55 and 100% of the prototype specimen. They found that the peak strengths for the prototype and repaired specimens were similar, indicating that the epoxy injection techniques are effective in restoring the strength of the specimens. Figure 2-11 shows the measured slips of the prototype and repaired specimen during cycles 6th and 7th. The bond appeared to be restored quite well with both techniques.

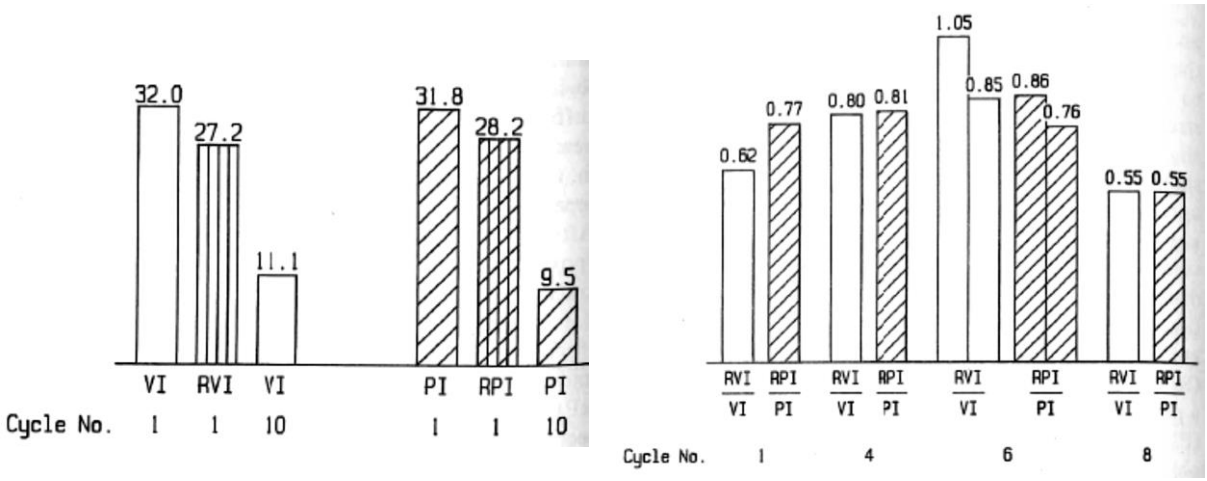

Figure 2-10. Stiffness comparison (a) and energy dissipated ratio (b) for repaired to prototype models (French et al, 1990)

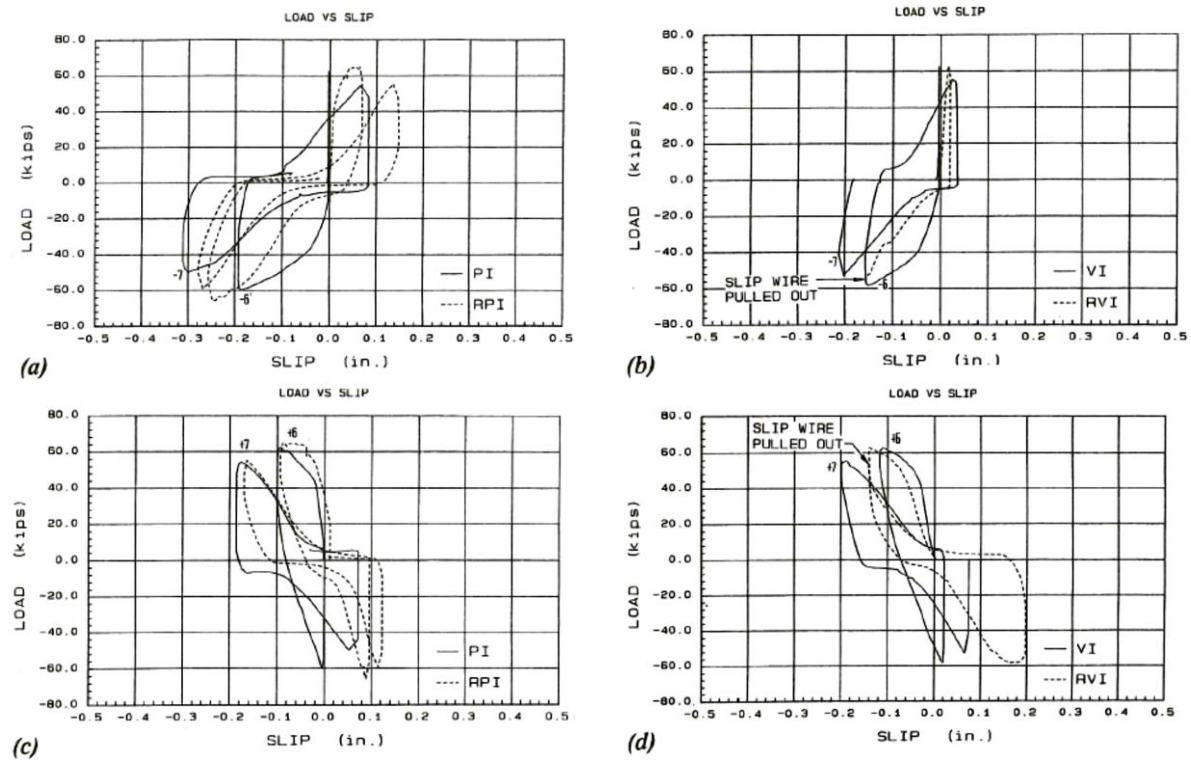

Figure 2-11. Measured slips at cycles 6 and 7 for: *PI* and *RPI* at top beam reinforcement (upper left); *VI* and *RVI* at top beam reinforcement (upper right); *PI* and *RPI* at bottom beam reinforcement (lower left); and *VI* and *RVI* at bottom beam reinforcement (lower right) (French et al, 1990).

Filiatrault and Lebron (1996) investigated experimentally the effectiveness of the epoxy pressure injection technique, testing two full-scale exterior beam-column joints typical of a first-floor beam-column joint of a prototype three-storey office building, under reversed cyclic loading. The first specimen (*S1*) was typical of older construction (1950s and 1960s), whereas the second one (*S2*) was typical of new structures incorporating seismic detailing. Similar to French et al (1990), the repaired specimens were subjected to the same loading protocol as the prototype specimens. The discussion hereafter is based on specimen *S2*.

A Medium Penetration (MP) commercial epoxy with a low viscosity of 0.4 poise and a pot life of 12 minutes was chosen for the repairs.

Significant inelastic deformation occurred in the beam longitudinal reinforcement (with measured strains over 40,000με) while the shear mechanism of the joint remained elastic. The test was completed up to a displacement ductility level of 4 without any significant loss of strength. Both the positive and negative probable strengths were reached and maintained throughout the test. The hysteresis loops were large and stable with high energy dissipation per cycle.

The epoxy repaired plastic hinge also reached ductility levels of 4 but with slightly higher loads than the prototype specimen (for ductility levels above 3). However, the hysteresis loops of the repaired specimen exhibited more pinching than the prototype one.

As shown in Figure 2-12, the stiffness of the epoxy-repaired specimen *S2* was around 85% of the stiffness of the prototype specimen up to a ductility of 2.5. For higher ductility levels, the prototype and repaired specimens developed similar stiffness values.

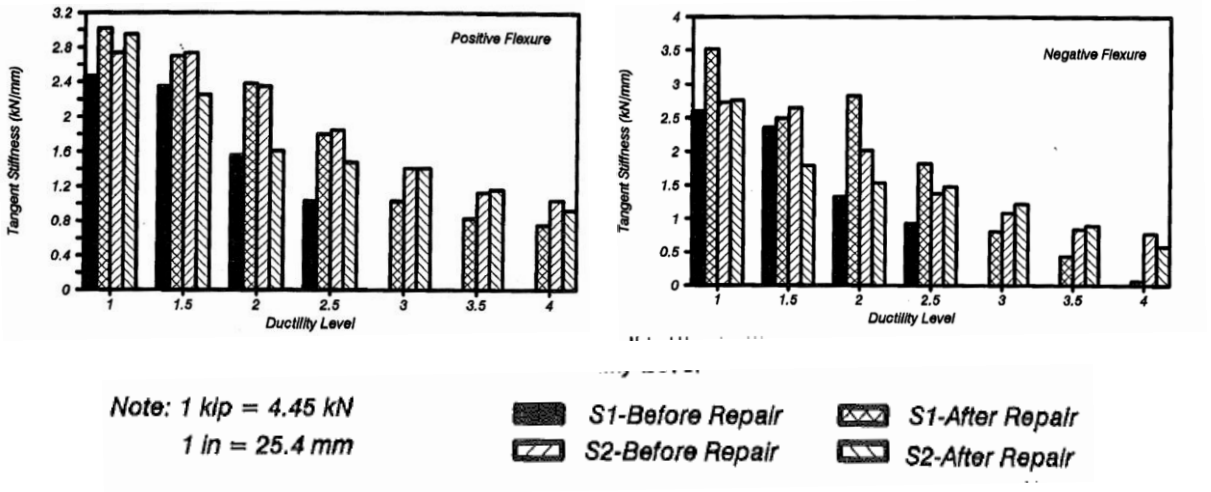

Figure 2-12. Tangent stiffness degradation for the poor detailed (S1) and seismic detailed (S2) beam-column joint (Filiatrault and Lebrun, 1996).

The energy dissipation was assessed by computing the cumulative external work during each test. As shown in Figure 2-13, more energy dissipation was observed in the prototype specimen. At the end of the tests, the epoxy-repaired specimen dissipated 77% of the energy dissipated by the prototype specimen.

In general, they concluded that the epoxy repairing technique is a possible repair procedure for moderate earthquake damage, especially for well-designed beam-column joints for which the strength, stiffness and energy dissipation are increased as a result of the repairing procedure.

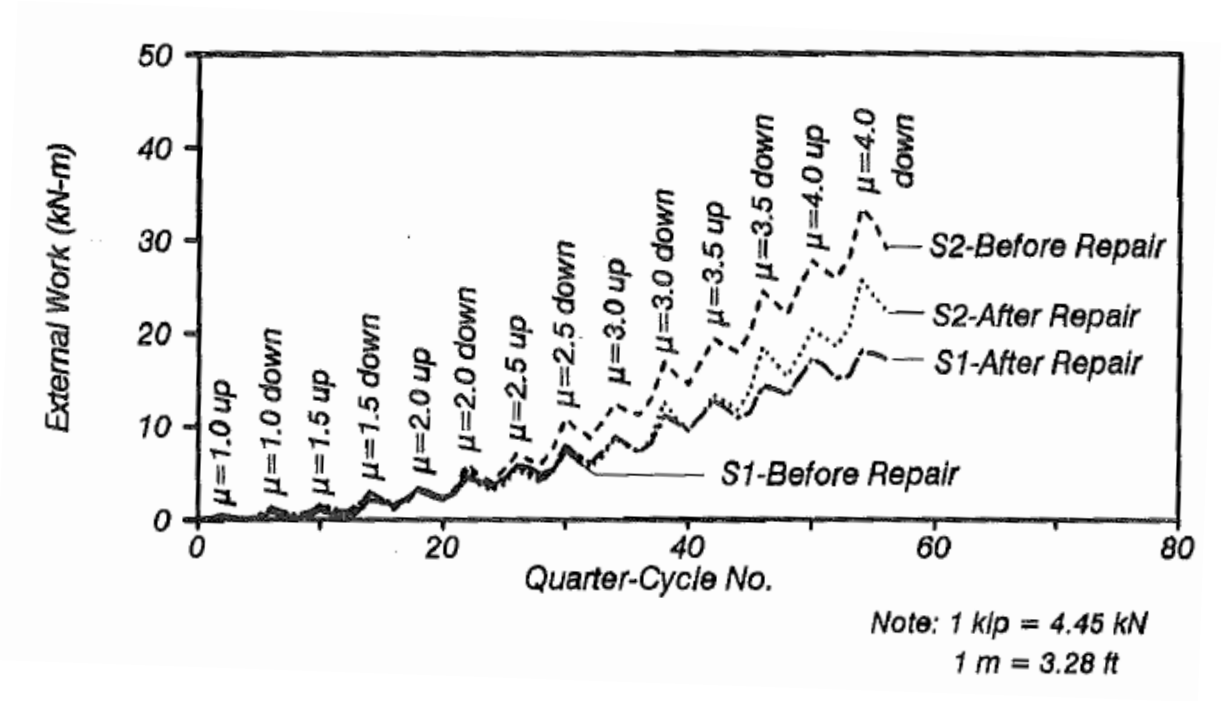

Figure 2-13. Cumulative external work (Filiatrault and Lebrun, 1996).

Tsonos (2002) and Tsonos and Papanikolaou (2003) tested two modern one-half scale exterior beam-column joints designed as per the ACI-318 and ACI-ASCE 352 (specimen *A*) and the Eurocode 2 and Eurocode 8 (specimen *E*). The specimens were subjected to a constant axial load of 200kN and a reverse cyclic loading regime. The displacement increased gradually by 5 mm (drift angle of 0.5%) at each subsequent cycle. The specimens behaved as expected, developing a plastic hinge at the beam end. The specimen *E* developed also some hairline cracking and loss of the concrete cover within the joint region, and anchorage failure of the beam longitudinal bars.

The specimens were repaired by removing and replacing all the spalled concrete with high strength mortar and epoxy resin crack injection. The spalled concrete within the joint of

specimen *E* was removed and replaced with a thick layer of epoxy resin paste. The specimens were let cured for seven days and retested again following the same loading protocol.
The failure mode of the repaired specimens was "*nearly identical*" to that of the prototype specimen *A*, with the difference that some of the beam longitudinal bars in the repaired specimens *RA* and *RE* fractured at 5% and 6% drifts. Figure 2-14 shows the load-displacement curves of the prototype and repaired specimens. The prototype specimens exhibited a stable hysteretic behaviour up to 4.0% drift, beyond which the strength and stiffness degraded gradually.
The repaired specimens exhibited a stable behaviour up to 4.5% drift. The strength and stiffness started degrading due to buckling and fracture of some of the beam longitudinal bars. It is possible that the buckling started during the prototype test and worsened during the post-repair test. The lower strength and stiffness in the negative direction in test *RE* was due to bond degradation of the top bars in the beam and consequently lack of good anchorage.

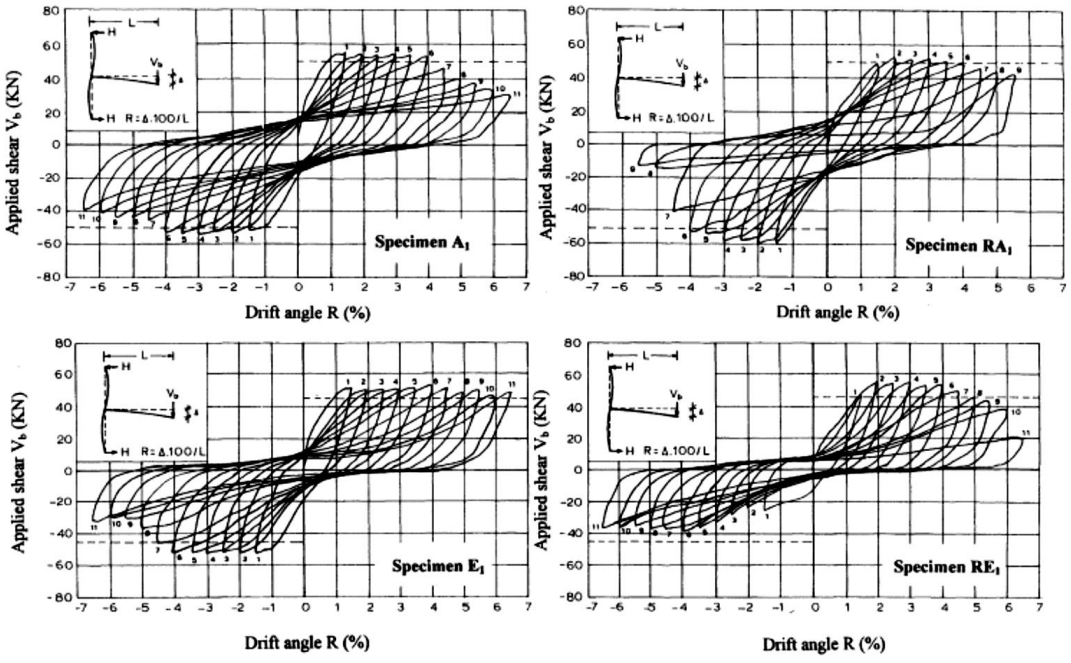

Figure 2-14. Force-displacement curves of the prototype and repaired specimens (Tsonos, 2002).

It was observed that the bond was not fully restored along the development length of the beam reinforcement. This observation agrees with other researchers which have found that epoxy injection techniques can, at least, partially restore the bond between steel and concrete (e.g., Tasai, 1992, Karayannis et al, 1998).

In general, the strength, stiffness and energy dissipation characteristics of the repaired specimens was comparable to those of the prototype specimens. The only exception was the specimen designed according to the Eurocodes at lower drift levels.

Karayannis and Sirkelis (2008) also investigated the effectiveness of the epoxy injection in the repair of damaged beam-column joints. One modern beam-column joint was subjected to a constant axial load of 70kN (P_u/f'_cA_g = 5%) and reverse cyclic loading regime. The displacement increased gradually by 10 mm (drift angle of 1.0%) at each subsequent cycle, up to a drift level of 4% (specimen *B1*). The specimen was repaired by epoxy injecting the cracks and then subjected to the same loading protocol with two extra loading cycles at 5% and 6% (specimen *B1R*).

The prototype specimen *B1* started developing cracks within the joint and at the beam-end (i.e., at the plastic hinge region), and continued developing at the beam-end until the formation of a plastic hinge. A major crack 20 mm at the beam-column interface was observed.

The epoxy-repaired specimen *B1R* developed cracks within the beam only from the start of the test, and eventually developed a plastic hinge away from the column face at a point where it was not epoxy-repaired (i.e., the plastic hinge was relocated). Figure 2-15 shows the force displacement curves and energy dissipation of both specimens. It can be observed that the strength of the repaired specimen did not degrade significantly even at drift levels of 6%. The energy dissipation characteristics of both specimens was comparable (see also Table 2-4).

Table 2-4. Observed maximum load per cycle and hysteretic energy dissipation estimated as the are under the load-displacement curves (Karayannis and Sirkelis, 2008).

	P_{max} (kN/cycle)		E	P_{max} (kN/cycle)		E	P_{max} (kN/cycle)		E	P_{max} (kN/cycle)		E
	+ 1st	- 1st	(kNm)	+ 2nd	- 2nd	(kNm)	+ 3rd	- 3rd	(kNm)	+ 4th	- 4th	(kNm)
B1	24.0	22.0	0.214	23.5	22.0	0.638	22.5	22.0	1.089	16.0	21.5	1.309
B1R	24.0	24.5	0.186	25.0	24.5	0.740	26.0	24.5	1.314	26.0	24.0	1.812

They also computed damage indices as per Park and Ang (1985) and determined that the damage indices of the repaired specimen were lower and those of the prototype specimen, at all drift levels. They concluded that "*the use of epoxy resin even in the cases of large-scale damage* [referring to cracks equal to or greater than 20 mm] *can restore the response of the specimens*".

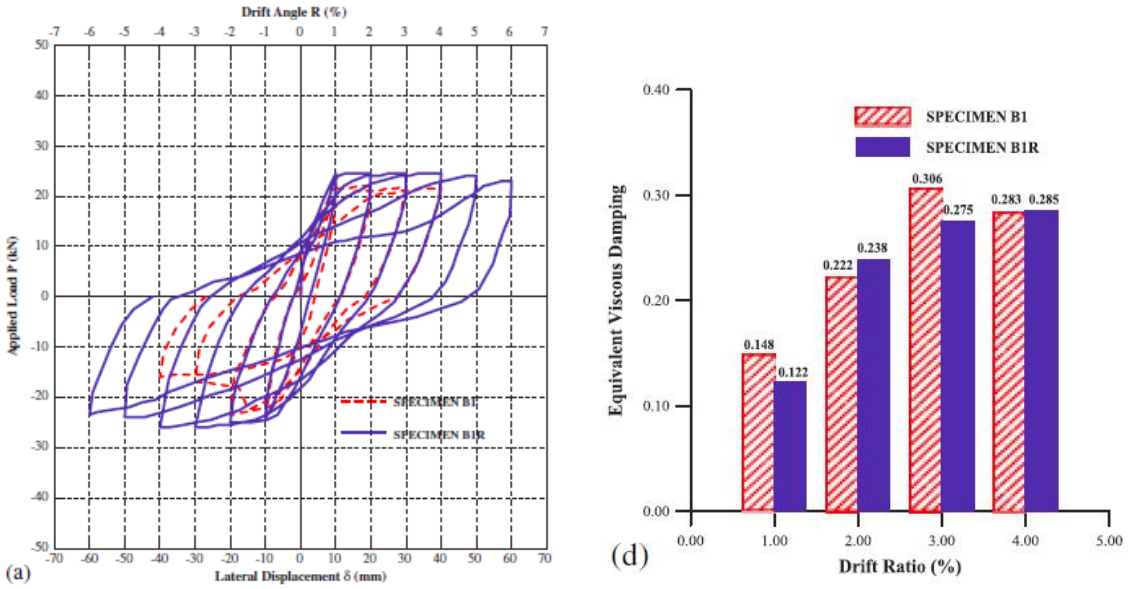

Figure 2-15. Force-displacement curves (left) and equivalent viscous damping values (right) of the prototype and epoxy-repaired specimens (Karayannis and Sirkelis, 2008).

2.2.3 Shear walls

Takahashi et al (1988) investigated the correlation between seismic damage and inelastic behaviour of RC shear walls. Both flexural-shear and flexural failure modes were experimentally tested. In the case of walls with flexural-shear failure modes, three specimens were subjected to loading histories representative of severe, moderate, and slight damage. The walls were subsequently repaired by epoxy injecting the cracks and removing and replacing the crushed and spalled concrete with epoxy-mortar. After letting the specimens cure they were retested again using the moderate damage loading history. They observed that the behaviour of the specimen subjected to severe damage with that of the repaired specimen agreed very well (see Figure 2-16), suggesting that the epoxy injection techniques are effective for restoring stiffness, strength and ductility of RC walls.

Lefas and Kotsovos (1990) investigated the effect of loading history and repair methods on ductile RC shear walls. The walls were tested to failure using different loading regimes, repaired by either replacing the damaged concrete in the compressive zone, or a combination of concrete replacement and epoxy injecting the cracks, and retested to failure. They found that, although the effect of epoxy repairs on the ultimate strength of the (severely damaged "to failure") walls was negligible, it improved the stiffness and energy-dissipation characteristics of the walls at the Serviceability Limit State.

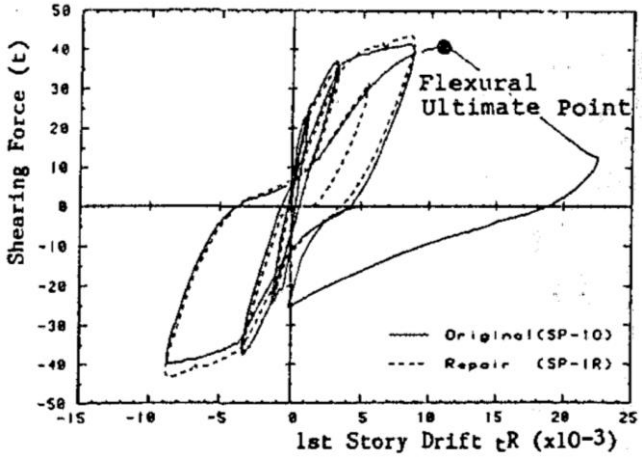

Figure 2-16. Load-deformation curves for a RC wall subjected to severe damage, before and after repairs (Takahashi et al, 1988).

Chiou et al (2003) tested large-scale (approximately half-scale) specimens under reversed displacement control cyclic lateral loading. The specimens were not axially loaded, and the loading history included only one cycle at each displacement. Three of the specimens, a framed wall with a central doorway (*DFW*), a frame with wing walls (*WFW*), and a solid framed wall (*LWF1*) were repaired by low-pressure epoxy injection techniques.
Ductility ratios at peak displacement of 1.27, 1.28, and 1.84, respectively, were achieved in the prototype tests.
They observed that the specimens repaired by epoxy injection experienced the same failure mechanisms as the prototype ones. A comparison of the performance of the prototype and epoxy-repaired specimens is summarised in Table 2-5. They concluded that "*the strength, deformation capacity, ductility ratio and energy dissipation characteristics of the repaired specimens were better or close to those of the prototype ones. However, their rigidity tends to be softer*". No maximum and residual cracks were reported, and there is no indication of fractured bars at any stage of the tests.

Table 2-5. Cyclic resistance of specimens as ratio of the prototype upon repaired specimens with epoxy injection (Chiou et al, 2013)

Specimen	Strength ratio	Rigidity ratio	Deformation ratio	Ductility Ratio	Energy diss. Ratio
DFW	0.98	0.95	1.03	1.09	1.01
WFW	1.01	0.60	1.68	1.24	2.51
LWF1	1.17	0.36	3.27	2.78	4.90

2.2.4 Full-scale frame and shear wall buildings

Okmoto et al (1985) performed a full-scale test on a seven-storey reinforced concrete structure under pseudo-dynamic loading. The structure consisted of three three-bay frames (the central one with a full height shear wall) in the direction parallel to the load, and four two-bay frames in the perpendicular direction. The prototype structure was subjected to four different earthquakes with increased damage or intensity levels. The structure was also subjected to free vibration in order to determine its natural period. The earthquake sequence induced maximum drift levels varying from 0.15% to 1.56%. The initial (uncracked) natural period was found to be 0.43 sec. At the end of the earthquake sequence, the natural period elongated to 1.36 sec.

At peak displacement, the damage consisted of a 4 mm wide flexural cracks at the base of the wall, shear cracks in the shear wall greater than 7 mm wide, crushing and spalling in beams connected to the wall, spall at the base of the walls, and buckling of beam longitudinal bars framing into the wall at the seventh storey.

The cracks in the walls and beams were injected with epoxy resin and the spalled concrete was removed and replaced with epoxy mortar. The buckled bars were cut and replaced with butt-welded bars, and supplemental confinement with U-shaped stirrups were provided at those locations. Additionally, non-structural elements (spandrel and partition walls, ceilings and glazing at some locations) were also installed. The repaired structure was subjected to the same earthquake sequence except for the last earthquake which was replaced by a static loading test due to limitations in the actuator capacity.

The natural period of the repaired structure without the non-structural elements was found to be 0.63 sec (i.e., 1.47 times the prototype's natural period, and 0.46 times the period of the damaged structure prior to the repairs). The natural period was further reduced to 0.52 sec after the installation of the non-structural components. In other words, the initial stiffness of the repaired structure was smaller than that of the prototype structure, although it was partially recovered by the repair works. They found that the maximum displacement response of the prototype and repaired structure was almost the same. The cracking pattern was also very similar, with the difference that crushing and spalling of the repaired beams did not occur.

More recently, Yu et al (2014) validated the effectiveness of the epoxy injection repairs by testing a one-fourth scale, eight-storey, two-bay (in both orthogonal directions) reinforced concrete frame structure in the shake table. The structure was subjected to four earthquakes of different intensities, varying from what can be considered frequent earthquakes up to rare

earthquakes of intensity 8.5. After running the tests, the cracks were classified by their width, quantity and location. Table 2-6 summarizes the results.

The type of observed damage consisted of wide cracks and concrete crushing at the beam-column interface; diagonal and vertical cracks within the beam plastic hinge region; minor cracking at the beam soffits at mid-span; horizontal cracks in the columns at the top floor; and cracks at the top of the slabs at the supports where the negative moment is developed. In general, the damage was more noticeable in the upper floors compared to the lower ones.

Table 2-6. Quantity of cracks categorized by width and location (Yu et al, 2014).

Crack location	**Crack widths (mm)**			
	0.01 - 0.10	**0.10 - 0.30**	**0.30 - 1.0**	**≥ 1.0**
Mid-span of beam	54	42	2	-
Beam-end	45	60	18	12
Interface of joint	-	-	-	131
Column	22	16	4	2

The structure was epoxy repaired, let cure for 28 days and subjected to the same earthquake sequence. They observed that all cracks in the repaired structure formed at different locations, none of the repaired cracks opened-up again. The failure mode varied from joint failure to beam plastic hinging, and the new cracks developed away from the column face at a distance equal to 0.5 to 1 times the beam depth. Opposed to the prototype test, the beams at the lower levels exhibited more damage compared to the ones at upper levels. The damage in the columns at lower levels was similar (i.e., slight) to that of the prototype test, however the cracking at upper levels was less than in the prototype test.

Figure 2-17 shows the comparison of the natural frequency and damping ratio of the prototype and epoxy-repaired structure measured at each of the earthquakes. As expected, the frequency of both prototype and epoxy-repaired structures decreased (i.e., the stiffness degraded) with the increase of the number of earthquakes and their intensity level. However, the degradation was less in the epoxy-repaired structure.

In terms of frequency, it can be observed that the initial stiffness of the epoxy-repaired structure was only slightly exceeded by that of the prototype structure. The natural frequency of the structure went from 1.6-1.7 Hz (in the *X* and *Y* directions, respectively) in its pre-earthquake condition, to 0.65-0.75 Hz (in the *Y* and *X* directions, respectively) in its damaged condition. The natural frequencies in its repaired condition ended up being 1.6 Hz in both directions, which compares very well to the pre-earthquake natural frequencies. In other words, the epoxy injection was very effective in restoring the initial stiffness of the structure.

At large earthquake intensities, the epoxy-repaired structure resulted stiffer (i.e., with a higher natural frequency) than the prototype structure. Overall, the damping or energy dissipation characteristics of the epoxy-repaired structure was higher at all earthquake intensities.

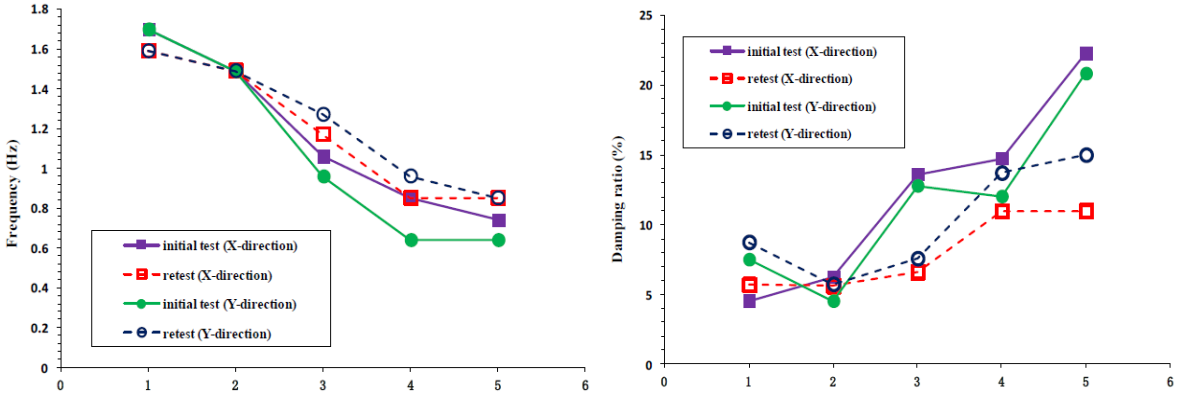

Figure 2-17. Comparison of the natural frequency (left) and damping ratio (right) of the prototype and epoxy-repaired structure, in both orthogonal directions, measured at each of the earthquakes (Yu et al, 2014).

2.3 Damage evaluation and repair strategies

Hose et al (2000), acknowledging that although "*current design methodologies expect that a structure will not collapse at a maximum level design earthquake, the amount of damage in a structure after a small and moderate earthquakes is unknown*", defined five different damage levels for bridge components and systems based on experimental tests performed over 15 years preceding the publication. The damage levels were correlated with a general repair description and the socio-economic impact. For each damage level, qualitative and quantitative performance descriptions are provided.

Brown and Lowes (2007) correlated deterministically fourteen damage states with repair methods typically employed. They stated that "*in defining damage states associated with concrete cracking, two critical damage states are the concrete crack width at which surface finishes, such as paint or plaster, have to be repaired and the crack width at which epoxy injection of cracks is required to restore the component to its pre-earthquake strength and stiffness*".

More recently, Maeda et al (2017) classified the structural damage into five different classes depending on the severity of the observed damage.The previous research work by Maeda et al (2017), Brown and Lowes (2007) and Hose et al (2000) on damage levels and repair methods is summarised and grouped in Table 2-7 in an effort to seek agreement and unify the repair criteria.

Table 2-7. Comparison of damage levels definition and repairs methodologies found in literature.

Level	Maeda et al (2017) - buildings	Brown and Lowes (2007) – beam-column joints		Hose *et al* (2000) – bridge components	
I Slight	Some cracks less than 0.2 mm are observed.	Initial hairline cracking at the beam-column interface.	Repair: replace and repair finishes.	Onset of hairline cracks.	No repair
		Initial hairline cracking within the joint area.		Theoretical first yield of longitudinal reinforcement. Crack widths less than 1 mm.	Possible repair.
		Maximum crack width within the joint is less than 0.5 mm.			
II Minor	Cracks 0.2 to 1 mm wide are observed.	Maximum crack width within the joint is greater than 0.5 mm.	Inject cracks with epoxy and replace finishes.	Initiation of inelastic deformation. Onset of concrete spalling. Development of diagonal cracks. Crack widths 1 mm to 2 mm wide. Length of spalled region greater than 10% of cross-section depth.	Minimum repair
		Transverse reinforcement yields.			
III Moderate	Heavy cracks 1 to 2 mm wide are observed. Some spalling of concrete is observed.	Maximum crack width within the joint is greater than 1.3 mm.			
		Initiation of beam-bar slippage in the joint.			
		Spalling of at least 10% of the joint surface concrete.	Patch spalled concrete, inject cracks with epoxy, and replace finishes.	Wide crack widths and spalling over full local mechanism region. Crack widths greater than 2 mm. Diagonal cracks extend over two-thirds the cross-section depth. Length of spalled region greater than 50% of cross-section depth.	Repair.
IV Severe	Many heavy cracks greater than 2 mm wide are observed. Reinforcing bars are exposed due to spalling of the cover concrete.	Joint shear strength begins to deteriorate.			
		Spalling of more than 30% of the joint surface concrete.			
		Crack widths in excess of 1.3 mm extend into the beam and/or	Remove and replace damaged concrete, replace finishes.		
V Collapse	Buckling of reinforcement, concrete crushing and vertical deformation of columns and/or shear walls are observed. Side-sway, subsidence of upper floors, and/or fracture of reinforcing bars are observed in some cases.	Spalling of more than 80% of the joint surface concrete.		Buckling of main reinforcement, rupture of transverse reinforcement, crushing of core concrete. Crack widths greater than 2 mm in concrete core. Measurable dilation greater than 5% of original member dimension.	Replacement.
		Crushing of concrete extends into joint core.			
		Buckling of col. long. reinf., or loss of beam reinf. anchorage in joint.	Replace damaged steel, concrete and finishes.		

As can be seen from Table 2-7, Maeda et al (2017) do not suggest repair actions for each of the damage classes. However, from Figure 2-18 it can be inferred that, since the lateral and vertical load carrying capacity is mantained for damage classes I to III (the vertical load carrying capacity is also mantained up to damage class IV), damaged buildings categorized within those classes can be repaired.

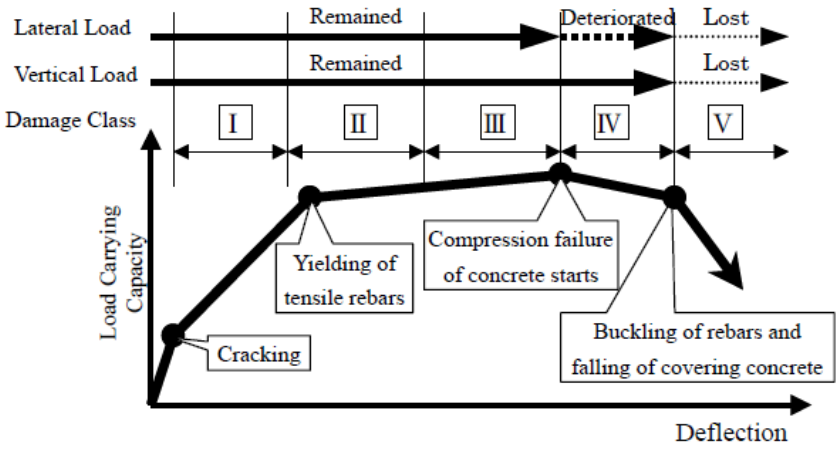

Figure 2-18. Idealized lateral force-displacement relationships for ductile structures and damage class (Maeda et al, 2017).

In fact, Sugano et al (2010) proposed a correlation between different damage levels with limit states in order to be applied during performance-oriented seismic rehabilitations during major earthquakes (Table 2-8).

Table 2-8. Limit states in the performance evaluation guidelines of the Architectural Institute of Japan, AIJ (Sugano et al, 2010).

Evaluation item	Limit State	Damage Level	Structural behaviour
Serviceability: Function maintenance	Serviceability Limit State	I	No yielding Residual cracks less than 0.2 mm wide
Repairability: Minor repairs	Repairability Limit State I	II	No cover concrete crushing Residual cracks less than 1.0 mm wide
Repairability: Repairable	Repairability Limit State II	III	No core concrete crushing Residual cracks less than 2.0mm wide
Safety: Human life protection	Safety Limit State	IV	No strength loss Maintaining axial force capacity

The similarities between the damage levels specified by Sugano et al (2010) and Maeda et al (2017) are evident. Sugano et at (2010) considered that a structure with a damage level I (no yielding and residual cracks less than 0.2 mm wide) requires cosmetic repairs only. A structure with a damage level II (no cover concrete crushing and residual cracks less than 1.0mm wide) requires minor repairs, whereas a structure with a damage level III (no core concrete crushing and residual cracks less than 2.0 mm wide) is still repairable.

The North American rehabilitation guidelines appear to be less conservative than the previous researchers and repair guidelines. The ATC-20 state that "*the effect of any crack more than 3.2 mm to 6.4 mm wide on the element and on the strength and stability of the overall structure should be carefully considered… Small cracks in concrete structural members may need only cosmetic repair. Still larger or more extensive cracks may require epoxy injection repair. Even larger cracks, crushing failures, or reinforcing steel bond slip failures, especially those associated with significant frame displacements, may require shoring, frame realignment, element replacement, or upgrade modifications… The more likely loss of bond to the concrete in such structures* [reinforced with higher-strength steels to reduce the required area of steel] *plus the possible fracture of the steel due to lower ductility will have to be investigated prior to epoxy injection repair of cracks over about 1/8"* [3.2 mm] *wide*".

Although there is no guidance on expected crack widths for each damage state described, we can infer that "*small cracks*" refer to cracks less than 0.2 mm wide, "*larger or more extensive cracks*" to cracks less than 3.2 mm wide, and "*larger cracks*" to cracks greater than 3.2 mm wide. The repair strategies outlined for each damage state are in line with the ones proposed by other researchers (e.g., Table 2-7).

FEMA P-154 state that cracking in columns and walls can affect the overall strength of the structure, its width and type (e.g., temperature, shrinkage, flexural or shear cracks) are worth noting, and "*for simplicity in rapid visual screening, concrete crack widths of 1/8"* [3.2 mm] *or greater should be considered significant*".

The ASCE 41-13, provide some guidance to determine the structural performance based on the observed damage. Table 2-9 shows examples of the expected damage at each performance level, for reinforced concrete frame and wall buildings. Immediate Occupancy is defined as the "*post-earthquake damage state in which a structure remains safe to occupy and essentially retains its pre-earthquake strength and stiffness*". Collapse Prevention is defined as the "*post-earthquake damage state in which a structure has damaged components and continues to support gravity loads but retains no margin against collapse*". Damage Control

is defined as the "*post-earthquake damage state between Life Safety and Immediate Occupancy performance levels*" (i.e., a significant lateral strength and stiffness degradation).

Table 2-9. Structural performance levels and illustrative example (ASCE 41-13).

		Structural Performance levels		
Lateral system	**Type**	**Collapse Prevention**	**Life Safety**	**Immediate Occupancy**
Concrete frames	Primary element	Extensive cracking and hinge formation in ductile elements. Limited cracking or splice failure in some nonductile columns Severe damage in short columns	Extensive damage to beams. Spalling of cover and shear cracking in ductile columns. Minor spalling in nonductile columns. Joint cracks	Minor cracking. Limited yielding possible at a few locations. Minor spalling of concrete cover
	Secondary element	Extensive spalling in columns and beams. Limited column shortening. Severe joint damage. Some reinforcing buckled.	Major cracking and hinge formation in ductile elements. Limited cracking or splice failure in some nonductile columns. Severe damage in short columns.	Minor spalling in a few places in ductile columns and beams. Flexural cracking in beams and columns. Shear cracking in joints.
	Drift	Transient drift sufficient to cause extensive non-structural damage. Extensive permanent drift.	Transient drift sufficient to cause non-structural damage. Noticeable permanent drift.	Transient drift that causes minor to no non-structural damage. Negligible permanent drift.
Concrete walls	Primary element	Major flexural or shear cracks and voids. Sliding at joints. Extensive crushing and buckling of reinforcement. Severe boundary element damage. Coupling beams shattered and virtually disintegrated.	Some boundary element cracking and spalling and limited buckling of reinforcement. Some sliding at joints. Damage around openings. Some crushing and flexural cracking. Coupling beams: extensive shear and flexural cracks; some crushing, but concrete generally remains in place.	Minor diagonal cracking of walls. Coupling beams experience diagonal cracking.
	Secondary element	Panels shattered and virtually disintegrated.	Major flexural and shear cracks. Sliding at construction joints. Extensive crushing. Severe boundary element damage. Coupling beams shattered and virtually disintegrated.	Minor cracking of walls. Some evidence of sliding at construction joints. Coupling beams experience x-cracks. Minor spalling
	Drift	Transient drift sufficient to cause extensive non-structural damage. Extensive permanent drift.	Transient drift sufficient to cause non-structural damage. Noticeable permanent drift.	Transient drift that causes minor to no non-structural damage. Negligible permanent drift.

Comparing Table 2-8 and Table 2-9, it appears that the *Repairability Limit State I* (minor repairs) corresponds approximately to the Immediate Occupancy Performance Level; *the Repairability Limit State II* (repairable) to the Life Safety Performance Level, and the Safety Limit State to the Collapse Prevention Performance Level.

FEMA-97 (1985) stated that cracks less than 6 mm wide in reinforced concrete elements can be repaired with epoxy injection techniques. Similarly, the Mexican Seismic Rehabilitation Guidelines for Buildings Damaged During the 19 September 2017 Earthquake (Jefatura de Gobierno, 2017) classify the damage into three different categories, as shown in Table 2-10. Epoxy resin injection techniques can be used to repair cracks between 0.2 mm and 5 mm wide (although some supplemental strengthening elements may be required to compensate for any loss of strength and stiffness, especially for severe damaged components). Cracks greater than 5 mm wide can be repaired with high strength mortars or epoxy mortars.

Table 2-10. Damage levels definition as per the Mexican Seismic Rehabilitation Guidelines (Jefatura de Gobierno, 2017).

Damage Level	Damage description (for concrete elements)
Slight	Cracks less than 0.2 mm wide
Intermediate	Cracks greater than 0.2 mm but less than 1.0 mm wide
Severe	Cracks greater than 1.0 mm wide Exposed longitudinal bars, buckled bars Spalled concrete. Punching shear cracks around columns in flat slabs

It is interesting, however, that Filiatrault and Lebrun (1996) suggested that although epoxy pressure injection method is recommended for cracks less than 6mm wide, some researchers have suggested that the maximum crack width should be not more than 1.0mm for shear cracks and 1.5mm for flexural cracks.

Tudor and Ciuhandu (1992) are in the same line of thinking. Based on previous experimental tests in coupling beams tested to damage levels equivalent to 75% and 90% of their maximum capacity repaired with epoxy-injection or concrete jacketing, they concluded that epoxy-repair of shear cracks between 0.3 mm and 1 mm wide, and flexural cracks between 0.3 mm and 1.5 mm wide, makes the coupling beam perform as intended (i.e., the coupling beam is restored to its pre-earthquake condition). Concrete jacketing would be required for wider cracks and/or when the coupling beam's original capacity needs to be enhanced.

Also, Priestley et al (1996) states that residual crack widths of 1.0 mm are "*frequently taken as the maximum width that can be tolerated in normal environmental conditions without*

requiring remedial action". This crack width is associated with steel strains expected during SLS events in bridge components, and correspond to a Damage Level I (i.e., minor repairs) as per Sugano et al (2010).

2.4 Summary and concluding remarks

In this Chapter, a literature review on previous research about the effectiveness of epoxy injection repairs for seismic applications has been presented. The focus of this literature review was repairs of damaged beam-column joints and structures designed according to modern codes, in which a stable inelastic behaviour is expected to occur.

In some cases, the specimens had to be repaired with a combination of epoxy crack injection, repairs of spalled or crushed concrete with epoxy mortar, and replacement of buckled bars.

Regarding beam-column joints subassemblies, some researchers observed that the repaired specimens had a reduced initial stiffness compared with the prototype (or undamaged) specimen, however, it was observed that typically the repaired specimens not only developed the same or better stiffness at higher displacement values, but they were stronger than the prototype ones, maybe due to relocation of the plastic hinge or strain-hardening of the longitudinal reinforcement (which has to be considered during the post-earthquake evaluations due to potential increase of rotation/strain demands and shear demands thus violating the capacity design principles).

The repaired specimens exhibited higher displacement ductility capacities. Although the bond between the steel and concrete was partially restored, it allowed the repaired specimen to dissipate at least the same amount of hysteretic energy.

Although the cracking pattern between the prototype and epoxy-repaired specimens was very similar, new cracks in the repaired specimens formed adjacent to the epoxy injected cracks; the repaired cracks did not open-up.

Therefore, even when the specimens had failed or suffered severe damage, evidenced by wide cracks, concrete crushing and spalling, and buckling of longitudinal reinforcement, the strength and ductility exhibited by the repaired specimens was similar or in some cases, better than the prototype specimen.

Probably two of the most interesting research programs available in literature are the ones by Okamoto et al (1985) and Yu et al (2014). They performed tests on a full-scale shear wall building and on a one-fourth scale frame building, respectively, subjected to earthquake loading. Using free vibration, they determined the fundamental periods of the structure in

their "as when new", damaged, and repaired conditions. Assuming that the mass is constant at any of the three building conditions, the change in stiffness is inversely proportional to the square of the fundamental period of the building.

$$k = (4 \cdot \pi^2 \cdot m) \cdot \frac{1}{T^2} = cst \cdot \frac{1}{T^2} \quad (2\text{-}1)$$

Table 2-11 shows a summary of the periods of the structures measured at each condition. Normalized initial stiffness values are also shown, along with the loss of stiffness in the damaged and repaired condition and the percent of the lost stiffness that was recovered after the structure was repaired. In the case of the shear wall building (Okamoto et al, 1985), the repairs (epoxy crack injection, epoxy mortar in spalled concrete, buckled bars replacement) were able to restore 40% of the lost stiffness, bringing the initial stiffness from 10% to 47% of the initial stiffness when it was new. On the other hand, the repairs (epoxy crack injection) of the frame structure were able to restore 88-100% of the lost stiffness, bringing the initial stiffness from 15-22% to 100-89%.

It is noteworthy that Okamoto et al (1985) reported flexural and diagonal cracks greater than 4.0 mm and 7.0 mm, respectively, as well as concrete crushing and spalling and buckling of beam longitudinal bars. Yu et al (2014) reported cracks greater than 1.0 mm wide in a one-fourth scale structure. Arguably, these crack widths and their effect are equivalent to wider cracks developed and repaired in a full-scale structure. Therefore, although the damage level was severe, the ability of the epoxy injection and repairs in general to restore the initial stiffness of the structure is significant.

Table 2-11. Summary table of results obtained from full-scale tests before and after repairs (*X* and *Y* represent the two orthogonal directions of the frame structure).

Building type (Reference)		Period (sec)	Normalized stiffness (%)	Loss of stiffness (%)	Stiffness recovery (%)
Shear wall building (Okamoto et al, 1985)	When new	0.43	100	-	-
	Damaged	1.36	10	90	-
	Repaired	0.63	47	53	40
Frame building (Yu et al, 2014)	When new (*X*)	0.63	100	-	-
	When new (*Y*)	0.59	100	-	-
	Damaged (*X*)	1.33	15	85	-
	Damaged (*Y*)	1.54	22	78	-
	Repaired (*X*)	0.63	100	0	100
	Repaired (*Y*)	0.63	89	11	88

In terms of damage assessment and repair guidelines, although there is some discrepancies between the assessment criteria and repair recommendations, it appears that there is consensus within the international community that concrete elements with cracks less than 0.2 mm wide only require cosmetic repairs; epoxy injection repairs of cracks less than 2.0 mm wide and concrete patching of spalled cover concrete (i.e., minor to moderate damage) is an appropiate repair strategy; and for severely damaged components (e.g., cracks greater than 2.0 mm wide, crushing of the concrete core, buckling of the longitudinal reinforcement) local replacement of steel and/or concrete in addition to epoxy crack injection is more appropriate.

2.5 References

Ahmad, S., Elahi, A., Barbhuiya, S., Farooqi, Y. (2013) "Repairs of cracks in simply supported beams using epoxy injection technique," *Materials and Structures*, Vol. 46: 1547-1559.

American Concrete Institute (2007) *Causes, evaluation, and repair of cracks in concrete structures (ACI 224.1R-07)*, ACI Committee 224, Michigan.

American Society of Civil Engineers (2013) *Seismic evaluation and retrofit of existing buildings (ASCE 41-13)*, Reston, Virginia.

Applied Technology Council, ATC (1994) *Procedures for earthquake safety evaluation of buildings (ATC-20)*, California.

Applied Technology Council, ATC (2015) *Rapid visual screening of buildings for potential seismic hazards: A handbook (FEMA P-154)*, Third Edition, California.

Basunbul, I.A., Gubati, A.A., Al-Sulaimani, G.J., Baluch, M.H. (1990) "Repaired reinforced concrete beams," *ACI Materials Journal*, Vol. 87(4): 348-354.

Bertero, V.V., Rea, D., Mahin,S., Atalay, M.B. (1972) *Rate of loading effects on uncracked and repaired reinforced concrete members*, EERC Report 72-9, University of California, Berkeley.

Brown, P. Lowes, L.N. (2007) "Fragility functions for modern reinforced-concrete beam-column joints," *Earthquake Spectra*, Vol. 23(2): 263-289.

Celebi, M., Penzien, J. (1973) *Hysteretic behaviour of epoxy-repaired reinforced concrete beams*, EERC Report 73-5, University of California, Berkeley.

Chiou, Y.J., Liou, Y.W., Mo, Y.L., Hsiao, F.P., Sheu, M.S., Shih, C.T. (2003) "Repair of large scale reinforced concrete framed shear walls with opening," *ACI Special Publication*, Vol. 211: 263-291.

Chung, H.W. (1981) "Epoxy repair of bond in reinforced concrete members," *ACI Journal*, Vol. 78(1): 79-82.

Federal Emergency Management Agency (1985) *NERHP Recommended provisions for the development of seismic regulations for new buildings – Part 3 Appendix: Existing buildings (FEMA-97)*, Building Seismic Safety Council, Washington, D.C.

Filiatrault, A., Lebrun, I. (1996) "Seismic rehabilitation of reinforced concrete joints by epoxy pressure injection technique," *ACI Special Publication*, Vol. 160: 73-92.

French, C.W., Thorp, G.A., Tsai, W.J. (1990) "Epoxy repair techniques for moderate earthquake damage," *ACI Structural Journal*, Vol. 87(4): 416-423.

Hose, Y., Silva, P. Seible, F. (2000) "Development of a performance evaluation database for concrete bridge components and systems under simulated seismic loads," *Earthquake Spectra*, Vol. 16(2): 413-442.

Jefatura de Gobierno (2017) *Normas para la rehabilitación sísmica de edificios de concrete dañados por el sismo del 19 de septiembre de 2017*, Gaceta Oficial de la Ciudad de México, No. 211 bis, pp. 20.

Karayannis, C.G., Chalioris, C.E., Sideris, K.K. (1998) "Effectiveness of RC beam-column connection repair using epoxy resin injections," *Journal of Earthquake Engineering*, Vol. 2(2): 217-240.

Karayannis, C.G., Sirkelis, G.M. (2008) "Strengthening and rehabilitation of RC beam-column joints using carbon-FRP jacketing and epoxy resin injection," *Earthquake Engineering and Structural Dynamics*, Vol. 37: 769-790.

Kunieda, M., Kamada, T., Rokugo, K (2001) "Evaluation of bond properties of crack injection repair for concrete structures," *Tenth International Congress of Fracture*, Honolulu, Hawaii.

Lefas, I.D., Kotsovos, M.D. (1990) "Strength and deformation characteristics of reinforced concrete walls under load reversals," *ACI Structural Journal*, Vol. 87(6): 716-726.

Maeda, M., Nishida, T., Matsukawa, K., Murakami, M. (2017) "Revision of guideline for post-earthquake damage evaluation of reinforced concrete buildings in Japan," *Sixteenth World Conference on Earthquake Engineering*, Santiago, Chile.

Mansur, M.A., Ong, K.C.G. (1985) "Epoxy-repaired beams," *Concrete International*, Vol. 7(10): 46-50.

Okamoto, S., Wight, J., Nakata, S., Yoshimura, M., Kaminosono, T. (1985) "Testing, repair and strengthening, and retesting of a full scale seven story reinforced concrete building," *ACI Special Publication*, Vol. 84: 133-161.

Ozaka, Y., Suzuki, M. (1986) "Shear failure of reinforced concrete beams and effect of repair by epoxy resin injection," *ACI Special Publication*, Vol. 93: 637-670.

Park, R., Ang, A.H.S. (1985) "Mechanistic seismic damage model for reinforced concrete," *Journal of Structural Engineering*, Vol. 111(4): 722-739.

Sugano, S., Fukuyama, H., Maeda, M., Kosa, K., Teshigawara, M., Nakamura, S., Kitajima, K., Tsukishima, D. (2010) *Technical committee on performance-oriented seismic rehabilitation*, Committee Report JCI-TC084A, pp. 79-99.

Takahashi, J., Shibata, A., Shiga, T. (1988) "Crack indices of reinforced concrete shear walls for seismic damage evaluation," *Ninth World Conference on Earthquake Engineering*, Tokyo-Kyoto, Japan.

Tasai, A. (1988) “Resistance of flexural reinforced concrete members after repair with epoxy resin,” *Ninth World Conference on Earthquake Engineering*, Tokyo-Kyoto, Japan.

Tasai, A. (1992) “Effective repair with resin for bond failure of RC members,” *Tenth World Conference on Earthquake Engineering*, Balkema, Rotterdam.

Tasai, A., Yamada, T., Otani, S., Aoyama, H. (1985) “Performance of reinforced concrete flexural members after repair,” *Transactions of the Japan Concrete Institute*, Vol. 7: 591-598.

Tsonos, A.G. (2002) “Seismic repair of reinforced concrete beam-column subassemblies of modern structures by epoxy injection technique,” *Structural Engineering and Mechanics*, Vol. 14(5):542-563.

Tsonos, A.G., Papanikolaou, K. (2003) “Post-earthquake repair and strengthening of reinforced concrete beam-column connections (theoretical and experimental investigation),” *Bulletin of the New Zealand Society for Earthquake Engineering*, Vol. 36(2): 73-93.

Tudor, D.F., Ciuhandu, G.C. (1992) “Design principles concerning the strengthening of coupling beams,” *Tenth World Conference on Earthquake Engineering*, Balkema, Rotterdam.

Yu, J., Zhang, Y., Lu, Z. (2014) “Seismic rehabilitation of RC frame using epoxy injection technique tested on shaking table,” *Structural Engineering and Mechanics*, Vol. 52(3): 541-558.

3 EXPERIMENTAL PROGRAM

3.1 Introduction

Structures designed following modern (i.e. 1980s, post capacity design principles) codes are supposed to withstand major earthquakes by developing inelastic action and energy dissipation in concentrated regions referred to as plastic hinges. Therefore, and consistently with the current seismic performance-based design guidelines (SEAOC, 1995), structural damage is expected to occur. In particular and in very simple terms, modern structures should be capable of remaining fully operational (i.e. with negligible structural and non-structural damage) after frequent earthquakes, operational (i.e. with some non-structural damage without significant structural damage) after occasional ones, and allow for life safety (i.e. without collapsing) during a rare or design level earthquake.

The above philosophy implicitly means that modern structures should also be able to withstand several frequent and/or occasional earthquakes over their life span, and that they might suffer some level (minor-to-moderate) of damage and require some post-earthquake structural and non-structural repairs. Interestingly enough, one of the most controversial issues highlighted by the 2010-2011 Christchurch earthquakes sequence (CES) has been the lack of: a) comprehensive and robust guidelines to assess the residual capacity of damaged modern buildings, as well as b) in depth and evidence-based knowledge for selection and implementation of a reliable repairing technique capable of bringing (either totally or partially) the structure back to its pre-earthquake condition. Arguably, partly (although not exclusively) as a result of such lack of knowledge and guidelines, many modern buildings, in a number exceeding typical expectations from past experience at international levels, have ended up being demolished.

Although epoxy repair techniques have been extensively used for earthquake repairs over the last 40-50 years, research on the effectiveness of this technique on real or full-scale elements is scarce. Most of the investigations have been focused on partial-scale laboratory specimens.

In addition, the level of damage reached prior to repair the specimens has typically been severe or extensive, similar to what is expected to occur under a life safety limit state condition, in which case it is likely that the building would require extensive repairs and strengthening or ultimately demolished. Very little information is available on minor-to-moderate damaged specimens, for which repairs appear to be the only required intervention. This chapter describes experimental campaign performed on three "modern designed" beam-column joints extracted from a 1980s multi-storey reinforced concrete frame building, aiming at: a) assessing the residual capacity of existing reinforced concrete buildings to sustain subsequent aftershocks and/or other design level earthquake during the remaining life of the building, and b) the identification and better understanding of the effectiveness of epoxy injection techniques, widely proposed and adopted in practice, for partly or fully restoring the seismic capacity of moderately damaged reinforced concrete members.

3.2 Building description and observed damage

The PWC building (see Figure 3-1) was a 22-storey structure located on Armagh Street in the Christchurch's Central Business (CBD) area, New Zealand. The lateral system consisted of precast perimeter reinforced concrete (RC) frames with wet joints (typical of emulation of cast-in-place approach) in the beams at mid-span. The gravity system consisted of precast double-tees with a reinforced concrete topping, supported on steel beams and concrete columns. The foundation system consisted of raft foundations. It was designed following capacity design principles and built in the late 1980s. The perimeter frames had a hoop detail in the beam-ends intended to relocate the plastic hinge 500mm away from the column face. During the CES, the building appeared to behave as expected, with the beams developing plastic hinges at both ends along the full height of the structure, with a general trend of diminishing level of damage along the elevation. The columns or joints did not show any signs of damage. The building experienced more damaged in the EW direction, consistent with the direction of the strongest earthquake component recorded in the surrounding area. Maximum observed residual cracks varied between 0.8 mm and 20 mm wide in the EW direction, and between 0.4 mm and 8 mm in the NS direction. Residual drifts and tilting (due to liquefaction and lateral spreading) were also observed. More detailed information on the observed damage can be obtained in Giorgini et al (2013) and Fleishman et al (2014).
The building was considered uneconomical to be repaired and consequently demolished in 2012 (see Figure 3-2).

Figure 3-1. Aerial view of the PWC building (photo courtesy of Stefano Pampanin).

Figure 3-2. Photos taken during the deconstruction process of the PWC building (photos courtesy of Jan Geesink of Arrow International).

It is noteworthy that most of the observed cracks were within, instead of outside, the plastic hinge relocation detail (see Figure 3-3) which thus apparently did not work as intended per the original design. Four H-frame specimens were extracted from the 16th floor level during the demolition process for experimental purposes (see Figure 3-4 and Figure 3-5).

Figure 3-3. Typical damage observed in the superstructure of the PWC building, level 9 interior unit H4 (left) and level 4 corner unit H2 (courtesy of Stefano Pampanin, Fleishman et al, 2014).

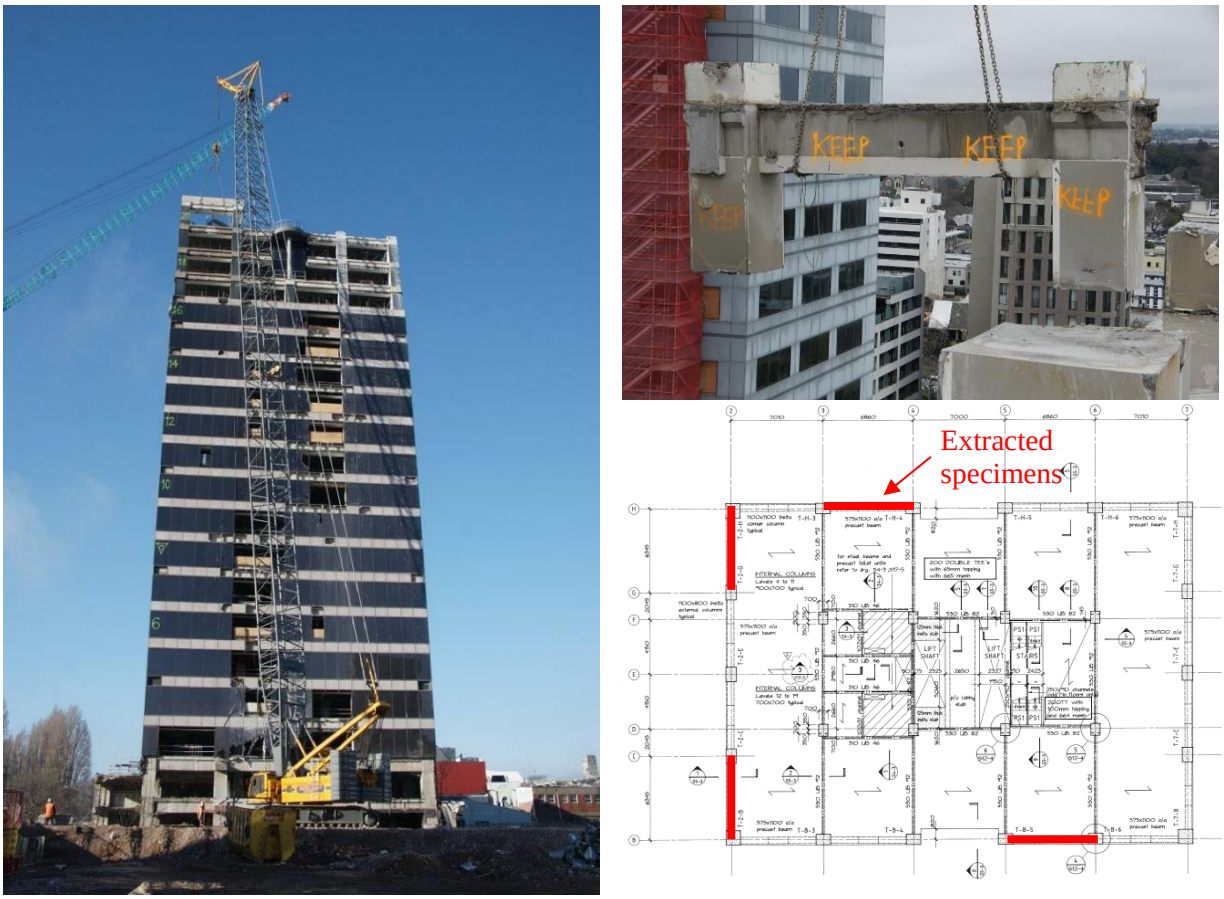

Figure 3-4. Elevation of the PWC building during the deconstruction process (left); extraction of one of the H-frame specimens (upper-right); typical floor plan view at the upper levels (lower-right), red lines indicate locations where the specimens were taken out of the 16th floor level (Photos courtesy of Stefano Pampanin).

Figure 3-5. Specimens identification (left) and extraction (right) (photos courtesy of Stefano Pampanin).

3.3 Specimens description

The H-frame specimens extracted during the deconstruction process were later cut in two T-shape specimens due to laboratory crane capacity limitation, each with a weight between 10.5 ton and 13 ton. The beams were 2550 mm long (measured from the column face to the point of load application), 575 mm wide by 1100 mm high. The (main) longitudinal reinforcement consisted of top and bottom 4 D-28 straight bars and 2 additional D28 hooked bars (within the plastic hinge relocation detail); the transverse reinforcement consisted of 2 R-12 stirrups (one interior, one exterior) spaced at 150 mm crs. There was also secondary reinforcement to provide vertical support to the flooring system (see Figure 3-6. The columns were 2700 mm long, either 1100 mm square (at the building's corners) or 1100 mm by 800 mm (at the building's interior columns). The nominal steel yield strength and concrete compressive strengths, as specified in the drawings, were 300MPa and 30MPa, respectively.

Figure 3-7 shows photos of the H-frame specimens stored in the yard, the wire saw-cut process to convert each H-frame into two T-frame specimens, loading, transportation and unloading of the specimens in the Structures Laboratory at the University of Canterbury.

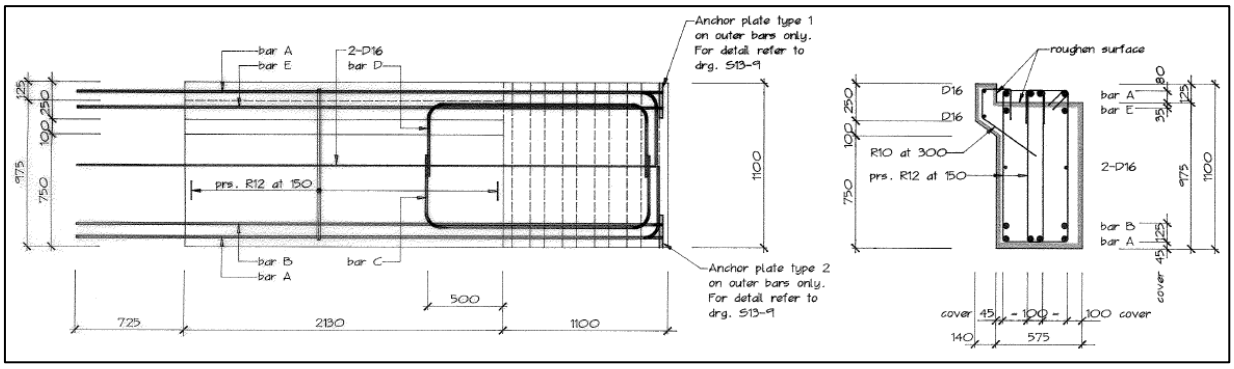

Figure 3-6. Typical section and elevation view of beams tested (Holmes, 1988).

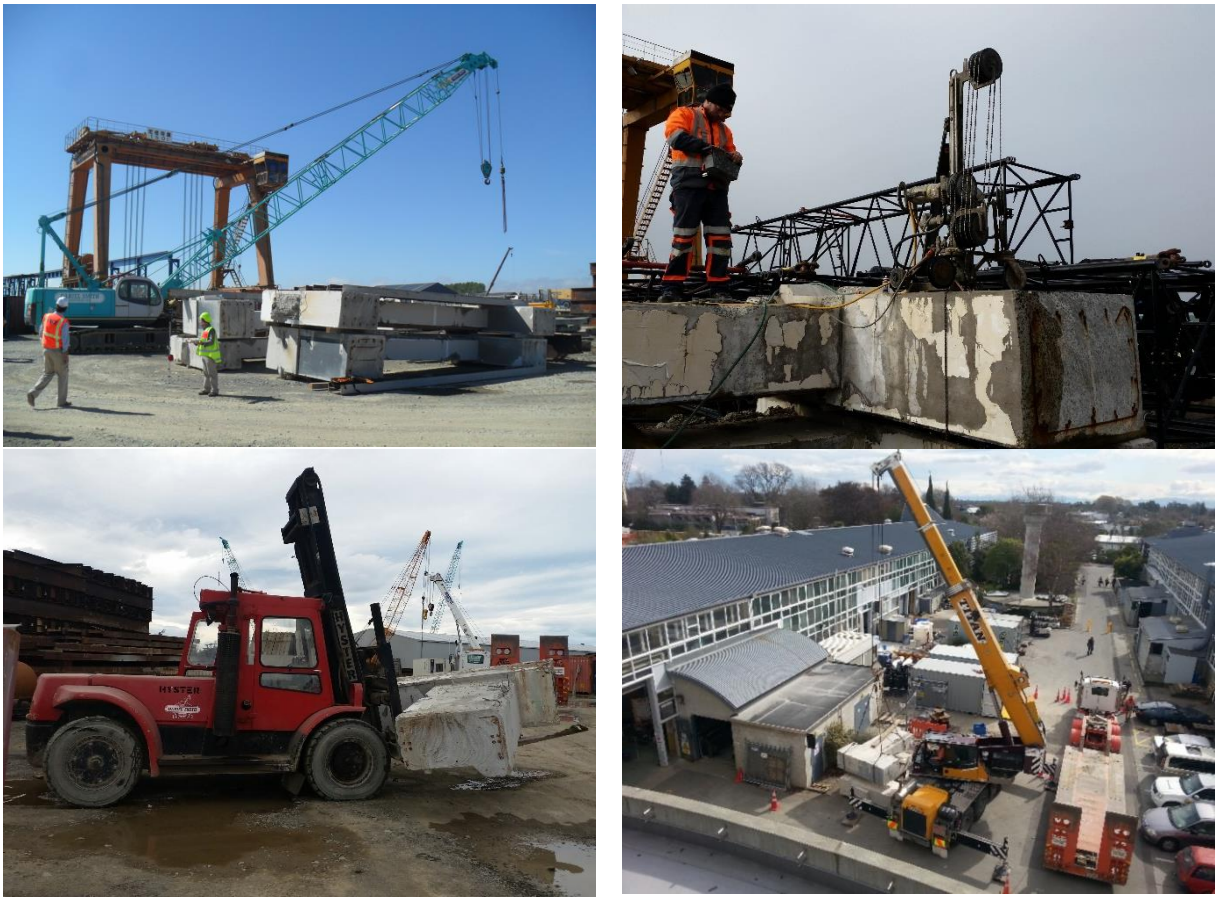

Figure 3-7. Specimens storage at Daniel Smith Industries (upper-left); wire saw-cutting of the H-frames (upper-right); loading of the specimens in the yard (bottom-left) and unloading at the University of Canterbury (bottom-right).

3.4 Material properties

3.4.1 Reinforcing steel

Two samples of the longitudinal reinforcement were extracted from the mid-span of the beam, were less inelastic action is expected. The samples were subjected to a uniaxial tensile force as per the NZS3112:1986 (see Figure 3-8) to obtain their yield and ultimate strength and strain properties. Table 3-1 shows the results obtained using the nominal bar diameter.

Table 3-1. Measured steel material properties, assuming 28 mm bar diameter.

Sample	E_s (GPa)	ε_{sh} (mm/mm)	ε_u (mm/mm)	f_y (MPa)	f_u (MPa)
1	241	0.0185	0.177	382	579
2	245	0.0200	0.172	385	581

It was observed that the elastic modulus was not representative of the elastic modulus of typical steels. In addition, the yield strength was slightly high for Grade 300 steel. It was concluded that the reason for such high values was the fact of using the nominal diameter

instead of the real bar diameter, which was non-uniform (i.e., the bar was slightly elliptical). The results were adjusted by estimating the area of steel required in order to obtain an elastic modulus E_s of 200 MPa. The adjusted material properties are shown in Table 3-2, and Figure 3-9 shows the corresponding stress-strain curves. It is evident that after the adjustment in the bar diameter the yield and ultimate strengths are representative of Grade 300 steel.

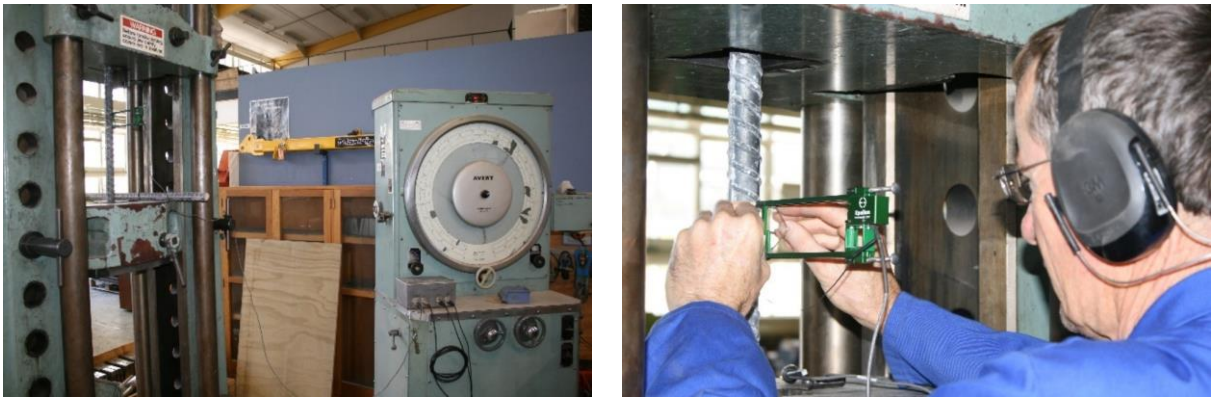

Figure 3-8. Uniaxial tensile test of deformed (unmachined) D28 bars, extracted at the mid-span of the beam.

Table 3-2. Adjusted steel material properties, assuming a modulus of elasticity E_s= 200 GPa (or a 30.8 mm bar diameter).

Sample	E_s (GPa)	ε_{sh} (mm/mm)	ε_u (mm/mm)	f_y (MPa)	f_u (MPa)
1	200	0.0185	0.177	314	477
2	200	0.0200	0.172	317	478

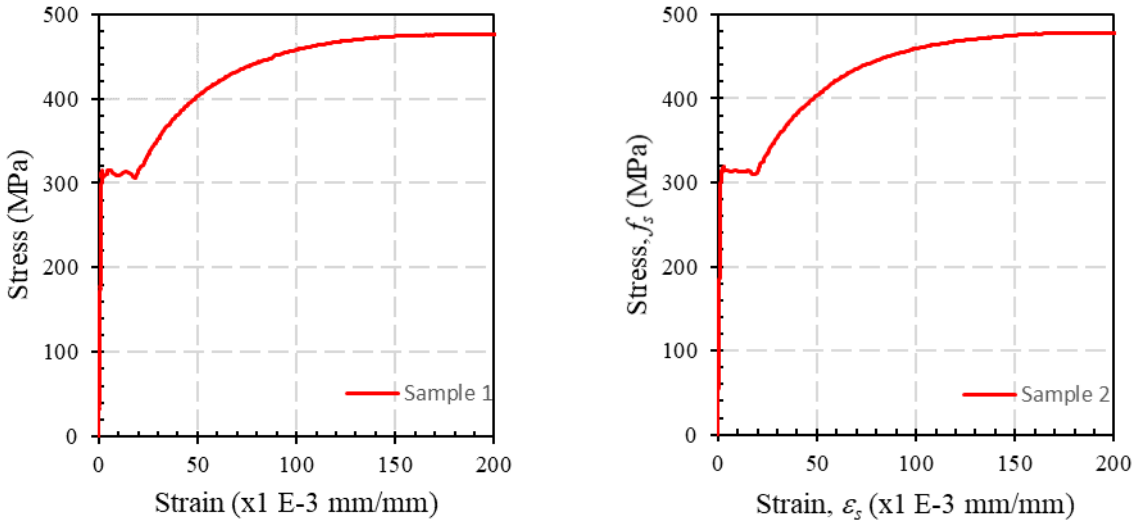

Figure 3-9. Stress-strain curves of sample 1 (left) and 2 (rigt), after adjusting the modulus of elasticity.

3.4.2 Concrete

Three 100 mm diameter concrete cores were also extracted from the mid-span of the beam and tested under uniaxial compressive load as per NZS3112:1986, and subjected to a uniaxial compressive force (see Figure 3-10). The beam was deep enough so as to allow the extraction of the cores from the top, middle, and bottom of the beam section (see Figure 3-11).

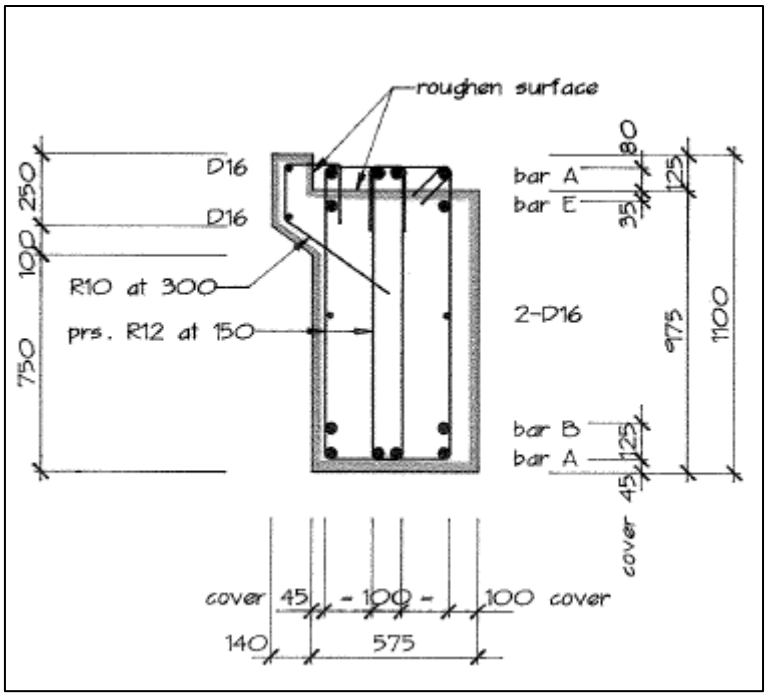

Figure 3-11. Location of concrete cores extracted for testing.

shows the results. On average, a concrete strength of 36 MPa (i.e., 1.2 times the specified concrete strength) can be assumed.

Table 3-3. Results of uniaxial compressive tests in concrete cores extracted from the beam at mid-span, at different locations in the cross section.

Core location	Maximum Force (kN)	Maximum Stress (MPa)
Top	280	41.2
Middle	216	31.8
Bottom	251	36.9

3.4.3 Epoxy resin

The commercial epoxy Sikadur 52 was used to inject the cracks in the damaged specimens. As per the manufacturer's specification, it is a solvent free, non-shrinkage, two-component low-viscosity liquid based high strength epoxy resin, suitable for injecting cracks from 0.2mm

up to 5.0 mm wide. The pot life (at 20°C) is 20 min. It develops compressive strengths of 45 MPa after 7 days (at 20°C) and tensile strengths of approximately 25 MPa. The bond strength in sandblasted concrete is as high as approximately 3.5 MPa.

Figure 3-10. Uniaxial compressive tests on concrete cores extracted at the mid-span of the beam, at the top, middle and bottom of the cross-section.

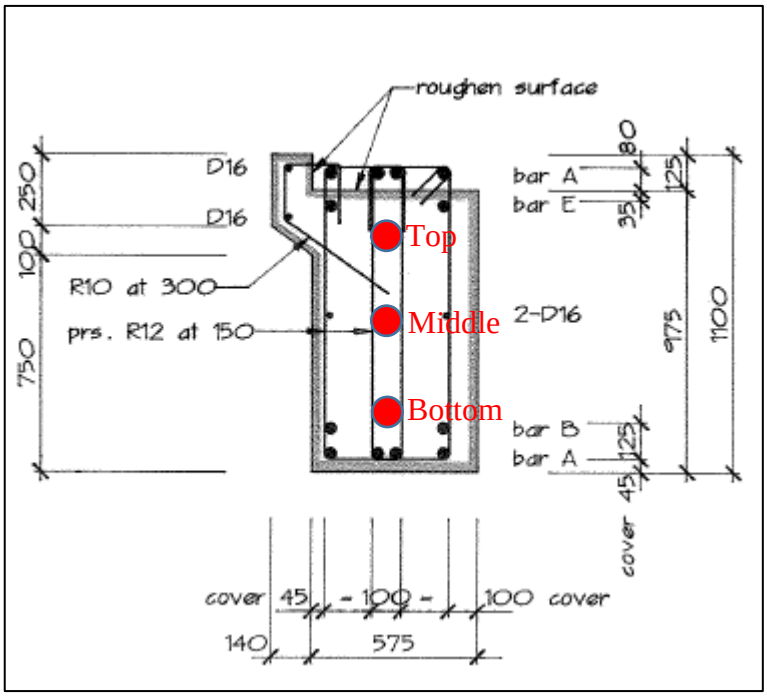

Figure 3-11. Location of concrete cores extracted for testing.

3.5 Epoxy injection repairs

The epoxy repair works were conducted by BBR CONTECH Christchurch Branch, concrete specialists with broad experience in epoxy injection repairs following the 2010-2011 Canterbury earthquakes sequence, with the technical support from the product manufacturer (Sika). As shown in Figure 3-12, the damaged specimens were repaired in the same horizontal position as they were tested. The repair process started with grinding down the surface along the crack lines in order to seal the crack surface with epoxy mortar. It was necessary to seal the crack at every side of the specimen to prevent leakage. Injection ports were simultaneously installed at 100-200 mm crs. or closer depending on the cracking pattern. The two components were mixed and the resin was injected under low pressure (34.5 MPa) via the injection ports using an air-operated pressure pump. The injection port was sequentially interchanged to allow the resin to travel and fill the interior of the cracks. The ports were capped as the resin started leaking through them. Once the injection process finished, the surface was ground down again to remove the hardened epoxy mortar, leaving the surface flush. A total 4.8 L and 10.9 L of epoxy resin were required in order to repair the specimens 2 and 3, respectively.

Epoxy mortar was not required at any stage of the tests as none of the specimens exhibited crushed or spalled concrete. Therefore, the repair works only required epoxy injection of the cracks.

Figure 3-12. Sealing process with epoxy mortar and installation of injection ports (upper-left); resin injection with an air-operated pump (upper-right); epoxy resin leaking from and capping of the injection ports (lower-left); surface finish once the epoxy mortar has been removed (lower-right).

3.6 Test setup

As shown in Figure 3-13 and Figure 3-14, the reaction frame used for the tests consisted of steel braced frames anchored to the RC strong floor. The beam-column joint was placed horizontally on top of steel beams and clamped to the braced frames using steel channels and post-tensioned Macalloy bars. The beam-end was vertically supported on Teflon pads. A steel frame with a roller prevented the beam-end to uplift due to any accidental eccentricity that might occur at the actuator-to-beam connection.

No axial and gravity loads were applied at the column or beam. The actuator was located approximately at the theoretical inflection point at mid-span of the beams oriented in the NS direction of the building.

Due to crane capacities and restrictions in the laboratory, an articulated movable crane was required in order to place the specimen on the reaction frame (see Figure 3-15). A total of three beam column joints out of the eight extracted (i.e. four “H” frames) were tested during the experimental campaign.

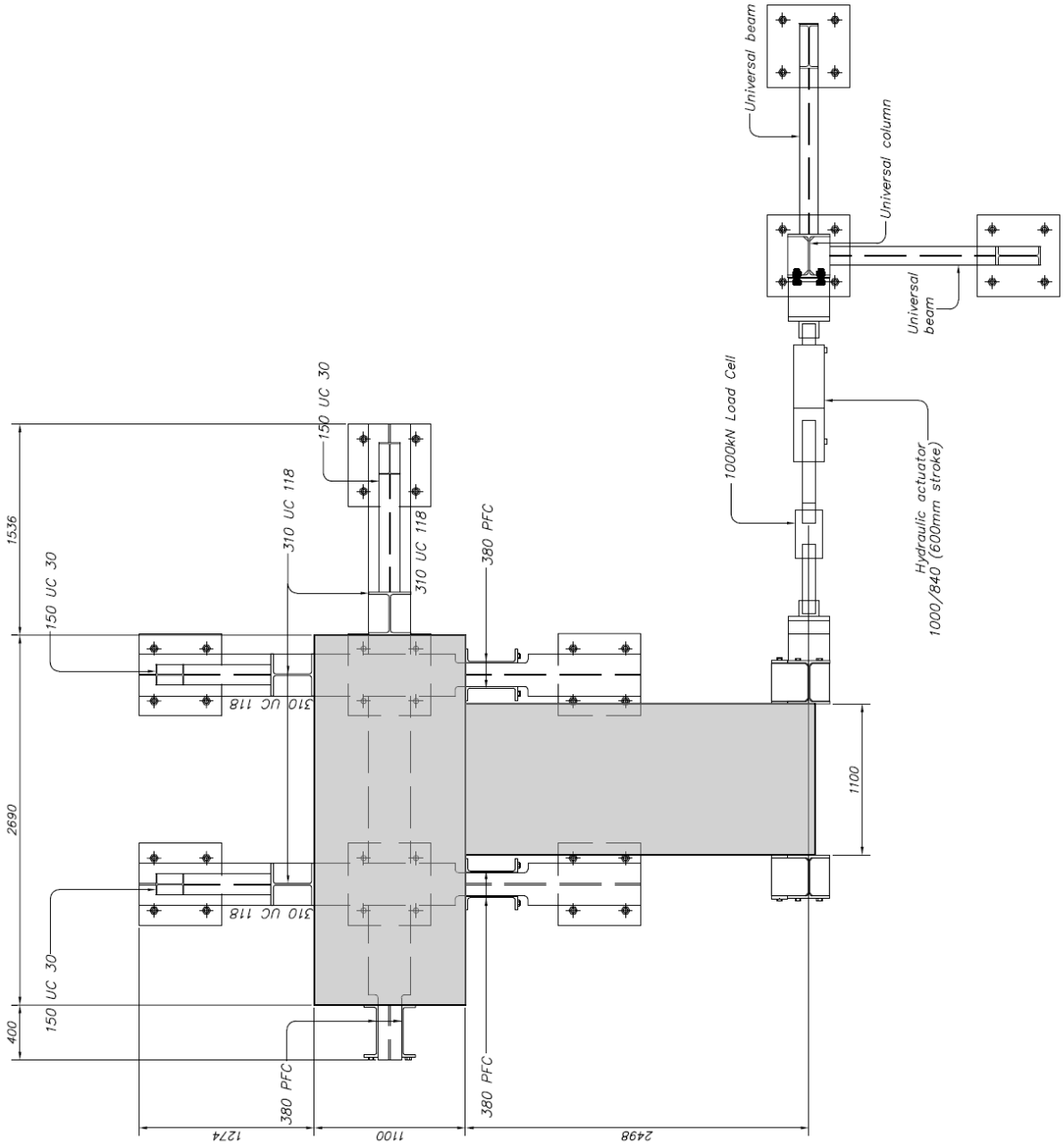

Figure 3-13. Plan view of the reaction frame.

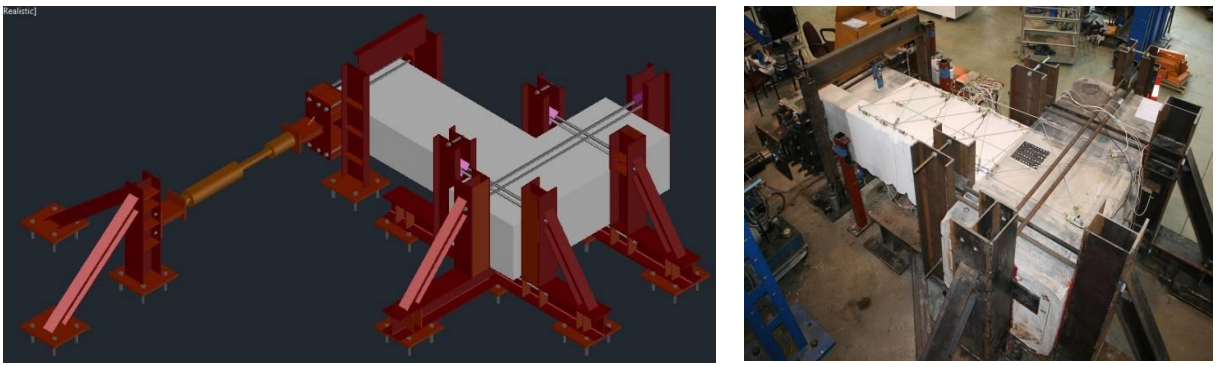

Figure 3-14. 3D CAD view of the reaction frame (left); specimen 1 during the tests (right).

Figure 3-15. Placing of one of the specimens on the reaction frame with the help of a movable crane.

3.7 Loading Protocol and Testing Procedure

3.7.1 Loading protocol

A quasi-static displacement-controlled cycling loading protocol was applied at the beam-end (increasing "total" beam rotations of ±0.1%, ±0.2%, ±0.5%, ±0.75%, ±1.0%, ±1.5%, ±2.0%, ±2.5%, ±3.5%, and ±4.5%, see Figure 3-16) as per the acceptance criteria of the American Concrete Institute (ACI, 2001).

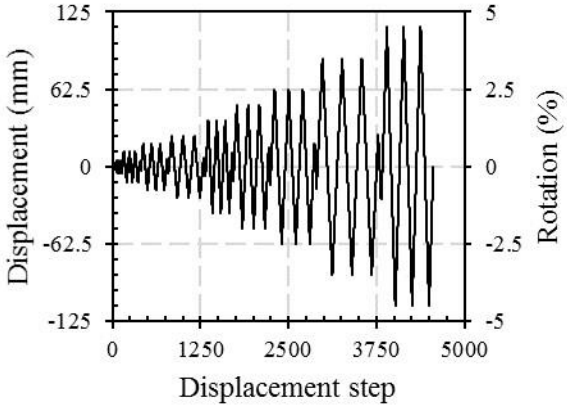

Figure 3-16. Applied loading protocol.

The beam rotations shown in Figure 3-16 can be related to frame rotations based on the following equations. Equations (3-2) and (3-3) are per Priestley et al (2013).

$$\theta_c = \theta_p \cdot \frac{L'_b}{L_b} + \theta_y \tag{3-1}$$

$$\theta_y = 0.5 \cdot \varepsilon_y \cdot \frac{L_b}{h_b} \tag{3-2}$$

$$L_P = 0.08 \cdot L + 0.022 \cdot f_y \cdot d_b \tag{3-3}$$

In the previous equations, θ_c = column of frame rotation; θ_p = beam plastic hinge rotation; θ_y = yield rotation; $L = 0.5(L'_b+L_p)$; f_y = reinforcing steel yield strength; and d_b= beam reinforcement bar diameter. The other terms are defined in Figure 3-17. For this particular case, h_b= 1100 mm, L_{PHRD}= 500 mm, L_P= 350 mm, L_b= 6100 mm, L'_b= 3550 mm, and the yield rotation θ_y= 0.44%. For a beam rotation of ±4.5% (i.e., θ_p = ±4.06%), the column or frame rotation is approximately ±2.8%.

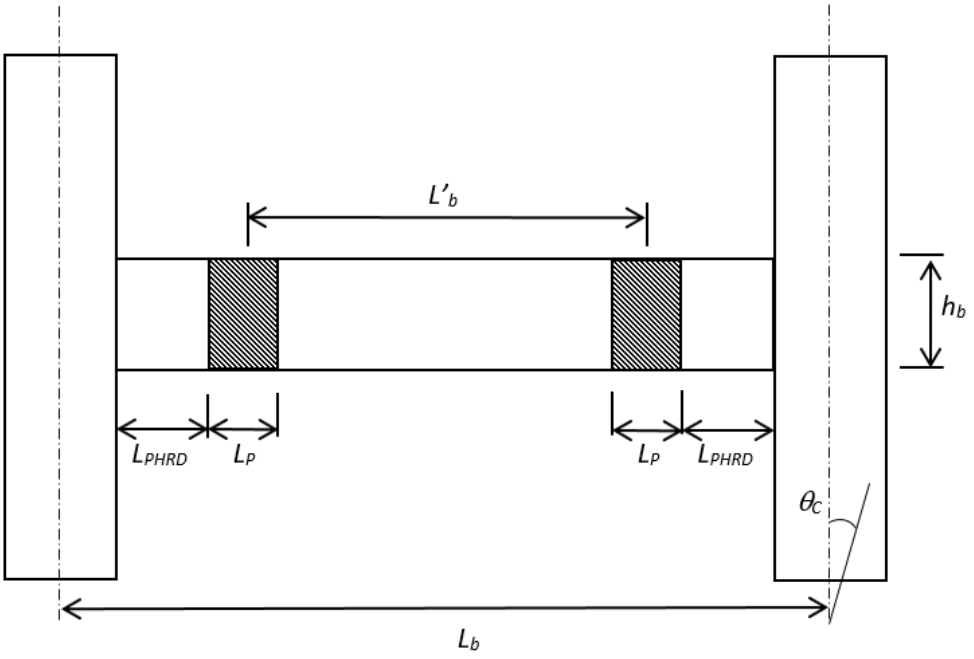

Figure 3-17. Relationship between beam rotations and frame rotations

3.7.2 Testing procedure

The first specimen tested (Test 1) corresponds to one of the frames oriented in the NS direction, with no visible residual cracks and consequently considered as "slightly damaged". The specimen was subjected to a standard quasi-static reverse cyclic testing loading protocol up to a maximum "total" rotation of 2.5% (see Section 3.8 for a better understanding of "total" rotation).

The second specimen tested corresponds to one of the frames oriented in the EW direction, in which the building experienced more damage. Residual cracks varying between hairline and 0.8 mm in width were observed prior to commencing the test. The specimen was subjected to the same standard loading protocol up to a maximum "total" rotation of 1% (Test 2.1), enough to re-activate all the existing cracks and develop residual (static) cracks between 0.1 mm and 2.0 mm in width. The specimen was subsequently repaired by epoxy pressure injection as described in Section 3.5, one of the most typical repairing techniques (to the

authors' knowledge) that has been proposed and/or applied in Christchurch following the CES. After letting the repaired specimen cure for seven days, it was retested again following the same loading protocol until reaching complete failure (Test 2.2).

The third and last specimen tested corresponds to the second half of the "H frame" where the second specimen was extracted from. Residual cracks varying between hairline and 1.0mm in width were observed prior to the test. The specimen was subjected to the standard loading protocol up to a maximum "total" rotation of 1.5% (Test 3.1), enough to re-activate all the existing cracks and develop new ones with residual (static) cracks between 0.1mm and 6mm in width (i.e., about the upper bound limit to which epoxy injections are still applicable). The specimen was subsequently repaired by epoxy pressure injection, let cure for seven days and retested again following the same loading protocol until reaching complete failure (Test 3.2).

Table 3-4 describes the observed damage prior to commencing the tests, as well as the maximum beam rotation applied at every test.

Table 3-4. Summary of the experimental program.

	Observed (pre-test) Damage		**Max. Beam Rotation**
Test 1 (NS)	No visible residual cracks		2.5 %
Test 2 (EW)	Test 2.1	Hairline – 0.8 mm	1.0 %
	Test 2.2	0.1 mm – 2.0 mm	4.5 %
Test 3 (EW)	Test 3.1	Hairline – 1.0 mm	1.5 %
	Test 3.2	0.1 mm – 6.0 mm	4.5 %

Figure 3-18 and Figure 3-19 shows the cracking pattern of specimens 2 and 3 in their original or post-CES condition (i.e., prior to tests 2.1 and 3.1) and prior to epoxy repair them (i.e., post tests 2.1 and 3.1). The cracking pattern of specimen 1 is not shown as its post-CES did not have any residual crack. Cracks faraway of the plastic hinge region were not mapped prior to the epoxy crack injection (photo at the left-hand side in Figure 3-18 and Figure 3-19). The specimens show some spalled concrete, which was induced during the lifting of the specimens in the deconstruction process. It was not due to the earthquakes.

3.8 Instrumentation and data collection

Figure 3-20 shows the instrumentation used during the tests. The instrumentation consisted of 33 linear potentiometers for measuring displacements at different points along the beam and beam-column joint (required for further estimation of rotations and shear deformations), 1 load cell for measuring the applied load in the actuator, and 2 rotational potentiometers at the beam-end for measuring beam elongation and applied displacements.

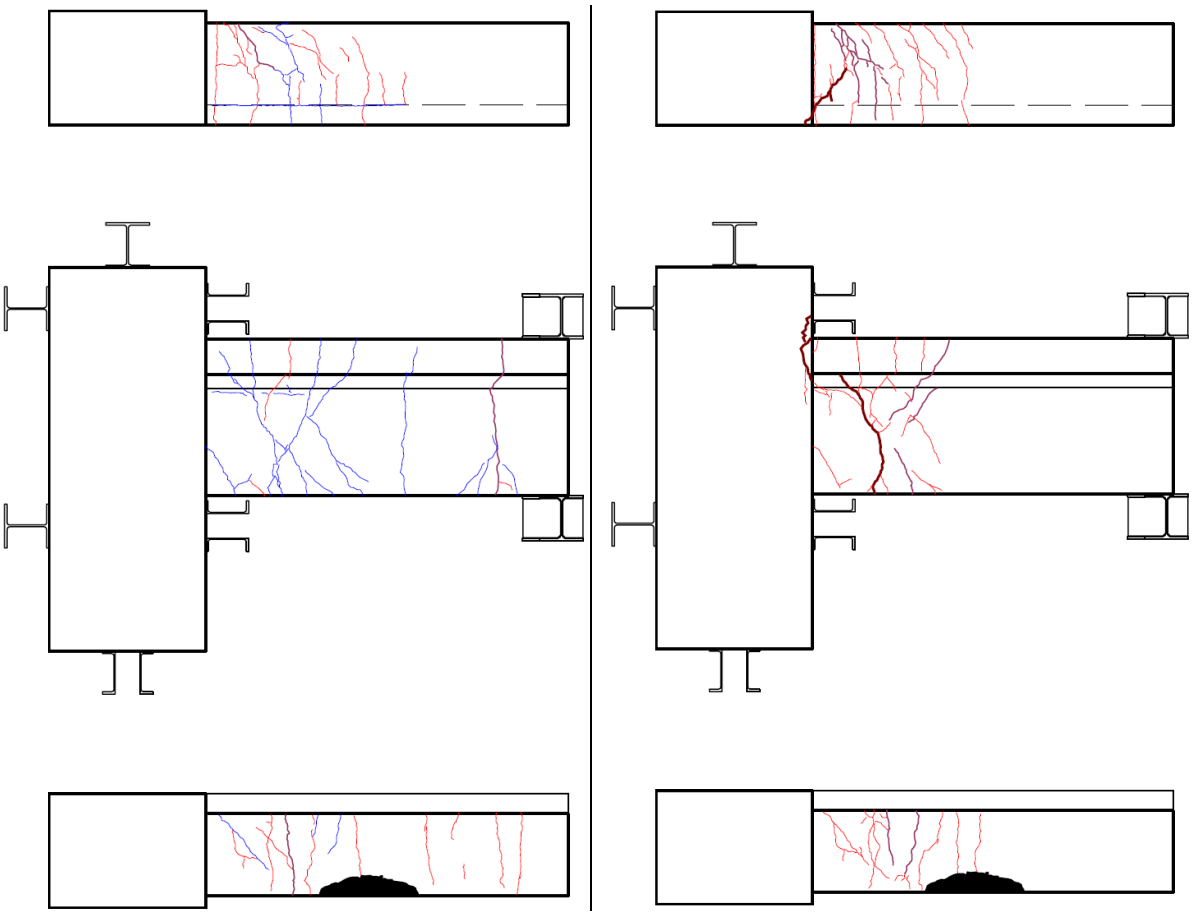

Figure 3-18. Crack mapping in specimen 2 as observed prior to commencing Test 2.1 (left) and after completion of Test 2.1 prior to epoxy repair the specimen (right).

During the deconstruction process, the beams adjacent to the extracted "H frames" were cut-out approximately at the column face. The flexural beam capacity of these beams relied upon straight D28 bars developed over a length of 1100mm (i.e. without a standard hook), just above the minimum required as per the NZS3101:2006. Two additional spring potentiometers were located at the bar end at the cut-out section to measure bar slips during the test, if any. Three additional rotary potentiometers were strategically installed to capture rigid body translations and rotations of the specimen due to axial elongation of the post-tensioned Macalloy bars, slip at the reaction frame-to-strong floor connections, relative movement between the specimen and the reaction frame, and any other deformation in the reaction frame that might have occurred during the test. The rigid body translation and rotation is further translated into an equivalent lateral displacement at the beam-end and thus extracted from the "total" applied displacement and rotation.

The instrumentation was connected to a data logger (computer) through four-pin serial cables. Figure 3-21 shows the kinematics of the rigid body translation and rotation used to derive the

following equations, where $d\theta$ is the rigid body rotation, $d\Delta$ is the rigid body translation in the direction of the applied displacement, Δ_{eff} is the effective applied displacement, and δ_{eff} is the effective beam elongation.

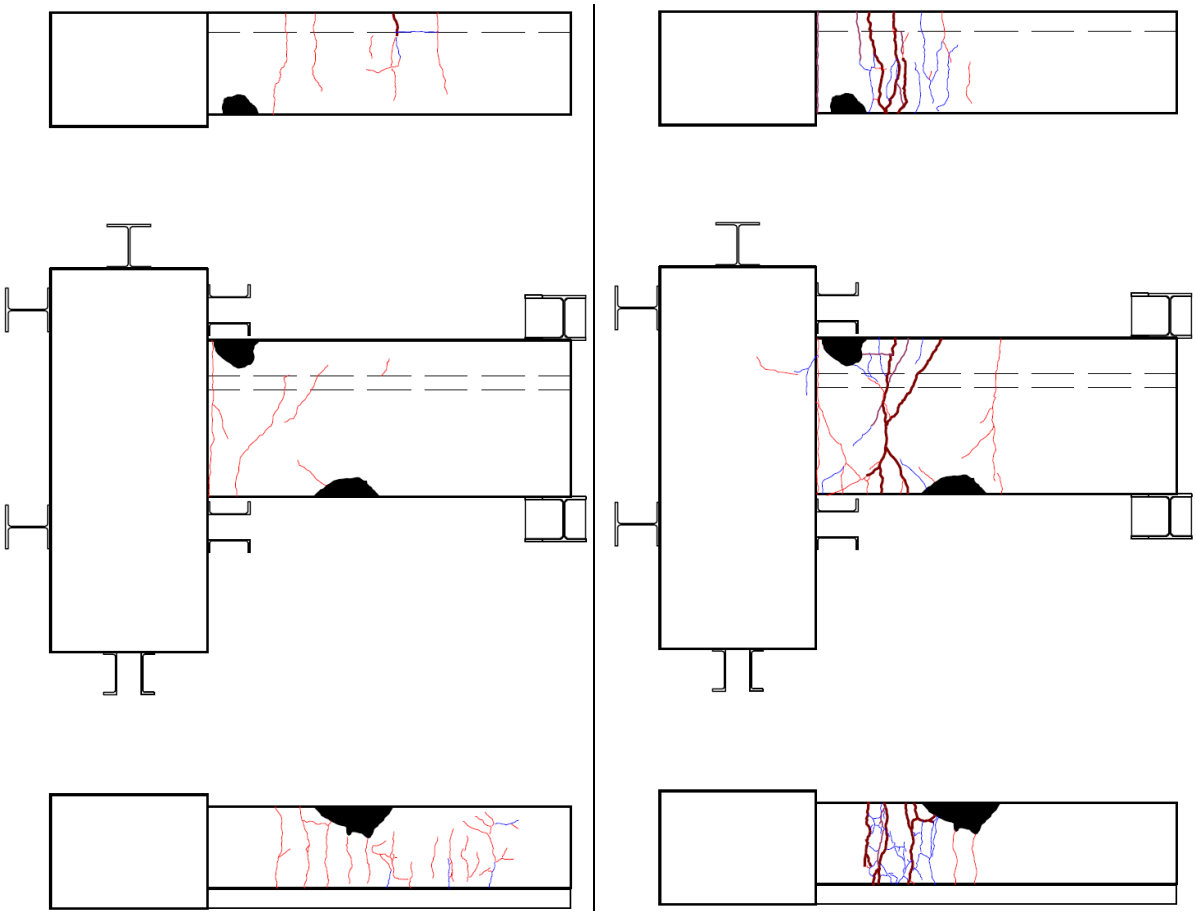

Figure 3-19. Crack mapping in specimen 3 as observed prior to commencing Test 3.1 (left) and after completion of Test 3.1 prior to epoxy repair the specimen (right).

$$d\theta = 2 \cdot \sin^{-1}\left(\frac{dg_6 + dg_7}{2 \cdot L_g}\right) \tag{3-4}$$

$$d\Delta = L_b \cdot \sin(d\theta) \tag{3-5}$$

$$\Delta_{eff} = g_9 - \sum_{i=1}^{n} d\Delta - g_5 \tag{3-6}$$

$$\delta_{eff} = g_8 - \frac{g_6 - g_7}{2} \tag{3-7}$$

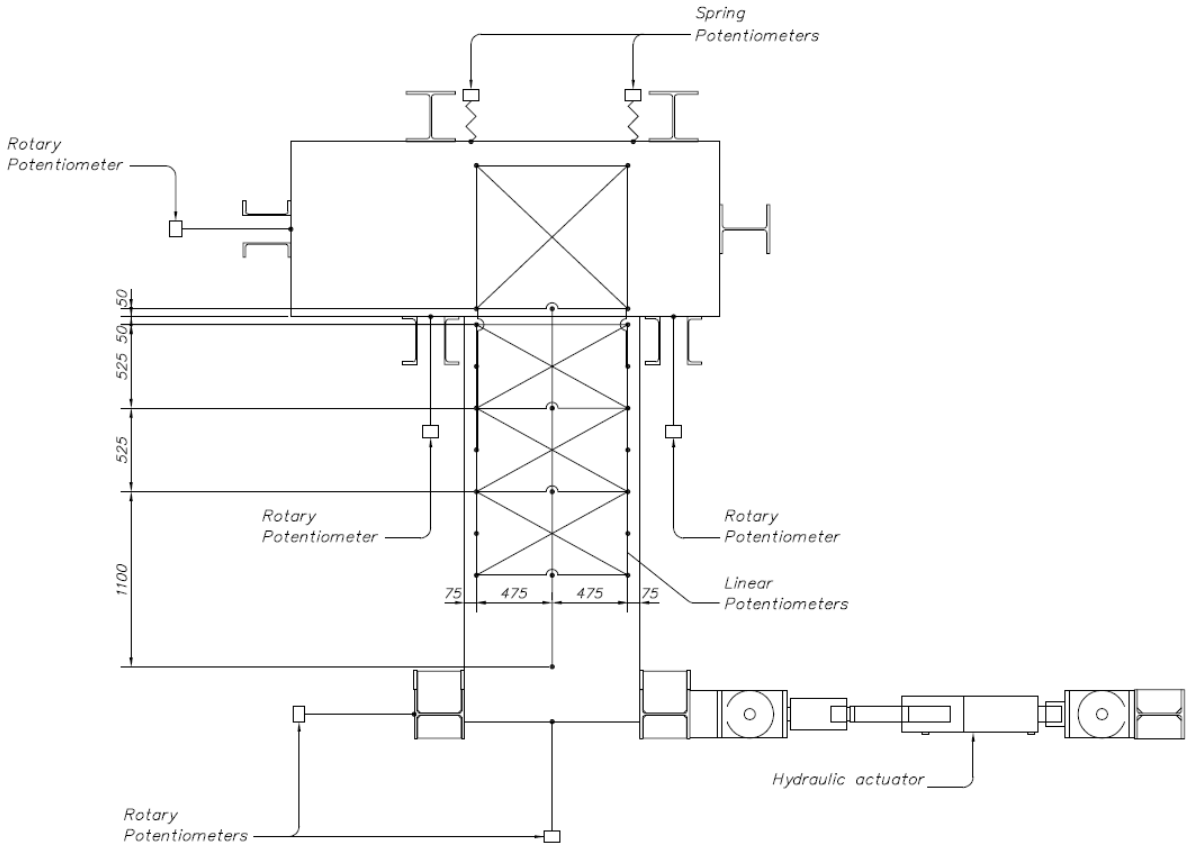

Figure 3-20. Location of all the instrumentation within the specimen.

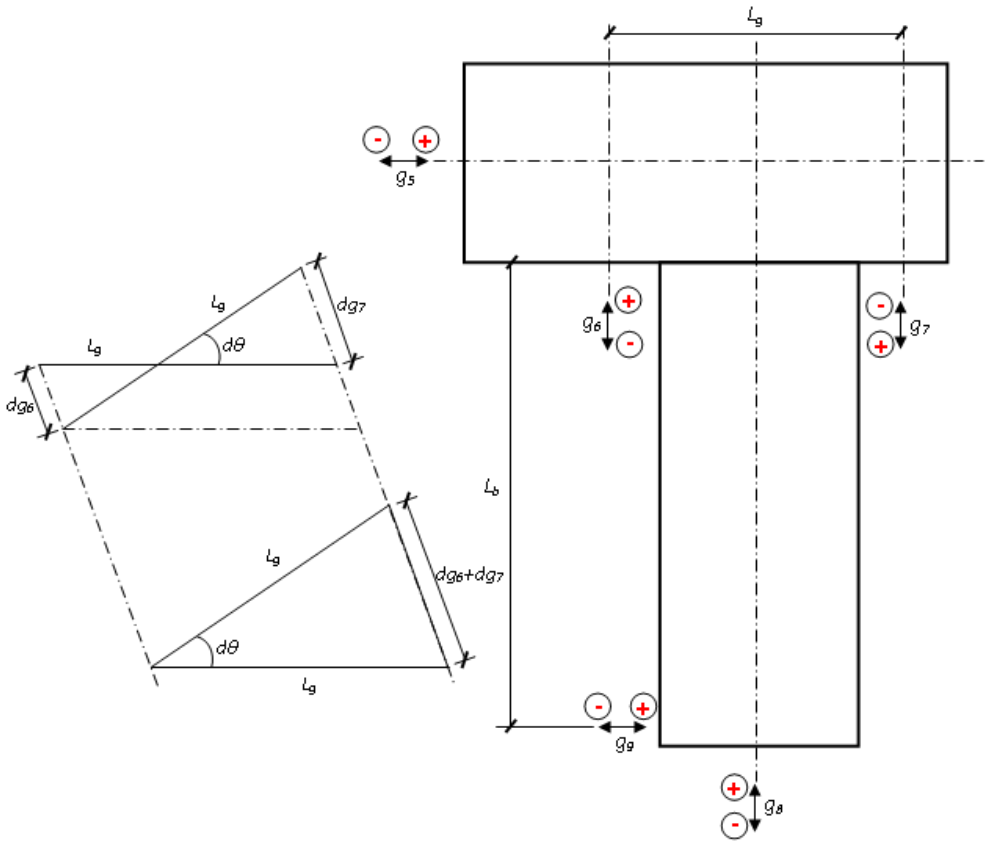

Figure 3-21. Kinematics of the rigid body translation and rotation.

3.9 References

ACI (2001) *Acceptance Criteria for Moment Frames Based on Structural Testing (T1.1-01) and Commentary (T1.1R-01),* A. I. T. G. First Edition, Farmington Hills, Michigan.

Fleishman, R.B., Restrepo, J.I., Pampanin, S., Maffei, J.R., Seeber, K., Zahn, F.A. (2014) "*Damage evaluations of precast concrete structures in the 2010-2011 Canterbury earthquake sequence*," Earthquake Spectra, Vol. 30(1): 277-306.

Giorgini, S., Pampanin, S., Carr, A.J., Cubrinovsky, M. (2013) "*Seismic behaviour of a 22-storey building during the Canterbury earthquakes*," Proceedings of the 2013 NZSEE Conference, Wellington, New Zealand.

Holmes (1988) *Price Waterhouse Centre,* Structural drawings, issue for construction.

NZS 3112:1986, *Methods of tests for concrete*, Standards Association of New Zealand, Wellington.

Priestley, M. J. N., Calvi, G. M, Kowalski, M. J. (2007) *Displacement-based seismic design of structures,* IUSS Press, Pavia, Italy.

Structural Engineers Association of California, SEAOC, Vision 2000 Committee (1995) *Performance based seismic engineering of buildings*, Sacramento, California.

4 EXPERIMENTAL RESULTS

4.1 Introduction

The first part of this chapter describes the global response of the specimens tested prior to and after the epoxy repairs. Special attention is given to the cracking pattern, crack widths, and failure mechanism. In the second part, comparison of the cracking pattern, hysteretic behaviour, and energy dissipation and stiffness are made, aiming at evaluating the effectiveness of the epoxy repairs in the cyclic performance of beam-column joints. Maximum and residual crack width measurements, and crack width ratios are also presented. Lastly, the nonlinear finite element modelling of the specimen is presented, along with preliminary results of a parametric study on the relocation of the plastic hinges.

4.2 Global Response

4.2.1 Test 1

Cracks 0.1 mm wide opened up at 0.2% "total" beam rotation. These cracks might be pre-existing ones (earthquake induced) that closed due to the low level of inelastic action. At 1.5% total rotation most of the deformation was concentrated at a single diagonal crack 4 to 12 mm wide (see Figure 4-1), and shear distortions became more evident. The reason of these diagonal cracks could be excessive principal tensile stresses as a result of the diagonal compression strut, induced by the hooked bars within the plastic hinge relocation detail. It was not possible to test the specimen up to failure due to the excessive and unexpected shear deformation (and sliding shear mechanism) of the specimen. The reaction frame was later modified in order to accommodate such displacement. It is worth noting that some of the specimens were also part of the structure's gravity system, and the inclusion of the gravity load effect during the test may have triggered the specimen's shear failure at an earlier stage. Figure 4-2 shows the residual cracking pattern at 1.5% and 2.5% total beam rotation. In this figure it is evident the development of a diagonal compression strut.

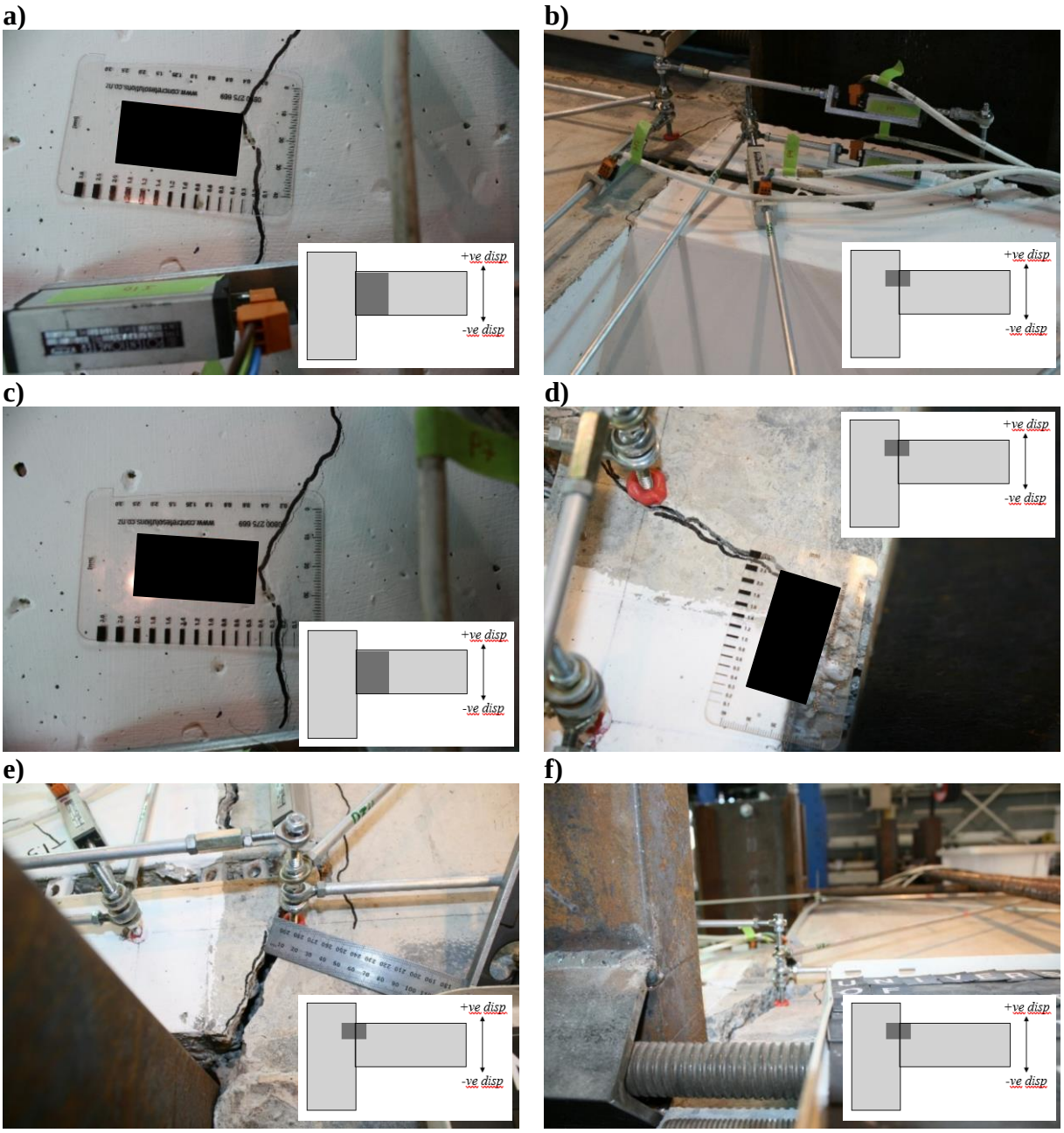

Figure 4-1. a) Crack 0.1 mm wide at 0.2% beam rotation; b) initiation of diagonal crack due to socket for fixing non-structural components; c) crack 0.1 mm wide increasing to 0.2 mm at 0.75% beam rotation; d) diagonal crack due to socket developing further to up to 3 mm wide at 1% beam rotation; e) diagonal crack at socket 10 mm wide at 1.5% beam rotation; f) vertical dislocation at the diagonal crack at 1.5% beam rotation.

As described in Section 3.8, during the deconstruction process, the beams adjacent to the extracted "H frames" were cut-out approximately at the column face. The flexural beam capacity of these beams relied upon straight D28 bars developed over a length of 1100 mm (i.e. without a standard hook), just above the minimum required as per the NZS3101:2006.

Figure 4-3 shows the bar-slip measured with two spring potentiometers located at the bar end at the cut-out section. The maximum slip observed during the test minimum (in the order of 40 μm), therefore it can be considered that the bar anchorage length was appropriate.

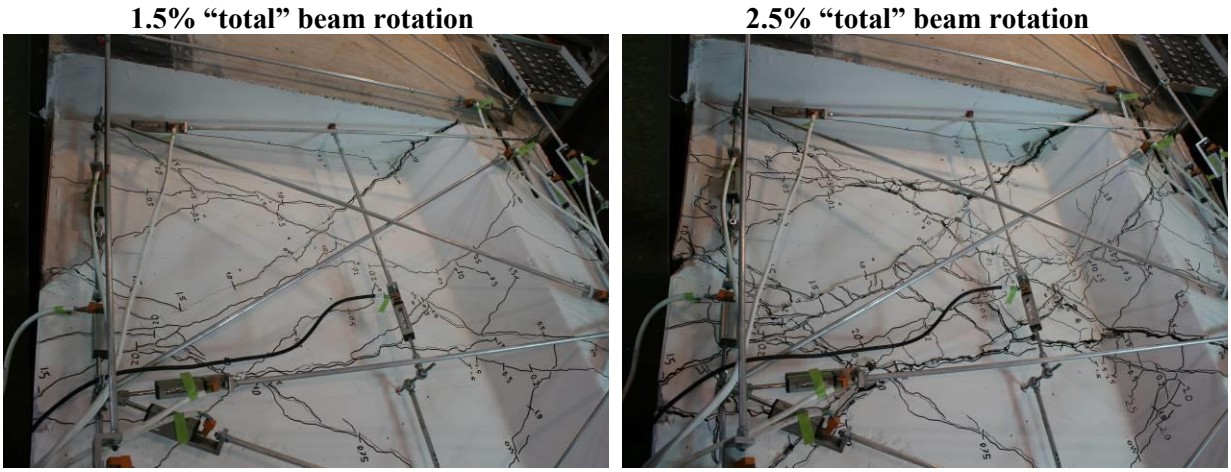

Figure 4-2. Residual racking pattern observed during Test 1, at 1.5% and 2.5% "total" beam rotation.

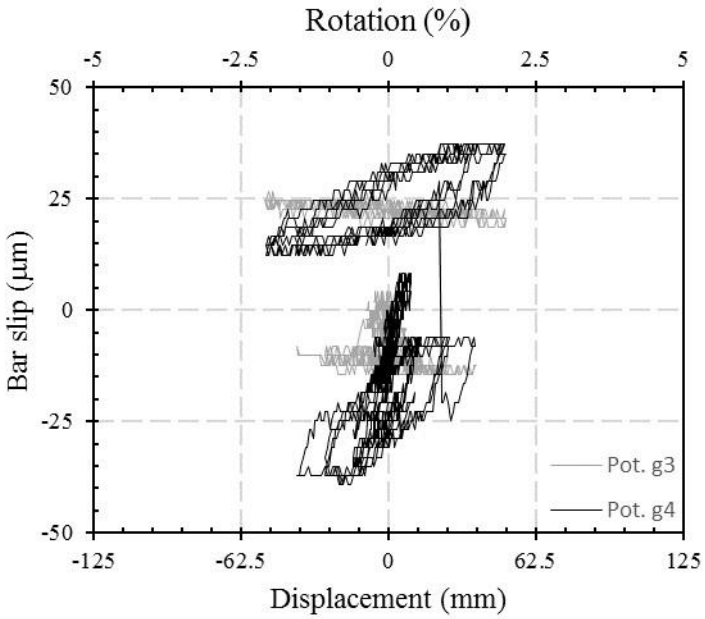

Figure 4-3. Bar-slip measured during Test 1.

4.2.2 Test 2.1

Cracks 0.1 mm wide were also observed at 0.2% "total" beam rotation. Maximum cracks 3 mm wide were observed at 1% "total" beam rotation. By comparing the cracking pattern before and after the test, it is believed that most of the pre-existing cracks were activated at this beam rotation level. Residual (static) cracks between 0.1 mm and 2.0 mm wide were

observed at the end of the test. The same diagonal crack initiating at the socket location was observed in this test (see Figure 4-4).

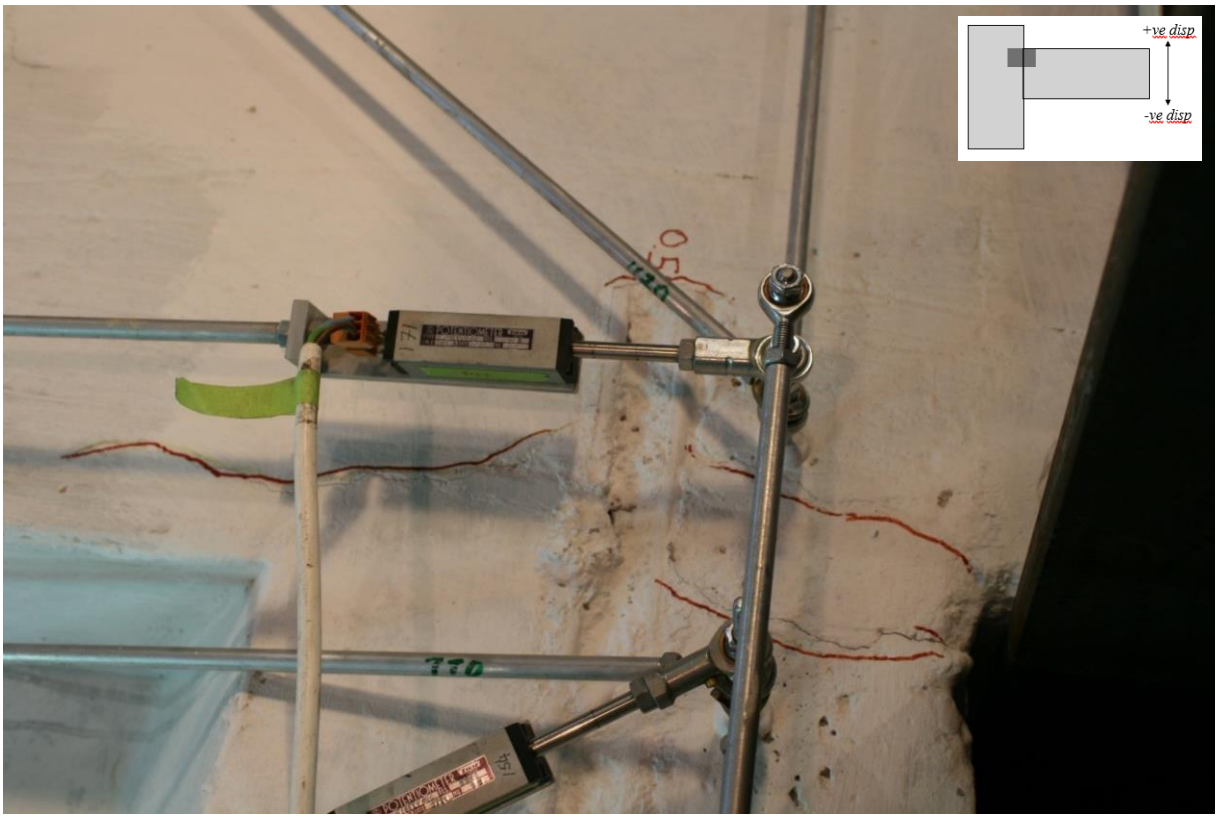

Figure 4-4. Initiation of diagonal crack at the socket location, Test 2.1.

4.2.3 Test 2.2

Appendix C shows photographs taken during the epoxy repair process of specimen 2. Cracks 0.1 to 0.2 mm wide started developing at 0.1% "total" beam rotation (Figure 4-5). A new crack extended from the column face towards the interior of the joint and did not follow the injected crack path. At 0.75% "total" beam rotation, hairline cracks and cracks 0.1 mm wide started developing outside the plastic hinge relocation detail (see Figure 4-6). At beam rotations of 1.5%, residual (static) cracks started becoming comparable to the maximum observed (70-90% of the maximum crack width) (see Figure 4-7 and Figure 4-8). Maximum cracks 9 to 18 mm wide were observed at 2.5% "total" beam rotation (see Figure 4-9). As shown in Figure 4-10, most of the repaired cracks re-opened up during the Test 2.2.

Figure 4-5. Cracks developing at 0.1% beam rotation

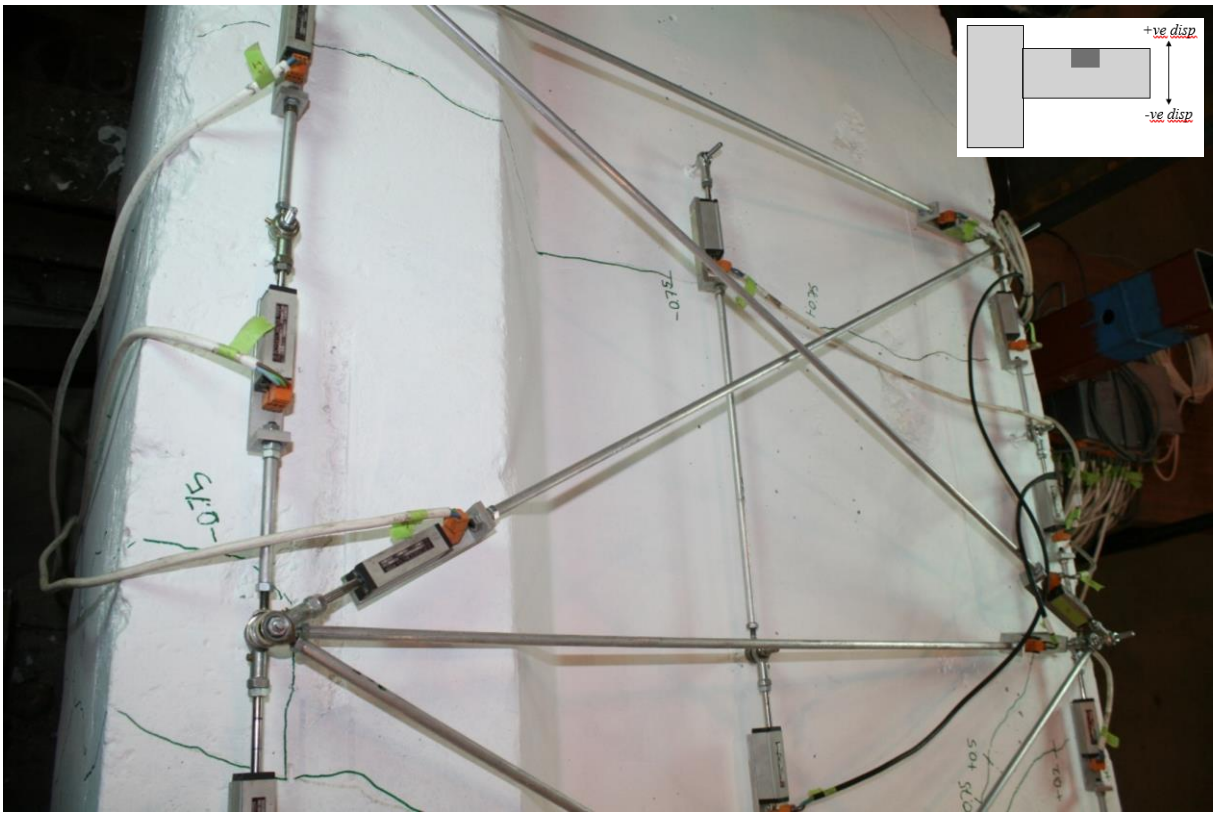

Figure 4-6. Crack developing outside the plastic hinge relocation detail, PHRD, at 0.75% beam rotation

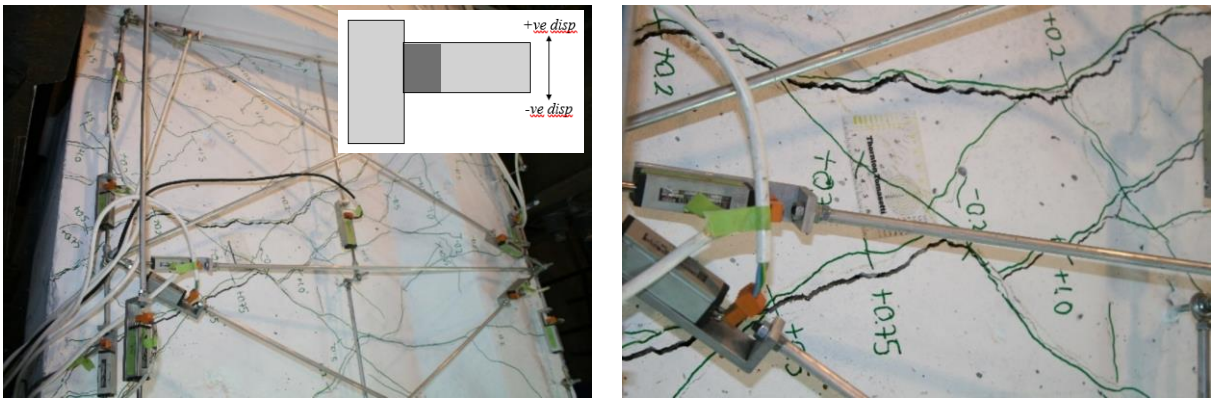

Figure 4-7. Diagonal cracks developing at 1.5% beam rotation.

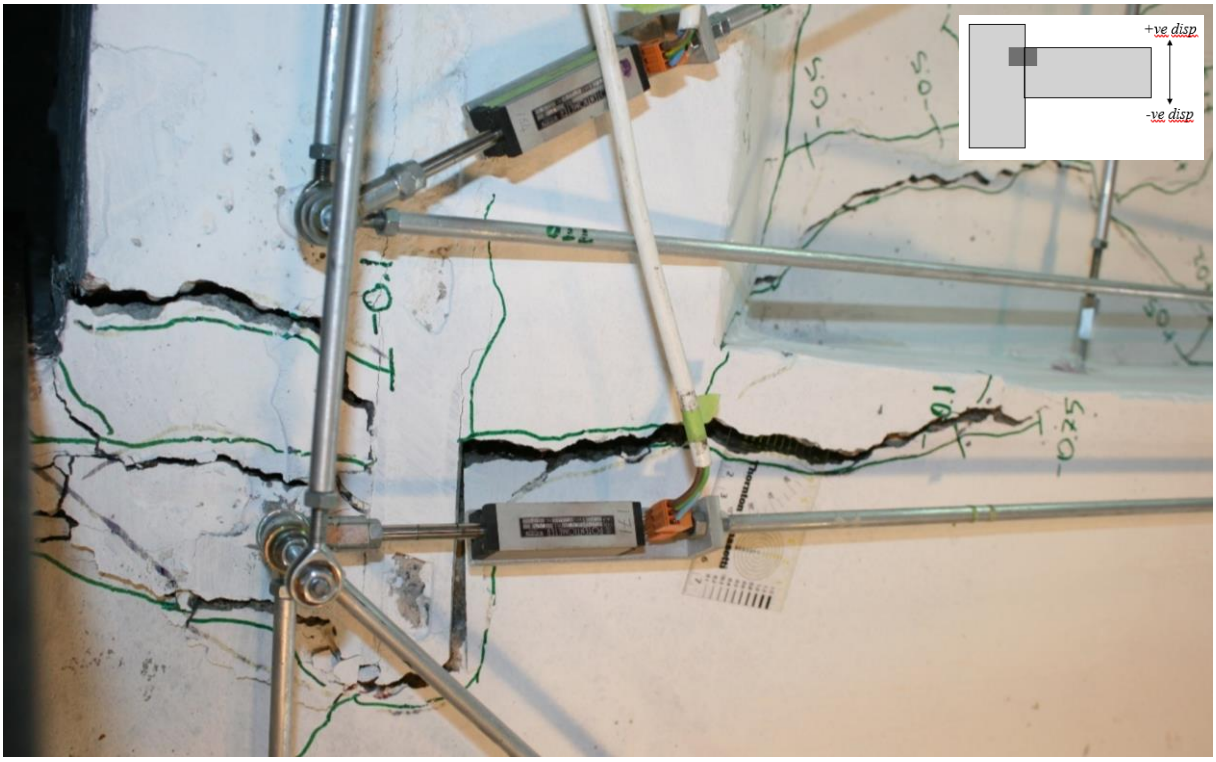

Figure 4-8. Crack at the socket for non-structural components, at 1.5% beam rotation.

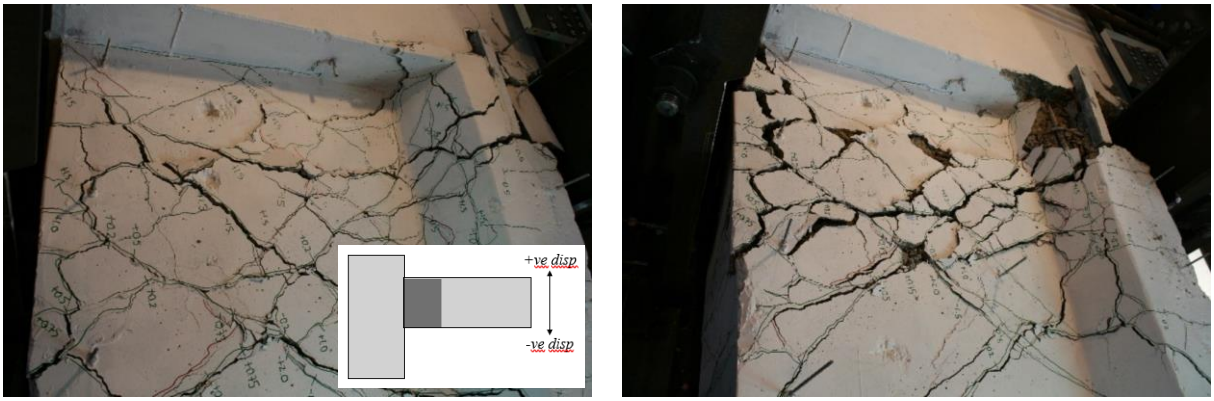

Figure 4-9. Cracked beam at 2.5% (left) and 3.5% (right) beam rotation.

Test 2.1 (pre-repair) **Test 2.2 (post-repair)**

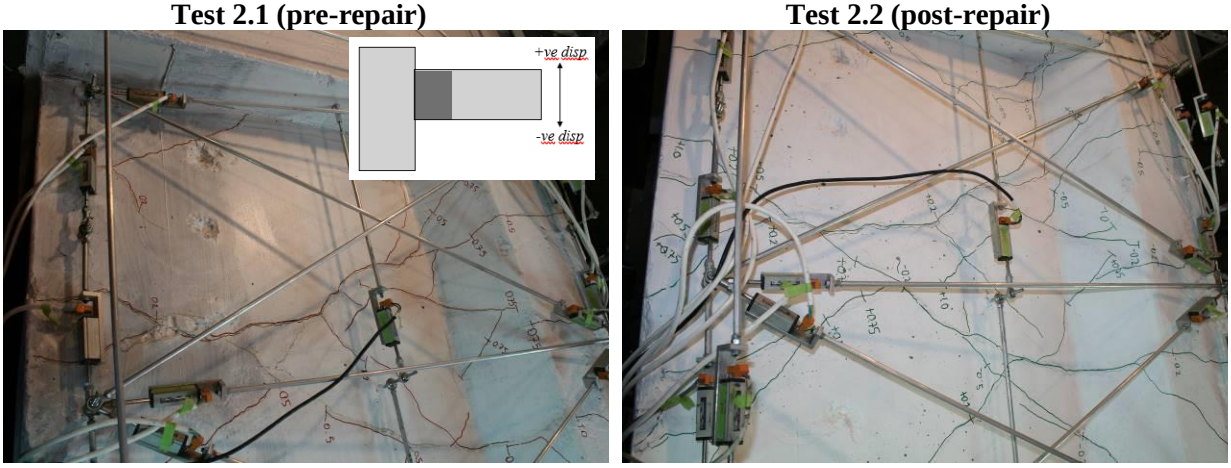

Figure 4-10. Residual cracking pattern observed during Test 2 at 1.0% "total" beam rotation.

4.2.4 Test 3.1

Existing cracks 0.1 to 0.15 mm wide opened up at 0.1% "total" beam rotation. The cracks continued increasing in quantity and in width, reaching 7 mm at 1.5% "total" beam rotation (see Figure 4-11). As in the Test 2.2, residual cracks started becoming comparable to the maximum observed at this beam rotation level. Some sliding with diagonal cracking was observed at the wet joint close to the mid-span. Residual (static) cracks between 0.1 mm and 6 mm wide were observed at the end of the test.

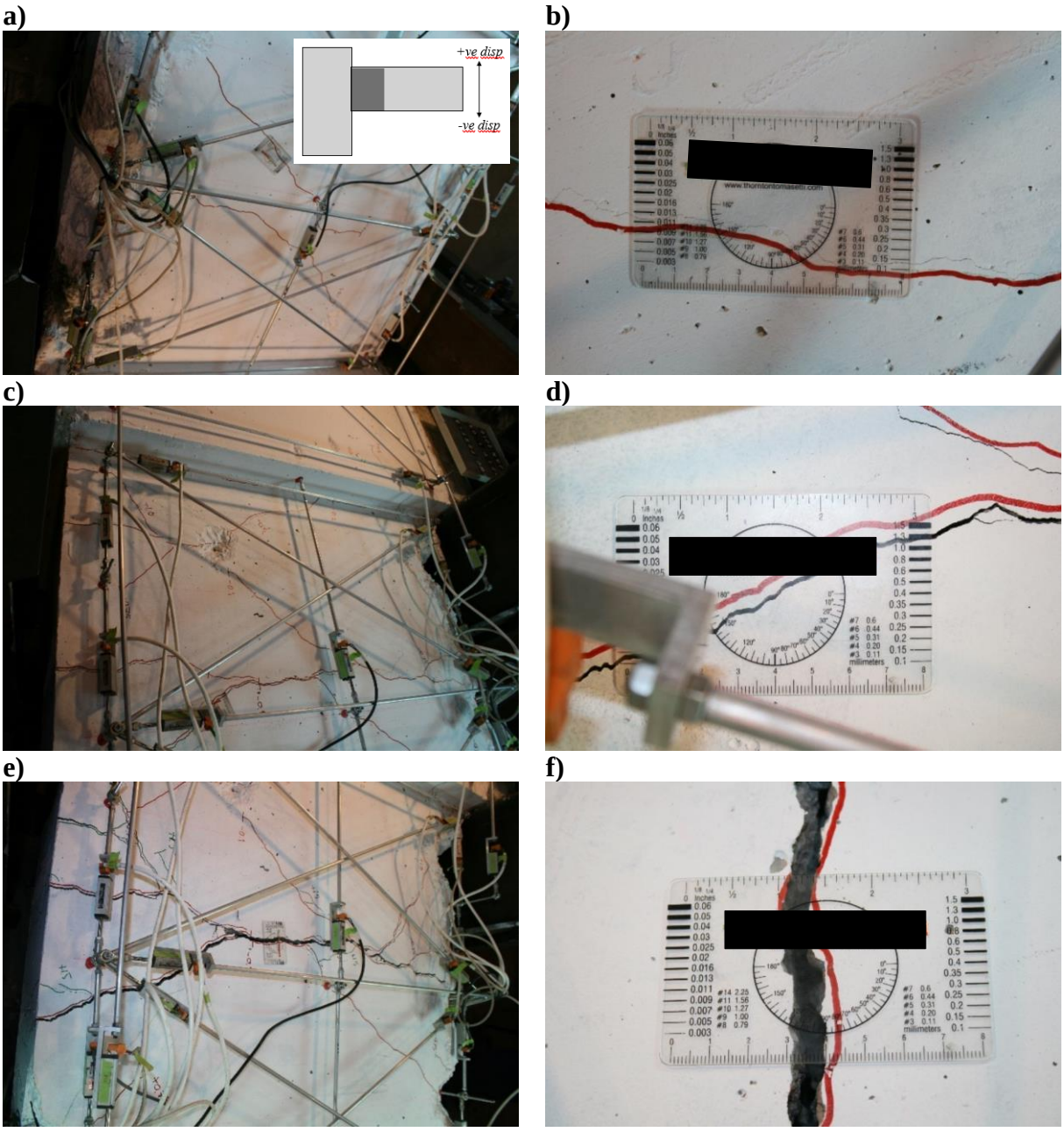

Figure 4-11. a) and b) Cracks 0.10 to 0.15 mm wide opening at 0.1% beam rotation; c) and d) cracks 1.30 mm wide opening at 1.0% beam rotation; e) and f) cracks 7.0 mm wide opening at 1.5% beam rotation.

4.2.5 Test 3.2

Appendix D shows photographs taken during the epoxy repair process of specimen 3. Cracks 0.1 mm wide were observed at 0.1% "total" beam rotation (see Figure 4-12). Sliding and diagonal cracking was observed at the cold joint, even at such low rotation level (see Figure 4-13). New flexural cracks were observed outside the plastic hinge relocation detail. As in the Test 3.1, residual (diagonal) cracks started becoming comparable to the maximum observed at 1.5% "total" beam rotation level.

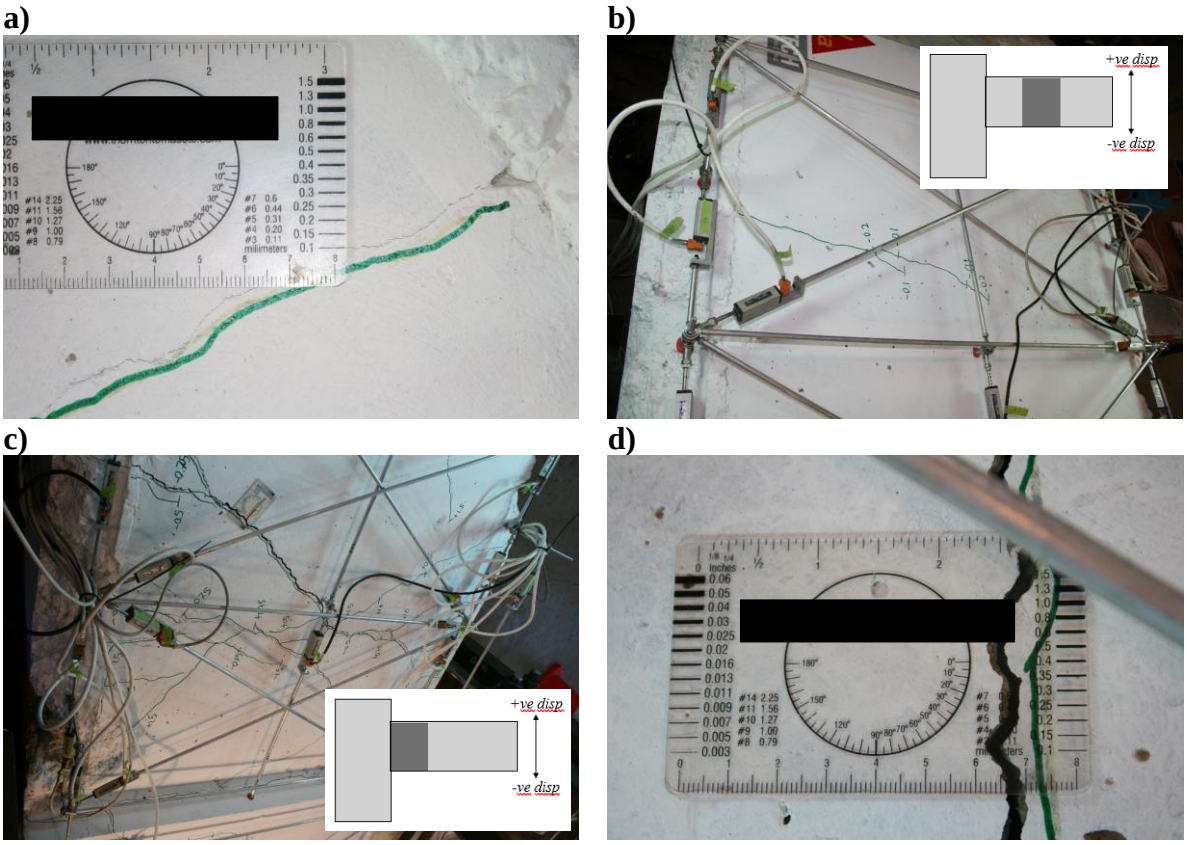

Figure 4-12. a) cracks 0.10 mm wide at 0.1% beam rotation; b) cracks developing outside the PHRD at 0.2% beam rotation; c) and d) cracks 4.0 mm wide at 1.5% beam rotation.

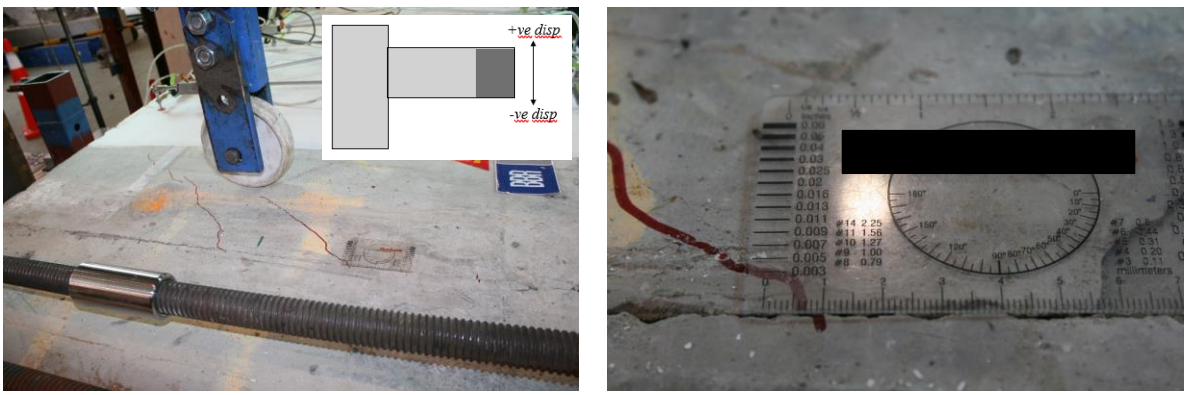

Figure 4-13. Sliding and diagonal cracking at the mid-span's cold joint.

Maximum cracks of 10mm in width were observed at 2.5% beam rotation (see Figure 4-14). Figure 4-15 shows the cracking pattern at 3.5% and 4.5% "total" beam rotation level. Figure 4-16 shows a crack at 4.5% beam rotation with the epoxy that has penetrated during the repair works. As shown in Figure 4-17, most of the repaired cracks opened-up during the Test 3.2.

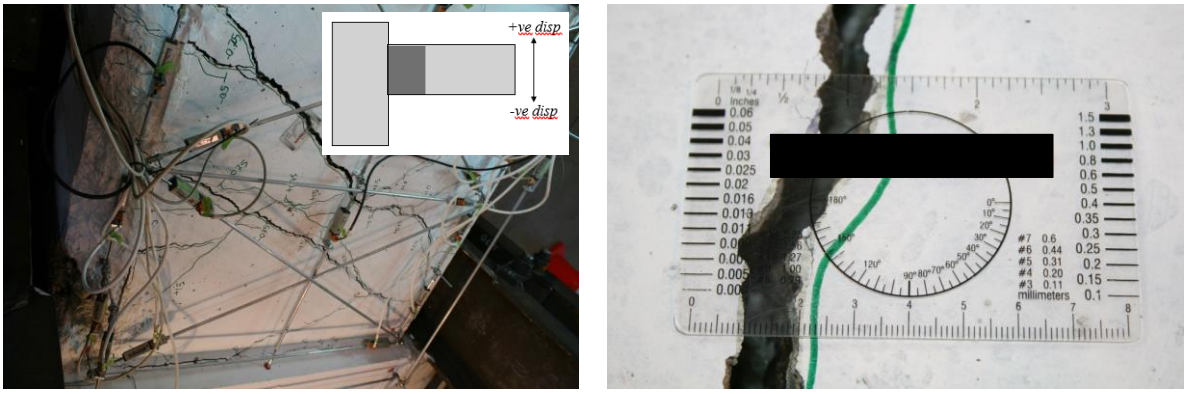

Figure 4-14. Cracks 10. 0mm wide at 2.5% beam rotation, Test 3.

Figure 4-15. Cracked beam at 3.5% (left) and at 4.5% (right) beam rotation.

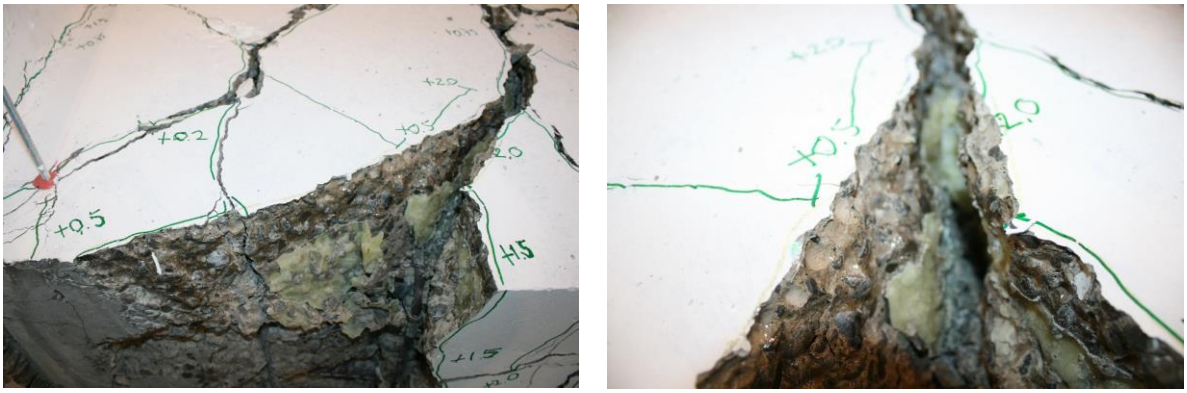

Figure 4-16. Crack opened-up at 4.5% beam rotation, showing the epoxy which has penetrated during the injection process.

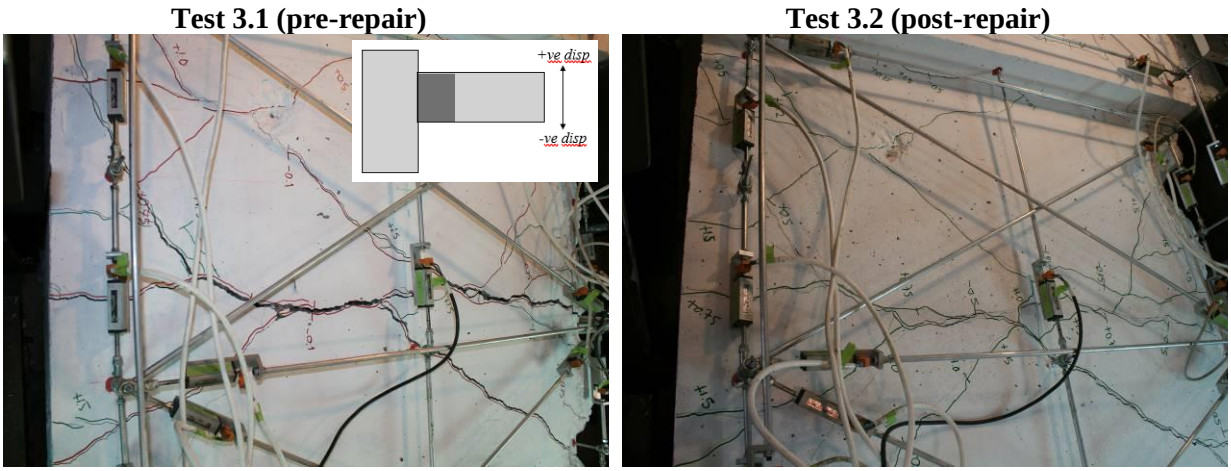

Figure 4-17. Residual cracking pattern observed during Test 3 at 1.5% "total" beam rotation.

4.3 Damage comparison

Figure 4-18 shows cracking patterns in Tests 1, 2.2 and 3.2, at different levels of "total" beam rotation. It is evident that the damage in Test 2.1 is more severe at lower (below 1.5%) rotation levels. Test 1 experienced the most severe damage at 2.5%, while Test 3.2 experienced the less damage at all rotation levels, with some of the damage in the form of flexural cracks outside the plastic hinge relocation detail.

In Figure 4-19 to Figure 4-23, solid grey lines represent force-displacement curves measured in "total" displacement units, whereas solid black lines are in "effective" displacement units (i.e., the "total" applied displacement minus the equivalent lateral displacement at the beam end due to rigid body translation and rotation). The onset of nonlinearity occurs at about 0.5% "effective" beam rotation. Rotation ductility demands of around 1.20 and 2.10 were achieved at the end of Tests 2.1 and 3.1, respectively.

All the tests show a relatively stable hysteretic behaviour at early stages, with however a sudden drop in strength during the last 3 cycles in both repaired configurations (Tests 2.2 and 3.2). Higher pinching behaviour, due to cracks opening and closing and more likely due to bond-slip degradation, was observed in the repaired configurations, in particular for Test 2.2. When considering Test 3.2, the relocation of cracks outside the plastic hinge relocation detail led to higher shear forces for the same displacement demand and a more stable hysteresis loop with less pinching. Overall, the effective displacement (capacity) achieved in the test was lower than in other tests.

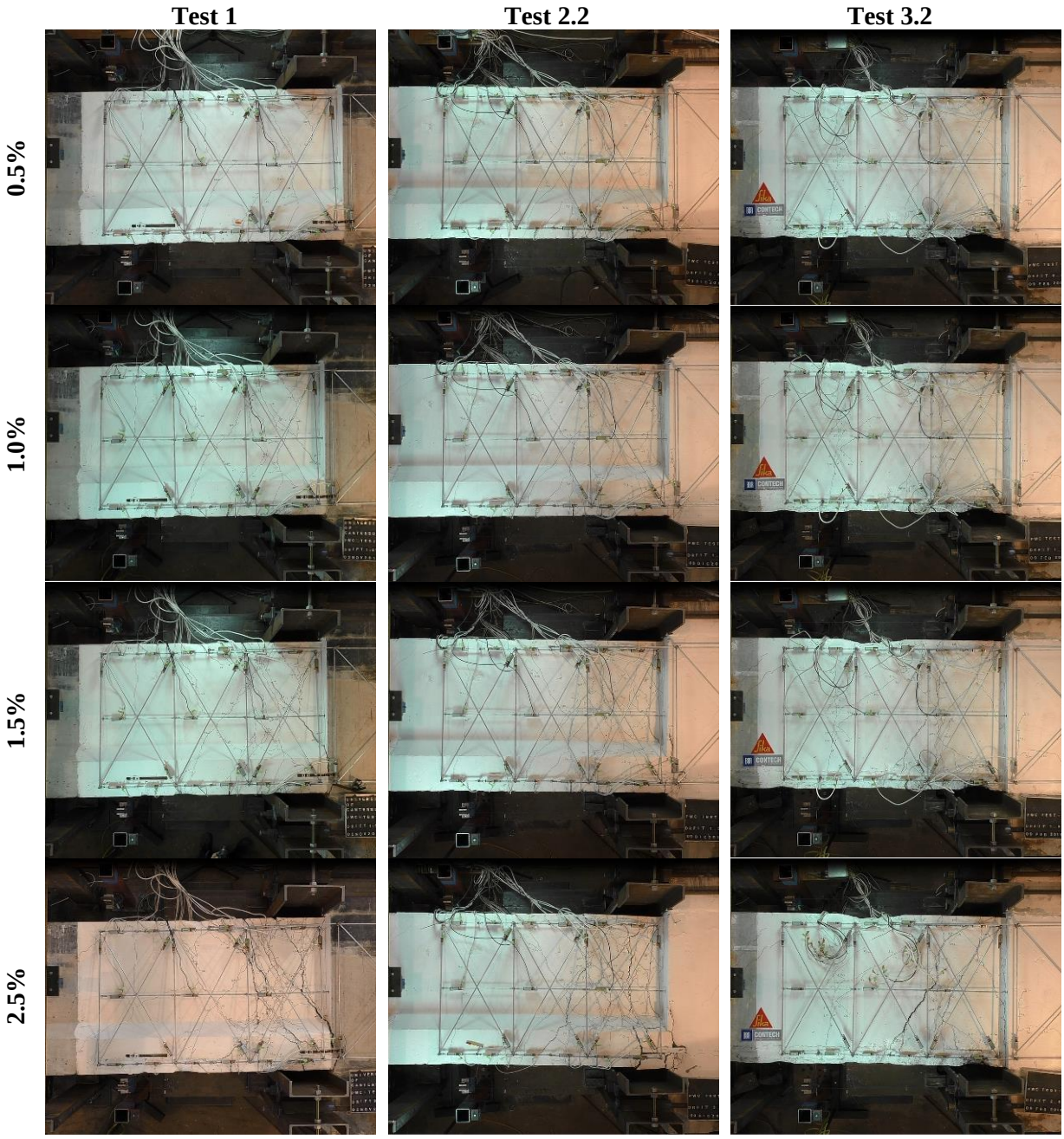

Figure 4-18. Observed damaged at different beam rotations (in "total" displacement units).

Figure 4-19 to Figure 4-23 also show the axial beam elongation for all the tests. It can be noted that the beam elongation is permanent and cumulative. Maximum elongations in Tests 2.1 and 2.2 were 2 mm and 7.2 mm, respectively, equivalent to 0.08% and 0.29% increase in beam length. These beam elongations were consistent with the maximum crack widths observed at the end of the tests. Maximum elongations in Tests 1, 2.2 and 3.2 were 21 mm, 26 mm, and 30 mm, equivalent to 0.85%, 1.05%, and 1.20% increase in beam length, respectively. It is worth noting that the testing apparatus allowed for free beam elongation without any restraint action from the floor diaphragm as in fact would occur in the real

building. Therefore, while the results are important to develop a better understanding of the behaviour of a “free” subassemblies, the beam elongation results are not fully representative of what we would have observed following the earthquakes. Figure 4-24 shows the comparison of the hysteretic behaviour before and after the epoxy repairs. The response of both specimens is very similar.

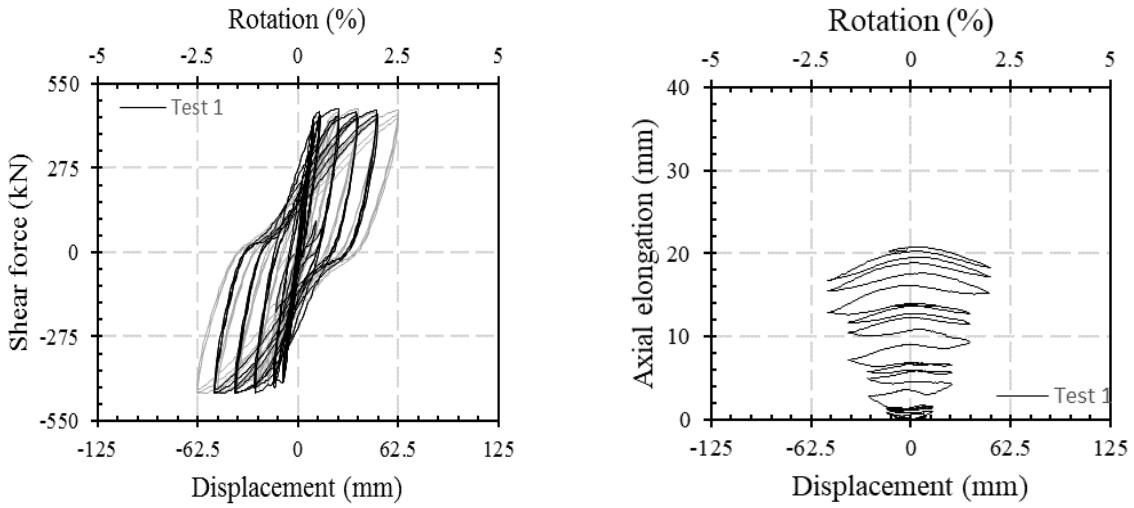

Figure 4-19. Force-displacement curves and axial beam elongation, Test 1.

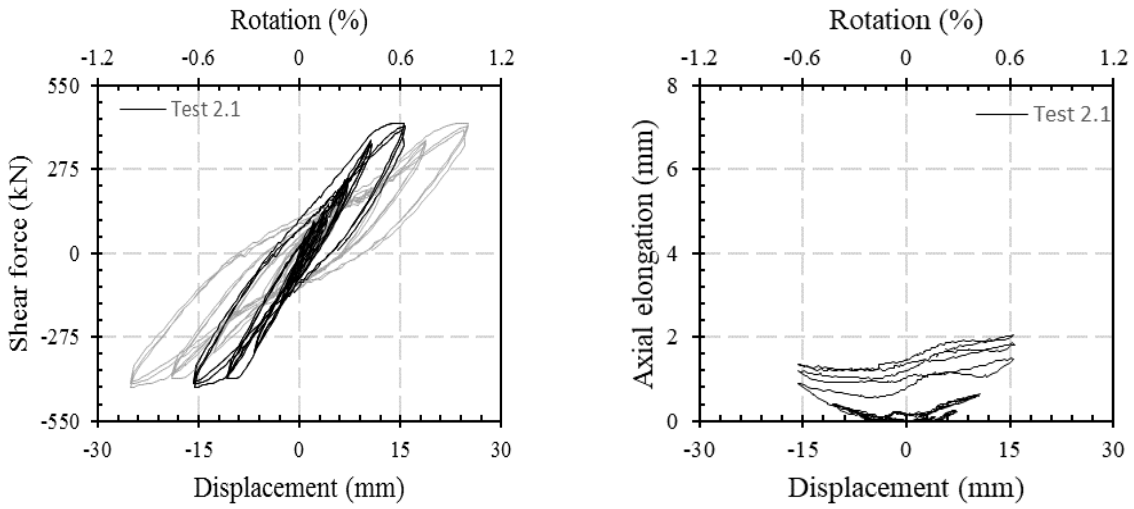

Figure 4-20. Force-displacement curves and axial beam elongation, Test 2-1.

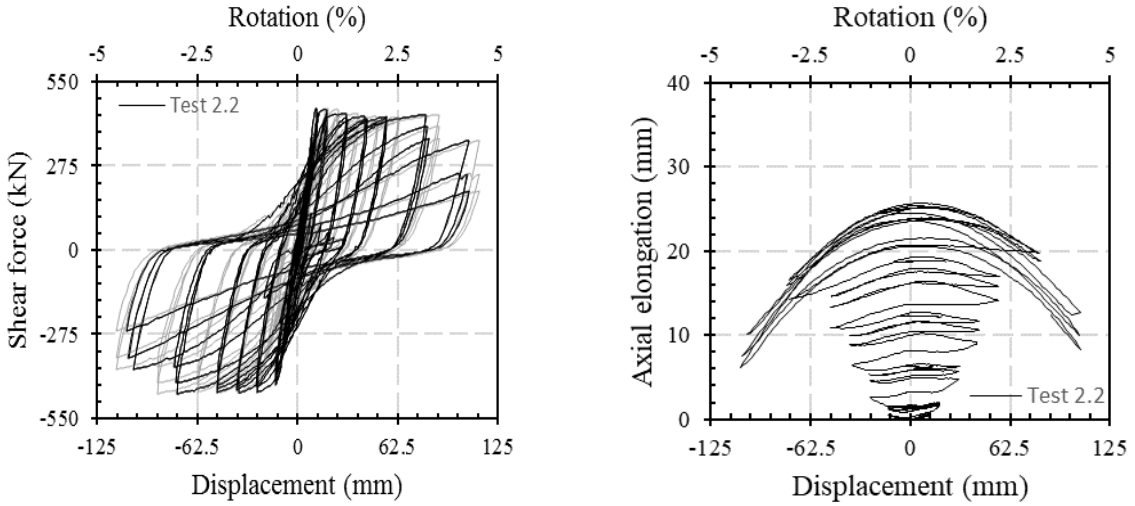

Figure 4-21. Force-displacement curves and axial beam elongation, Test 2-2.

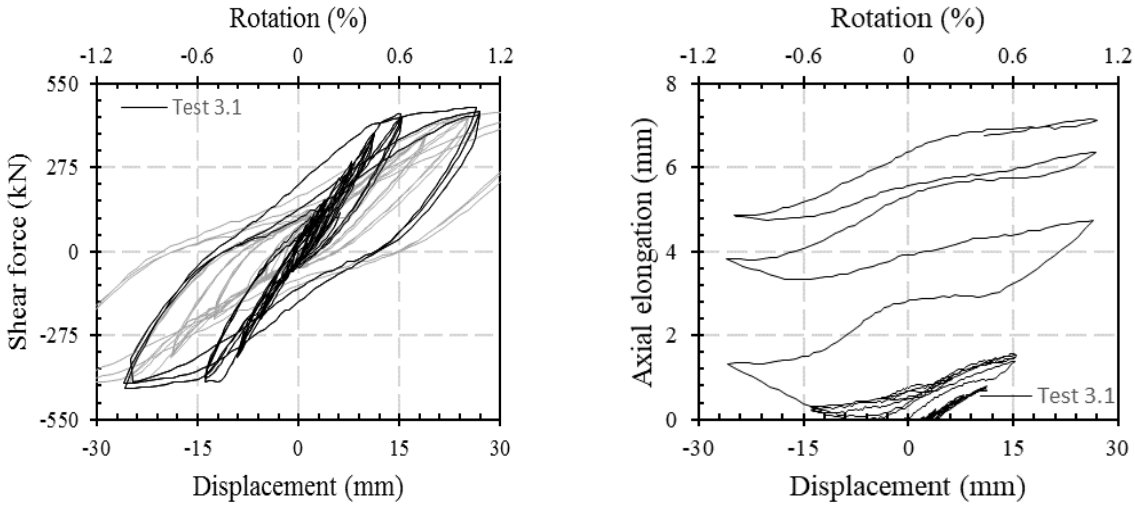

Figure 4-22. Force-displacement curves and axial beam elongation, Test 3-1.

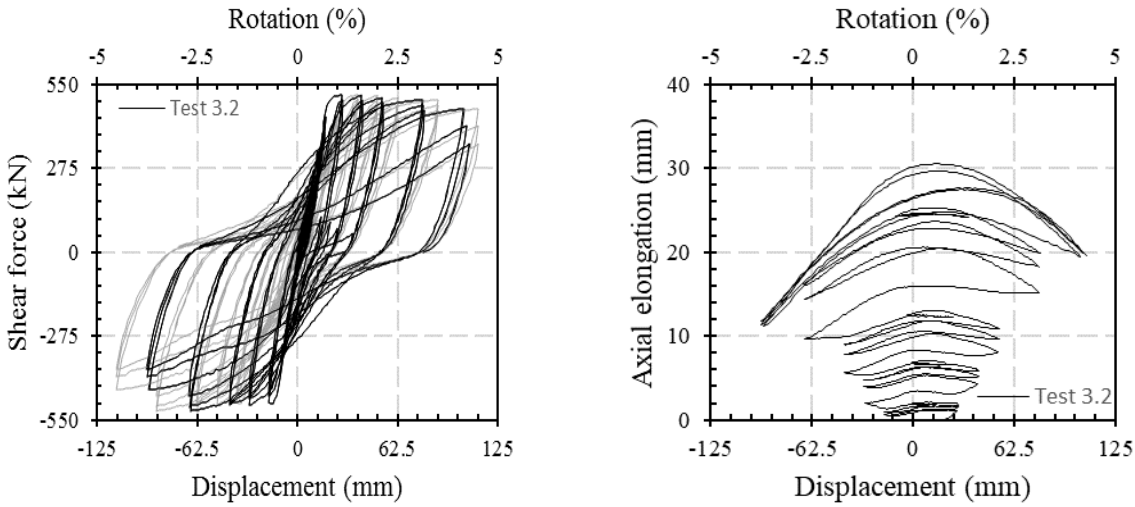

Figure 4-23. Force-displacement curves and axial beam elongation, Test 3-2.

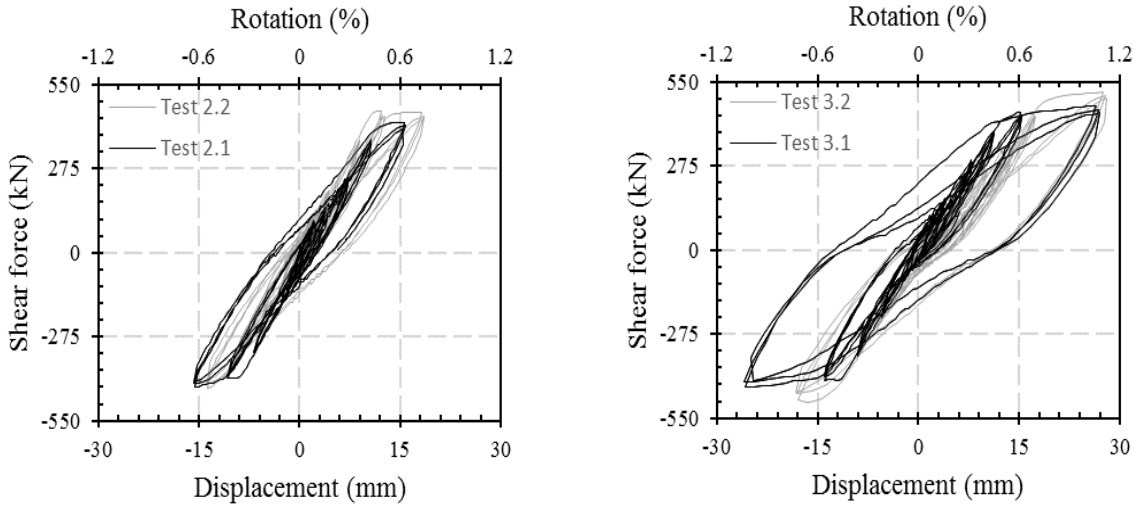

Figure 4-24. Comparison of hysteretic behaviour before (Test X.1) and after (Test X.2) the epoxy repairs.

4.4 Energy dissipation characteristics

Figure 4-25 shows cumulative energy dissipation computed as the sum of the area enclosed within the force-displacement curves, computed in "effective" displacement units. As shown in the figures, more energy is dissipated in Test 3.2 than in Test 2.2 (and arguably more than in Test 1 if we can infer that following the trend in the graph). This can be attributable to the less pinching as a result of more damage relocation (flexural type, outside the plastic hinge relocation detail). In general, reasonably good energy dissipation at both low (SLS) and high (ULS) rotation levels was achieved in the repaired specimens when compared with the slightly damaged specimen (Test 1). Appendix A shows Figure 4-25 in table format, including the energy dissipation at second and third cycles.

4.5 Stiffness deterioration

Figure 4-26 shows "peak-to-peak" secant stiffness for the first loading cycles, computed in "effective" displacement units as the slope of the line joining the maximum and minimum peaks in the force-displacement curves at each of the beam rotation levels.

As shown in the figure, there is a reduction of stiffness in the repaired specimens (both Test 2.2 and 3.2) at low rotation levels (below to the onset of nonlinearity, approximately) when compared with the (as-extracted) slightly damaged specimen (Test 1). There is a better stiffness recovering (at low rotation levels) in Test 2.2 than in 3.2, possibly because of its lower damage condition prior to the repairs. The secant stiffness of Test 2.2 is also closer to the one obtained in Test 1, and the same in Test 2.1. In general, the secant stiffness does not seem to be significantly affected at high (ULS) rotation levels when compared with Test 1.

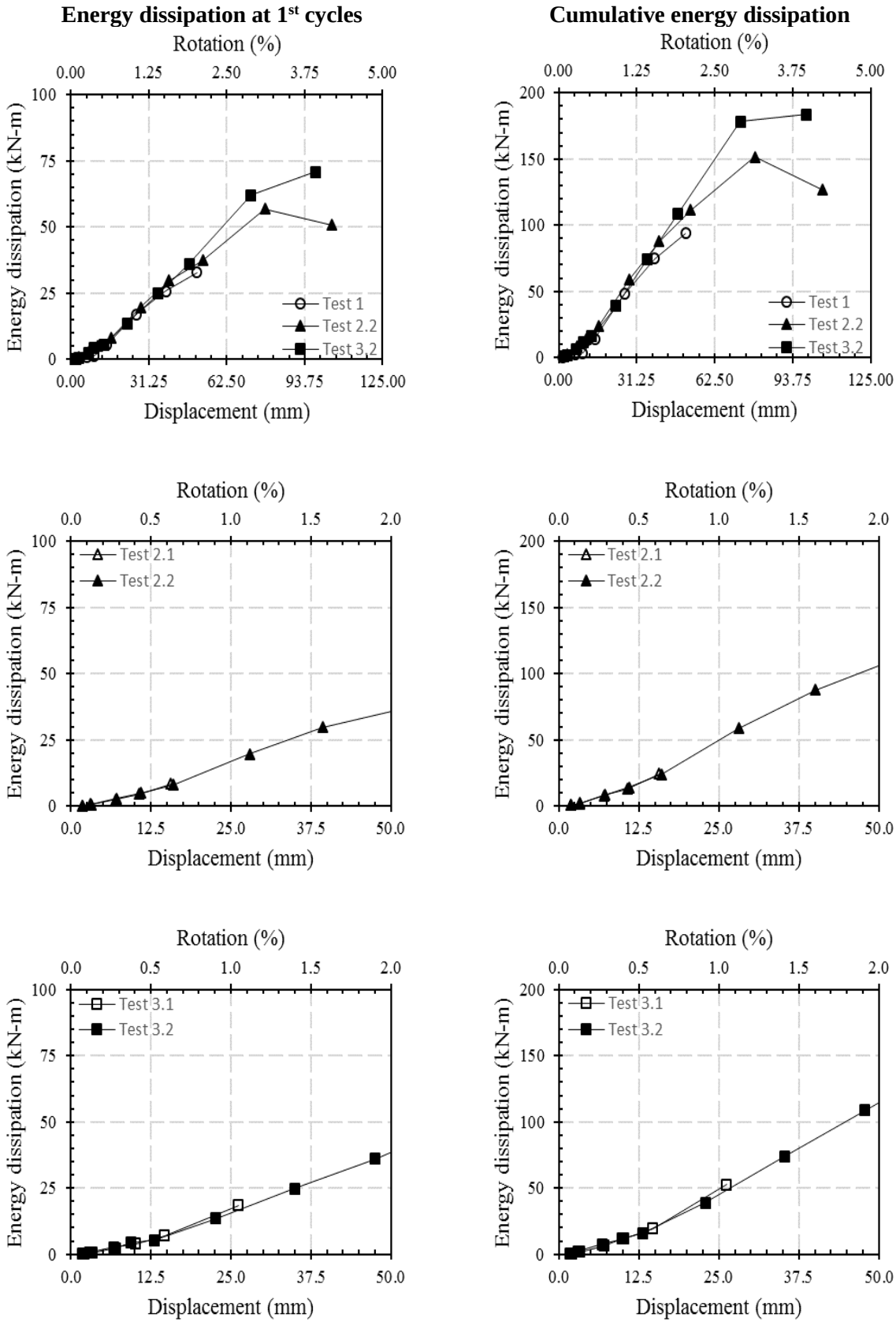

Figure 4-25. Energy dissipation characteristics at 1st cycles (left-hand side) and cumulative (right-hand side) at each beam rotation level.

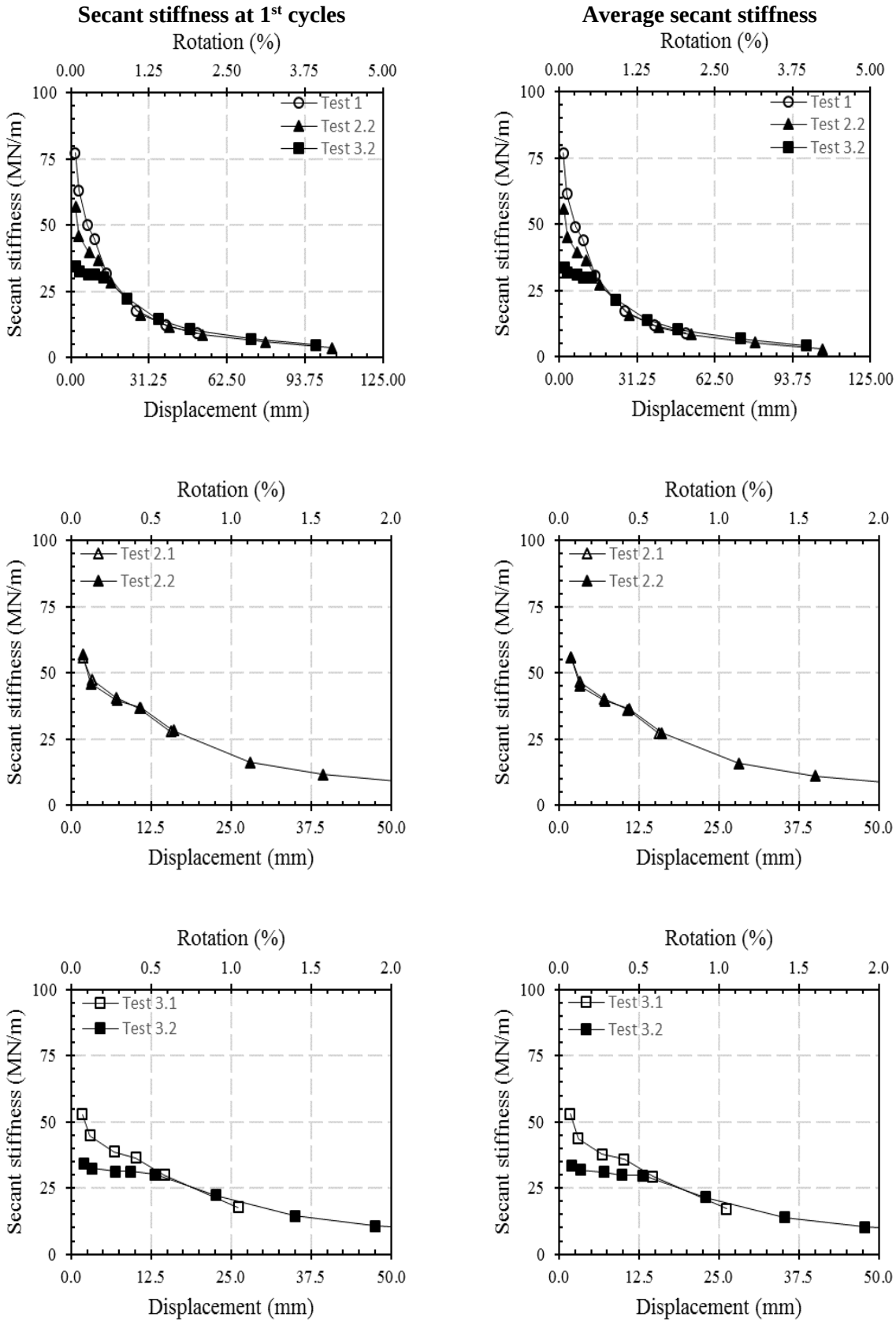

Figure 4-26. Secant stiffness degradation at 1st cycles (left-hand side) and average (right-hand side) at each beam rotation level.

Appendix A shows Figure 4-26 in table format, including the secant stiffness at second and third cycles.

4.6 Crack widths investigation

Figure 4-27 shows maximum and (static) residual crack widths measured during the tests. The top figures correspond to the most critical crack(s) observed within the plastic hinge relocation detail (i.e., shear-flexural cracks); the bottom ones correspond to flexural cracks observed outside the plastic hinge relocation detail during the Test 3.2. The maximum crack widths are measured at peak force, whilst the residual crack widths at zero force. Worth reminding that these residual cracks are "static" ones. The dynamics effects during the earthquake, as well as any axial load contribution, i.e. slab engagement effect resisting to the beam elongation, would further reduce them, thus increasing the maximum/residual ratio (Christopoulos et al, 2003; Pampanin et al, 2003).

Crack width ratios computed as the residual crack width upon the maximum residual crack width are shown in Figure 4-28. It is evident how the crack width ratios are rotation (i.e. curvature or strain) dependant, showing a change of slope from negative to positive at rotations near or at the onset of nonlinearity. The negative slopes below the onset of nonlinearity are due to the fact that at low rotation levels the residual cracks are very small and almost constant (hairline-to-0.1 mm in width), regardless of the increase of the maximum crack widths as the rotation level increases. This is in line with recent post-earthquake observations (Pampanin et al, 2012; SESOC, 2011) where hairline-minor residual crack width could in fact hide non-negligible, if not significant, damage, including tensile fracture of the bars, especially in lightly reinforced shear walls.

The average crack width ratio obtained for flexural cracks is 0.43 (with a standard deviation of 0.15), whereas for flexural-shear cracks is 0.56 (with a standard deviation of 0.22). Figure 4-29 shows the crack mapping in specimen 3 after completion of Test 3.1 prior to epoxy repair the specimen, and during Test 3-2 after epoxy repairs at 2% total beam rotation.

Appendix A shows Figure 4-27 and Figure 4-28 in table format.

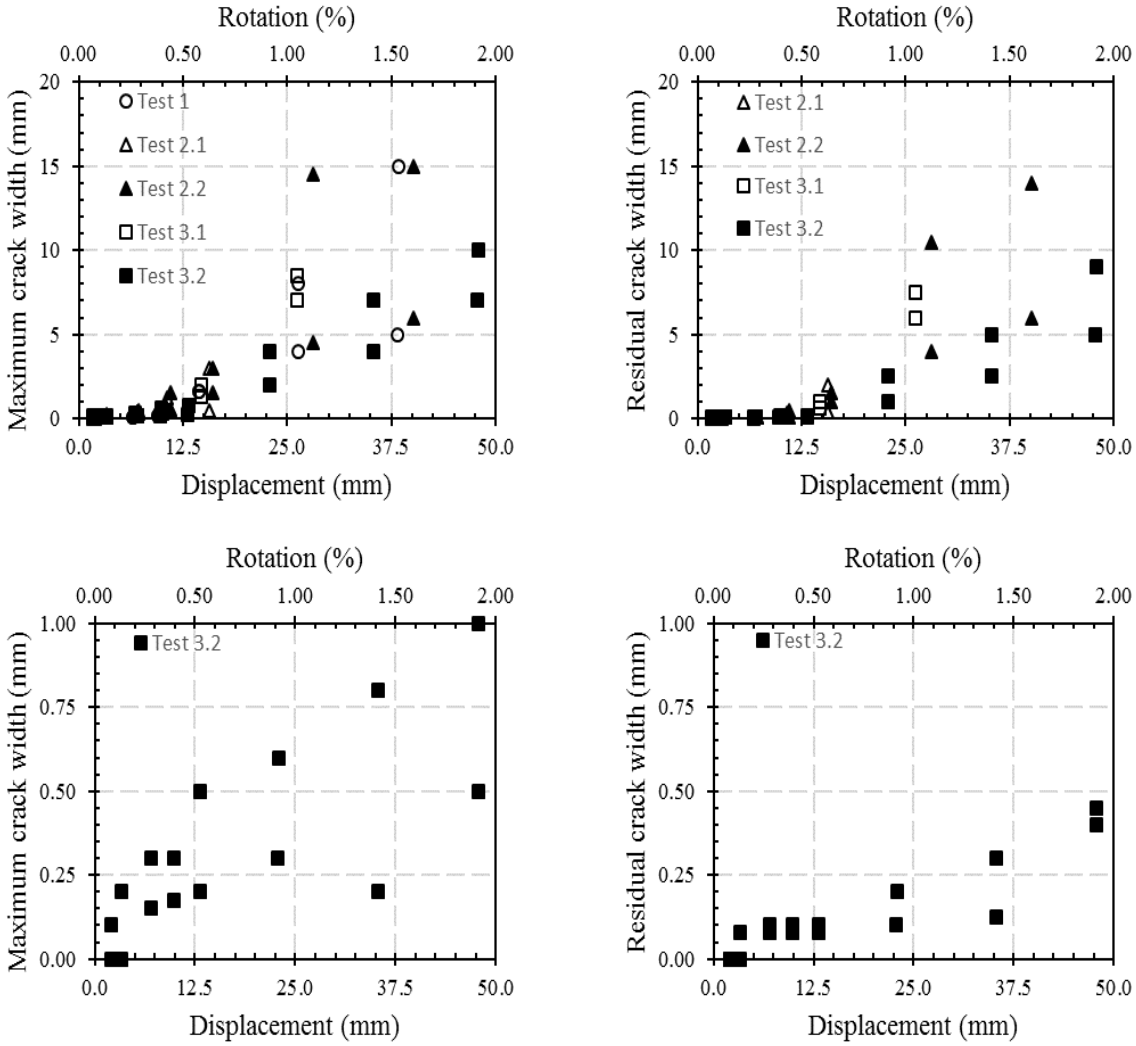

Figure 4-27. Maximum and residual crack widths measured within (top) and outside (bottom) the plastic hinge relocation detail.

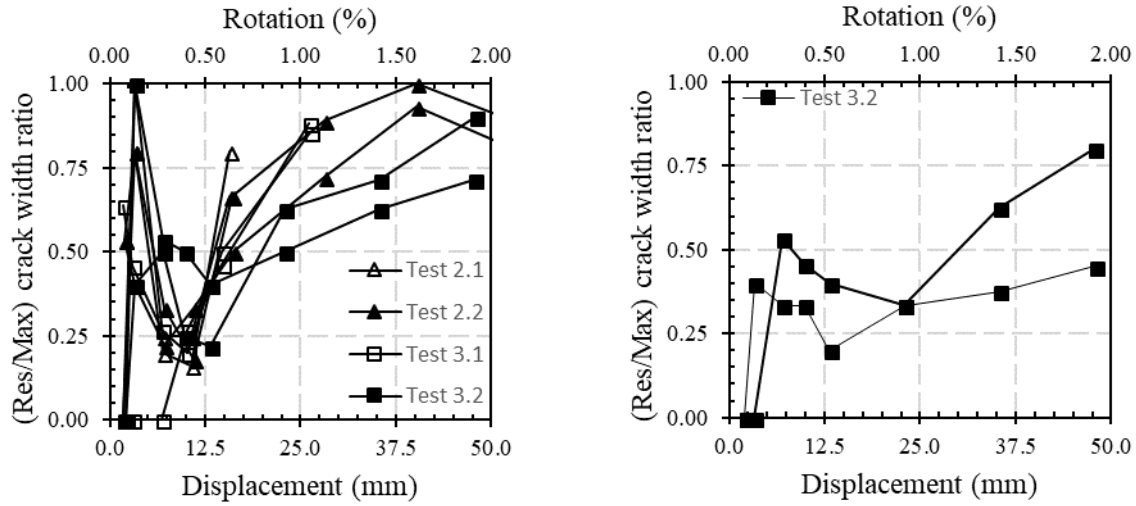

Figure 4-28. Crack with ratios (residual divided by maximum) computed within (top) and outside (bottom) the plastic hinge relocation detail.

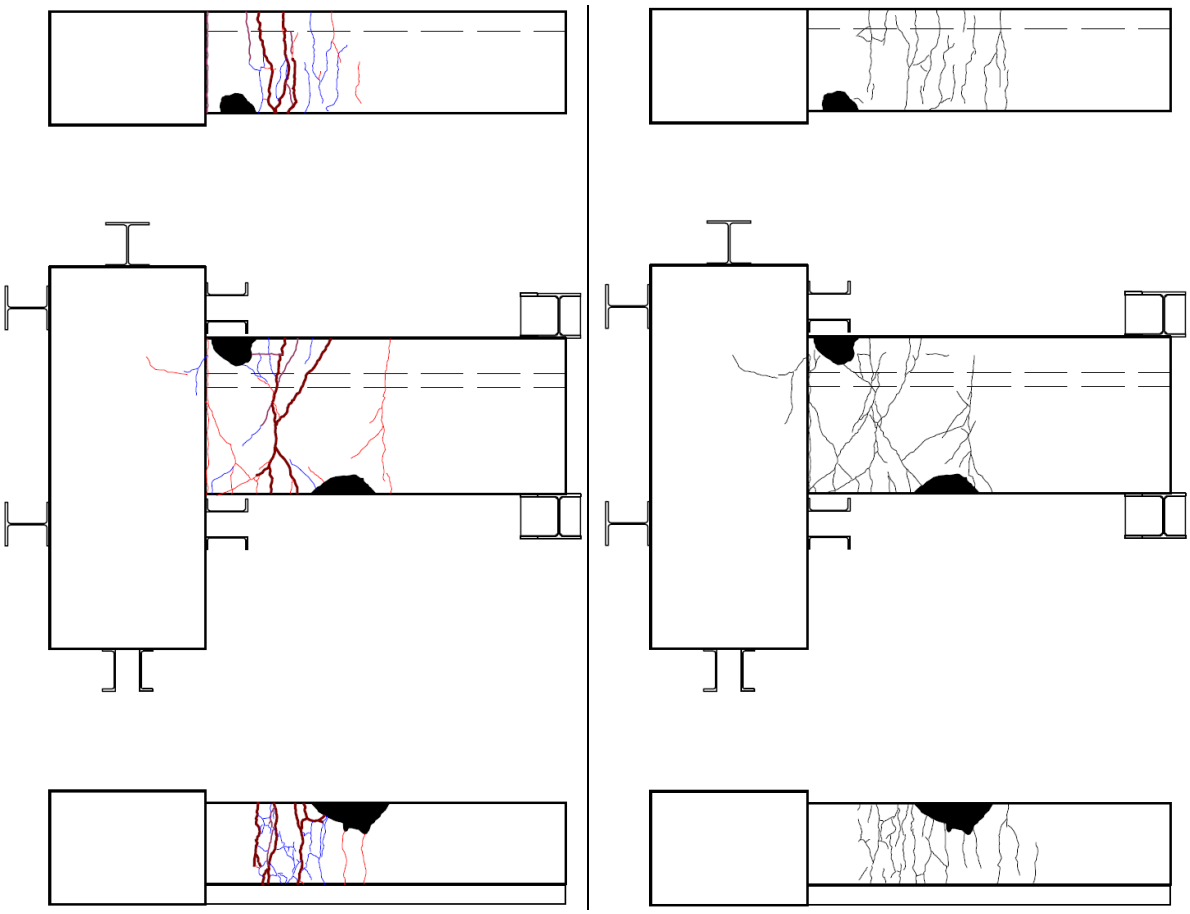

Figure 4-29. Crack mapping in specimen 3 after completion of Test 3.1 prior to epoxy repair the specimen (left) and during Test 3-2 after epoxy repairs at 2% total beam rotation (right).

4.7 Effect of epoxy repairs on beam shear distortion and curvature

Figure 4-30 shows a comparison of beam distortions and curvatures measured in the test 3 prior to (Test 3.1) and after epoxy repairs (Test 3.2). It can be observed that, within the plastic hinge relocation detail (PHRD), after the onset of nonlinearity the epoxy repaired specimen exhibited less shear distortion and more flexural deformation (i.e., curvature) compared to the original specimen. The opposite effect was observed outside the PHRD, although to a less extent. Appendix B shows beam distortions and curvatures versus displacement curves for tests 2 and 3, within and outside the PHRD region.

4.8 Numerical investigation

4.8.1 Nonlinear finite element numerical model

The nonlinear finite element (FE) code MASA was used to model the specimen (see Section 6.2.1 for a detailed description of the finite element code and modelling assumptions). Hexahedral elements with side lengths of approximately 25 mm in the joint area and the

plastic hinge regions, and 75 mm elsewhere were used to create the mesh of the elements. Linear elastic elements were used at the vicinities of the supports and the point of load application so that local failure of concrete elements due to excessive stresses is avoided. Mirror symmetry (i.e., symmetry about a vertical plane across a mid-section in the beam-column joint) was used to reduce the total number of nodes and elements and thus the required computational time.

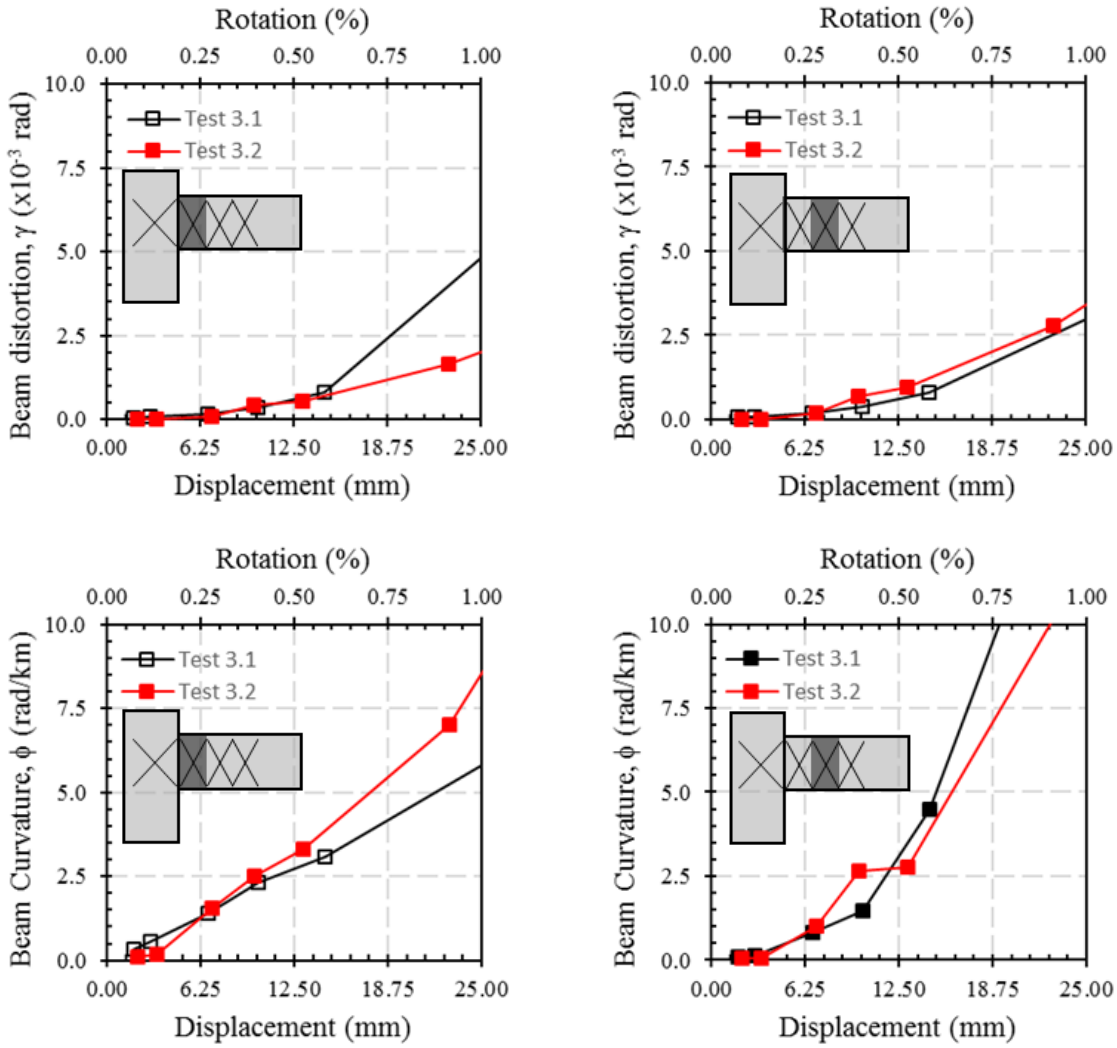

Figure 4-30. Comparison between beam shear distortions and curvature measured in the original (Test 3.1) and epoxy-repaired specimen (Test 3.2), within (top and bottom left) and outside (top and bottom right) the plastic hinge relocation detail (PHRD).

4.8.2 Numerical versus experimental comparison

Figure 4-31 shows snapshots of the cracking patterns in the specimen during the experimental campaign at beam rotations (in "total" displacement units) of 0.5%, 1.0%, 1.5%, and 2.5%, as well as the expected cracking pattern obtained with the FE model. As seen in this figure, the simulation agrees reasonably well with the observations.

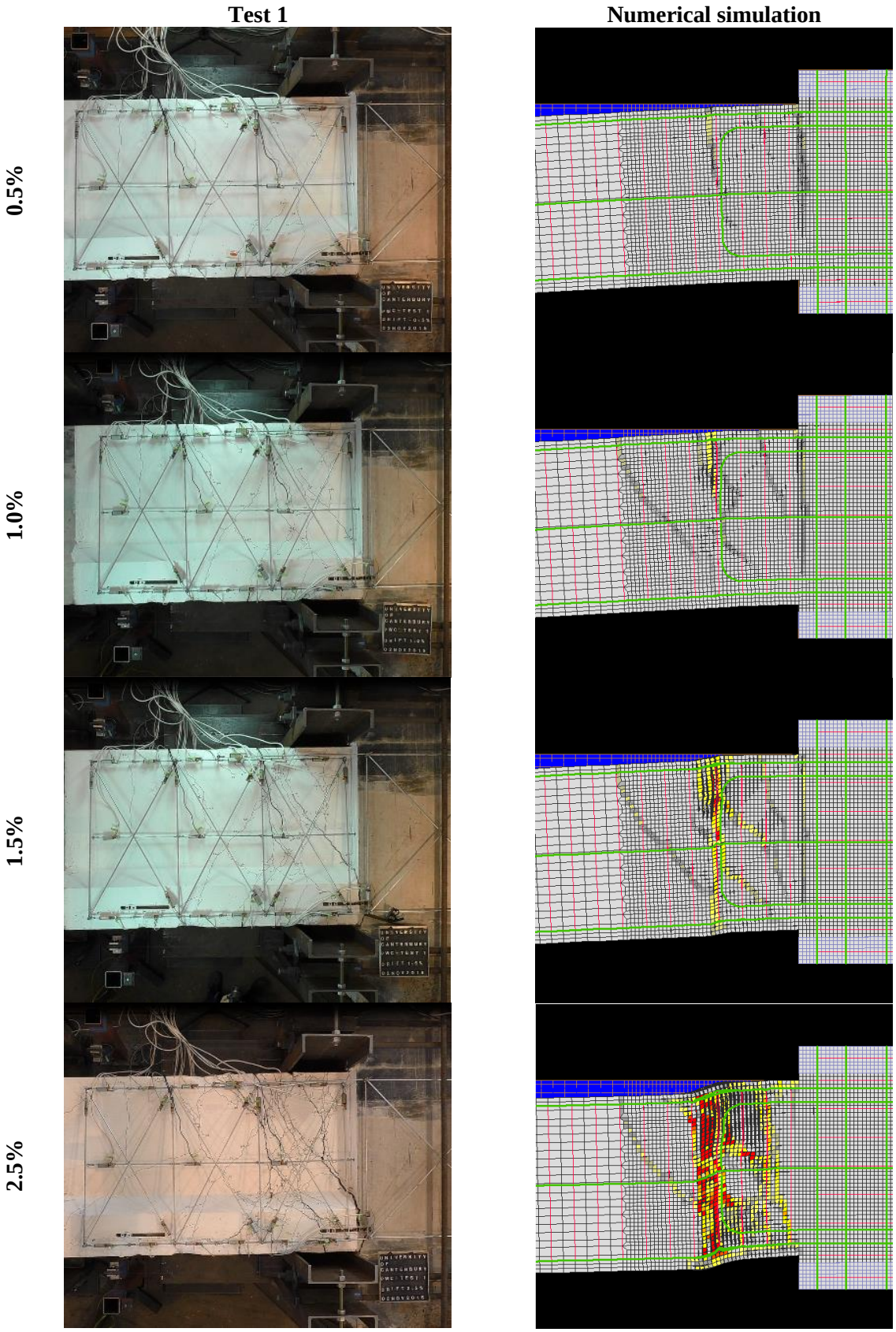

Figure 4-31. Observed damaged at different beam rotations in "total" displacement units (left); deformed shape (scaled-up) and cracking pattern obtained with the finite element simulation (right). Scale for the cracks widths in the simulation is shown in Figure 4-33.

Shear distortions became more critical after 1.5% beam rotations. Most of the damage occurs within the plastic hinge relocation detail, with some cracking developing outside this region. The main difference between the observations and simulation is that MASA is not able to capture the appearance of the diagonal crack propagating from the socket.

Figure 4-32 shows the cyclic lateral force-displacement response from the quasi-static test (light-grey curves) measured in "effective" displacement units (i.e., the "total" applied displacement minus the equivalent lateral displacement at the beam end due to rigid body translation and rotation), and the cyclic curve obtained from numerical analysis. Although the model is not able to capture the pinching at higher rotation levels (due to the formation of diagonal cracks) and there is some strength degradation at the last cycle (not observed during the test), the model is able to capture the hysteretic behaviour at lower rotation levels as well as some features at higher rotation levels such as the loading and unloading stiffnesses.

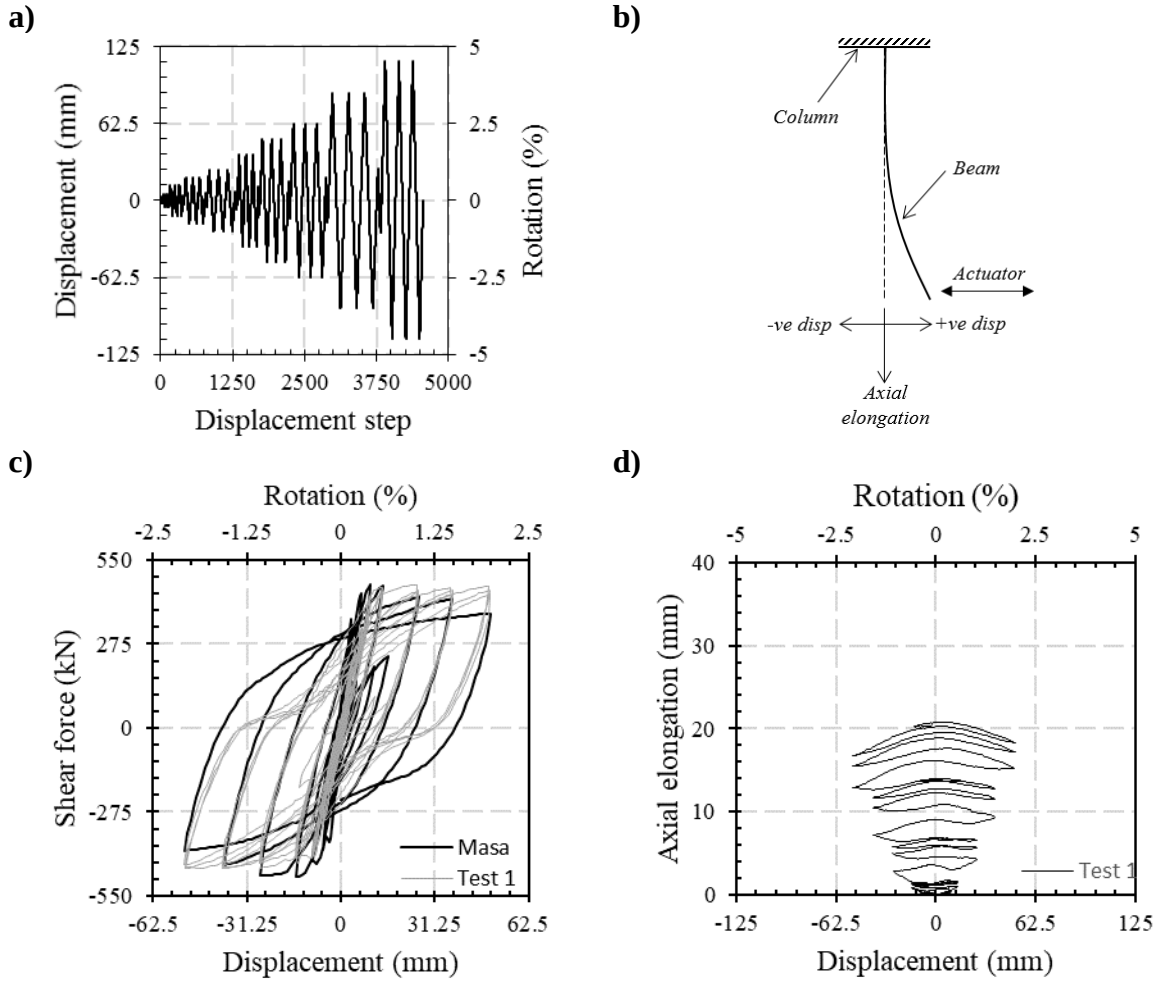

Figure 4-32. a) Applied loading protocol, b) displacement sign convention, c) force-displacement curves (light-grey curves correspond to the test, dark curves correspond to the nonlinear FE simulation), and d) beam elongation curve obtained during the test.

4.8.3 Parametric study

The effect of transverse volumetric ratio and shear span on the cracking pattern was numerically investigated. In particular, during the experimental campaign it was observed that, contrary to the expectations, the damage in the specimen was concentrated within the plastic hinge relocation detail (PHRD). This observation was consistent with the observations in the building following the 2010-2011 Canterbury earthquakes. Therefore, it is of special interest to investigate the effect of these two parameters on the relocation of the damage outside the PHRD. The original specimen had transverse reinforcement A_v/S= 3 mm^2/mm and a shear span L/d= 4 (being L the clear distance measured between plastic hinge relocation details). As seen in Figure 4-33, by increasing the amount of transverse reinforcement within the PHRD A_v/S to 11 mm^2/mm and keeping the same shear span L/d of 4, the damage is relocated. The same effect is observed when the shear span L/d is increased to 7 and the shear reinforcement is kept unchanged (i.e., A_v/S= 3 mm^2/mm).

4.9 Summary and Concluding Remarks

This paper presents the results of the experimental campaign on three modern designed beam-column joints extracted from a 1980s 22-storey reinforced concrete frame building in the Christchurch's Central Business District (CBD), damaged after the 2010-2011 Christchurch earthquakes sequence (CES). Two of the specimens were tested under quasi-static cyclic loading to a level of cracking pattern consistent with what can be considered a moderate level of damage, repaired with an epoxy injection technique, and subsequently retested until reaching failure. The main observations can be summarised as follows:

- All the specimens failed in a flexure-shear mechanism. Severe diagonal cracking was developed within the plastic hinge relocation detail due to excessive principal tensile stresses as a result of the diagonal compression strut induced by the hooked bars details. In the repaired specimens 2.2, and more clearly in 3.2, the epoxy injection allowed for some damage relocation outside the plastic hinge relocation detail.
- A reasonable level of energy dissipation at both low (SLS) and high (ULS) rotation levels was achieved in the repaired specimens. The computed values are comparable to the ones from the unrepaired specimens. A secant stiffness reduction was observed in the repaired specimens at low rotation levels (below to the onset of nonlinearity, approximately). However, this stiffness reduction does not seem to be equally affected at high (ULS) rotation levels.

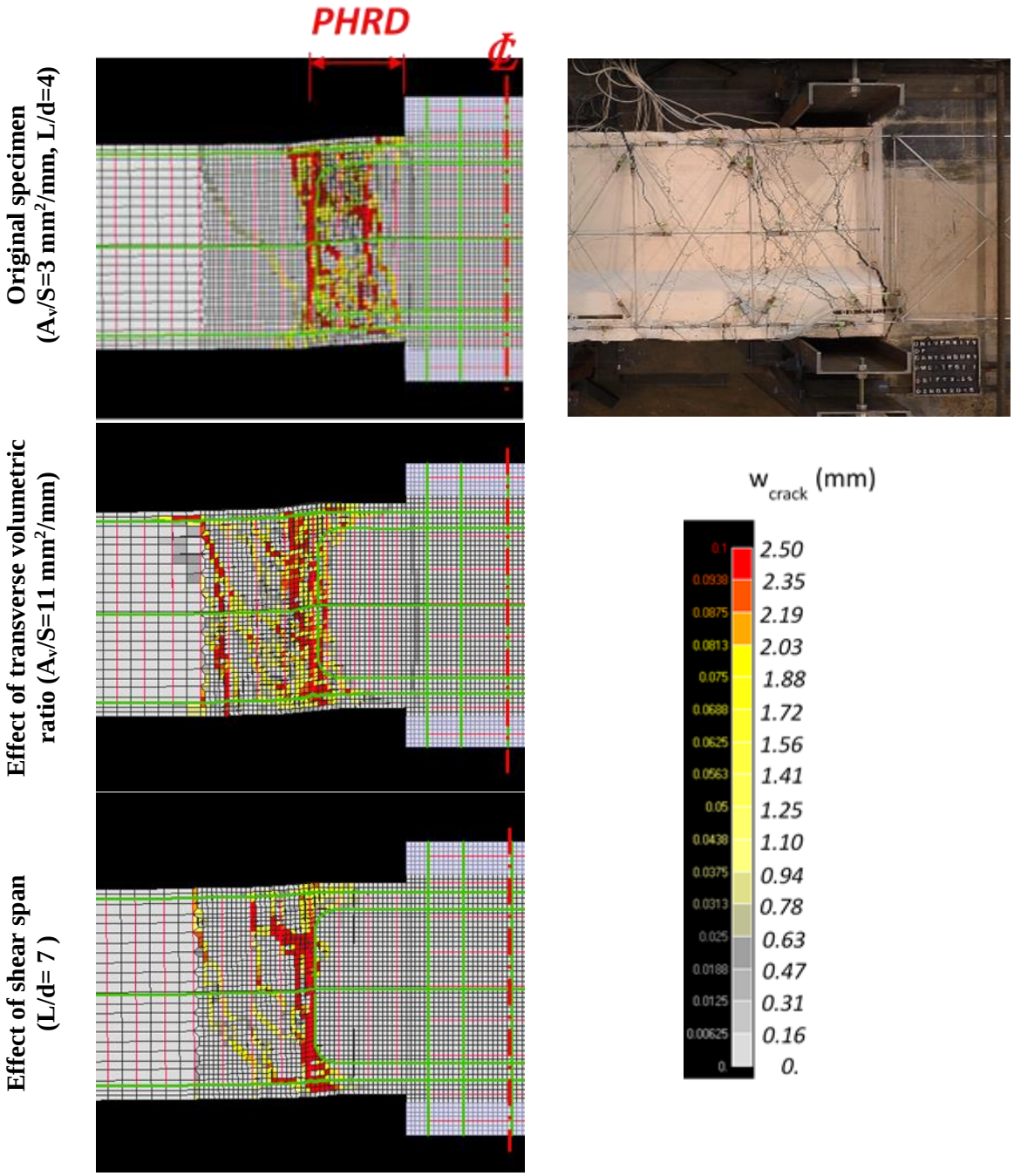

Figure 4-33. Effect of transverse volumetric ratio and shear span on the relocation of the damage outside the plastic hinge relocation detail (PHRD).

- The crack width ratios (for both, shear-flexural or flexural only) are beam rotation (i.e., curvature and strain) dependant. There is a change from negative to positive slopes at rotations near or at the onset of nonlinearity. In fact, negligible-to-minor residual cracks can derive from non-negligible level of maximum crack width.
- The results obtained with nonlinear finite element (FE) simulation agreed reasonably well with the experimental observations. The flexure-shear failure mechanism within

the PHRD could have been avoided by either increasing the shear reinforcement within the PHRD, increasing the shear span of the beam, or a combination of both.

4.10 References

Christopoulos, C., Pampanin, S., Priestley, M.J.N. (2003), Performance-based seismic response of frame structures including residual deformations. Part 1: Single-degree of freedom systems. *Journal of Earthquake Engineering*, **7** (1), 97-118.

Pampanin, S., Christopoulos, C., Priestley, M.J.N. (2003), Performance-based seismic response of frame structures including residual deformations. Part 2: Multi-degree of freedom systems. *Journal of Earthquake Engineering*, **7** (1), 119-147.

Pampanin, S., Kam, W.Y, Akguzel, U., Tasligedik, A.S., Quintana-Gallo, P. (2012), Seismic performance of reinforced concrete buildings in the Christchurch CBD in 22 February 2011 earthquake. Part I and II. *Natural Hazards Research Platform, Recovery Project*. University of Canterbury, Christchurch, New Zealand.

SESOC (2011), Preliminary observations from Christchurch earthquakes, *Structural Engineering Society New Zealand*, Auckland, New Zealand.

5 EFFECT OF STRAIN RATE AND MATERIAL CHARACTERISTICS

After the 2010-2011 Canterbury earthquake sequence, in a number of cases few major crack openings were observed instead of a well distributed cracking pattern expected in those plastic hinge locations, were plastic deformation was expected to occur, causing a large amount of deformation concentrated at a single location and leading to a sudden fracture of the reinforcing steel, potentially due to low-cycle fatigue (SESOC, 2011). In order to provide reliable estimates of the residual capacity of a plastic hinge region, it is necessary to address the main issues of how such plastic strains and fatigue life relationships are affected by factors such as rate of loading, bond deterioration, longitudinal reinforcement ratios, as well as material characteristics (e.g., strain hardening of steel, concrete tensile strengths).

This Chapter presents the results of an experimental and numerical investigation on a modern (i.e., relatively well-designed according to post-1970s seismic codes) reinforced concrete beam-to-column joint, targeting at identifying and understanding qualitatively and quantitatively the effect of those factors on the cracking pattern and nonlinear behaviour of reinforced concrete plastic hinges. Figure 5-1 shows the key steps followed during this investigation.

A well-designed according to NZS3101:2006 reinforced concrete beam-column joint is modelled by using the nonlinear finite element (*FE*) code MASA. Experimental results of a beam-column joint with the same characteristics are used in order to validate the FE model and confirm its suitability to adequately represent the nonlinear behaviour of the beam-column joint. Subsequently, parametric analyses are performed in order to investigate the influence of various parameters on the cracking pattern in the plastic hinge region, at various limit states.

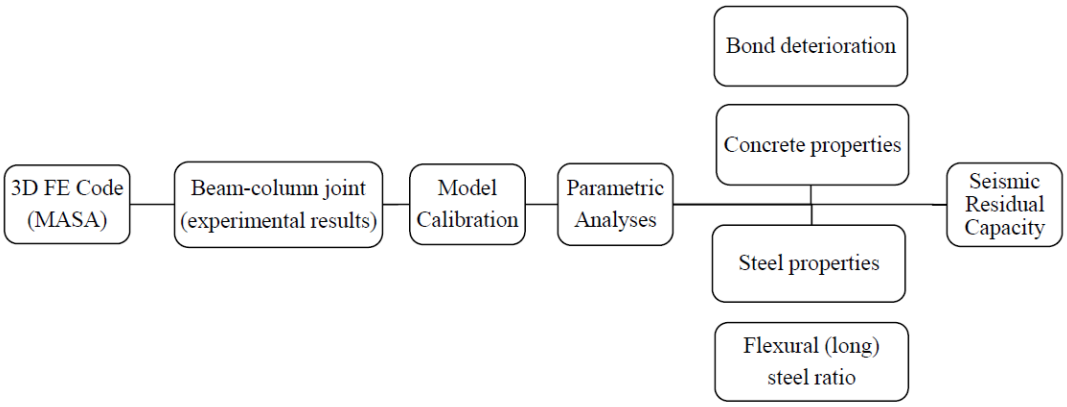

Figure 5-1. Overview of the research methodology followed in this investigation.

5.1 Literature review

It has been demonstrated by previous researchers that bond characteristics between the concrete and reinforcing steel are highly dependent on the cracking pattern and the strain rate (i.e., velocity). In fact, after the 2010-2011 Canterbury earthquake sequence, in a number of cases few major crack openings were observed instead of a well distributed cracking pattern as it would be expected in those plastic hinge locations where plastic deformation is expected to occur, causing a large amount of deformation concentrated at a single location and potentially leading to fracture of the reinforcing steel, potentially due to low-cycle fatigue (SESOC, 2011).

Bertero et al (1972) stated that "*the quasi-static stress-strain relationship is altered by increasing the rate of strain, and this may modify the mode of failure with increased probability of brittle failure*". They tested longitudinal reinforcing bars and concrete cylinders under uniaxial tensile and compressive loading, respectively, at different strain-rates. It was determined that strain-rate increases the yield strength and compressive strength. The increase in the steel yield strength was 16% and 28% for average strain-rates of 5,000 and 50,000 μmm/mm/sec. The increase in the concrete compressive strength was 12.5% and 20% for the same average strain-rates of 5,000 and 50,000 μmm/mm/sec.

They also tested six beams under a four-point loading condition, inducing a zone of constant bending moment in the central third of the beams. Two beams (prototype 1 and 2) were first loaded monotonically until reaching a peak displacement of ten times the yield displacement, one beam was loaded at high strain-rate (velocity of 254 mm/sec, or strain-rate of approximately 40,000 μmm/mm/sec), and one beam under quasi-static loading (velocity of 2.54 mm/sec), after which both were cyclically loaded until failure (see Figure 5-2).

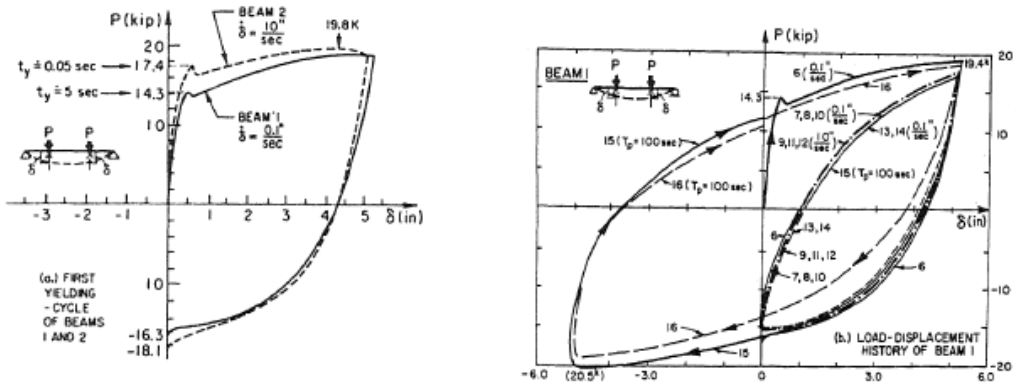

Figure 5-2. Monotonic load-displacement curves of prototype beams 1 and 2 (left), and cyclic load-displacement curve of prototype beam 1 (right) (Bertero et al, 1972).

The "*dynamic*" secant stiffness at first yielding resulted 10% higher than the quasi-static stiffness. They stated that "*since a 10% increase in the stiffness of a structure will lead to a decrease of less than 5% in its period, it can be concluded that the strain-rate will not significantly affect the initial linear seismic response of buildings*".

The cracking and yielding strength at high strain-rates were 25% and 22% higher than the quasi-static strengths, respectively. The ductility and therefore the maximum and ultimate strengths were not significantly affected by the strain-rate. A similar conclusion was obtained regarding the energy absorption and dissipation characteristics.

Regarding the failure mode, they concluded that "*it would appear that for ductile reinforced concrete members subjected primarily to flexure, seismic strain-rates will not affect the failure mode*". They also state that "*it might not be so for flexural members under high shear and/or axial forces. This* [i.e., strain-rate] *could trigger a brittle shear failure during an earthquake*". There was no indication of fractured bars at any stage of the tests.

Shah et al (1987) performed free vibration tests on small-scale models of reinforced concrete beam-column joints, subjected to large cyclic displacements at rates of 2.5 x 10^{-3} Hz and 1.0 Hz. They observed more damage as the rate of loading increased. The damage was measured in terms of energy absorbed, equivalent damping, as well as the stiffness and damping obtained from free vibration tests. They concluded that the extent of damage appears to be the result of differential bond behaviour at different rates of loading. Figure 5-3 shows the failure modes and cracking pattern for the two different strain rates. It is clear how the flexural cracks are widely distributed for the specimen tested at the slow rate, whilst for the fast rate the damage is concentrated in a single crack at the column face.

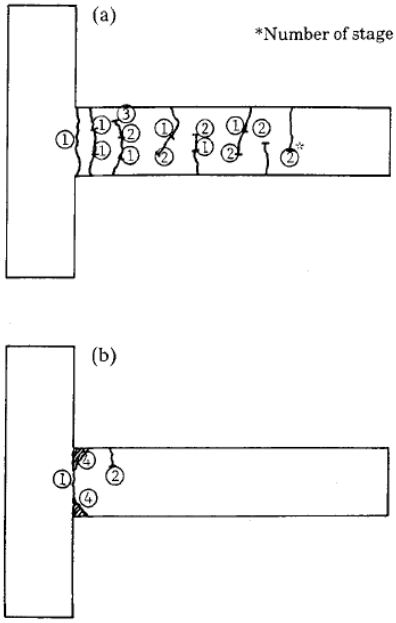

Figure 5-3. Failure modes at a) 2.5 x 10^{-3} Hz and b) 1.0 Hz rates (Shah et al, 1987).

5.2 Experimental Investigation

Prior to perform parametric analyses the *FE* model has been validated with the experimental results of a beam-column joint designed according to the concrete code in NZ (NZS3101:2006, including amendments 1 and 2, recently amended after the 2010-2011 Canterbury earthquake sequence) to achieve a weak-beam and strong-column hierarchy, previously tested at the University of Canterbury (Kam, 2010).

5.2.1 Specimen Description

The test specimen is a two-thirds scale, two-dimensional exterior reinforced concrete beam-column joint (see Figure 5-4). The materials characteristics are summarised in Table 5-1. The beam is 255 mm wide by 325 mm high with 4-D12 deformed longitudinal bars (top and bottom) and plain D6 bars as transverse reinforcement. The column is 255 mm square with 12-D12 deformed longitudinal bars and plain D6 bars as transverse reinforcement. Following capacity design principles, the column was designed to remain elastic throughout the experimental test by allowing the yield moment capacity of the column to be well above the yield moment capacity of the beam. The plastic hinge region as well as the joint is detailed with two stirrups (one internal and one external) in order to prevent a brittle shear failure.

5.2.2 Experimental Program and Testing Procedure

As shown in Figure 5-4, the column was pinned at the base to represent the point of contra-flexure at mid-height of the column, whereas the beam was vertically supported by a load cell

restraining the vertical direction and allowing lateral movement (i.e., simulating a roller support at mid-span of the beam length).

Table 5-1. Material characteristics.

	f_y (MPa)	f_u (MPa)	E_S (MPa)
Steel	320	440	200000

	f'_c (MPa)	f_t (MPa)	E_C (MPa)
Concrete	33	4.0	27000

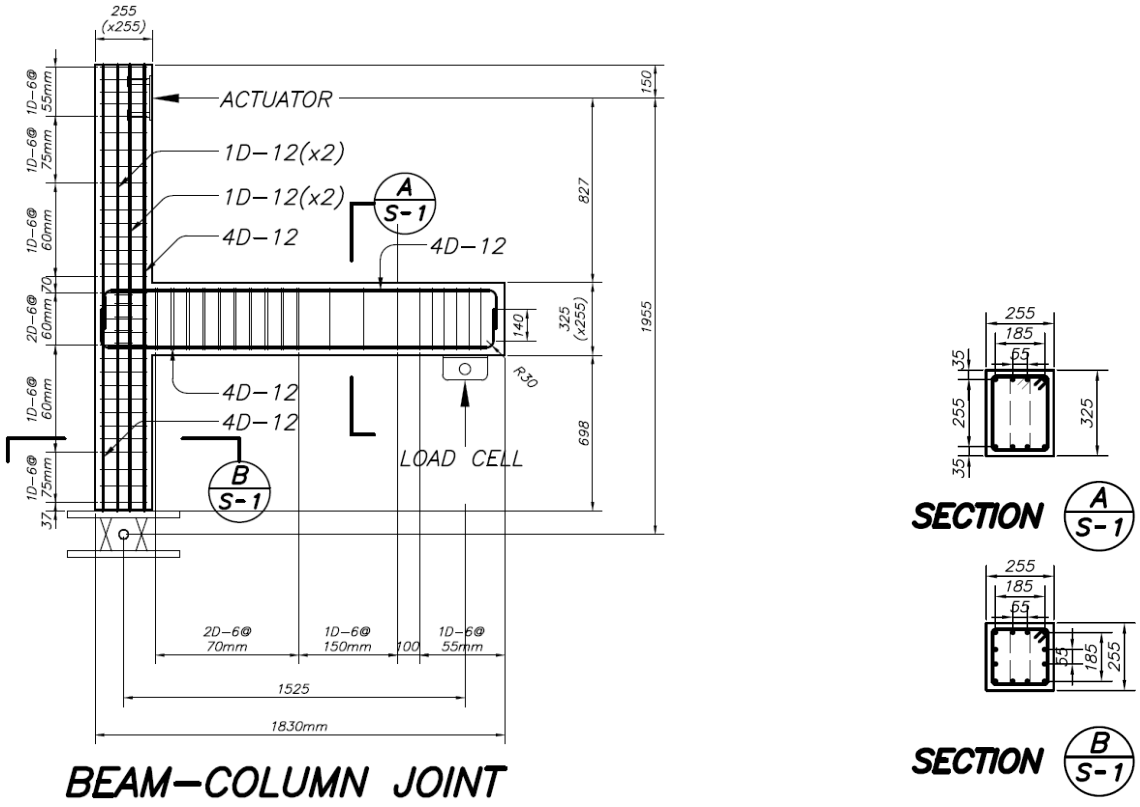

Figure 5-4. Experimental setup of the two-thirds scale specimen and material characteristics.

A constant axial force of 65 kN, representing the gravity loads, was applied at the top of the column, and a quasi-static displacement-controlled cycling loading protocol was applied at the top of the column (increasing top drifts of ±0.1%, ±0.2%, ±0.35%, ±0.5%, ±0.75%, ±1.0%, 1.5%, ±2.0%, ±2.5%, ±3.5%, and ±4.5%, see Figure 5-5) as per the acceptance criteria of the American Concrete Institute for moment frames (ACI, 2001).

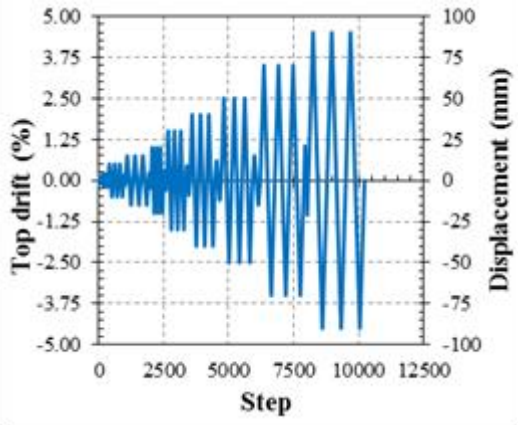

Figure 5-5. Schematic representation of the applied loading protocol.

5.3 Numerical Investigation

5.3.1 Finite Element Numerical Model

The nonlinear finite element (*FE*) code MASA was used to model the specimen (see Section 6.2.1 for a detailed description of the finite element code). Hexahedral elements with side lengths of approximately 15 mm in the joint area and the plastic hinge regions, as well as 50 mm elsewhere were used to create the mesh of the elements. Linear elastic elements were used at the vicinities of the supports and the point of load application so that local failure of concrete elements due to excessive stresses is avoided. Mirror symmetry (i.e., symmetry about a vertical plane across a mid-section in the beam-column joint) was used to drastically reduce the total amount of nodes and elements and thus the required computational time. The material properties used in the simulations are listed in Table 5-2. *BCJ-1* refers to the original (i.e., experimentally tested) beam-column joint; whereas *BCJ-2* to *BCJ-12* are used for parametric analyses under monotonic loading.

5.3.2 Numerical versus experimental comparison

Figure 5-6a shows the cyclic lateral force-displacement response from the quasi-static test. The hysteresis loops show a fat and reasonably stable shape with some minor pinching, which might be attributed to the opening and closing of cracks as well as some level of bond degradation. The monotonic curve obtained from numerical analysis is also shown in the same figure; the agreement between this curve and the envelope of the cyclic response is evident. Figure 5-6b shows the same monotonic curve with indications for different limit states. In particular, for normal structures, *Level 1* (Serviceability Limit State, *SLS*) refers to a 50% probability of exceedance in 50 years intensity level; *Level 2* (Damage Control Limit State, *DLS*) to a 10% probability of exceedance in 50 years intensity level; and *Level 3*

(Ultimate Limit State, *ULS*) to a 2% probability of exceedance in 50 years. The strain limits proposed in Priestley et al. (2007), described in Section 6.2.2, were adopted in this study in order to define the aforementioned limits states, with the difference that the confined concrete and steel strain limits were limited to 0.015 and 0.06, per NZSEE (2017).

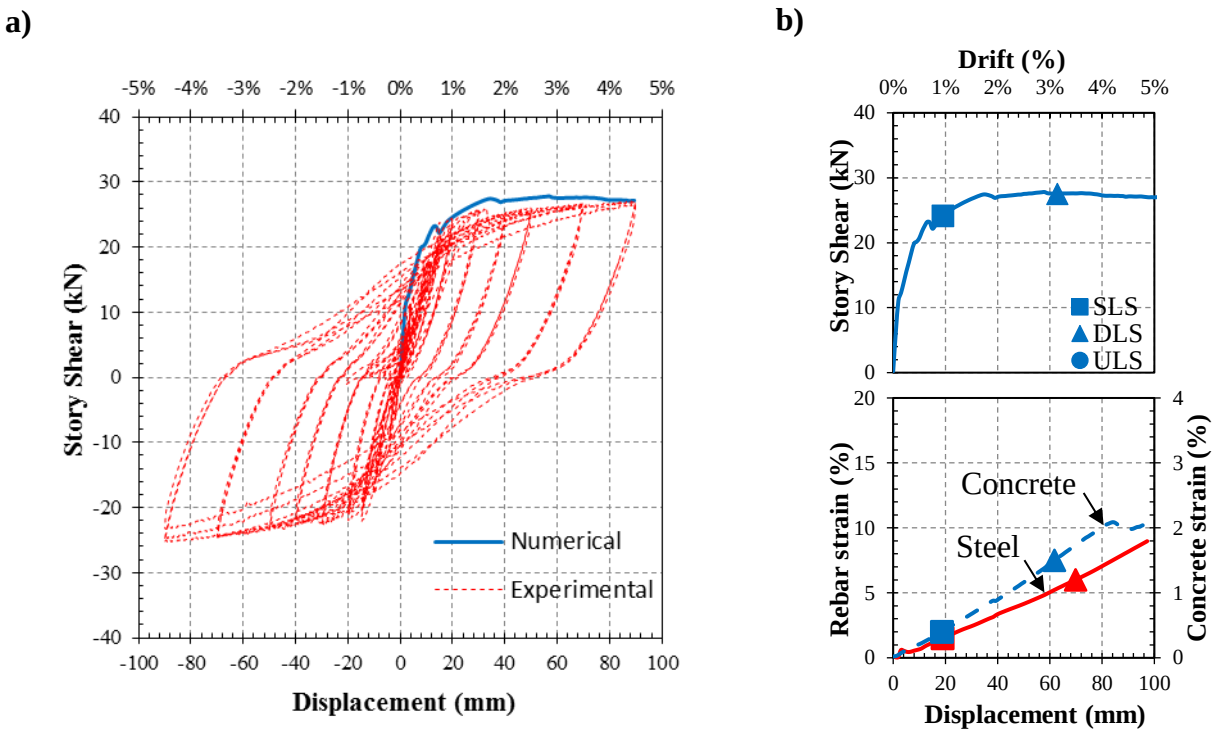

Figure 5-6. (a) Cyclic and monotonic lateral force displacement response from the experimental (dotted line) and numerical (solid line) results (*BCJ-1*), respectively; (b) Monotonic curve from the numerical simulation (*BCJ-1*, top); and steel and concrete strains (bottom) from the numerical simulation (the dashed-line represents concrete strain, whereas the solid line represents the rebar strain). The solid square represents the Serviceability Limit State (*SLS*); the solid triangle the Damage-control Limit State (*DLS*); and the solid circle the Ultimate Limit State (*ULS*, not observed here since it occurs at higher drift levels).

Figure 5-6b also shows the strains measured at the bottom steel rebars and top concrete fibre of the plastic hinge obtained from the *FE* model. It is evident how they follow a linear trend increasing in proportion to the applied lateral displacement. It is interesting to note that both the *SLS* and *DLS* strain limits occur almost simultaneously at the steel and concrete fibres, at 0.95% and ~4.7% drift angles, respectively.

Figure 5-7 shows photographs of the cracking pattern in the specimen during the experimental campaign at drifts angles of 1.0%, 1.5%, 2.0%, 2.5%, 3.5%, and 4.5%. Several minor cracks and one-to-two major cracks form and propagate through the beam height as the drift angle increases. At the end of the experimental test (i.e., at 4.5% drift angle), two major cracks and

concrete crushing at the plastic hinge zone along with minor cracking at the beam-column joint and their surroundings are apparent.

Figure 5-7 also shows the expected cracking pattern obtained with the *FE* model under monotonic loading. As seen in this figure, the two major cracks as well as minor cracks at the joint area observed during the experimental test are well simulated by the numerical model.

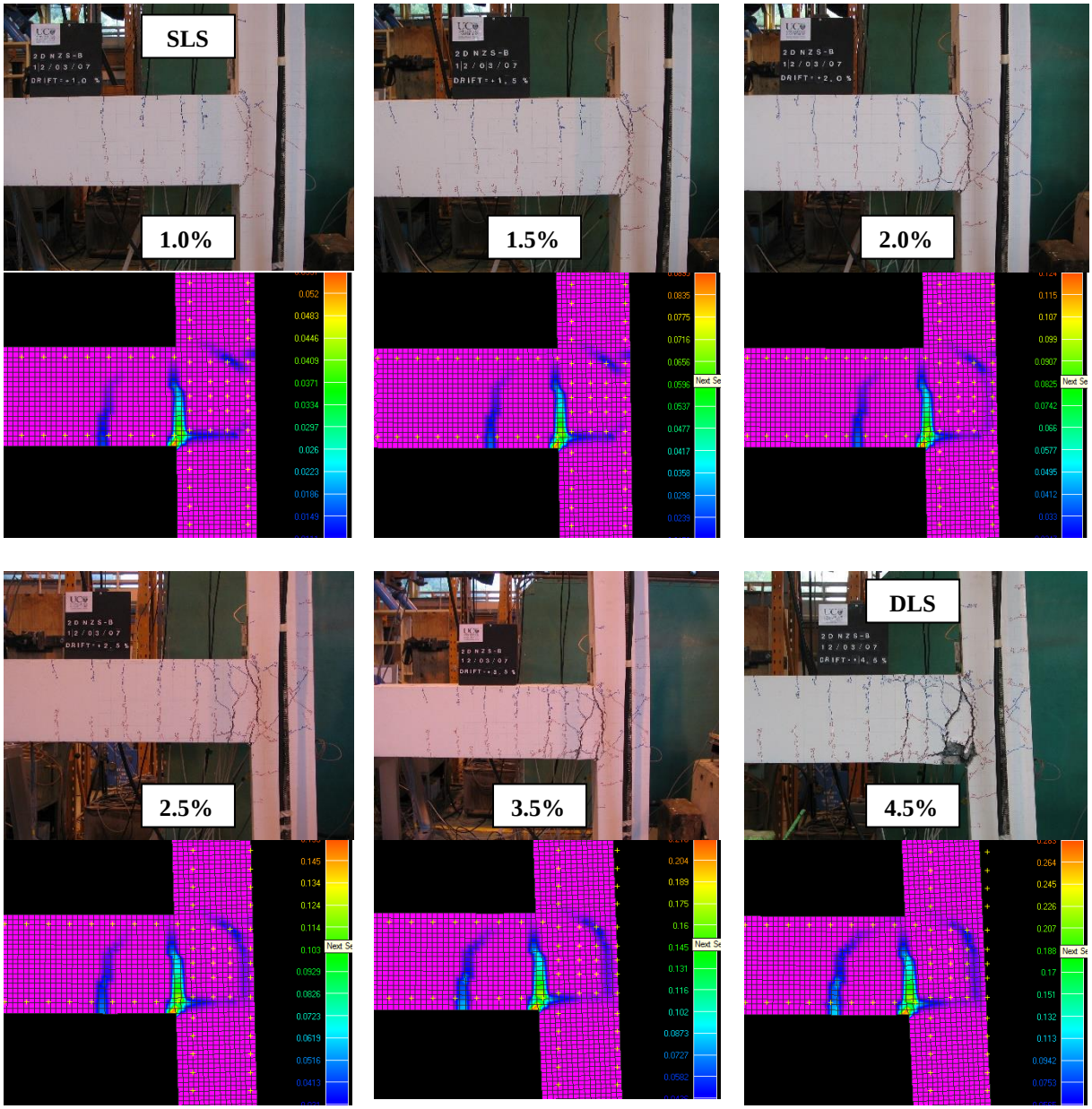

Figure 5-7. Photographs showing the cracking pattern at drift angles of 1.0%, 1.5%, 2.0%, 2.5%, 3.5% and 4.5%. The figure below each photograph represents the corresponding cracking pattern obtained with the *FE* modelling (i.e., monotonic loading *BCJ-1*).

One intriguing aspect of this experimental and numerical campaign is the formation of few major cracks in the plastic hinge region of a well-designed and detailed beam-column joint.

This peculiarity agrees very well with observations following the 2010-2011 Canterbury earthquake sequence, where in a number of cases few major crack openings were observed instead of a well distributed cracking pattern expected in those plastic hinge locations where plastic deformation was expected to occur. The small number of cracks induces a large amount of deformation concentrated at a single location, which might lead to fracture of the reinforcing steel, potentially due to low-cycle fatigue. This effect may be attributed to a combination of low reinforcement ratios, low-rate of strain-hardening of the steel, high concrete tensile strengths, and high speed of loading (SESOC, 2011; Kam et al., 2011).
In this beam-column joint, the longitudinal reinforcement ratio ρ_s is 0.61%, very close to the lower bound limit ρ_{min} of 0.45% as per NZS3101:2006. In addition, the tensile concrete strength f_t is 4 MPa, close enough to an expected upper bound limit of 5 MPa.

5.4 Parametric Analysis Under Monotonic Loading

The objective of the parametric analyses was to identify the most critical parameters and combinations of them that may affect the cracking pattern and the residual capacity of typical plastic hinges (see Figure 5-1). Table 5-2 lists the different range of values for each parameter assumed during the parametric analyses. As previously mentioned, the model *BCJ-1* was used as the benchmark, and each series of the tabulated values was then modified accordingly. The bond characteristics were computed as suggested by Lettow (2007), with a difference s_2-s_1 (length of the slipping plateau, see Figure 6-3c) fixed at 0.80 mm; and s_3, the slip at which the mechanical bond resistance is lost, assumed to be 8.5 mm and 10 mm for D12 and D16 bars, respectively (Christoph, 2012).

Table 5-2. Material and bond characteristics used for numerical simulation and parametric analyses (the bond parameters are schematically defined in Figure 6-3, refer to Table 6-1 for the definition of each parameter).

	BCJ-1	BCJ-2	BCJ-3	BCJ-4	BCJ-5	BCJ-6	BCJ-7	BCJ-8	BCJ-9	BCJ-10	BCJ-11	BCJ-12
f'_c (MPa)	33	20	20	20	20	40	40	40	40	33	33	33
f_t (MPa)	4.00	3.58	3.58	3.58	3.58	5.06	5.06	5.06	5.06	2.00	3.50	5.00
E_c (MPa)	26983	21750	21750	21750	21750	27900	27900	27900	27900	26983	26983	26983
f_y (MPa)	320	300	300	500	500	300	300	500	500	320	320	320
f_u (MPa)	440	412.5	412.5	687.5	687.5	412.5	412.5	687.5	687.5	440	440	440
ρ_s (%)	0.61	0.61	1.09	0.61	1.09	0.61	1.09	0.61	1.09	0.61	0.61	0.61
$\tau = \tau_m + \tau_f$ (MPa)	13.7	10.7	11.9	10.7	11.9	15.1	16.8	15.1	16.8	13.7	13.7	13.7
τ_m (MPa)	8.21	6.39	7.11	6.39	7.11	9.04	10.06	9.04	10.06	8.21	8.21	8.21
k_1 (MPa/mm)	35.2	28.6	34.1	28.6	34.1	38.7	45.1	38.7	45.1	35.2	35.2	35.2
k_2 (MPa/mm)	1.28	1.04	0.85	1.04	0.85	1.41	1.13	1.41	1.13	1.28	1.28	1.28
k_{sec} (MPa/mm)	16.0	13.0	14.2	13.0	14.2	17.6	18.8	17.6	18.8	16.0	16.0	16.0
s_1 (mm)	0.86	0.82	0.84	0.82	0.84	0.86	0.89	0.86	0.89	0.86	0.86	0.86

5.4.1 Influence of concrete and steel strength, and longitudinal reinforcement ratio

Figure 5-8 shows the results of numerical simulations with unconfined compressive concrete strength f'_c of 20 MPa, with longitudinal reinforcement ratio ρ_s of 0.61% (*BCJ-2* and *BCJ-4*) and 1.09% (*BCJ-3* and *BCJ-5*, respectively). *BCJ-2* and *BCJ-3* have a yield strength f_y of 300 MPa, whereas *BCJ-4* and *BCJ-5* of 500 MPa. The nonlinear behaviour of *BCJ-2* is similar to *BCJ-1*, although its reduction in shear capacity is coupled with a reduction in the expected level of damage (see Figure 5-8a, e). Furthermore, although the plastic hinges of *BCJ-3* and *BCJ-4* have comparable yield moment capacities (in terms of area of steel times nominal yield strength), there are significant differences in the nonlinear behaviour; while *BCJ-3* has a peak shear capacity at *SLS* and then drops abruptly (see Figure 5-8f); the nonlinear behaviour of *BCJ-4* is more uniform with a strength drop at higher drift angles ~3% (see Figure 5-8g). Nevertheless, the expected cracking pattern is comparable in both cases with joints severely damaged at drift angles close to the *ULS*. *BCJ-5* behaves in a similar fashion as *BCJ-3*, although more damage at the joint is expected due to a higher shear demand at higher drifts (see Figure 5-8h).

Figure 5-9 shows the results of numerical simulations with unconfined compressive concrete strength f'_c of 40 MPa, with longitudinal reinforcement ratio ρ_s of 0.61% (*BCJ-6* and *BCJ-8*) and 1.09% (*BCJ-7* and *BCJ-9*, respectively). *BCJ-6* and *BCJ-7* have a yield strength f_y of 300 MPa, whereas *BCJ-8* and *BCJ-9* of 500 MPa. The nonlinear behaviour of *BCJ-6* is similar to *BCJ-1*, although a single major crack opening instead of two major cracks is expected to occur (see Figure 5-9a, e).

Furthermore, although the plastic hinges of *BCJ-7* and *BCJ-8* have comparable yield moment capacities (in terms of area of steel times nominal yield strength), their nonlinear behaviour and cracking pattern show significant differences; less and major cracks are expected to occur for smaller f_y and larger ρ_s (i.e., *BCJ-7*). *BCJ-9* behaves in a similar fashion as *BCJ-3* and *BCJ-5*, although more shear capacity strength drop is expected to occur (see Figure 5-9h).

By comparing Figure 5-8 and Figure 5-9, it is evident how f'_c affects the cracking level at the joint. Furthermore, it is interesting to note how the residual shear strength of the beam-column joints is influenced also by f'_c irrespective of f_y and ρ_s, being on average 23 kN and 30 kN for f'_c of 20 MPa and 30 MPa, respectively. Therefore, the increased level of damage observed in Figure 5-8 with respect to Figure 5-9 can be attributed to a reduced shear capacity due to a low concrete compressive strength.

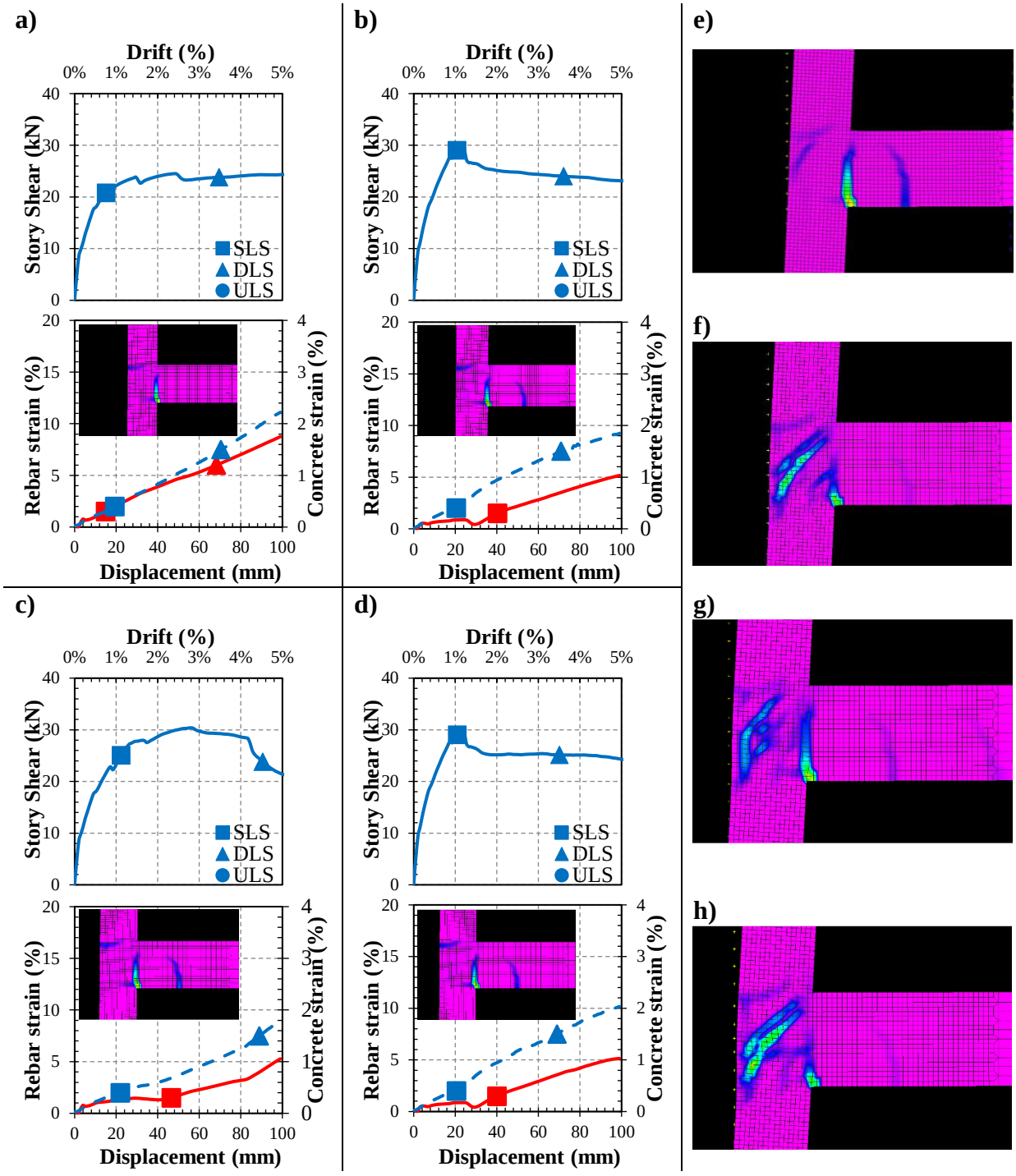

Figure 5-8. Monotonic story shear vs displacement response from the numerical simulations; and steel and concrete strains for simulations: a) *BCJ-2*; b) *BCJ-3*; c) *BCJ-4*; and d) *BCJ-5* (the dashed-line represents concrete strains, whereas the solid line represent the rebar strain; the small snapshot represent the cracking pattern at *SLS*). Snapshots for e) *BCJ-2* at *DLS*; f) *BCJ-3* at drift equivalent to *DLS* of *BCJ-2*; g) *BCJ-4* at drift equivalent to *DLS* of *BCJ-4*; and h) *BCJ-5* at *DLS*. The solid square represents the Serviceability Limit State (*SLS*); the solid triangle the Damage-Control Limit State (*DLS*); and the solid circle the Ultimate Limit State (*ULS*, not observed here).

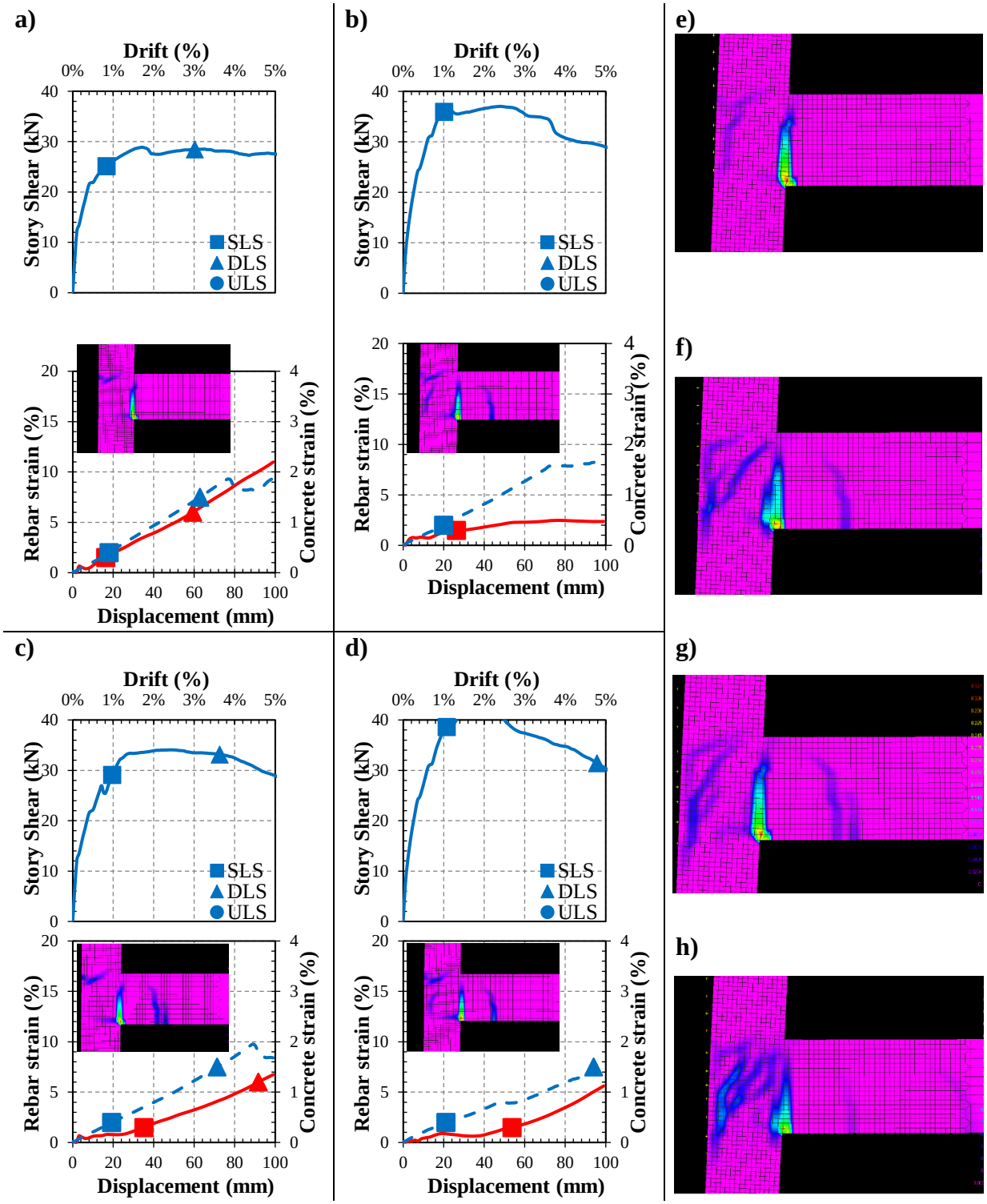

Figure 5-9. Monotonic story shear vs displacement response from the numerical simulations; and steel and concrete strains for simulations: a) *BCJ-6*; b) *BCJ-7*; c) *BCJ-8*; and d) *BCJ-9* (the dashed-line represents concrete strains, whereas the solid line represent the rebar strain; the small snapshot represent the cracking pattern at *SLS*). Snapshots for e) *BCJ-6* at *DLS*; f) *BCJ-7* at drift equivalent to *DLS* of *BCJ-6*; g) *BCJ-8* at 4.5% drift; and h) *BCJ-9* at 4.5% drift. The solid square represents the Serviceability Limit State (*SLS*); the solid triangle the Damage-control Limit State (*DLS*); and the solid circle the Ultimate Limit State (*ULS*, not observed here).

In addition, the previous figures show drifts at *SLS* fairly constant irrespective of f'_c, f_y and ρ_s (1.0% on average, except for *BCJ-2* and *BCJ-6* where values around 0.8% were obtained). The above might be explained with the fact that the yield curvature is relatively insensitive to the axial load and reinforcement ratio, depending mainly on structural geometry and material sizes (Priestley et al., 2007).

Table 5-3 shows the material characteristics as well as the reinforcement ratios and minimum reinforcement content (ρ_{min}, as per NZS 3101:2006, clause 9.3.8.2.1, refer to Equation 6-6) for each of the simulations. It is interesting to note that although multiple cracks are expected to occur since the longitudinal reinforcement content is above the minimum required, large plastic deformations at few locations (one-to-two major cracks) were observed in the simulations.

Table 5-3. Material characteristics and reinforcement ratios for simulations *BCJ-2, BCJ-3, BCJ-6* and *BCJ-7* (ρ_{min} as per NZS 3101:2006, and the tensile strength of concrete estimated as $f_t = 0.8\sqrt{f'_c}$).

Simulation	f_y (MPa)	f'_c (MPa)	$\sqrt{f'_c}$ (MPa)	f_t (MPa)	ρ_s (%)	ρ_{min} (%)
BCJ-2	300	20	4.5	3.6	0.61	0.37
BCJ-3	300	20	4.5	3.6	1.09	0.37
BCJ-6	300	40	6.3	5.0	0.61	0.53
BCJ-7	300	40	6.3	5.0	1.09	0.53

5.4.2 Influence of f_t on the cracking pattern and limit states

In the previous figures it was observed that variations on f'_c affect the expected cracking pattern in the beam-column joints. Since the unconfined compressive concrete strength has a strong impact on the tensile concrete strength, additional simulations with f_t of 2 MPa (*BCJ-10*), 3.5 MPa (*BCJ-11*) and 5 MPa (*BCJ-12*), representing realistic values for f'_c of 30 to 35 MPa (assuming an upper characteristic modulus of rupture of $\sqrt{f'_c}$; Henry, 2013), were performed, keeping the other parameters unchanged.

In Figure 5-10, although the overall behaviour of the three simulations is comparable in terms of strength, stiffness and strain limits, the cracking pattern is strongly affected by the tensile strength of concrete f_t, being more uniform (i.e., larger amount and less intense cracks) for lower values, and more concentrated in one single crack for higher values. This behaviour is consistent with the observations occurred in the aftermath of the Canterbury earthquakes sequence, and confirms the primary role that the tensile strength of concrete, for other constant parameters, can have in the cracking pattern and thus residual capacity of structural components and connections.

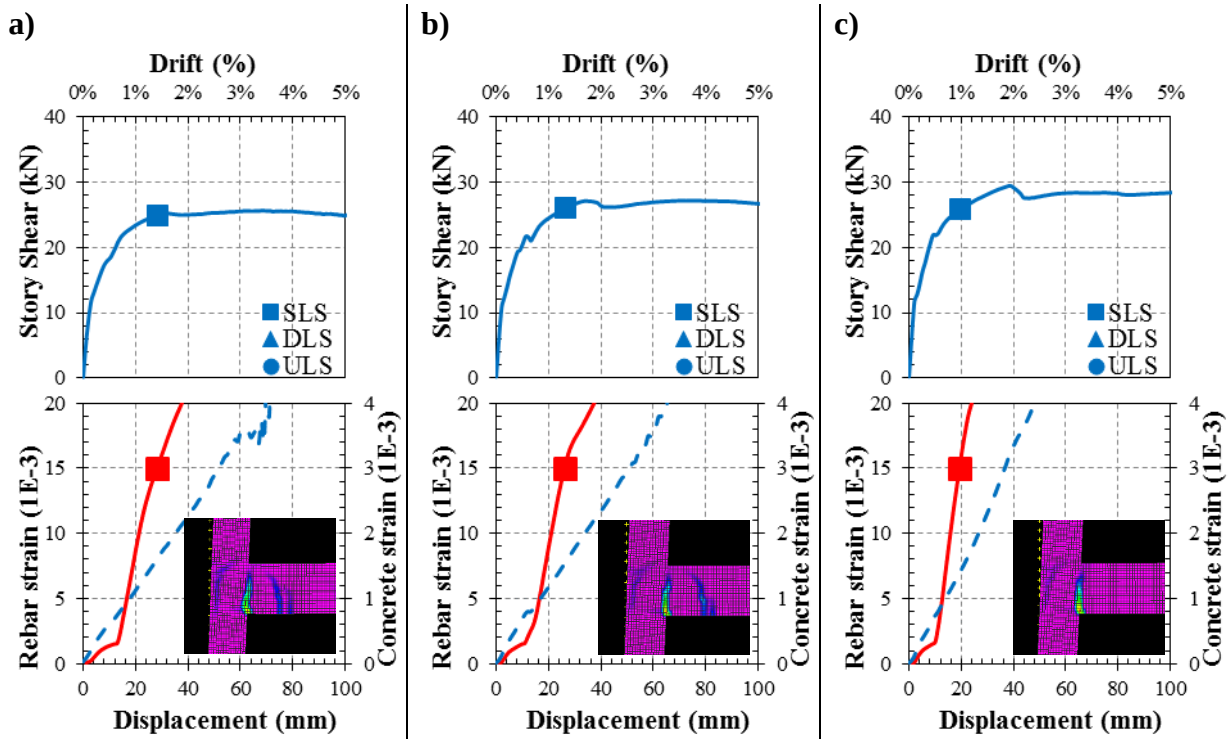

Figure 5-10. Monotonic story shear vs displacement response from the numerical simulations; and steel and concrete strains for simulations: a) f_t 2 MPa; b) f_t 3.5 MPa; c) f_t 5 MPa (the dashed-line represents concrete strains, whereas the solid line represent the rebar strain; the small snapshot represent the cracking pattern at *DLS*). The solid square represents the Serviceability Limit State (*SLS*). For all simulations, f'_c of 33 MPa, f_y of 320 MPa and ρ_s of 0.61% were used.

5.4.3 Rate of loading and cyclic response of the specimen

The same model was further modified in order to make it more compatible with what was observed during the test, specifically the technique in which the hook within the joint is modelled has been improved. After this modification, *FE* simulations with different rates of loading were performed (see Ozbolt and Sharma, 2011; and Ozbolt et al, 2011, for theory and applications of MASA under dynamic loads), and as can be seen in Figure 5-11, no evident difference on the cracking pattern, strength and stiffness is observed, apart from a localised strain concentration migrating towards the plastic hinge at higher rates of loading. These results, although preliminary, are in agreement with Chung and Shah (1989). They observed that beam-column joints tested at high rate of loading with a relatively large amount of shear reinforcement (typical for well-detailed beam-column joints) maintained load carrying capacities similar to those tested at low rate of loading.

Different rates of loading were also applied for different tensile concrete strengths. As can be seen from Figure 5-12, strain rate effects appear to be not as critical for high strain concentrations due to single crack openings as it is the tensile concrete strength.

Similarly, different rates of loading were applied for different reinforcement ratios (ρ_s varying from 0.43% to 1.09%). From Figure 5-13 it is evident that strain rate effects do not (preliminary) influence on the cracking pattern for different reinforcement content. However, small variations in the cracking pattern were observed for low reinforcement content as it approaches to the minimum required as per NZS 3101:2006 (ρ_{min} = 0.45%).

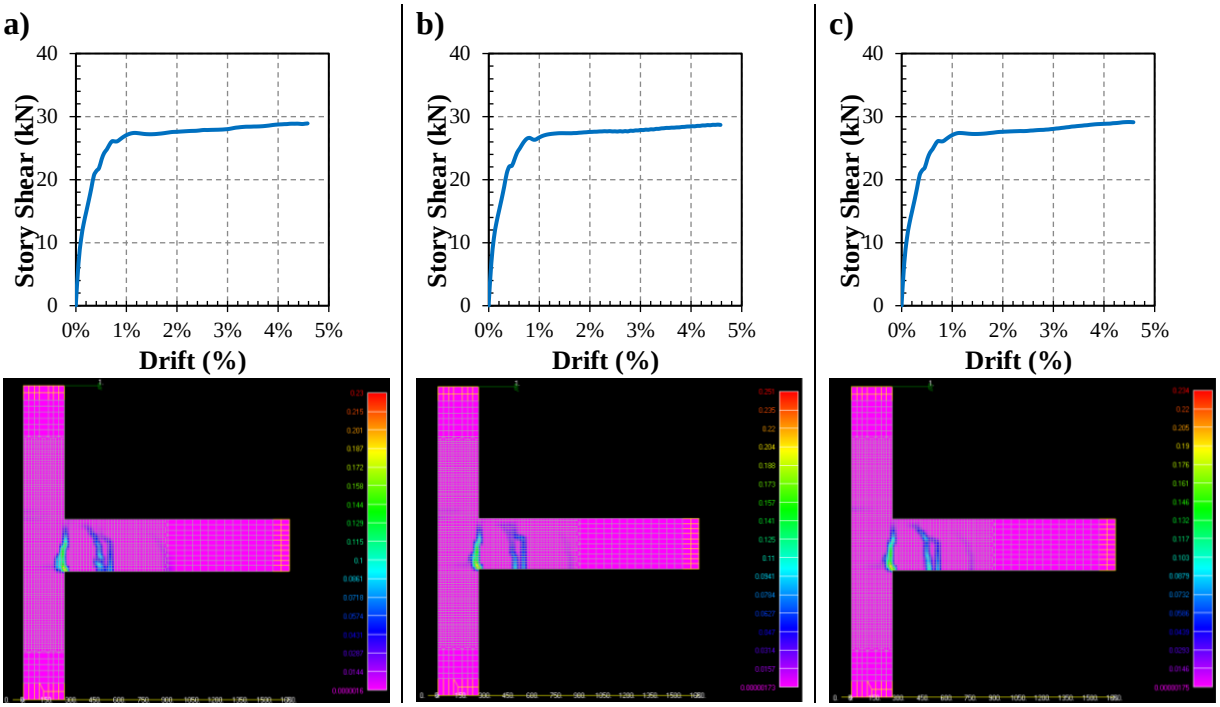

Figure 5-11. Monotonic story shear vs displacement response and snapshots from the numerical simulations: a) pseudo-static case; b) rate of loading of 10cm/s; and c) rate of loading of 100cm/s. For all simulations, f'_c of 33 MPa, f_y of 320 MPa and ρ_s of 0.61% were used.

Figure 5-14 shows the variation of steel strain and neutral axis depth with the applied displacement for the same *FE* simulations as shown in Figure 5-13. It is evident how the strain rate effect is more critical for low reinforcement ratios. More so, the figure shows similar results for rates of loading of 10 cm/s and 100 cm/s, differentiating between those from static (mono) and dynamic load.

In addition, a cyclic analysis was also performed by applying six (pseudo-static) cycles of 1.5% drift, for different reinforcement content. Figure 5-14 shows the results. It is evident how the maximum strain decreases cycle after cycle (due to damage in the concrete and bond deterioration). More so, it is interesting to note how the secant stiffness and hysteretic damping decrease considerably in the first cycle(s) but then becomes almost unchanged for further cycles. This is an important feature to bear in mind when accounting for residual capacity during the design and assessment processes.

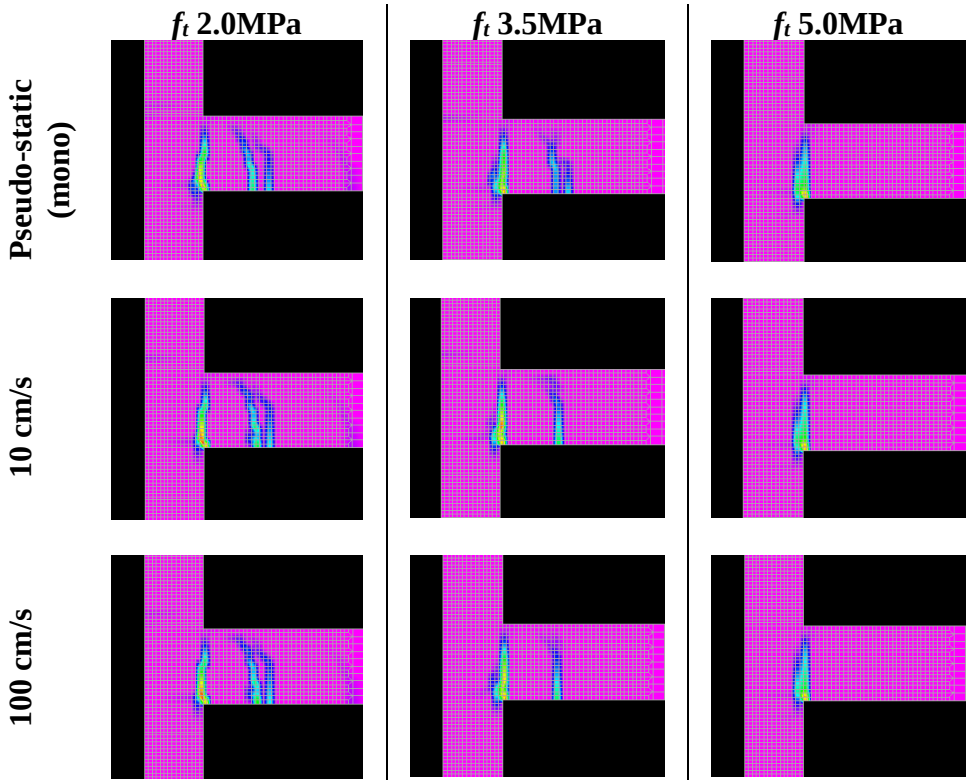

Figure 5-12. Screenshots from *FE* simulations varying the concrete tensile strength and rate of loading. For all simulations, f'_c of 33 MPa, f_y of 320 MPa and ρ_s of 0.61% were used.

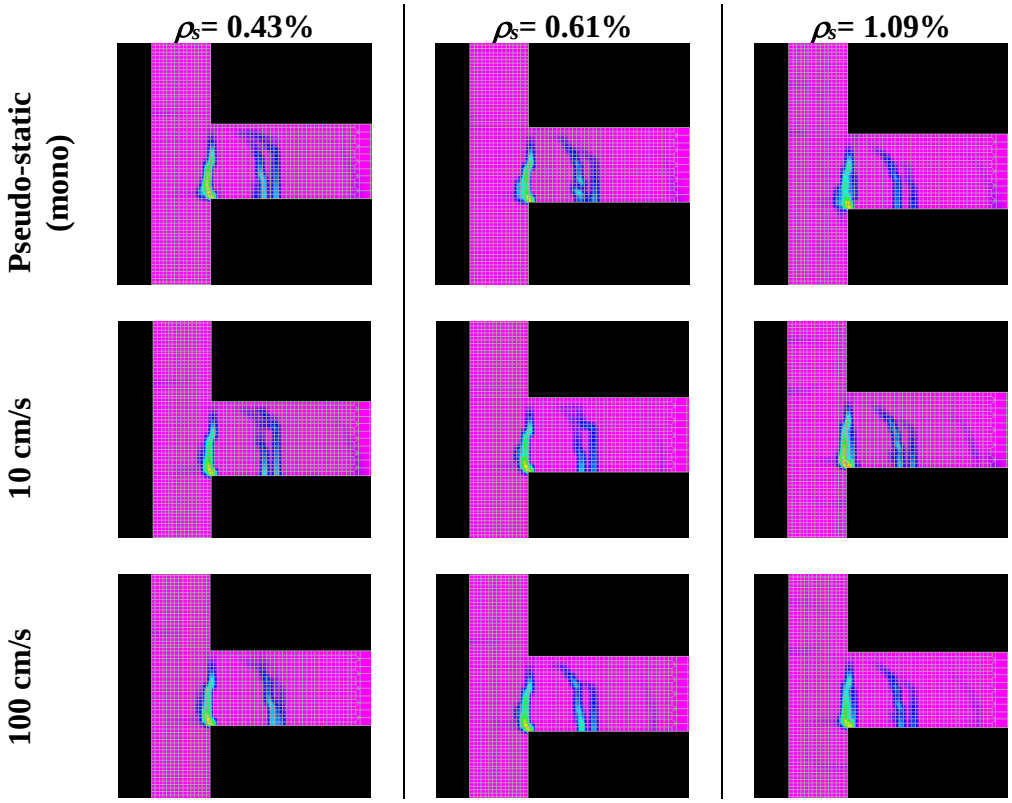

Figure 5-13. Screenshots from *FE* simulations varying the longitudinal reinforcement content and rate of loading. For all simulations, f'_c of 33 MPa and f_y of 320 MPa were used.

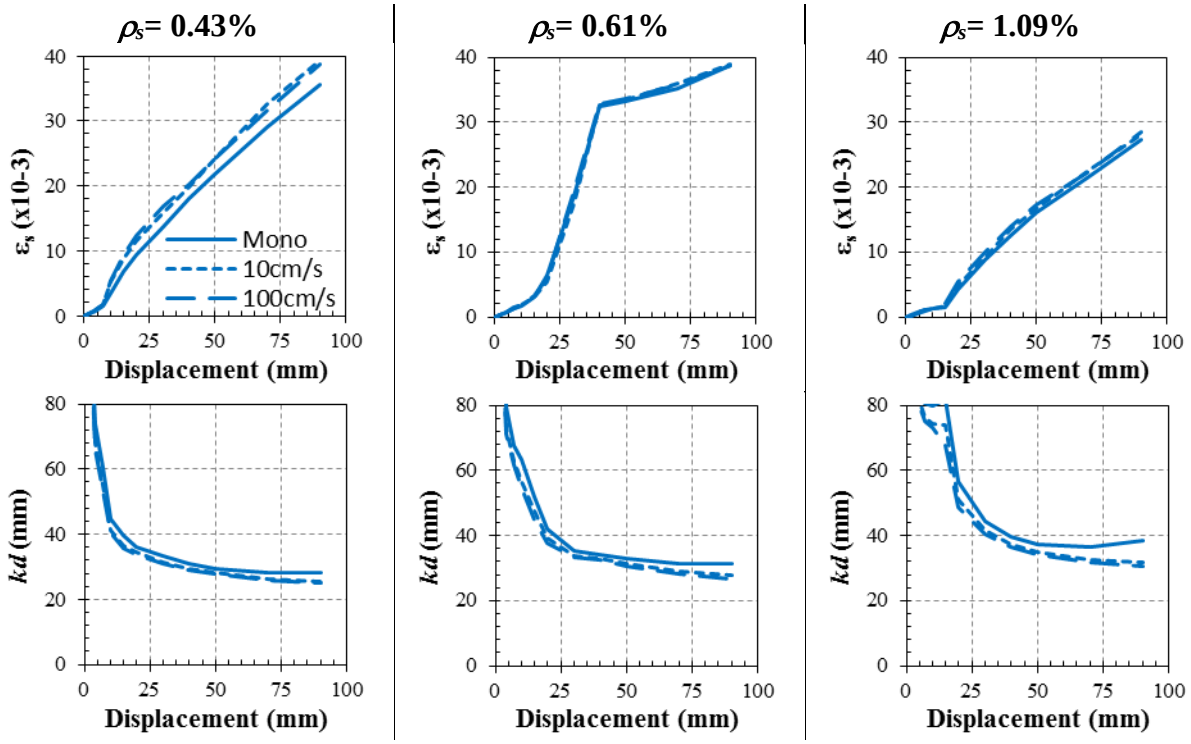

Figure 5-14. Steel strains and neutral axis depth from *FE* analyses varying the longitudinal reinforcement content and rate of loading. For all simulations, f'_c of 33 MPa and f_y of 320 MPa were used.

5.5 Conclusions

This Chapter presents the results of experimental and numerical investigations on well-designed reinforced concrete beam-to-column joints, targeting at identifying and understanding qualitatively and quantitatively the effect of parameters such as bond deterioration, steel and concrete material properties, as well as the amount of longitudinal reinforcement, on the cracking pattern and nonlinear behaviour of reinforced concrete plastic hinges. The main conclusions of the parametric investigation are as follows:

1. Two major cracks in the plastic hinge region were observed during the experimental test and numerical simulations, which agrees well with observations following the 2010-2011 Canterbury earthquake sequence, where in a number of cases few major crack openings were observed instead of a well distributed cracking pattern expected in those plastic hinge locations, condition attributed to either a low-rate of strain-hardening of the steel, low reinforcement ratio, high speed of loading, and high concrete tensile strengths as in the present case. The negative aspect of the small number of cracks in a plastic hinge is mainly the large amount of deformation induced at a single location, leading to fracture of the reinforcing steel potentially due to low-cycle fatigue.

2. Parametric analyses under monotonic loading have shown that lower amount of cracks but with wider openings are expected to occur for larger f'_c and smaller ρ_s values. Moreover, it was observed that although the overall behaviour in terms of strength, stiffness and strain limits is not significantly affected by variations in f_t, it strongly affects the expected cracking pattern in the beam-column joints, the latter being more uniformly distributed (i.e., more cracks and smaller crack widths) for lower f_t values. Furthermore, the seismic residual shear strength of the beam-column joints was observed to be influenced also by f'_c irrespective of the f_y and ρ_s values.
3. Strain rate effects do not seem to play an important role on the cracking pattern. However, small variations in the cracking pattern were observed for low reinforcement content as it approaches to the minimum required as per NZS 3101:2006. More investigation is needed to ascertain the above statement and define the relationship between key parameters and strain rates which could determine a change in the cracking pattern.
4. Although multiple cracks are expected to occur since the longitudinal reinforcement content is above the minimum required as per NZS3101, large plastic deformations at few locations (one-to-two major cracks) were observed in the numerical simulations. As in the previous case, more investigation is needed to determine whether the minimum steel per code has to increase in order to enforce a well distributed cracking pattern within the plastic hinges.
5. In the cyclic response, the plastic strain at the most critical location decreases cycle after cycle (for the same drift demand), while the secant stiffness and hysteretic damping tend to become stable after a few cycles.

5.6 References

Abdalla, J. A., Hawileh, R. A., Abdelrahman, K. (2009) "Energy-based prediction of low-cycle fatigue life of BS 460B and BS B500B steel bars," *Materials and Design*, Vol. 30: 4405-4413.

ACI. (2001) *Acceptance Criteria for Moment Frames Based on Structural Testing (T1.1-01) and Commentary (T1.1R-01),* A. I. T. G. 1, ed., Farmington Hills, Michigan.

Bertero, V.V., Rea, D., Mahin,S., Atalay, M.B. (1972) *Rate of loading effects on uncracked and repaired reinforced concrete members*, EERC Report 72-9, University of California, Berkeley.

Chung, L., Shah, S.P. (1989) "Effect of loading rate on anchorage bond and beam-column joints," *ACI Structural Journal*, Vol. 86(2): 132-142

Eligehausen, R., Genesio, G., Ozbolt, J., Pampanin, S. (2009) "3D analysis of seismic response of RC beam-column exterior joints before and after retrofit," *Concrete Repair, Rehabilitation and Retrofitting II*, 1141-1147.

Hawileh, R., Rahman, A., Tabatabai, H. (2010) "Evaluation of the low-cycle fatigue life in ASTM A706 and A615 grade 60 steel reinforcing bars," *Journal of Materials in Civil Engineering*, Vol. 22(1): 65-76.

Henry, R.S. (2013) "Assessment of the minimum vertical reinforcement limits for RC walls," *2013 New Zealand Society of Earthquake Engineering Conference*, Wellington, New Zealand.

Kam, W.Y. (2010) *Selective weakening and post-tensioning for the seismic retrofit of non-ductile RC frames*, Doctoral thesis, University of Canterbury, Christchurch, New Zealand.

Kam, W.Y., Pampanin, S., Elwood, K. (2011) "Seismic performance of reinforced concrete buildings in the 22 February Christchurch (Lyttelton) Earthquake," *Bulletin of the New Zealand Society for Earthquake Engineering*, Vol. 44(4): 239-278.

Kunnath, S. K., El-Bahy, A., Taylor, A. W., Stone, W. C. (1997) *Cumulative seismic damage of reinforced concrete bridge piers*, National Institute of Standards and technology, Technical Report NISTIR-6075.

Lettow, S. (2006) *Ein Verbundelement für nichtlineare Finite Elemente Analysen – Anwendung auf Übergreifungsstöße (A bond element for nonlinear finite element analysis – Applied on splices)*, PhD Dissertation, IWB, Universität Stuttgart, Germany (in German).

Mahrenholtz, C. (2012) *Seismic bond model for concrete reinforcement and the application to column-to-foundation connections*, PhD thesis, Institut fur Werkstoffe im Bauwesen der Universitat Stuttgart.

Mander, J. B., Cheng, C. T. (1995) "Replaceable hinge detailing for bridge columns," *ACI Special Publication*., Vol. (187): 185-204.

Mander, J. B., Panthaki, F. D., Kasalanati, A. (1994) "Low-cycle fatigue behaviour of reinforcing steel," *Journal of Materials in Civil Engineering*, Vol. 6(4): 453-468.

NZSEE (2017) *The seismic assessment of existing buildings, technical guidelines for engineering assessments, Part C: C5 – Concrete Buildings.* Downloaded from www.EQ-Assess.org.nz.

Ožbolt J., Sharma A. (2011) "Numerical simulation of reinforced concrete beams with different shear reinforcements under dynamic impact loads," *International Journal of Impact Engineering*, Vol. 38: 940-950.

Ožbolt J., Sharma A., Reinhardt H. (2011) "Dynamic fracture of concrete – compact tension specimen," *International Journal of Solids and Structures*, Vol. 48: 1534-1543.

Ožbolt J., Yijun L, Kozar I. (2001) "Microplane model for concrete with relaxed kinematic constraint," *International Journal of Solids and Structures*, Vol. 38: 2638-711.

Pampanin, S. (2012) "Reality-check and renewed challenges in earthquake engineering: implementing low-damage structural systems – from theory to practice," *Fifteenth World Conference in Earthquake Engineering*, Lisbon, Portugal.

Priestley, M. J. N., Calvi, G. M, Kowalski, M. J. (2007) *Displacement-based seismic design of structures,* IUSS Press, Pavia, Italy.

SESOC (2011) "Preliminary observations from Christchurch earthquakes" *Structural Engineering Society*, New Zealand.

Shah, S.P., Wang, M.L., Chung, L. (1987) "Model concrete beam-column joints subjected to cyclic loading at two rates," *Materials and Structures*, Vol. 20: 85-95.

6 CRACK WIDTHS ANALYTICAL INVESTIGATION

In Chapter 4 it was observed that the residual-to-maximum crack width ratios in reinforced concrete members are rotation- or drift- dependant, regardless if the cracks are due to shear-flexural or flexural induced. Figure 6-1 below, reproduced from Chapter 4 describes the phenomenon.

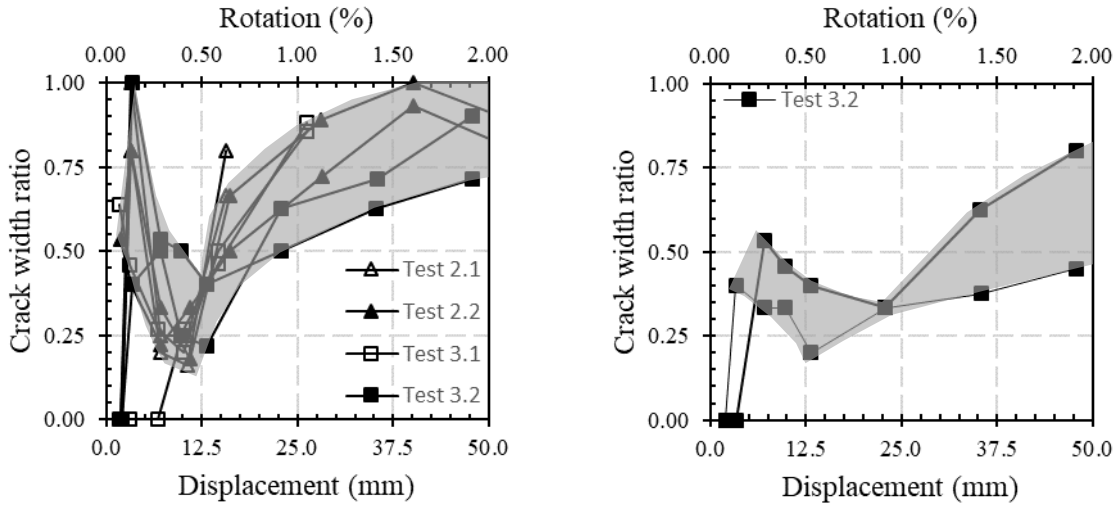

Figure 6-1. Crack width ratios experimentally measured within (left) and outside (right) the plastic hinge relocation detail (reproduced from Chapter 4).

In that specific test, the onset of nonlinearity occurred at about 0.5% “effective” beam rotation. From Figure 6-1 it is evident that the crack width ratios are also dependent on the onset of nonlinearity (see shaded area in Figure 6-1). In the elastic range the crack width ratios are inversely proportional to the beam rotation demands. On the other hand, once the onset of nonlinearity is reached, the crack width ratios are proportional to them.
Another interesting aspect to note is that, at very low (pre-yield) rotation levels, the residual crack widths are comparable to the maximum crack width at peak displacement. Crack width ratios of up to 1.0 and 0.55 were observed for shear-flexure and flexure only cracks,

respectively. These crack width ratios (w_{min}/w_{max}) were within the same order of magnitude to those measured at very high rotation levels, i.e. up to six times bigger in some cases. This phenomenon has been previously observed by other researchers looking at beam elongation (Restrepo-Posada, 1992; Fenwick et al., 1993). When the crack forms, the aggregate particles that are dislocated form a wedging action at the crack, stopping the crack to close completely even after the external load has been removed.

Previous research has suggested that the crack widths at the onset of nonlinearity depend on the bar diameter, the yield stress of the reinforcement, the reinforcement ratio, the modulus of elasticity of the reinforcement, and the bond-slip relationships (Noakowski, 1985).

There is a lack, however, of analytical models capable of characterizing the cracks due to seismic loading, as well as of simple relationships to estimate the corresponding strain in the steel with reasonable approximation. Sassi and Ranous (1996), for instance, suggested crack widths versus damage relationships for reinforced concrete walls, however there is still a lack of information relating the crack patterns with behaviour modes.

In this chapter, a numerical investigation using nonlinear finite element (*FE*) simulations is performed. The aim of the study is to gain a better understanding on how the residual crack widths, maximum crack widths, and steel strain at peak displacement are related, once the onset of nonlinearity has been exceeded. For this purpose, a parametric study is performed on a numerical model of a specimen tested in the laboratory. Prior to the parametric study, the model was validated comparing the numerical results with the experimental observations.

6.1 Experimental model

As previously anticipated, prior to perform parametric analyses the *FE* model has been validated with the experimental results of a one-half scale reinforced concrete cantilever beam tested at the University of Canterbury (Malek et al. 2016, see Figure 6-2). The reason for choosing this specimen for the numerical investigation is because the objective is to investigate the cracking behaviour of flexural dominated plastic hinges. This specimen was found appropriate for that reason. The beam is 250 mm wide and 350 mm deep, with a length of 1570 mm measured from the point of maximum moment to the point of load application, assumed to be the beam mid-span or point of contra-flexure in a seismic dominated frame. The beam is reinforced with 4-D16 top and bottom, and stirrups D10 spaced at 75 mm centres over a length of 400 mm, and 125 mm centres in the remaining length of the beam. The steel reinforcement is Grade 300 (f_y 300 MPa). The concrete compressive strength f'_c is 33 MPa.

The specimen was subjected to a quasi-static displacement-controlled monotonic loading until reaching failure. More details on the specimen, instrumentation and testing procedure can be found in Malek et al. (2016).

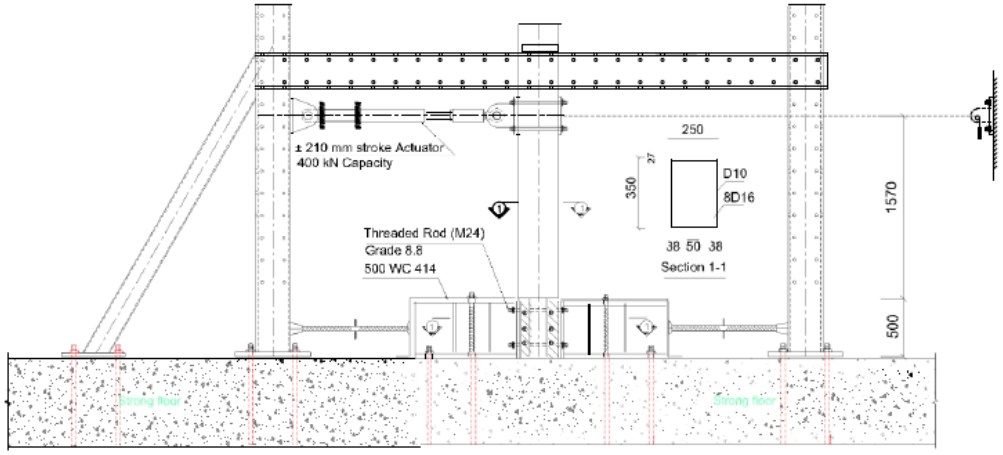

Figure 6-2. Test setup and specimen details (Malek et al., 2016).

6.2 Numerical investigation

6.2.1 Nonlinear finite element numerical model

The nonlinear *FE* code MASA (Macroscopic Space Analysis), developed at the Institute for Construction Materials (*IWB*) of the University of Stuttgart (Ožbolt et al., 2001), was used for this parametric study. The code is mainly intended for the nonlinear three-dimensional analysis of concrete and reinforced concrete structures. It can perform cyclic static (based on the secant system solver) and dynamic or rate dependent analysis (based on the explicit direct time integration). Physical (material) and geometrical (large displacements and finite strains) nonlinearities can also be accounted for.

The code can also be used perform creep and shrinkage analysis of concrete structures; analyse the concrete behaviour under high temperatures (e.g., fire), where besides degradation of concrete resistance due to the effect of high temperature (reduced strength and temperature strain induced damage), it is also possible to predict explosive spalling of concrete cover. Following principles of irreversible thermodynamics, it also can also be used to model corrosion and its effect on durability of reinforced concrete structures

The concrete is modelled according to a microplane model, consisting of a three-dimensional (3D) microscopic model in which the material is characterized by uniaxial relations between the stress and strain components on planes of various orientations called “microplanes”. The

smeared-crack (weak continuity) concept is used for the modelling of the fracture/cracking, crack propagation and damage phenomena.

In the smeared crack approach, tension-softening, shear transfer and their interaction are allowed to take place at the crack or band of microcracks. In MASA, the model formulation is based on concrete characteristics such as the tensile strength, fracture energy and maximum aggregate size. It can not only predict fracture/cracking but also complex shear-dominated and mixed-mode types of failure such as diagonal shear (Ožbolt and Bažant, 1996) . The results are mesh insensitive. For that purpose, it uses the so-called localization limiter to prevent localization of damage into a zero volume in order to make the analysis independent of the size and alignment of the finite elements.

The reinforcing bars are represented with one-dimensional (1D) truss elements with the constitutive law defined by Hoehler and Stanton (2006). The bond between the longitudinal reinforcement and concrete is modelled using discrete bond elements consisting of zero length 1D nonlinear springs (see Figure 6-3), whereas for transverse reinforcement a rigid connection between steel and concrete was assumed, neglecting the influence of the relative displacement between the stirrups and the concrete (Eligehausen et al., 2009). This discrete bond model is able to predict the bond behaviour of deformed bars under monotonic and cyclic loading; the bond deterioration is assumed to occur after some slip due to mechanical damage in the concrete-to-steel interface surrounding the ribs (Eligehausen et al., 1983; Lettow, 2006).

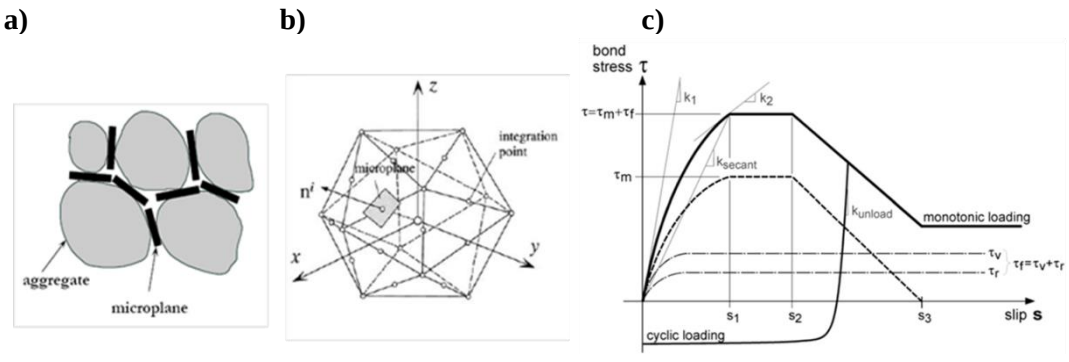

Figure 6-3. Microplane model: a) load transfer over a number of idealized contact planes; b) spatial discretization of unit-volume sphere by 21 microplanes (Ozbolt et al., 2001); c) Discrete bond model as implemented in MASA (Lettow, 2006).

Hexahedral elements with side lengths of approximately 25 mm within the fixed portion and 500 mm above the point of maximum moment (i.e., within the plastic hinge region), as well as 62.5 mm elsewhere were used to create the mesh of the elements. Linear elastic elements

were used at the point of load application so that local failure of concrete elements due to excessive stresses is avoided. Mirror symmetry (i.e., symmetry about a vertical plane across a mid-section in the beam) was used to drastically reduce the total amount of nodes and elements and thus the required computational time.

The material properties used in the numerical model are listed in Table 6-1. The bond characteristics were computed as suggested by Lettow (2006), with a difference s_2-s_1 (length of the slipping plateau, see Figure 6-3c) fixed at 0.80mm, and s_3, the slip at which mechanical bond resistance is lost, assumed to be 10 mm for D16 bars (Christoph, 2012). The bond element definition considers the influence of the transverse concrete compression and inelastic steel strains. Concrete cracking is represented by softened concrete elements which reduce the bond strength of the bond elements at the crack.

Table 6-1. Material and bond characteristics used for the numerical model (the bond parameters are schematically defined in Figure 6-3c). The bond characteristics were estimated per Lettow (2006).

Compressive concrete strength	f'_c **(MPa)**	33
Tensile concrete strength	f_t **(MPa)**	3.5
Concrete modulus of elasticity	E_c **(MPa)**	26000
Steel yield strength	f_y **(MPa)**	330
Steel ultimate strength	f_u **(MPa)**	510
Reinforcement content	ρ_s **(%)**	1.03
Mechanical and friction bond stress	$\tau = \tau_m + \tau_f$ **(MPa)**	15.2
Mechanical bond stress	τ_m **(MPa)**	9.1
Friction bond stress	τ_f **(MPa)**	6.1
Bond initial stiffness	k_1 **(MPa/mm)**	41.26
Bond tangent stiffness	k_2 **(MPa/mm)**	1.03
Bond secant stiffness	k_{sec} **(MPa/mm)**	17.19
Bond-slip at $\tau = \tau_m + \tau_f$	s_1 **(mm)**	0.89

For comparison purposes, the *CEB-FIP* Model Code (1990) estimates the design bond stress of concrete as $f_{bd} = \eta_1 \cdot \eta_2 \cdot \eta_3 \cdot f'_{td}$, where η_1 is a geometry factor (2.25 for ribbed bars); η_2 is an orientation factor for bond (typically equal to 1.0), η_3 is a bar size factor (equal to 1.0 for bar diameters equal to or smaller than 32 mm), and f'_{td} is the design tensile strength of concrete (3.5 MPa in this particular case). Thus, the design bond stress is in the order of 7.9 MPa, which is approximately half of the mechanical and friction bond stress of Table 6-1. This is due to the fact that, as described in NZS3101:2006, the design or code-based bond stress formulations are based on attainment of an average bond stress over a full

development length of the reinforcement, while Lettow (2006) utilizes a full bond-slip formulation.

6.2.2 Numerical versus experimental comparison

Figure 6-4 shows the monotonic lateral force-displacement response from the quasi-static test. In the same figure the monotonic curve obtained from the numerical analysis is shown; the agreement between this curve and the monotonic response of the experiment for beam rotations of up to 4% is evident. Figure 6-4 also shows the moment-curvature relationship obtained numerically. Both curves, the force-displacement and moment-curvature, have indications of different limit states. For normal structures, the Serviceability Limit State, *SLS* (Level 1) refers to a 50% probability of exceedance in 50 years intensity level; the Damage-control Limit State, *DC* (level 2) to a 10% probability of exceedance in 50 years intensity level; and the Ultimate Limit State, *ULS* (Level 3, not shown in the figure) to a 2% probability of exceedance in 50 years. The strain limits proposed in Priestley et al. (2007) and listed in Table 6-2 were adopted in this study.

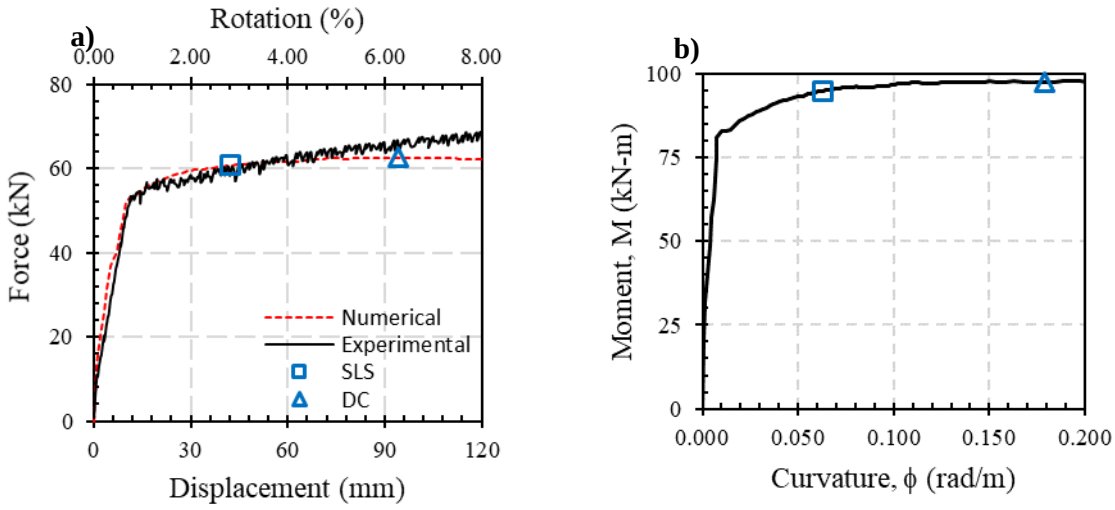

Figure 6-4. a) Monotonic lateral response from the experimental and numerical results; and b) moment-curvature relationship obtained numerically. The hollow square represents the Serviceability Limit State (*SLS*); the hollow triangle the Damage-Control Limit State (*DC*); the Ultimate Limit State (*ULS*) is not observed here since it occurs at higher displacement or rotation and curvature levels.

Table 6-2. Strain limits for different design intensity levels (Priestley et al., 2007).

Material	Level 1 (SLS)	Level 2 (DLS)	Level 3 (ULS)
Concrete compressive strain	0.004	$\varepsilon_{cu} < 0.02$	$1.5\ \varepsilon_{cu}$
Rebar tension strain	0.015	$0.60\varepsilon_{su} < 0.05$	$0.90\varepsilon_{su} < 0.08$

In the previous table,

$$\varepsilon_{cu} = 0.004 + \frac{1.4 \cdot \rho_s \cdot f_{yh} \cdot \varepsilon_{su}}{f'_{cc}} \quad (6\text{-}1)$$

$$f'_{cc} = f'_c \cdot \left\{ 2.254 \cdot \sqrt{1 + \frac{7.94 \cdot f_l}{f'_c}} - 2 \cdot \frac{f_l}{f'_c} - 1.254 \right\} \quad (6\text{-}2)$$

$$f_l = 0.50 \cdot C_e \cdot \rho_v \cdot f_{yh} \quad (6\text{-}3)$$

$$\rho_v = \rho_{ax} + \rho_{ay} \quad (6\text{-}4)$$

where ε_{cu} is the ultimate compression strain for confined concrete; f'_{cc} is the compression strength of the confined concrete (MPa); f'_c is the unconfined compression concrete strength (MPa); f_l is the lateral confining stress(MPa); ρ_v is the volumetric confinement ratio; ρ_{ax} and ρ_{ay} are the area ratio of transverse reinforcement in the *x* and *y* direction, respectively; and ε_{su} is the ultimate strain for the longitudinal reinforcement, assumed to be 0.015. For this specific case, the beam rotations for the *SLS* and *DC* limit states are 2.8% and 6.3%, respectively.

Figure 6-5 shows snapshots of the crack patterns obtained numerically at rotation angles from 0.5% to 6.5% in increments of 0.5%. As previously mentioned, these cracks are based on the smeared crack concept. Concrete elements in red represent approximately crack widths 2.5 mm wide or greater; whilst concrete elements in yellow represent cracks widths varying approximately between 0.9 mm and 2 mm wide. At the beginning of the simulation, one horizontal crack starts forming at the point of maximum moment. As the applied displacement increases, another horizontal crack forms which becomes diagonal extending towards the extreme concrete fibre in compression. Two secondary cracks, each one adjacent to the major cracks are also formed. Some additional cracking is also observed within the fixing block at the base of the specimen (represented by the grey block in the figure).

Figure 6-5 also shows a snapshot of the specimen at the end of the experiment. Although the beam failed at a much greater beam rotation (13%), the agreement between the cracking pattern of the experiment and the numerical simulation is remarkable. The numerical model was able to replicate the formation of the two major cracks as well as the secondary ones. The crushing of the extreme concrete fibre due to excessive compression forces observed during the experiment is also very well replicated by the numerical model (darker grey area observed at 6.5% beam rotation, where the two cracks meet).

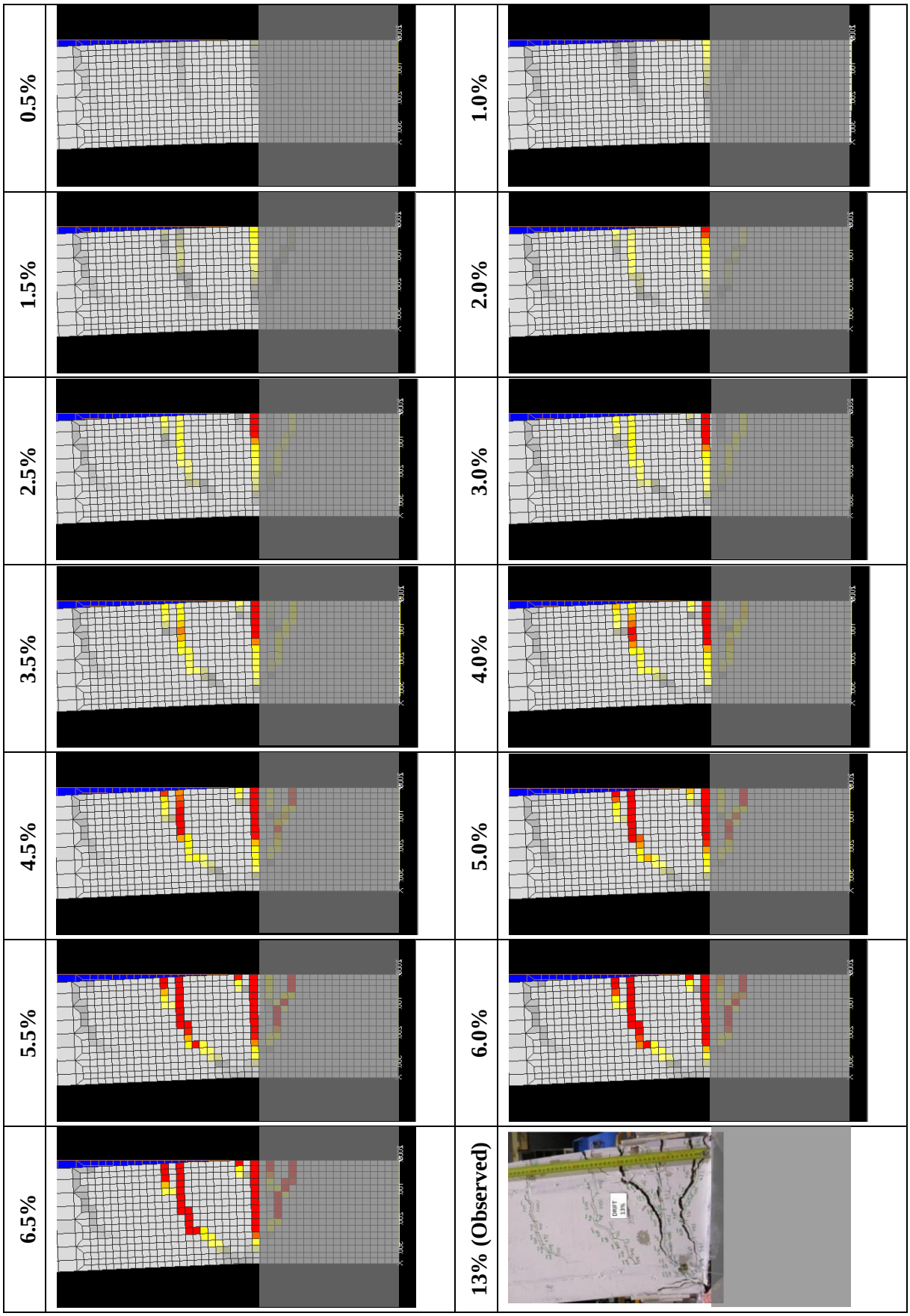

Figure 6-5. Cracking pattern obtained numerically, at different beam rotation levels.

6.2.3 Monotonic steel strain profiles

Steel strain profiles obtained from the nonlinear *FE* model described above are shown in Figure 6-6 for beam rotations of 1.0%, 1.5%, 2.0%, 3%, and 4%. Also shown in the figure is the strain penetration length estimated as suggested by Priestley et al. (2007).

$$L_{sp} = 0.022 \cdot d_b \cdot f_y \tag{6-5}$$

where d_b= bar diameter (mm), and f_y = bar yield strength (MPa). For this specific case (D16 bars and f_y = 300 MPa), L_{sp} is equal to 114 mm. From Figure 6-5 it is evident that the crack spacing is about 300 mm. This can be confirmed looking at Figure 6-6, where the distance between the points of maximum and minimum steel strain is 150 mm, or the half the crack spacing).

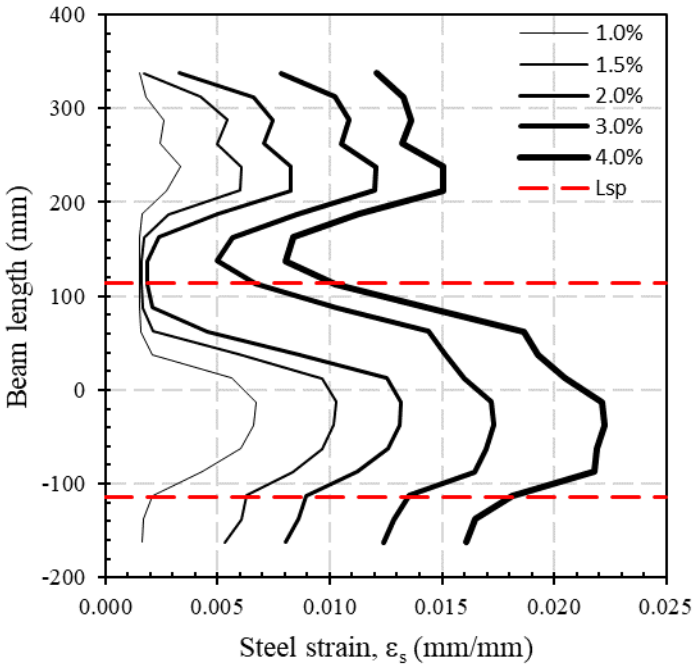

Figure 6-6. Steel strain profiles obtained analytically, within one beam depth and approximately one strain-penetration length, L_{sp}, below the point of maximum moment demand.

6.2.4 Cyclic steel strain profiles

Figure 6-8 and Figure 6-9 show the cyclic peak steel strains at equal displacement cycles corresponding to 1%, 2%, 3%, and 4% beam rotation, measured at the left and right rebars when the rebars are in tension (i.e., at peak displacements in the positive direction for the left rebar, and at peak displacements in the negative direction for the right rebar). The sign convention adopted is shown in Figure 6-7.

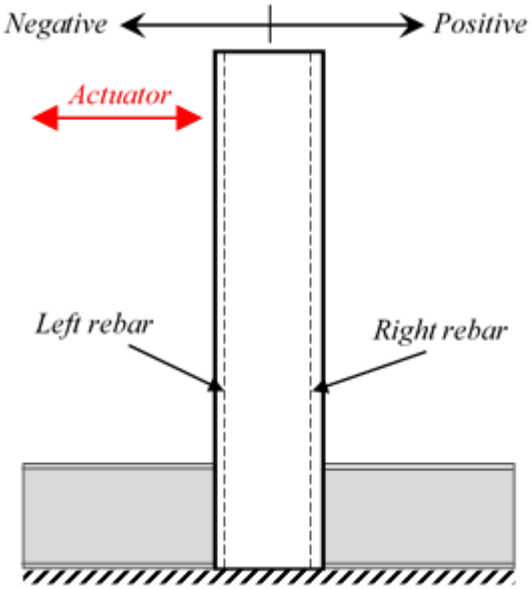

Figure 6-7. Sign convention for cyclic steel strains.

Looking at the figures it is evident that the peak strains decrease as the number of cycles increase, reaching in some cases a constant strain value. The reason for that is the cyclic bond deterioration. The loss of bond between the steel and concrete due to cyclic loading allows to spread the steel strain demand over a longer length of bar thus reducing its value. In other words, the rebars are somehow "self-protecting" due to the cyclic bond deterioration.
Figure 6-10 shows an example of steel strains measured in the rebars located within 200 mm above and below the point of maximum moment, for equal displacement cycles corresponding to 2.0% beam rotation. It is clear how the cyclic bond deterioration reduces the strain at the most critical location, whilst increases the steel strain at the less critical location, i.e. midpoint between two adjacent cracks, thus potentially inducing a secondary crack at that location. Therefore, for practical purposes, assuming a constant steel strain equal to the strain measured in the first cycle, when the bond has not been lost yet, is a conservative approach.

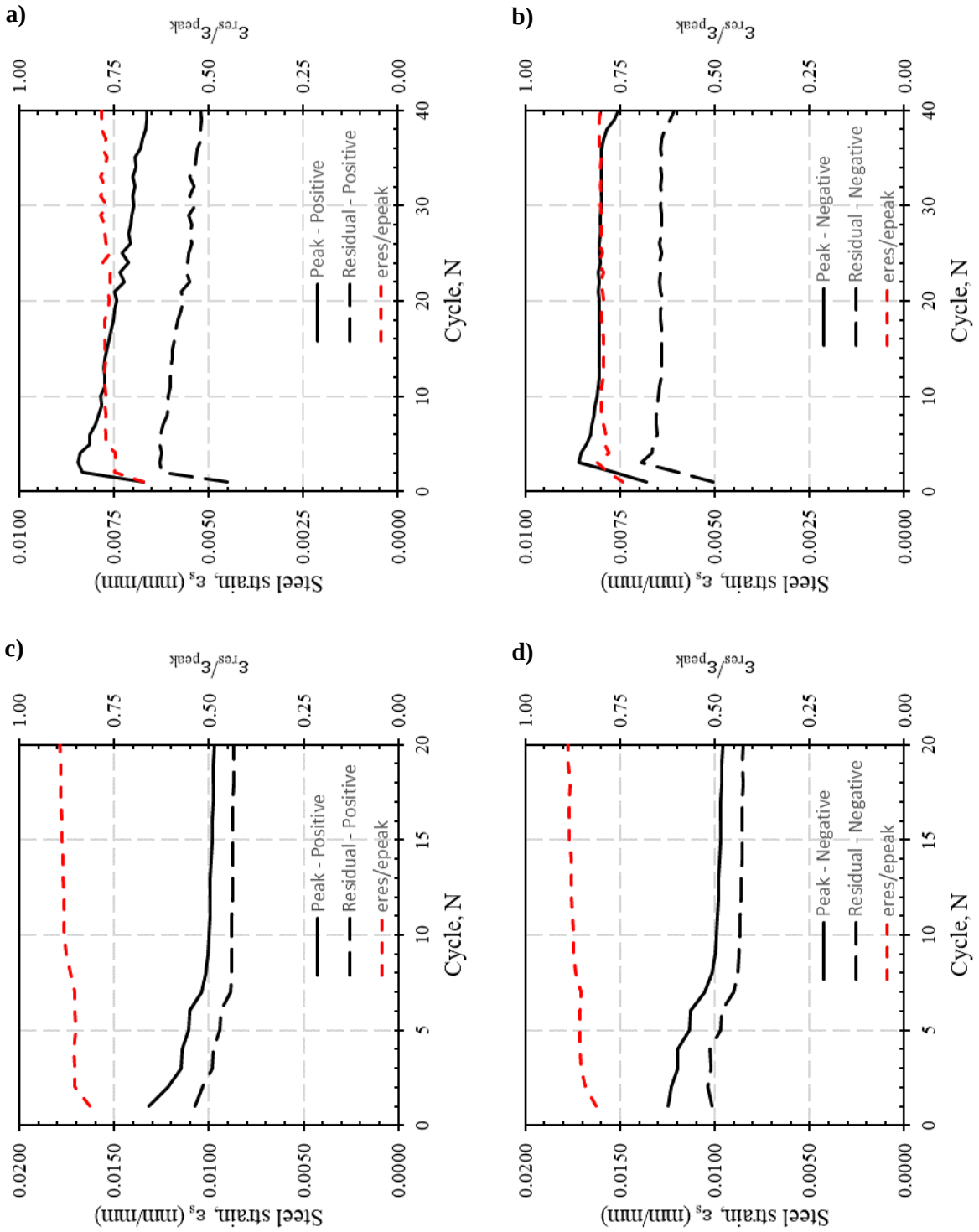

Figure 6-8. a) Cyclic steel strains measured at the left bar for "positive" equal displacement cycles at 1% beam rotation; b) cyclic steel strains measured at the right bar for "negative" equal displacement cycles at 1% beam rotation; c) cyclic steel strains measured at the left bar for "positive" equal displacement cycles at 2% beam rotation; d) cyclic steel strains measured at the right bar for "negative" equal displacement cycles at 2% beam rotation.

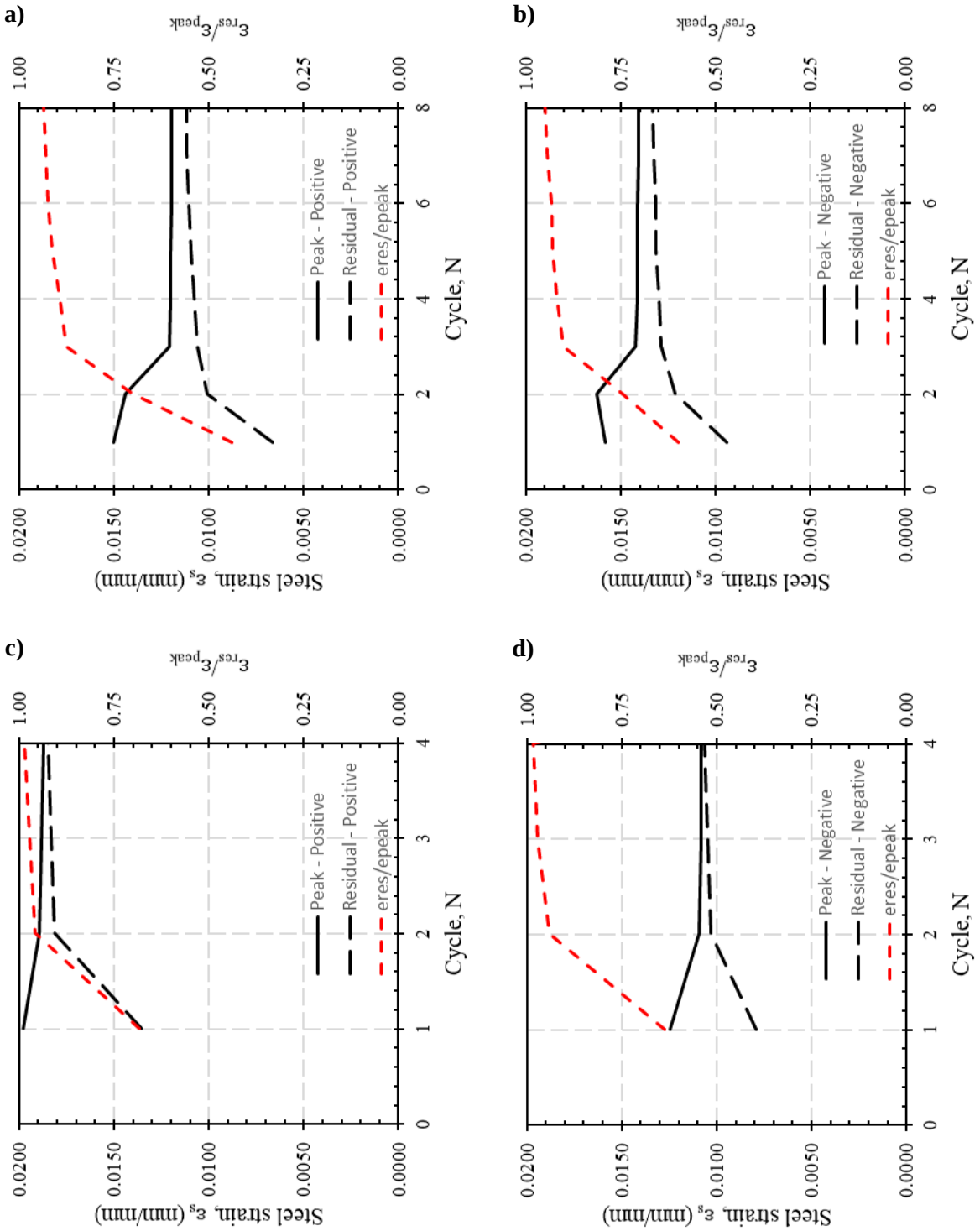

Figure 6-9. a) Cyclic steel strains measured at the left bar for "positive" equal displacement cycles at 3% beam rotation; b) cyclic steel strains measured at the right bar for "negative" equal displacement cycles at 3% beam rotation; c) cyclic steel strains measured at the left bar for "positive" equal displacement cycles at 4% beam rotation; d) cyclic steel strains measured at the right bar for "negative" equal displacement cycles at 4% beam rotation.

6.3 Analytical estimation of crack width ratios

Paulay and Priestley (1992) explained that "…*curvature ductility in plastic hinges is achieved primarily by very large inelastic tensile strains. Therefore, the main strain over the depth of a beam and along the length of a plastic hinge will be in tension, resulting in a lengthening of that part of the beam. Because the neutral-axis depth varies along the span, elongations also occur after cracking in elastic parts of the beam. However, these are negligible in comparison with those developed over plastic hinges*." Since the total elongation of the beam can be approximated as the sum of all the cracks formed along the beam (and more precisely within the plastic hinges), we may argue that the ratio of the beam length after load removal upon the beam length at peak displacement, both measured at the location of the steel in tension, gives an indication of the residual-to-maximum crack width ratio.

In this Section, the nonlinear *FE* model validated with the experimental results is used as the basis for a parametric study varying the longitudinal reinforcement content from the minimum to maximum allowed per the NZS3101:2006 code. The objective of this parametric study is to investigate the effect of the reinforcement content on beam elongation ratios, and thus on the crack width ratios. The NZS3101:2006 specifies the following reinforcement ratios:

$$\rho_{min} = \frac{\sqrt{f'_c}}{4 \cdot f_y} \tag{6-6}$$

$$\rho_{max} = 0.75 \cdot \alpha \cdot \beta \cdot \frac{f'_c}{f_y} \cdot \left(\frac{600}{600 + f_y} \right) \tag{6-7}$$

For this particular case (i.e., a beam 250 mm wide, 350 mm deep, with the material properties described in Table 6-2), the minimum and maximum reinforcement content becomes ρ_{min} = 0.44% (340 mm^2, or approximately 4-D10 bars top and bottom) and ρ_{max} = 3.40% (2650 mm^2, or approximately 4-D28 bars top and bottom). Different nonlinear *FE* models were developed by varying the longitudinal reinforcement between those two quantities. Figure 6-11 shows the moment-curvature relationships for the models used in this parametric study.

Figure 6-12 shows the corresponding force-displacement curves. Special care was taken in order to make sure that the shear demand, estimated as the maximum moment capacity considering over-strength factors divided by the lever arm, does not exceed the beam's shear capacity. Section 6.3.2 provides more detail on the computed shear capacities and how they compare with the maximum demands.

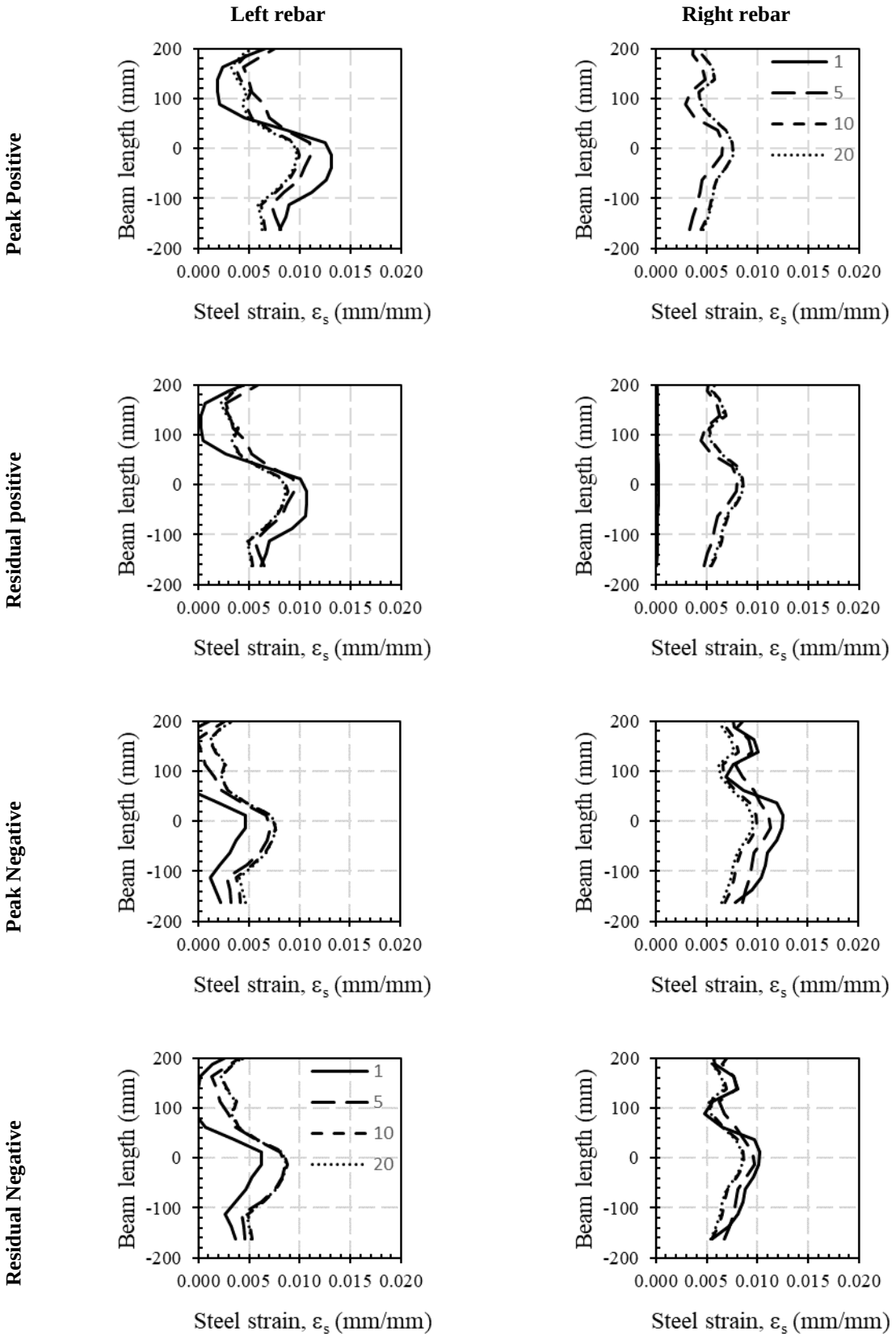

Figure 6-10. Example of steel strains measured in longitudinal reinforcement, at equal displacement cycles corresponding to 2.0% beam rotation.

Table 6-3. Material and bond characteristics used for the different numerical models (the bond parameters are schematically defined in Figure 6-3c). The bond characteristics were estimated per Lettow (2006).

Bar diameter	4-D10	4-D12	4-D16	4-D20	4-D25
f'_c (MPa)	33	33	33	33	33
f_t (MPa)	3.5	3.5	3.5	3.5	3.5
E_c (MPa)	26000	26000	26000	26000	26000
f_y (MPa)	330	330	330	330	330
f_u (MPa)	510	510	510	510	510
f_R	0.060	0.070	0.080	0.085	0.090
A_s (mm^2)	314	452	804	1257	1964
ρ_s (%)	0.40	0.58	1.03	1.61	2.52
$\tau = \tau_m + \tau_f$ (MPa)	12.1	13.7	15.2	16.0	16.7
τ_m (MPa)	7.3	8.2	9.1	9.6	10.0
τ_f (MPa)	4.8	5.5	6.1	6.4	6.7
k_1 (MPa/mm)	29.58	35.18	41.26	44.48	47.81
k_2 (MPa/mm)	1.48	1.28	1.03	0.89	0.74
k_{sec} (MPa/mm)	14.79	15.99	17.19	17.79	18.39
s_1 (mm)	0.82	0.86	0.89	0.90	0.91

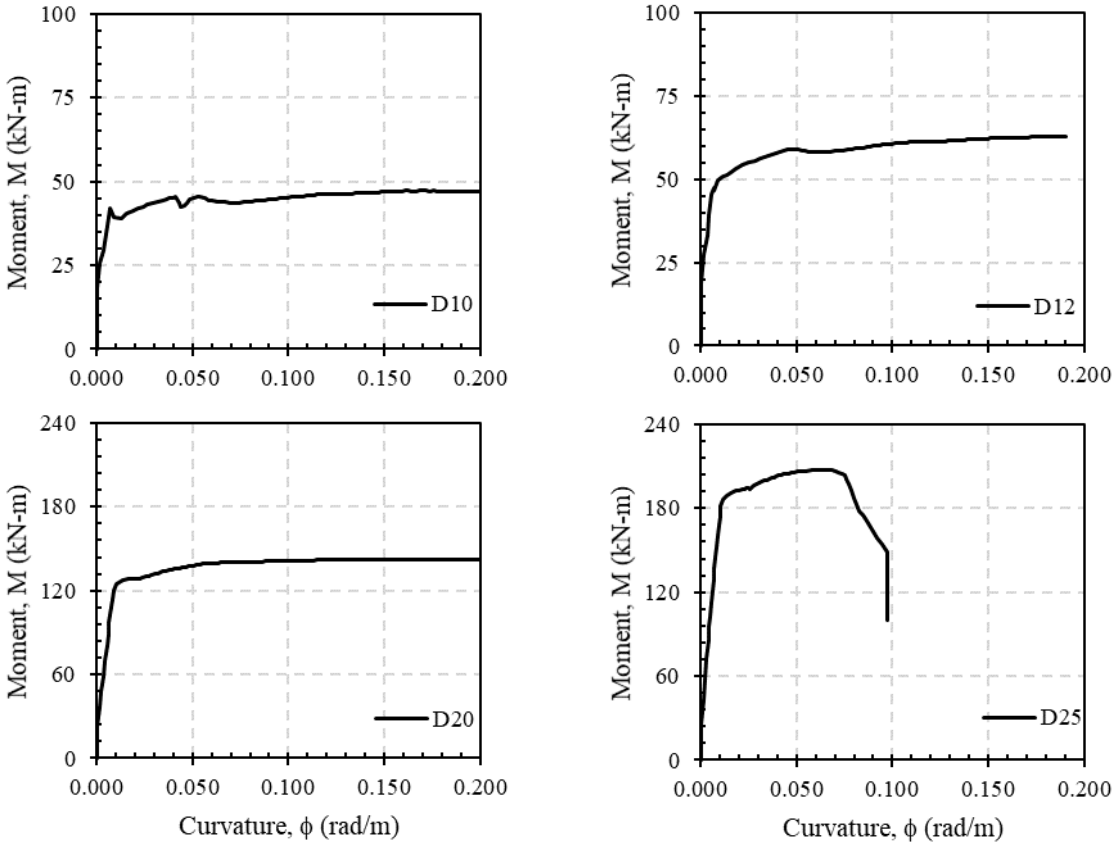

Figure 6-11. Moment-curvature relationships for different longitudinal reinforcement contents.

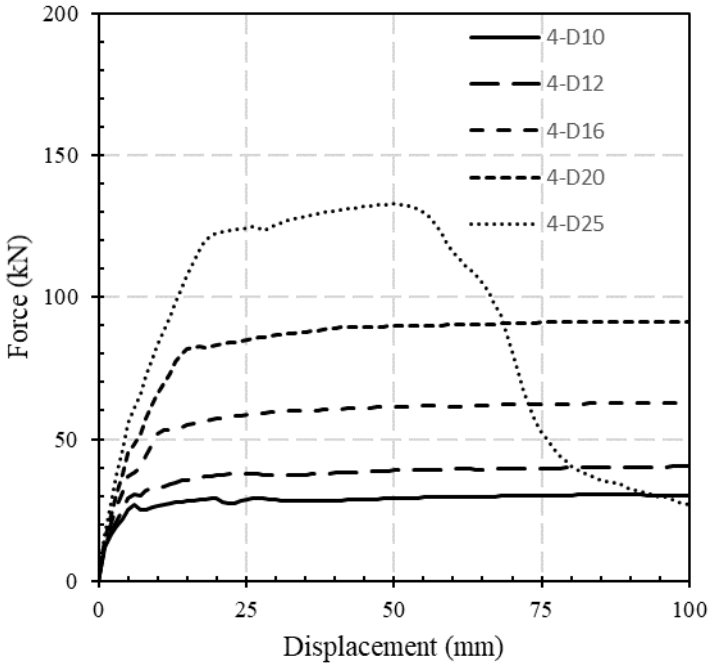

Figure 6-12. Lateral Force-Displacement curves of the beam for different longitudinal reinforcement content.

6.3.1 Relationships between beam rotation, curvature and peak strain demand

In the following figures, it is assumed that the beam length ratios are equivalent to crack width ratios (i.e., residual crack width divided by maximum crack width). No more reference is made to beam elongation ratios.

The similarities between Figure 6-13 and Figure 6-1 is evident. It is clear how the crack width ratios depend on the beam rotations, and therefore on the beam depth. However, there is no clear relationship between the crack width ratio and the beam rotation. Since the beam rotations depend on the plastic hinge length, which can be related to the beam depth, the same data is plotted against curvature demands as a means to eliminate the dependence on the plastic hinge length. Figure 6-14 shows the results. The scatter in the results is slightly reduced, however there is still a dependence on the beam depth. One step further, the crack width ratios are plotted against the strain in the steel at peak displacement (see Figure 6-15). It is evident how all the curves overlap each other. In other words, by eliminating the dependence on the plastic hinge length (from rotations to curvature) and beam depth (from curvature to steel strain), it is possible to develop a unique empirical equation relating the crack width ratios with the strain at peak displacement.

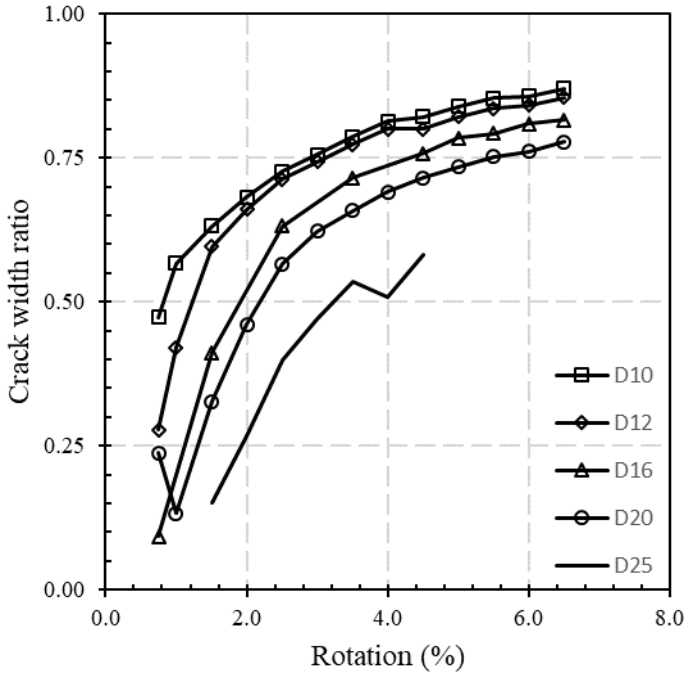

Figure 6-13. (Res/Max) crack width ratios versus beam rotation demands.

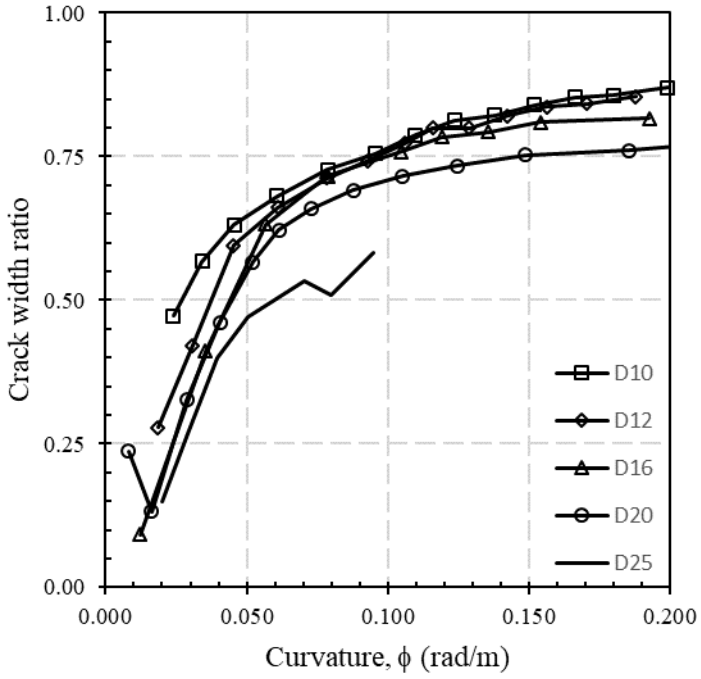

Figure 6-14. (Res/Max) crack width ratios versus beam curvature demands.

It is observed that the crack width ratios versus steel strain relationship follows a linear trend up to approximately 10 times the yield strain, ε_y. After that point, a second linear trend with a reduced slope is observed (see Figure 6-16).

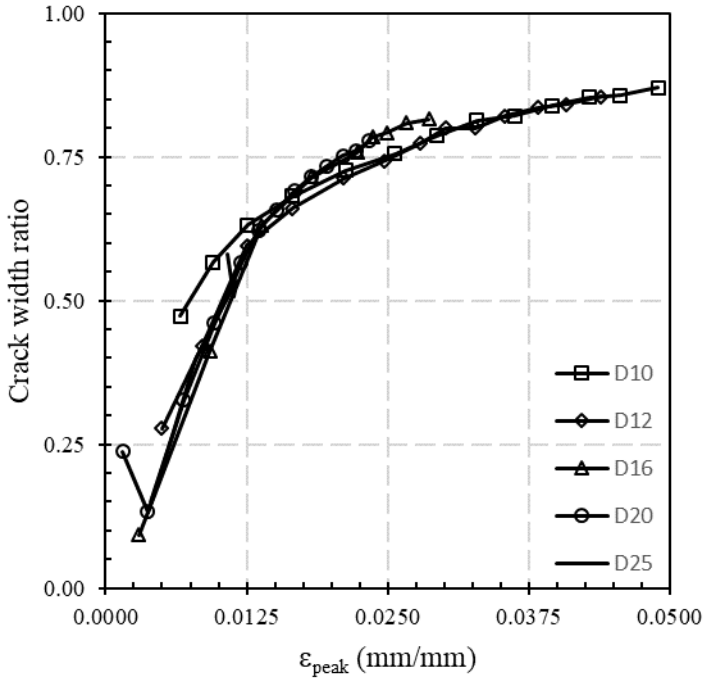

Figure 6-15. (Res/Max) crack width ratios versus steel strains at peak displacement.

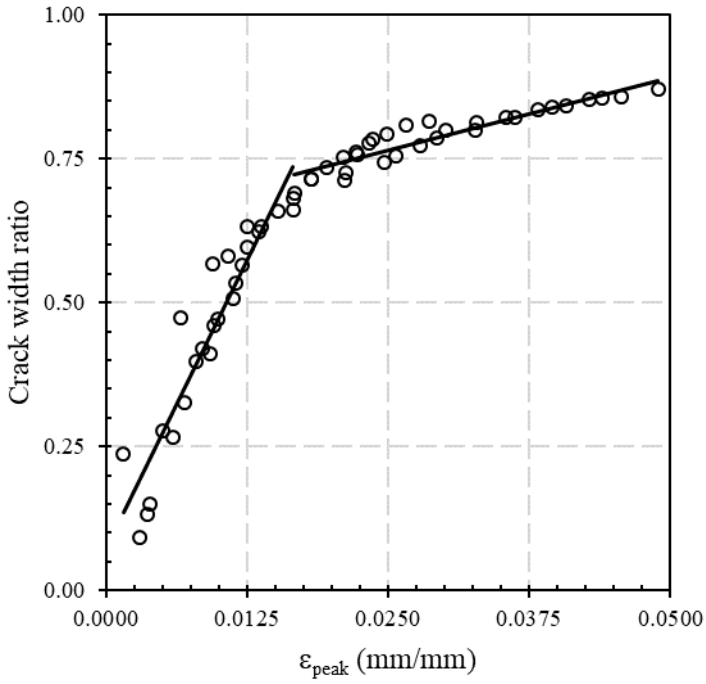

Figure 6-16. Graphical representation of the empirical relationships between (Res/Max) crack width ratios and steel strain at peak displacement.

The following empirical equations are obtained by linear regression analysis.

$$\frac{w_r}{w_m} = 39.9 \cdot \varepsilon_{peak} + 0.075, \quad (for\ \varepsilon_y \leq \varepsilon_{peak} \leq 10 \cdot \varepsilon_y) \tag{6-8}$$

$$\frac{w_r}{w_m} = 5.09 \cdot \varepsilon_{peak} + 0.637, \quad (for\ 10 \cdot \varepsilon_y \leq \varepsilon_{peak} \leq 0.05) \tag{6-9}$$

In the previous equations, the coefficients of determination, R^2, are 0.8843 and 0.8775, respectively. R^2 of 0.0 indicates that the model explains none of the variability of the response data around its mean. On the other hand, a R^2 of 1.0 indicates that the model explains all the variability of the response data around its mean. Therefore, the models above fit the data reasonably well.

6.3.2 Influence of beam shear-span

The parametric study described in Section 6.3.1 was performed using a shear span or *L/d* ratio constant and equal to 10. In order to investigate the effect of the shear span on the crack width ratios, two additional models with *L/d* of 4 and 8 were developed and compared with the original model. Figure 6-17 shows the force-displacement curves for the two additional models, as well as the original (*L/d*= 10) model.

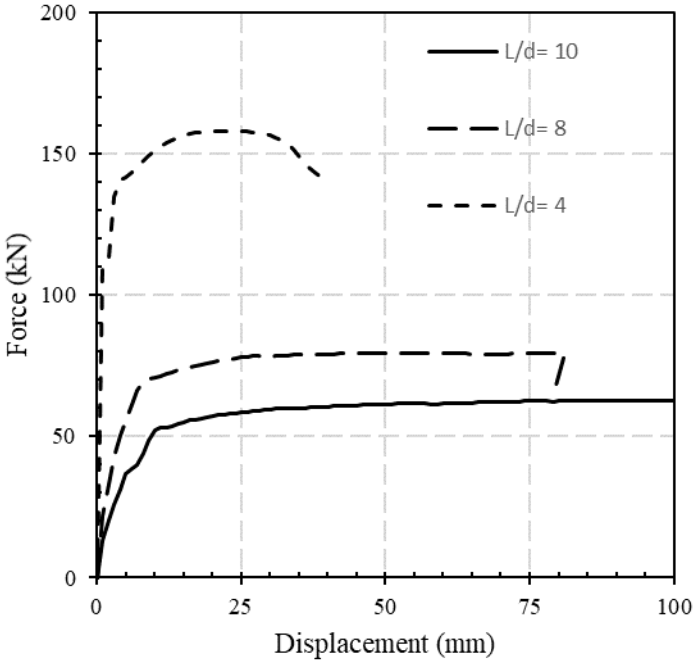

Figure 6-17. Lateral Force-Displacement curves of the beam for different shear spans.

Table 6-4 shows the capacities of the different models. For L/d = 8, more transverse steel was added in order to maintain a $\Omega = V_n/\phi V_s$ ratio similar to the case of L/d = 10 (where Ω is in the order of 1.5 for this particular case). For L/d= 4, more transverse steel was added in order to satisfy the limited ductile criteria, aiming at inducing a shear failure at high beam rotation (and displacement ductility) demands.

Table 6-4. Shear demand versus capacity estimation.

	L/d = 10	**L/d = 8**	**L/d = 4**
Long. reinforcement	4-D16 (top & bot)	4-D16 (top & bot)	4-D16 (top & bot)
Trans. Reinforcement (1)	D10 @ 125 mm	D12 @ 125 mm	D12 @ 125 mm
M_n (kN-m)	98	98	98
V_n (kN)	62	78	157
ϕV_c (kN)	57	57	57
ϕV_s (kN)	97	140	140
Failure criteria	$\phi V_s > \Omega V_n$	$\phi V_s > \Omega V_n$	$0.5 \cdot \phi V_c + \phi V_s > \Omega V_n$
Design philosophy	Ductile	Ductile	Limited ductile

Note (1): The transverse reinforcement is spaced @ 75 mm crs within the plastic hinge region.

Figure 6-18 shows the effect of the shear span on the crack width ratios. For L/d = 8, the effect on the crack width ratios is negligible. The difference observed between the crack width ratios obtained analytically for L/d = 8 with the empirical equations developed for L/d = 10 are because the empirical equations were calibrated considering more data. They also take into account the variability or scatter as result of considering different reinforcement contents. On the other hand, the difference between the empirical equation and the values obtained for L/d = 4 is more evident. This is because the cracks developed in the shorter beam are more of the shear-flexural type. In these type of cracks, the compression strut developed as part of the truss mechanism “lock-in” the cracks and stops their closure, thus increasing the crack width ratios (i.e., wider residual crack widths for the same maximum crack width). In other words, the empirical equations developed in Section 6.3.1 appear to provide reasonable results for flexural dominated plastic hinges, with shear spans of L/d = 8 or greater, and detailed for high ductility.

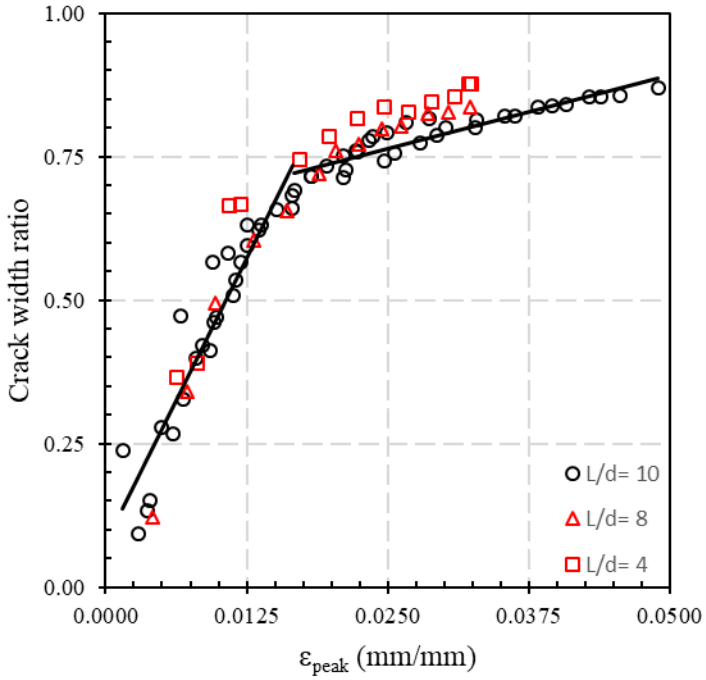

Figure 6-18. Effect of shear span on the crack width ratios.

6.3.3 Influence of axial force

After the 2010-2011 Christchurch earthquake sequences, there were a limited number of cases, typically occurred in shear walls, where the observed residual cracks were almost imperceptible and yet the bars crossing the cracks were fractured due to excessive tensile strains, potentially due to the development of a single crack (Kam et al. 2011). Although the axial force due to gravity loads is negligible in a beam, if any, when compared to a wall, the net effect of the beam elongating due to cyclic loading combined with the the restrain action from the reinforced concrete slab, impeding the beam from free elongation, results in induced axial loads in beams which could significantly reduce the maximum crack width, thus decreasing the (Res/Max) crack width ratio.

Earthquake induced beam axial forces, although are more complex phenomenon (e.g., it may also be affected by the stiffness of the column being pushed away, among), can be estimated as the cumulative shear friction effect of the slab reinforcement developed within the plastic hinge length. It can be demonstrated that for reasonable amounts of slab reinforcement contents (e.g., bars D12 and D16 spaced between 150 mm and 300 mm crs.), the normalized axial force $\nu=P_u/f'_c \cdot A_g$ induced in the beam is typically less than 0.10 (see Figure 6-19). In some rare cases characterized by small beam sections, heavily reinforced diaphragms, and low f'_c/f_y ratios, the normalized axial force in the beam, ν, can be as high as 0.18.

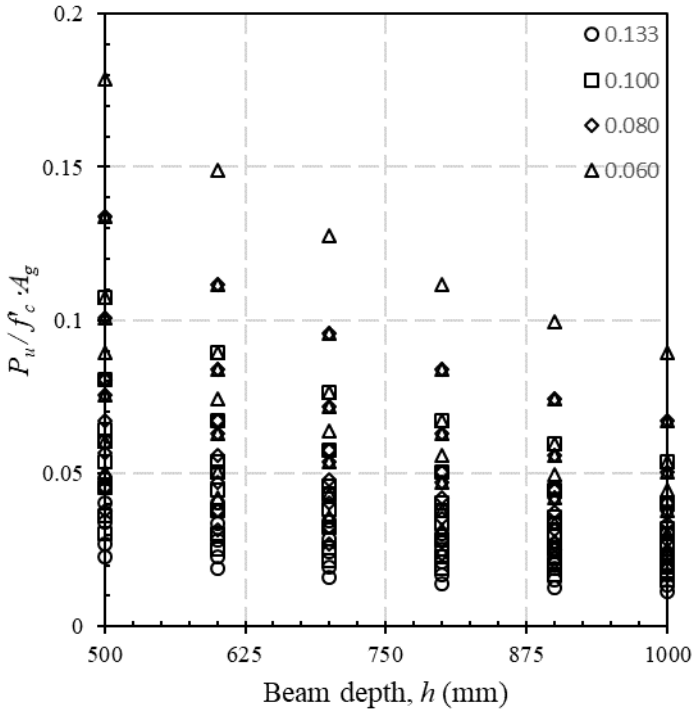

Figure 6-19. Normalized axial force in beams due to beam elongation, for different beam depths and different f'_c/f_y ratios (a constant beam width over depth ratio of 0.50 is assumed for all the cases).

Figure 6-20 shows the force-displacement curves for the same original model, with normalized axial loads, $P_u/f'_c \cdot A_g$, between 0.0 and 0.3. Figure 6-21 shows the corresponding crack width ratios versus steel strain at peak displacement. Different aspects are noteworthy in this figure. For axial loads of $0.10 f'_c \cdot A_g$, residual cracks are only observed for peak steel strains in the order of 0.005 (0.5%, or approximately $3 \cdot \varepsilon_y$); after that point the rate of increase is similar to the case of zero axial load until a peak strain of approximately 10·εy, after which the rate of increase is 2.5 times the case of zero load. For axial loads of $0.20 f'_c \cdot A_g$, residual cracks are only observed for peak steel strains in the order of 0.010 (1.0%, or approximately $6 \cdot \varepsilon_y$); after which the lateral strength of the beam starts to drop (see Figure 6-20). Lastly, for this specific case, axial loads of $0.30 f'_c \cdot A_g$ are sufficient to practically close the cracks regardless of the steel strain at peak displacement.

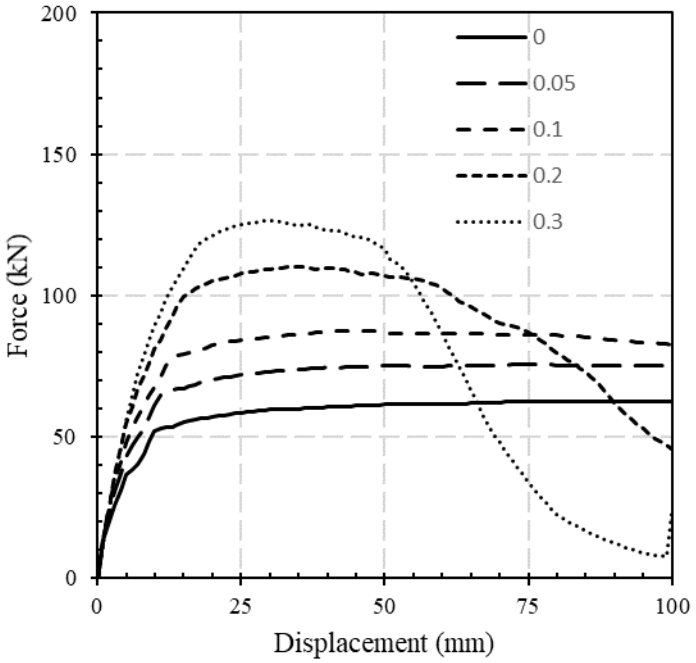

Figure 6-20. Lateral Force-Displacement curves for different beam axial load ratios.

Based on the above, the following empirical relationships for crack width ratios were obtained by linear regression.

For $\nu = P_u/f'_c \cdot A_g = 0.10$:

$$\frac{w_r}{w_m} = 47.1 \cdot \varepsilon_{peak} - 0.254, \quad (for\ 3 \cdot \varepsilon_y \leq \varepsilon_{peak} \leq 10 \cdot \varepsilon_y) \tag{6-10}$$

$$\frac{w_r}{w_m} = 12.68 \cdot \varepsilon_{peak} + 0.319, \quad (for\ 10 \cdot \varepsilon_y \leq \varepsilon_{peak} \leq 0.035) \tag{6-11}$$

In the previous equations, the coefficient of determination, R^2, are 0.9981 and 0.9889, respectively.

For $\nu = P_u/f'_c \cdot A_g = 0.20$:

$$\frac{w_r}{w_m} = 48.4 \cdot \varepsilon_{peak} - 0.537, \quad (for\ 6 \cdot \varepsilon_y \leq \varepsilon_{peak} \leq \sim 10 \cdot \varepsilon_y) \tag{6-12}$$

In the previous equation, the coefficient of determination, R^2, is 0.9770.

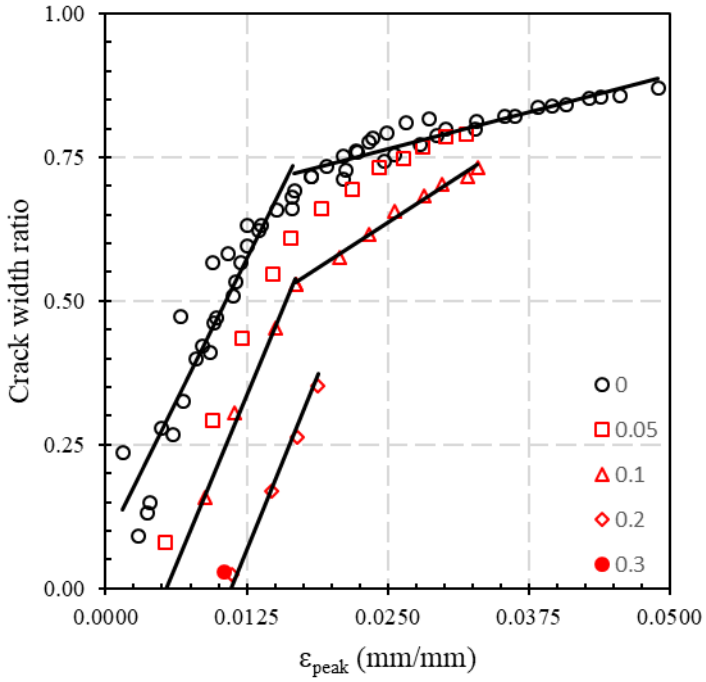

Figure 6-21. Effect of axial load on the (Res/Max) crack width ratios.

6.4 Estimation of maximum crack widths

Several empirical equations can be found in the literature to estimate maximum crack widths, however they are typically applicable for steel strains within the elastic range (e.g., fib Model; Borges, 1966; Hognestad, 1962; Kaar and Hognestead, 1965; Gergerly and Lutz, 1968). Beeby (1970) measured crack widths and their spacing in one-way reinforced concrete slabs. He concluded that the crack pattern at any point in the slab was the result of the interaction of the cracking at a point distant from a reinforcing bar (Figure 6-22b), and the cracking directly over a reinforcing bar (Figure 6-22c). For this particular case, he did not observe a significant difference in the results between round bars and deformed bars (the crack widths were about 20% greater in the case of round bars), potentially due to the testing apparatus and protocol. Beeby developed a series of quite complex equations that best fit the experiments. These equations depend on the probability of the crack width being exceeded.

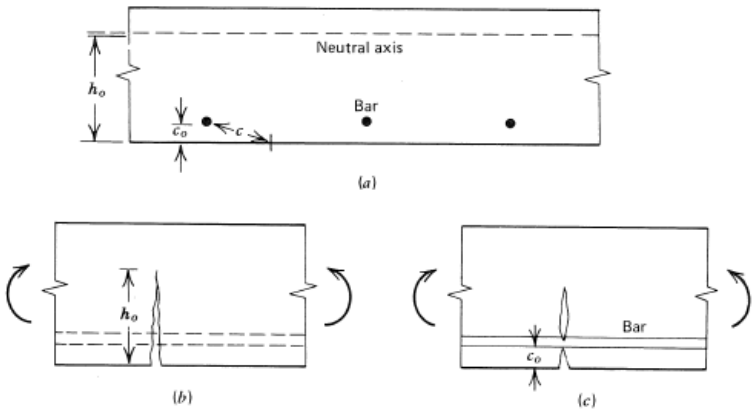

Figure 6-22. Effect of bar proximity on cracking: a) transverse section; b) crack at distance from a bar, h_o controlled; and c) crack at a bar, c_o controlled (Beeby, 1970).

He also developed a simple set of equations that provide a crack width that will be exceeded by approximately 20% of the results (i.e., 80% probability of not being exceeded). These equations are the following.

$$w_m = \frac{3 \cdot c \cdot \varepsilon_m}{1 + 2 \cdot (c - c_o)/(h - kd)} \tag{6-13}$$

$$\varepsilon_m = \left(\varepsilon_s - \frac{2.5 \cdot b \cdot h}{A_s} \cdot 10^{-6}\right) \cdot \frac{h - kd}{d - kd} \tag{6-14}$$

In the previous equations, h= overall depth of the section; kd= neutral axis depth; ε_s= strain in the steel at the crack; b= section width; h= section depth; A_s= area of steel; and d= effective depth. ε_m is equal to the steel strain at the crack, minus an empirical term that accounts for the tension stiffening effect of the concrete between cracks.

Nevertheless, as anticipated, Beeby's equations, as many other empirical equations available in literature, were developed based on tests with specimens that did not exceed the steel yield strength, thus significantly limiting their use for seismic applications.

6.5 Relationship between maximum crack width and peak steel strain

In this section, a tentative formulation to relate the maximum crack with the steel strain at peak displacement, is proposed. The formulation is based on results obtained from nonlinear finite element simulations.

Priestley et al. (1996) estimate the maximum crack width as the maximum strain at peak displacement multiplied by the crack spacing. It is believed, however, that is more appropriate

to take into account the strain gradient within the crack spacing, instead of considering its maximum value. The *fib* Model Code, for strain levels below the yield strain, estimates the mean steel strain over the strain penetration length as 0.60 times the steel strain at the crack. Therefore, using the maximum value as Priestley et al. (1996) suggest may lead to overestimations of the crack width, in particular at low strain levels.
Looking at Figure 6-6, the mean steel strain over a total length of S_{crack}, can be estimated as:

$$\varepsilon_{mean} = \frac{1}{S_{crack}} \cdot \int_{-0.5 \cdot S_{crack}}^{+0.5 \cdot S_{crack}} \varepsilon_s \cdot \delta L \tag{6-15}$$

Figure 6-23 shows the mean steel strain versus the peak strain obtained using the finite element models described in Section 6.3.1, for zero axial load. As expected, the mean strain depends on the bar diameter and more specifically, on the bond-slip.

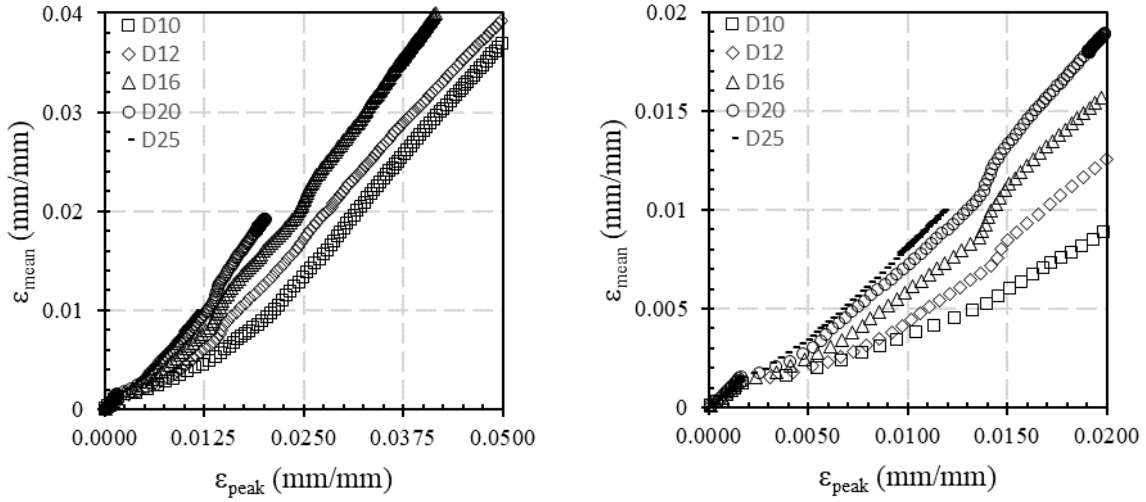

Figure 6-23. Mean steel strain over the crack length versus peak steel strain for peak steel strains up to 0.05 mm/mm (left), and up to 0.02 mm/mm (right).

From Figure 6-24, the bond between two adjacent cracks can be approximated with a parabolic function. The base of the parabola is half of the crack spacing, whilst the height is the maximum (mechanical plus frictional) bond stress that can be developed. Following Lettow (2006), the maximum bond stress can be defined as follows.

$$\tau_{max} = 20 \cdot f_R^{0.8} \cdot \sqrt{f'_c} \tag{6-16}$$

In the previous equation, f_R (unitless) is the related rib area and depends on the bar diameter; τ_{max} and f'_c are in MPa. The crack spacing, S_{crack}, in this particular case is equal to 300 mm. Integrating the bond stress over a length equal to the crack spacing multiplied by the crack spacing and the bar perimeter, gives the bond strength developed within the crack spacing. The following equation is obtained by normalizing the bond strength with the bar yield force.

$$\kappa = \frac{53.33 \cdot S_{crack} \cdot f_R^{0.8} \cdot \sqrt{f'_c}}{d_b \cdot f_y} \tag{6-17}$$

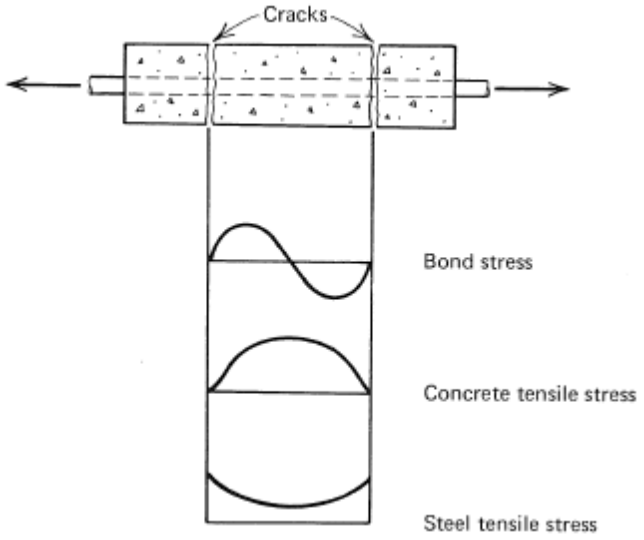

Figure 6-24. Cracking of a member with axial tension (Park and Paulay, 1975).

Equation (6-17) can be considered as a bond efficiency factor. It can be plotted for the different bar diameters utilized in the finite element models used for developing the Figure 6-23. From Figure 6-25 it can be seen that the bond strength increases at a lower rate compared with the bar yield strength. The lower rate of the bond strength for large bar diameters causes the steel strain gradient within two adjacent cracks to be less pronounced, thus increasing the mean steel strain as it was observed in Figure 6-23.

Indeed, Figure 6-26 is obtained by multiplying the mean steel strains of Figure 6-23 times the bond efficiency factor, κ. It is observed that all the curves except for the most lightly reinforced case (where $\rho_s = \rho_{min}$) follow the same trend. It appears that a simple linear relationship applies for these cases (i.e., for $\rho_s \geq 0.58\%$).

$$\kappa \cdot \varepsilon_{mean} = 2.114 \cdot \varepsilon_{peak} \tag{6-18}$$

In the previous equation, the coefficient of determination, R^2, is 0.9832. Combining Equations (6-16) and (6-17) the following expression can be obtained. A lower bound limit for the $\varepsilon_{mean}/\varepsilon_{peak}$ ratio of 0.60 is adopted as per the *fib* Model Code.

$$0.60 \leq \frac{\varepsilon_{mean}}{\varepsilon_{peak}} = \left(\frac{d_b \cdot f_y}{25.2 \cdot S_{crack} \cdot f_R^{0.8} \cdot \sqrt{f'_c}}\right) \leq 1.0 \tag{6-19}$$

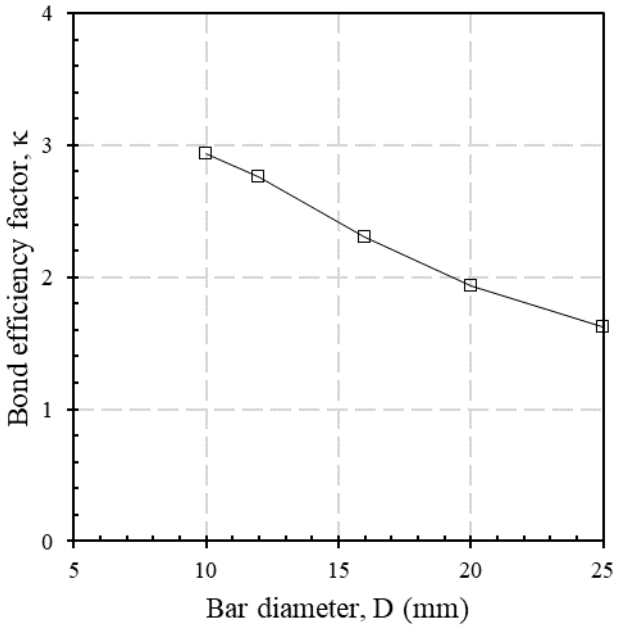

Figure 6-25. Bond efficiency factor, κ.

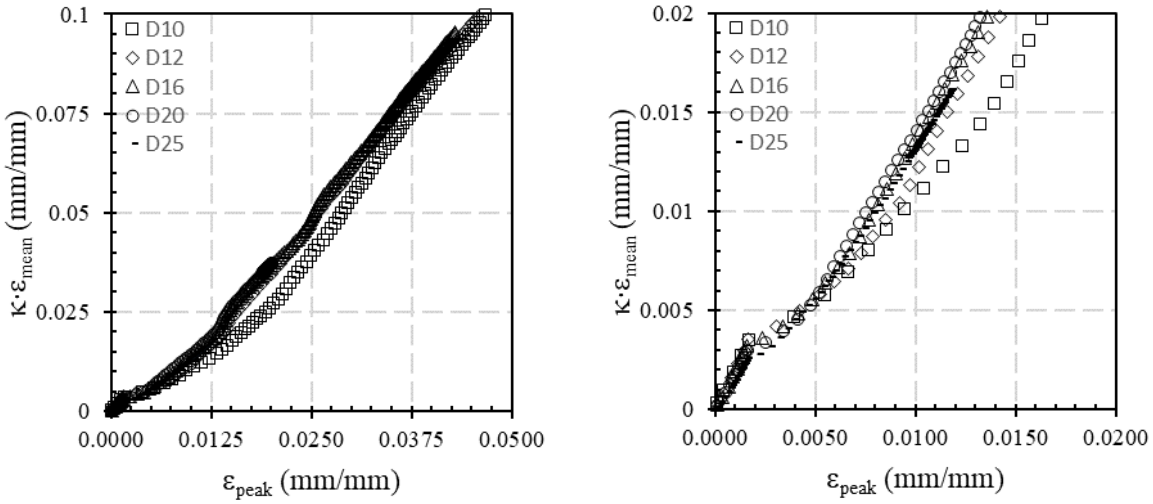

Figure 6-26. Mean steel strain, ε_{mean}, over the crack length multiplied by κ, versus peak steel strain ε_{peak}, for peak steel strains up to 0.05 mm/mm (left), and up to 0.02 mm/mm (right).

For better results, and for beams with minimum longitudinal reinforcement content as per the NZS3101:2006 (i.e., Equation 6-5 of this Chapter), the following equations can be used.

$$\kappa \cdot \varepsilon_{mean} = -324.4 \cdot \varepsilon_{peak}^3 + 37.23 \cdot \varepsilon_{peak}^2 + 1.187 \cdot \varepsilon_{peak} \quad \text{(for } \rho_s \geq 0.58\%\text{)} \tag{6-20}$$

$$\kappa \cdot \varepsilon_{mean} = -219.2 \cdot \varepsilon_{peak}^3 + 32.36 \cdot \varepsilon_{peak}^2 + 1.023 \cdot \varepsilon_{peak} \quad \text{(for } \rho_s = \rho_{min}\text{)} \tag{6-21}$$

In the previous equations, the coefficient of determination, R^2, is 0.9983 and 0.9979, respectively. It is noteworthy that the following conditions must be satisfied.

$$0.60 \leq \frac{\varepsilon_{mean}}{\varepsilon_{peak}} \leq 1.0 \tag{6-22}$$

The above equations were developed for beams with no axial load. Figure 6-27 shows a comparison of the mean strains in a beam reinforced with D16 bars with no axial load and with $P_u/f'_c \cdot A_g = 0.10$. For the majority of the peak steel strains (up to $\varepsilon_{peak} = 0.025$), the difference between the two curves is negligible. Figure 6-28 shows mean strain ratios computed as the mean strains for $P_u/f'_c \cdot A_g = 0.10$ upon mean strains for zero axial load. The minimum and maximum ratios are 0.91 and 1.10, respectively, with an average over the full range of peak strains of 0.984 and standard deviation of 0.052.

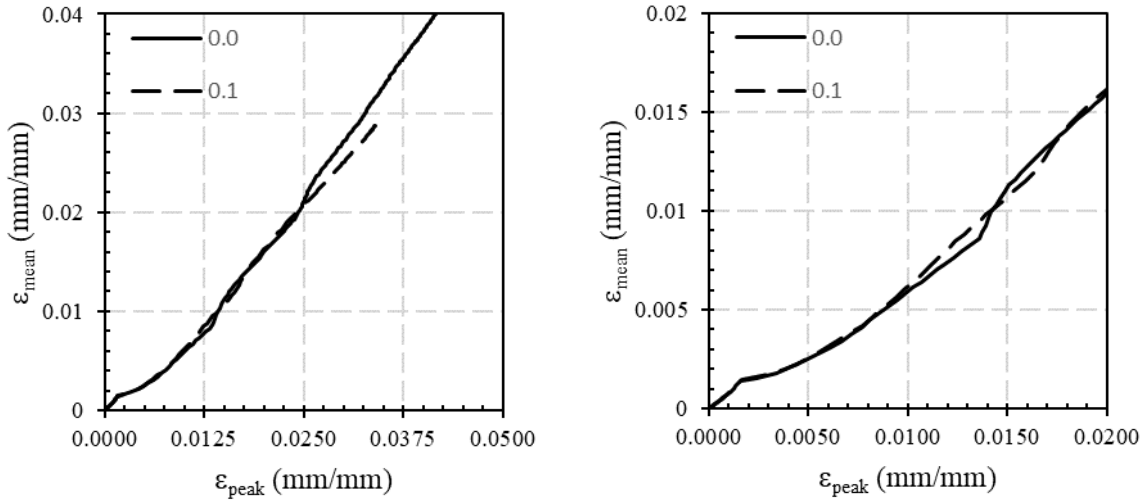

Figure 6-27. Comparison of mean steel strain, ε_{mean}, versus peak steel strain, ε_{peak}, for peak steel strains up to 0.05 mm/mm (left) and up to 0.02 mm/mm (right), for zero axial force and $P_u/(f'_c \cdot A_g)$ = 0.10, with D16 bars.

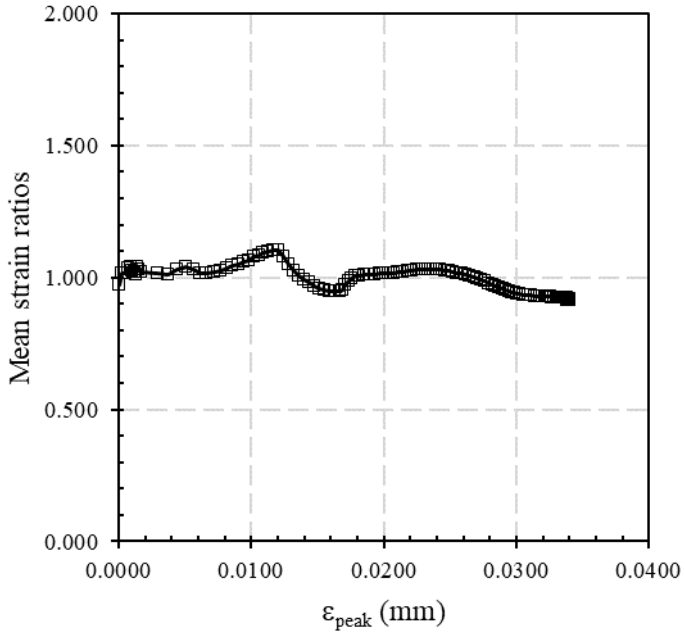

Figure 6-28. Mean strain ratios: Mean strain for $P_u/(f'_c \cdot A_g)$ = 0.10 divided by mean strain for $P_u/(f'_c \cdot A_g)$ = 0.0 ratios.

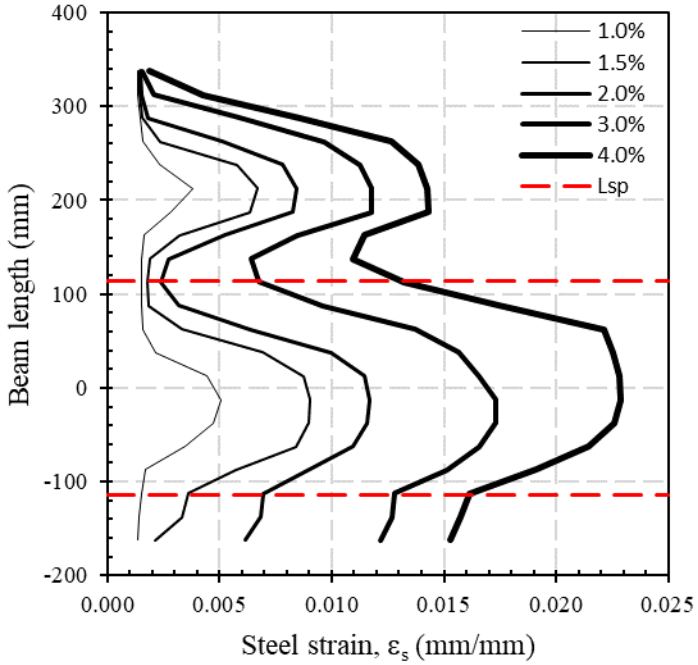

Figure 6-29. Steel strain profiles obtained analytically, within one beam depth and approximately one strain-penetration length, L_{sp}, below the point of maximum moment demand, for a specimen reinforced with D16 bars, with an axial load $P_u/(f'_c \cdot A_g)$ = 0.10.

6.6 Residual crack widths analytical estimation

Once the mean steel strain has been estimated, the maximum crack width, w_{max}, can be obtained with the following equation.

$$w_{max} = S_{crack} \cdot \varepsilon_{mean} \cdot \left(\frac{h - kd}{d - kd}\right) \quad (6\text{-}23)$$

In the previous equation, S_{crack}= crack spacing, which can be assumed or based on observations; ε_{mean}= mean steel strain over S_{crack}, estimated with equations 6-20 and 6-21; h= overall depth of the section; kd= neutral axis depth; h= section depth; and d= effective depth. It seems appropriate to estimate the peak steel strain at the most critical location, ε_{peak}, through section analysis (i.e., moment-curvature). In that way it can be related with the neutral axis depth. The maximum crack widths estimated with equation 6-23 can be converted to residual crack widths using the equation 6-8 to 6-12.

6.7 Conclusions

This chapter presented a numerical parametric study on reinforced concrete beams with the aim to investigate the maximum and residual crack widths. Simple equations were developed in order to relate the maximum and residual crack widths with the steel strain at peak displacement.

Non-linear finite elements simulations were used for that purpose. The numerical model was based on a specimen tested in the laboratory and was validated by comparing the numerical results with the experimental observations. The agreement between the finite element model and the experiment in terms of the force-displacement curves and cracking pattern was remarkable. The main conclusions of the parametric investigation are as follows:

1. The steel strain at the most critical location reduces cyclically due to the cyclic bond deterioration. Therefore, assuming a constant steel strain equal to the strain measured in the first cycle when the bond has not been lost, is a conservative approach.
2. It seems possible to develop a single relationship between residual crack width ratios and steel strain at peak displacement regardless of the amount of longitudinal reinforcement, for flexural dominated members. The relationship appears to be bilinear with a change of slope at about 10 ε_y, for members with zero axial load. The same relationship can be applied in members with shear spans L/d in the order of 8 and more.

3. Beam elongation is able to develop axial loads in beams of up to $0.10 f'_c \cdot A_g$. The axial load tends to reduce the residual crack width ratios. It was observed that axial load ratios $P_u/f'_c \cdot A_g$ of 0.30 are capable of closing the crack completely (because of the re-centring effect of the axial load) regardless the level of strain at peak displacement.
4. The mean steel strain between two adjacent cracks depends on the bar diameter and more precisely, on the bond. A bond efficiency factor estimated as the bond strength between two adjacent cracks divided by the bar yield strength, can be used to normalize the mean steel strain thus allowing for the use of a single curve relating the mean steel strain with the steel strain at peak displacement, for all bar diameters, provided that the member has a longitudinal reinforcement content, ρ_s, of at least 0.58%. A different curve can be used for cases with minimum reinforcement content.
5. At a preliminary investigation stage, the mean steel strain versus steel strain at peak displacements appears not to be affected by axial load ratios $P_u/f'_c \cdot A_g$ of 0.10.

6.8 References

Beeby, A.W. (1971) "Prediction and control of flexural cracking in reinforced concrete members," *ACI Special Publication,* Vol. 20: 55-75.

Borges, J.F. (1966) "Cracking and deformability of reinforced concrete beams," *International Association for Bridge and Structural Engineering*, Vol. 26: 75-95.

Comite Euro-International Du Beton (1993) *CEB-FIP Model Code 1990,* Secretariat Permanent, Lausanne.

Eligehausen, R., Genesio, G., Ozbolt, J., Pampanin, S. (2009) "3D analysis of seismic response of RC beam-column exterior joints before and after retrofit," *Concrete Repair, Rehabilitation and Retrofitting II*, 1141-1147.

Fenwick, R.C., Davidson, B.J., Megget, L.M., (1993) *Significance of elongation on seismic resistance of concrete frame structures*, First Project Report, EQC Project 93/157, University of Auckland, New Zealand.

Gegerly, P., Lutz, L.A. (1968) "Maximum crack width in reindorced flexural members," *ACI Special Publication*, Vol. 20: 87-117.

Hoehler, M.S., Stanton, J.F., (2006) "Simple phenomenonlogical model for reinforcing steel under arbitrary load," *Journal of Structural Engineering*, Vol. 132(7): 1061-1069.

Hognestad, E. (1962) "high strength bars as concrete reinforcement, part 2, control of flexural cracking," *Journal of the Portland Cement Association Research and Development Laboratories,* Vol. 4(1): 46-63.

International Federation for Structural Concrete (2013) *fib model code for concrete structures 2010,* Ernst & John, Germany.

Kaar, P.H., Hognestad, E. (1965) "High strength bars as concrete reinforcement, part 7, control of cracking in T-beam flanges," *Journal of the Portland Cement Association Research and Development Laboratories*, Vol. 7(1): 42-53.

Kam, W.Y., Pampanin, S., Elwood, K. (2011) "Seismic performance of reinforced concrete buildings in the 22 February Christchurch (Lyttelton) Earthquake," *Bulletin of the New Zealand Society for Earthquake Engineering*, Vol. 44 (4): 239-277.

Lettow, S. (2006) *Ein Verbundelement für nichtlineare Finite Elemente Analysen – Anwendung auf Übergreifungsstöße (A bond element for nonlinear finite element analysis – Applied on splices)*, PhD Dissertation, IWB, Universität Stuttgart, Germany (in German).

Mahrenholtz, C (2012) *Seismic bond model for concrete reinforcement and the application to column-to-foundation connections*, PhD thesis, Institut fur Werkstoffe im Bauwesen der Universitat Stuttgart.

Malek, A., Scott, A., Pampanin, S., MacRae, G.A., Hoult, N.A. (2016) "Damage assessment of RC beam using distributed fibre optics strain sensors," *2016 New Zealand Society of Earthquake Engineering Conference*, Christchurch, New Zealand.

Noakowski, P. (1985) *Continuous theory for the determination of crack width under the consideration of bond*, Beton-UND Stahlbetonbau

Ozbolt, J., Bazant, Z. (1996) "Numerical smeared fracture analysis: nonlocal microcrack

interaction approach," *International Journal for Numerical Methods in Engineering*, Vol. 39:

635-661.

Ožbolt J, Yijun L, Kozar I. (2001) "Microplane model for concrete with relaxed kinematic constraint," *International Journal of Solids and Structures*, Vol. 38: 2638-711.

Park, P., Paulay, T. (1975) *Reinforced Concrete Structures*, John Wiley & Sons, New York.

Paulay, T., Priestley, M.J.N. (1992) *Seismic Design of Reinforced Concrete and Masonry Buildings*, Wiley Interscience, USA.

Priestley, M. J. N., Calvi, G. M, Kowalski, M. J. (2007) *Displacement-based seismic design of structures*, IUSS Press, Pavia, Italy.

Priestley, M.J.N., Seible, F., Calvi, G.M. (1996) *Seismic Design and Retrofit of Bridges*, Wiley Interscience, USA.

Restrepo-Posada, J.I. (1992) *Seismic behaviour of connections between precast concrete elements*, PhD Thesis, University of Canterbury, Christchurch, New Zealand.

Sassi, H., Ranous, R. (1996) "Shear failure in reinforced concrete walls," *From Experience*, Structural Engineers Association of Southern California, Whittier, California.

7 ON THE FATIGUE LIFE OF REINFORCING STEEL

7.1 Introduction

Reinforced concrete frames have been widely used as part of the lateral force-resisting system in buildings located in high seismic risk areas. Beam, columns as well as beam-column joints, when properly designed and detailed following capacity design principles developed since the 1960s-1970s, are expected to sustain seismic internal actions during several post-elastic displacement cycles without significant strength and stiffness deterioration, by developing inelastic action and energy dissipation in concentrated regions referred as plastic hinges.
The development of inelastic action in structures with traditional monolithic connections inevitably leads to structural damage, often above what would be considered uneconomical to be repaired as it was observed after the 2010-2011 Canterbury earthquake sequence, where moderate-to-severe beam end hinging was exhibited (Kam et al, 2011).
Despite seismic assessment and rehabilitation guidelines may have been available since the inception of the first formal seismic codes in the first half of the 20th century, they are still mainly focused in mitigating the risk of death or injury from existing earthquake-prone buildings (typically referred as pre-1970s buildings, designed prior to capacity design principles).
Very little (if any) assistance for assessing the residual capacity of damaged modern buildings, has been provided yet. When considering the problem, even though there are other factors that strongly influence the plastic hinge cumulative cyclic behaviour (e.g., bond between steel and concrete, amount of longitudinal reinforcement, strength characteristics of steel and concrete, and strain-rate effects), past research has focused only on the low-cycle fatigue of the longitudinal reinforcement.
This Chapter presents a literature review on fracture of reinforcing steel due to low-cycle fatigue, including recent research using steel manufactured per New Zealand standards.

Experimental results describing the influence of the cyclic effect on the ultimate strain capacity of the steel are discussed, and preliminary equations to account for that effect are also proposed.

7.2 Low-cycle fatigue of reinforcing steel bars: Literature review

7.2.1 Specimens fabricated according to international (non-NZ) standards

As stated by Mander et al (1994), fracture of longitudinal reinforcement due to low-cycle fatigue might be one of the most typical failure modes that can occur in flexural members during an earthquake, especially for structures located in mid-to-high seismic zones when one-to-five fully reversed cycles of large strain equi-amplitudes up to ε_s= 0.06 mm/mm or 6% may be expected.

Despite the importance of this type of failure, in the past there was a lack of research on this topic. The engineering community was more interested in mechanical engineering applications rather than earthquake engineering ones, where the main focus was on specimens tested on low-strain amplitudes (usually less than 0.01 mm/mm or 1%) and high-cycle fatigue regimes (10^3-to-10^7 cycles). Thus, Mander pioneered the work on experimental low-cycle fatigue campaigns for seismic applications, testing ASTM A722 (f_u= 1083 MPa) and A615 grade 40 (f_y= 276 MPa) unmachined bars on constant amplitude cyclic fatigue conditions under a range of seismic (axial) strain amplitudes. The unsupported length of the specimens was six bars diameters, and incipient failure was defined as initiation of a fatigue crack in the test specimen.

The plastic-strain amplitude versus fatigue life relationship proposed by Coffin-Manson (Coffin, 1954; Manson, 1953) was used to fit the data, concluding that a single equation based on plastic strain, ε_p, and number of cycles can be developed to be universally applicable to all reinforcing steels.

$$\varepsilon_p = 0.08 \cdot \left(2 \cdot N_f\right)^{-0.5} \tag{7-1}$$

where N_f = number of cycles to failure.

Later, Kunnath et al (1997) observed that the model of Mander and Cheng (1994) under-predicted the final damage state of all their column specimens tested, attributing this effect to the fact that the Mander model was capable of evaluating the damage due to low-cycle fatigue of longitudinal reinforcement only, while all tested specimens experienced confinement

failure prior to low-cycle fatigue failure. They proposed a new cumulative fatigue model derived from the concrete column as a composite section, indirectly accounting for the cumulated damage due to shear, axial stress and loss of confinement

$$\varepsilon_p = 0.065 \cdot \left(N_f\right)^{-0.436} \tag{7-2}$$

Brown and Kunnath (2004) performed experimental tests to examine the low-cycle fatigue behaviour of standard ASTM A615 grade 60 (f_y= 420 MPa) reinforcing bars ranging from No. 6 (0.750 inches or 19.1 mm) to No. 9 (1.125 inches or 28.6 mm) diameter, aiming at: 1) determining expressions to ensure longitudinal bar fracture failure mode; 2) correlating failure limit states with seismic damage on reinforced concrete members; and 3) for damage prediction and design purposes. They concluded that fatigue life is influenced by the diameter of the bar and the geometry of the rolled-on deformations.

Hawileh et al (2010) evaluated experimentally the low-cycle fatigue behaviour of ASTM 706 and A615 grade 60 (f_y= 420 MPa) for further application in precast hybrid frame (PRESSS) connections, motivated by the fact that during an earthquake, the gap at the beam-to-column interface opens up and can induce high plastic strain levels (up to 6%) at the reinforcing bars, which might cause fracture after less than 10 cycles. They encased the specimens into a steel greased collar to provide lateral support against buckling (a typical detail for unbonded bars in PRESSS connections). The following low-cycle fatigue relationships were proposed for A706 and A615, respectively

$$\varepsilon_p = 0.103 \cdot \left(2 \cdot N_f\right)^{-0.54}, for\ A706\ bars \tag{7-3}$$

$$\varepsilon_p = 0.128 \cdot \left(2 \cdot N_f\right)^{-0.57}, for\ A615\ bars \tag{7-4}$$

They found that the low-cycle fatigue behaviour of A706 and A615 is very similar, even when the A706 exhibits higher ductility levels during monotonic tests. Interestingly enough, the average number of cycles to failure in tests with larger strain ranges were higher for A615 specimens.

Figure 7-1 shows all the plastic-strain, ε_p, to cycles to failure, N_f, relationships previously discussed. As can be seen from the figure, all the curves show a similar trend. It is interesting to note, however, that Kunnath et al (1997) that indirectly accounts for the accumulated

damage due to shear, axial stress and loss of confinement, predicts lower plastic-strain levels for low number of cycles to failure (less than around 10 cycles). On the other hand, larger plastic-strain levels are predicted for high number of cycles to failure.

The investigations on low-cycle fatigue previously discussed have been carried out with specimens manufactured according to ASTM standards, and maybe except for Hawileh et al (2010) where the specimens were encased in steel, buckling of the rebars was always present thus reducing the fatigue life of the rebars when compared with a buckling restrained specimen tested at the same strain amplitude.

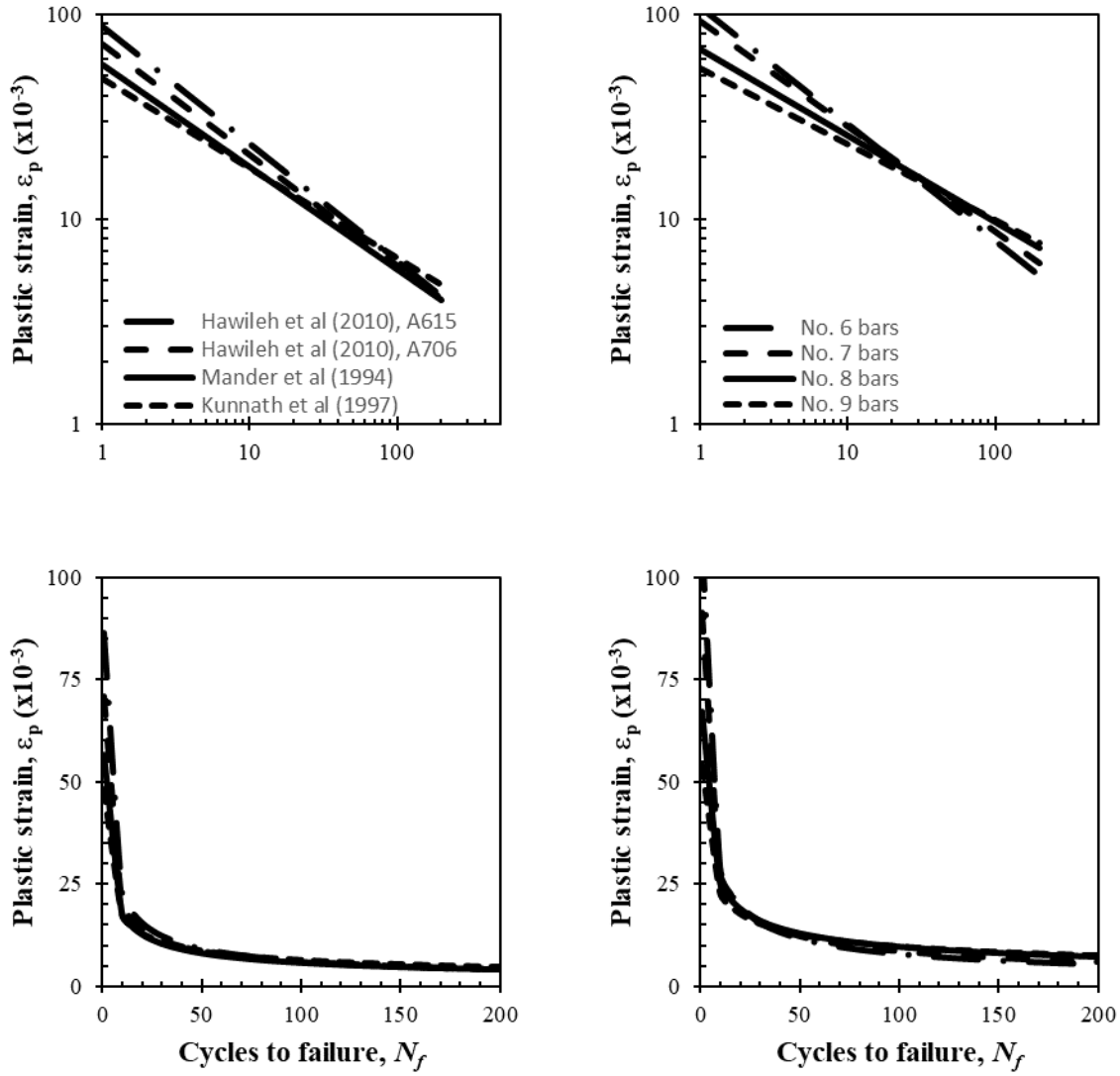

Figure 7-1. Plastic-strain with fatigue life relationships found in the literature, on a logarithmic (top) and arithmetic (bottom) scale. Figures at the right-hand side correspond to Brown and Kunnath (2004).

7.2.2 Specimens fabricated according to New Zealand standards

Loporcaro (2017) performed low-cycle fatigue tests on unmachined D12 bar specimens manufactured with NZ steel Grade 300E (f_y= 300 MPa). Bars 180 mm long were used, with an unsupported length (i.e., clear distance between the grips) of 72 mm or six bar diameters (as suggested by Mander et al, 1994). Monotonic tests were first performed to determine the mechanical properties of the steel (see Table 7-1).

During the monotonic tests the specimens did not show a clear yield point, therefore the yield strength was determined as the strength at which 0.2% plastic deformation occurs (i.e., offset yield point or proof stress).

Table 7-1. Mechanical properties of steel Grade 300E used for low-cycle fatigue tests (Loporcaro, 2012).

Specimen	Yield Strength, f_y (MPa)	Ultimate strength, f_u (MPa)	Ultimate strain, ε_u (mm/mm)
Monotonic-1	330	446	0.186
Monotonic-2	307	442	0.200
Monotonic-3	305	452	0.192

During the low-cycle fatigue tests, the specimens were subjected to fully reversed strain control cyclic loading, using a sinusoidal waveform with zero mean strain. The low-cycle fatigue test results are summarized in Table 7-2.

Table 7-2. Low-cycle fatigue tests input parameters and results (Loporcaro, 2017).

Sample	Strain amplitude (mm/mm)	Plastic strain (mm/mm)	Frequency, f (Hz)	Cycles to failure N_f
01	0.0078	0.0061	0.12	125
02	0.0078	0.0062	0.12	130
03	0.0083	0.0067	0.12	98
04	0.0107	0.0089	0.11	61
05	0.0140	0.0121	0.09	34
06	0.0140	0.0121	0.09	32
07	0.0178	0.0156	0.06	14
08	0.0179	0.0160	0.06	16
09	0.0179	0.0160	0.06	13
10	0.0271	0.0250	0.04	6
11	0.0272	0.0252	0.04	6
12	0.0275	0.0254	0.04	7

Loporcaro observed that during the cyclic loading, the specimens experienced an increase in the stress until they reached a stable hysteresis loop, a phenomenon called "*cycle-dependent hardening*". In line with other researchers, the data was used to calibrate the Coffin-Manson

empirical equations. The following equations were proposed for the total (elastic plus plastic) strain, ε_a, and plastic strain, ε_p, respectively.

$$\varepsilon_a = 0.0025 \cdot \left(2 \cdot N_f\right)^{-0.076} + 0.080 \cdot \left(2 \cdot N_f\right)^{-0.464} \quad (7\text{-}5)$$

$$\varepsilon_p = 0.080 \cdot \left(2 \cdot N_f\right)^{-0.464} \quad (7\text{-}6)$$

The coefficient of determination, R^2, obtained with equation (6-6) is 0.989. As in Section 7.2.1, buckling of the rebars was always present thus reducing the fatigue life of the rebars when compared with a buckling restrained specimen tested at the same strain amplitude.

7.3 Cyclic effect on ultimate (monotonic) strain capacity of steel reinforcement

7.3.1 Introduction

It is interesting to speculate that the cyclic loading on a reinforcing bar affects its strain capacity when compared to monotonic uniaxial loading. In fact, a new reinforcing bar fractures or initiates necking at one-fourth of a cycle (i.e., a monotonic push) with a peak strain equal to the maximum strain at the ultimate tensile stress, ε_{UTS}, obtained through monotonic uniaxial tests. On the other hand, and as previously explained in Section 7.2, if a new reinforcing bar is cyclically strained under equal strain cycles, ε_{cyclic}, it will fracture after N_f cycles. The number of cycles will obviously depend on the strain amplitude, ε_{cyclic}, at which the bar is being cyclically strained, and this strain is smaller than the ε_{UTS} (or at least for cases where $N_f > 1.0$). The above is schematically explained in Figure 7-2.

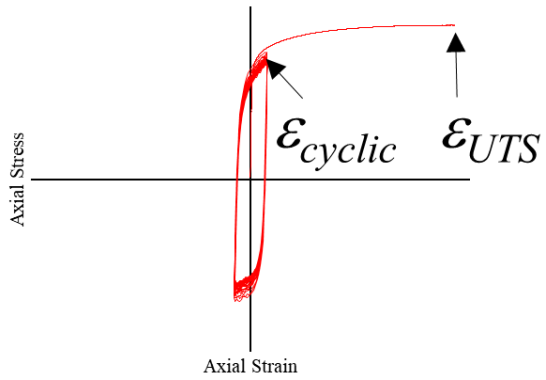

Figure 7-2. Stress-strain curves of uniaxial tests under monotonic and reverse cyclic loading.

Thus, it can be argued that if the bar is cyclically strained during n cycles at ε_{cyclic}, for $n < N_f$ cycles, unloaded and then tested monotonically, it will fracture at a strain ε'_{UTS}, where $\varepsilon_{cyclic} \leq \varepsilon'_{UTS} < \varepsilon_{UTS}$.

Research on the cyclic effect on the ultimate (monotonic) strain capacity of steel as previously discussed, is scarce. Probably the only and most notable is the work by Dowling (1977). This work is discussed in this Section. Experimental results describing the influence of the cyclic effect on the ultimate strain capacity of the steel are also discussed, and preliminary equations to account for that effect are proposed.

7.3.2 Cyclic effect on ultimate strain capacity of steel reinforcement: Literature review

Dowling (1977) performed an experimental study of crack growth in smooth specimens subjected to axial cyclic plastic deformation. The specimens were fabricated using A533B (f_y= 480 MPa and f_u= 625 MPa). Figure 7-3 shows the cyclic stress-strain curves and low-cycle fatigue data obtained with specimens fabricated with this material. The tests were performed on threaded-end specimens with reduced diameter as per the ASTM E 606-77T, under constant-amplitude deflection using a fully reversed sinusoidal waveform. Buckling of the specimens was prevented at all times.

Pairs of tests were performed under identical load control, one of them intended to measure strains, and the other one to monitor the crack growth. Dowling observed that this test setup, the constant amplitude deflection loading resulted in strain amplitudes in the specimen approximately constant during most of the fatigue life.

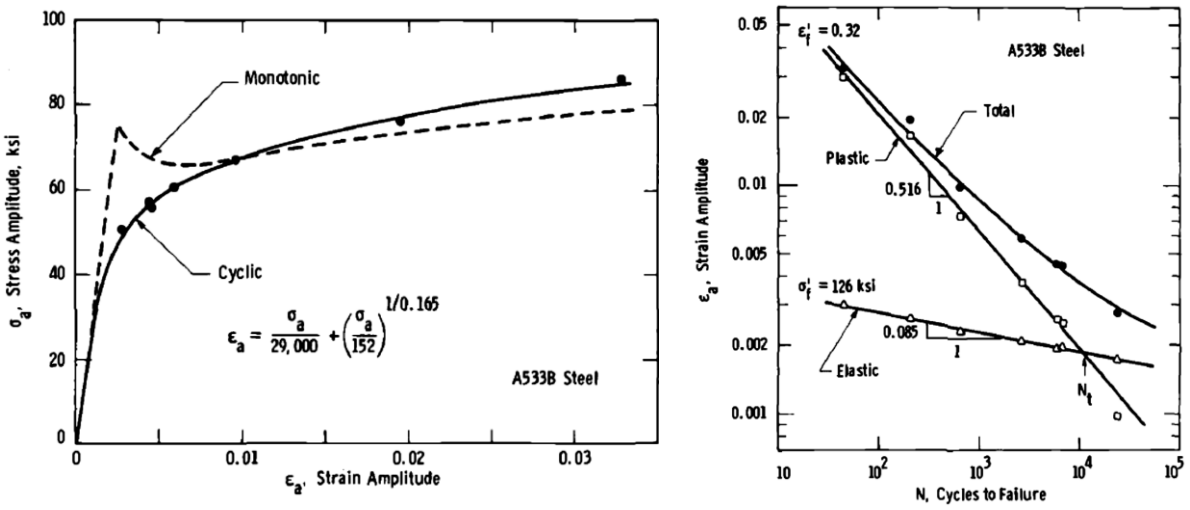

Figure 7-3. Cyclic and monotonic stress-strain curves (left), and low-cycle fatigue properties (right) (Dowling, 1977).

Figure 7-4 shows crack lengths versus the fatigue life measured during the tests, and Figure 7-5 shows strain versus life data for initiation cracks of 0.003 in (0.076 mm), 0.01 in (0.25 mm), and at failure. It was observed that cracks 0.003 in wide formed at about one-tenth of the total life of the specimens, whilst cracks 0.01 in wide formed at about one-half of their total life. Cracks are not reported for fractions of fatigue life, n/N_f, less than 10%. As it can be seen from Figure 7-4, there is no clear trend between the surface crack length and fatigue life with the strain level applied in the specimens. Also, the curves in Figure 7-5 are reasonably parallel. Based on the above, Dowling concluded that "*the fraction of life corresponding to any given crack size was independent of life over the range investigated*".

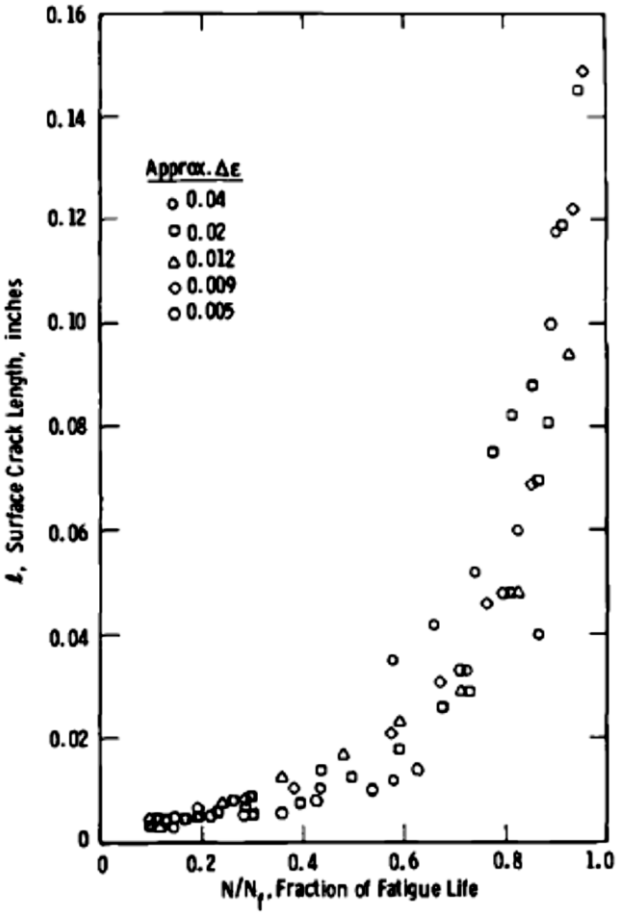

Figure 7-4. Length of largest crack present versus fraction of fatigue life (Dowling, 1977).

Dowling highlighted the fact that the size of the specimen affects the results. He stated that "*if different size specimens of identical material are tested, the larger specimens should tend to have longer fatigue lives due to the increased number of cycles required to propagate a crack across the specimen*".

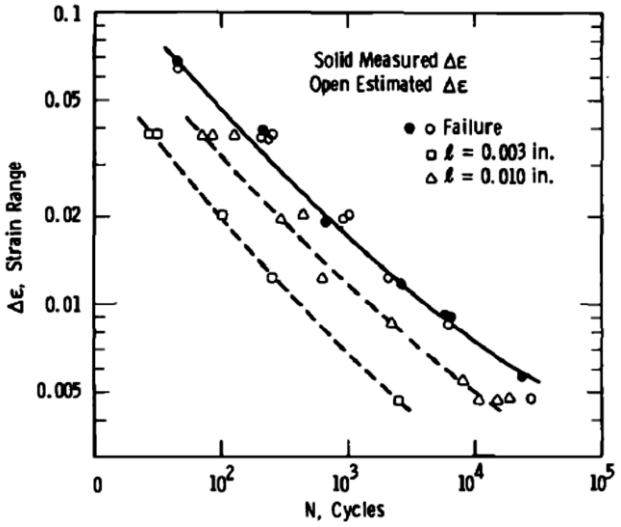

Figure 7-5. Strain versus life data for initiation of small cracks and for failure (Dowling, 1977).

However, he also emphasized that the size effect on the fatigue life is very complex. He stated that "*weakest-link statistical-type size effects have long been recognized…In this case, a larger size is expected to have an increased probability of a weak region or flaw of a given severity being present, and hence a lowered average fatigue strength"*. Although somewhat inconclusive, this could be the reason why Brown and Kunnath (2004) found that fatigue lives are influenced by the bar diameter as described in Section 7.2.1.

7.3.3 Cyclic reduction of ultimate strain in New Zealand Grade 300 steel

As speculated in Section 7.3.1, if a reinforcing bar is cyclically strained during n cycles at ε_{cyclic} for $n < N_f$ cycles, unloaded and then tested monotonically, it will fracture at a strain ε'_{UTS}, where $\varepsilon_{cyclic} \leq \varepsilon'_{UTS} < \varepsilon_{UTS}$.

The reduction of the monotonic ultimate strain after a fraction of the fatigue life of the bar has been exhausted appears to be in line with the results reported by Dowling (1977). In particular, it can be demonstrated that the greater the surface crack lengths (which increases with the fraction of fatigue life, n/N_f, as shown in Figure 7-4), the greater the reduction in the post-cyclic monotonic strain at which the bar fractures (because the length of the cracks reduces the effective net tensile area of the bar).

As part of a wider experimental campaign, tests on a limited number of samples were performed in order to validate the above. These tests are described in the following.

7.3.3.1 Experimental Campaign

As described in Section 7.2.2, in order to determine the number of cycles, N_f, required to fracture the bar, Loporcaro (2017) performed low-cycle fatigue tests on twelve specimens made with New Zealand steel Grade 300E.

As a continuation of the low-cycle fatigue study performed by Loporcaro (2017), twelve additional specimens where subsequently cyclically strained at several equi-amplitude strain levels, for two different fractions of their fatigue lives (six specimens were cyclically strained up to n/N_f = 33%, and six up to n/N_f = 66%), unloaded and tested monotonically up to failure in their un-age condition. The strain at the ultimate tensile stress was recorded at each of the tests. The specimens consisted of D12 unmachined bars Grade 300E, 180 mm long. Similar to Loporaro (2017), the clear distance between grips was approximately 72 mm, resembling a stirrup spacing of six bar diameters (i.e., the typical spacing for ductile plastic hinges as per the NZS3101:2006).

As described by Loporcaro (2017), stability problems in the MTS as well as inaccuracies in the strain measurements due to bar buckling forced to the implementation of an indirect method so that strain-controlled fatigue tests could be performed. For that purpose, an external rigid device was fixed to the MTS machine (see Figure 7-6).

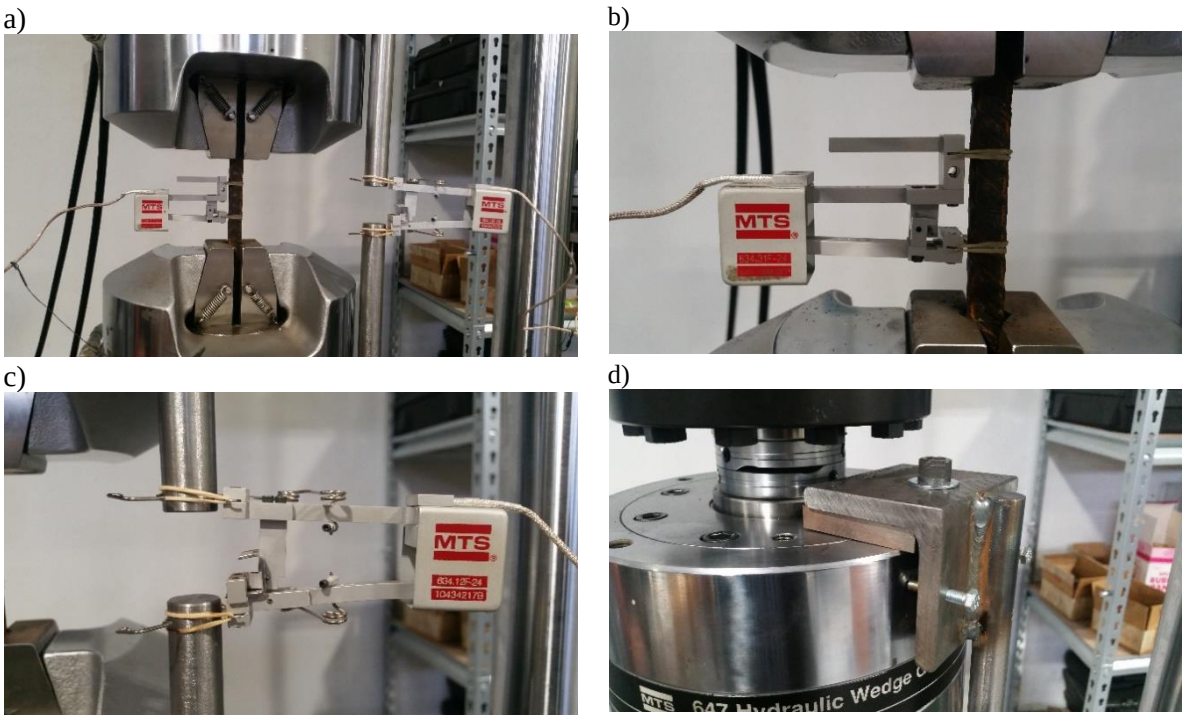

Figure 7-6. (a) Test setup adopted during the calibration process; setup of extensometer in the bar (b); (c) setup of extensometer in external device; (d) fixing of the external device to the MTS machine.

Two extensometers were initially installed to allow for a calibration process; one 25 mm gauge length extensometer was installed in the bar specimen (internal extensometer), and another one in the external device (external extensometer). The readings in the external extensometer were calibrated with the readings in the internal extensometer during monotonic tensile tests (see Loporcaro, 2017, for a detailed explanation of the calibration process). After the calibration, the external extensometer was used to perform the tests in the specimens without the need of the internal extensometer, thus avoiding stability problems and inaccuracies in the readings due to bar buckling (see Figure 7-7).

Figure 7-7. Test setup adopted for the cyclic and monotonic tests after the calibration process.

Maximum cyclic strain amplitudes of only 3% (0.03 mm/mm) were possible due to extensometer limitations. Although other researchers (e.g., Mander et al, 1994) applied equi-amplitude cyclic strains at constant frequencies typical of earthquakes, in this case the cyclic tests were performed at a frequency, f_{cyclic}, low enough as to avoid heating of the sample product of plastic strain energy dissipation.

$$f_{cyclic} = \frac{8x10^{-4}}{\varepsilon_p} \tag{7-7}$$

In the previous equation, εp is the plastic strain applied to the sample.

7.3.3.2 Experimental Results

One interesting feature of the test results is the bar failure mechanism. While some bars developed fracture at one single location, some others fractured at two locations (due to bar buckling). On the other hand, some bars did not fracture but experienced necking. The above is shown in Figure 7-8.

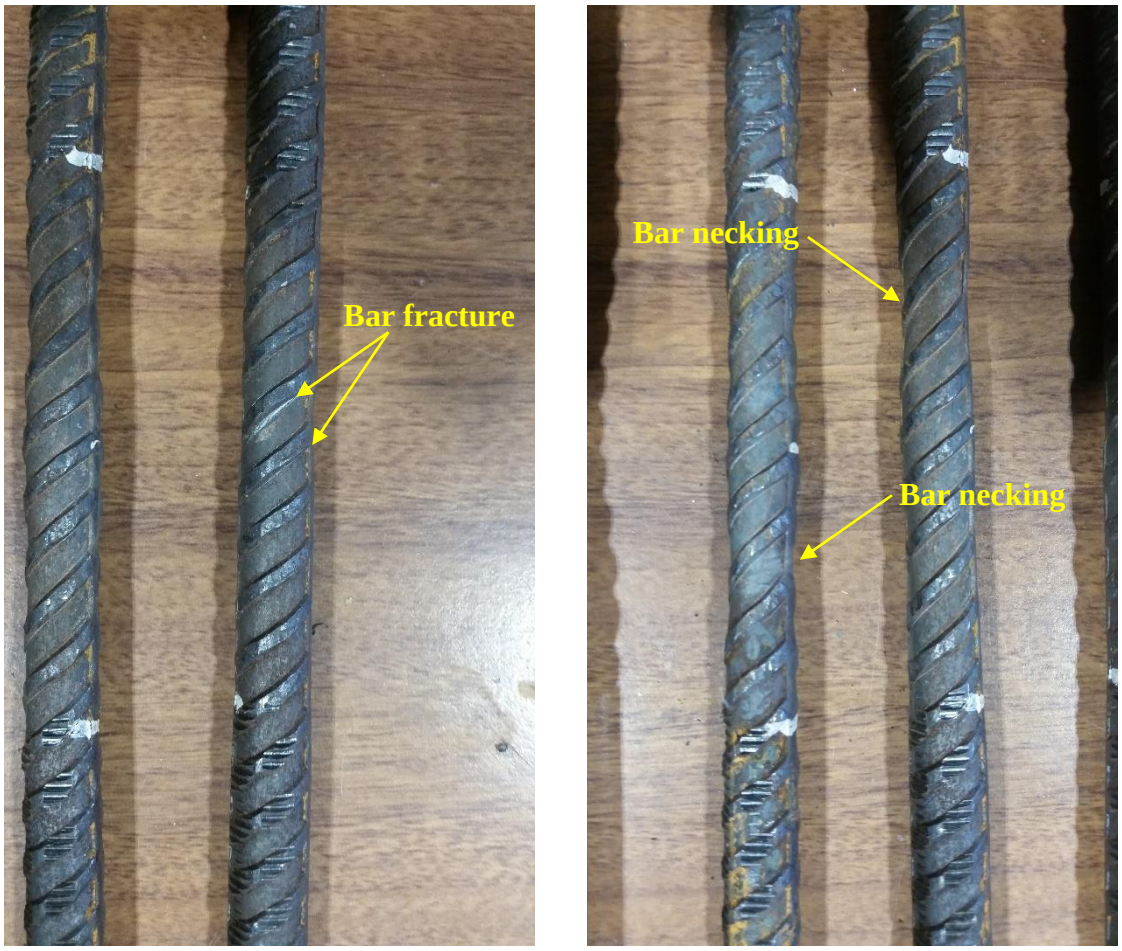

Figure 7-8. Bar specimens that experienced fracture at two locations adjacent to the rib (left); and bar specimens that experienced necking during the post-cyclic monotonic loading face.

Table 7-3 shows the ε'_{UTS} obtained monotonically after the specimens were pre-loaded cyclically. It can be observed that at each fraction of fatigue life investigated, there is not a clear trend between the ultimate monotonic steel strains with the strain level at which the specimens were pre-loaded cyclically. The similarity of this behaviour to that explained by Dowling (1976) in terms of surface crack sizes is apparent. Nevertheless, the reduction in the ultimate monotonic steel strain ε'_{UTS} due to cyclic loading is evident. In particular, the ultimate monotonic steel strain ε_{UTS} obtained with a new (not pre-loaded) bar is approximately

0.20 mm/mm (see Section 7.2.2). At a fatigue life of n/N_f = 33%, the average ε'_{UTS} is 0.1557 mm/mm or 78% of ε_{UTS} (with a standard deviation of 0.010), whilst at n/N_f = 66%, the average ε'_{UTS} is 0.1323 mm/mm or 66% of ε_{UTS} (with a standard deviation of 0.022).

Table 7-3. Monotonic ultimate strains for specimens pre-loaded cyclically at fractions of fatigue life of 33% and 66%. The specimens were fabricated using New Zealand Grade 300 bars.

Sample	Strain amplitude, ε_{cyclic}		N_f	n/N_f = 33%		n/N_f = 66%	
-	***Peak***	***Plastic***	-	***UTS***	ε'_{UTS}	***UTS***	ε'_{UTS}
1-2	0.0078	0.0062	125	422	0.1688	401	0.0931
1-1	0.0083	0.0067	98	427	0.1525	427	0.1404
1.3-1	0.0107	0.0089	61	434	0.1415	423	0.1419
1.5-1	0.0140	0.0121	32	435	0.1592	429	0.1498
2-1	0.0179	0.0160	16	428	0.1567	429	0.1363
3-1	0.0275	0.0254	7	425	0.1120	434	0.1670

The standard deviation is greater for n/N_f = 66% due to a low result obtained in the sample 1-2. Specimens 3-1 were not used because the bar at n/N_f = 66% developed double necking, and it was considered that the ultimate strain measurement was erroneous. Assuming a linear relationship between the ultimate strain and n/N_f, for n/N_f between 0 and 66%, the following equation was calibrated (solid line in Figure 7-9) for cases where buckling occurs.

$$\varepsilon_u = -0.109 \cdot \left(\frac{n}{N_f}\right) + 0.20, for\ unaged\ samples \tag{7-8}$$

In the previous equation, the coefficient of determination, R^2, is 0.9633. At a fatigue life n/N_f = 10%, the average $\varepsilon_{u,cyclic}$ is estimated to be 0.187 mm/mm or 94% of ε_{UTS}. On the other hand, assuming that the observations of Dowling (1976) applies for all types of steel, if buckling of the rebar does not occur, then at n/N_f = 10%, the average $\varepsilon_{u,cyclic}$ would be about 0.20 mm/mm (ie, equal to ε_{UTS} obtained monotonically).

As explained in Section 7.2, if a new reinforcing bar is cyclically strained under equal strain cycles, ε_{cyclic}, it will fracture after N_f cycles. Assuming that the ultimate monotonic steel strain ε'_{UTS} of the specimen when n/N_f approaches to 1.0 is equal to the cyclic strain amplitude applied, ε_{cyclic}, the set of curves shown in Figure 7-10 can be derived. These simple linear representations, although preliminary, allow relate the reduction in the monotonic steel strain at different levels of cyclic strain amplitudes.

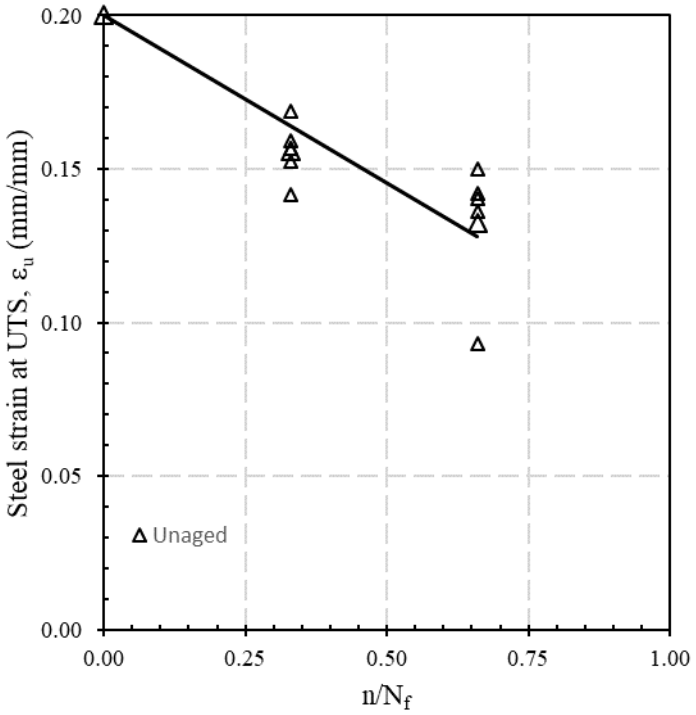

Figure 7-9. Reduction of the ultimate strain capacity in unaged samples due to the cyclic effect, obtained with experimental tests with rebar specimens that experienced buckling.

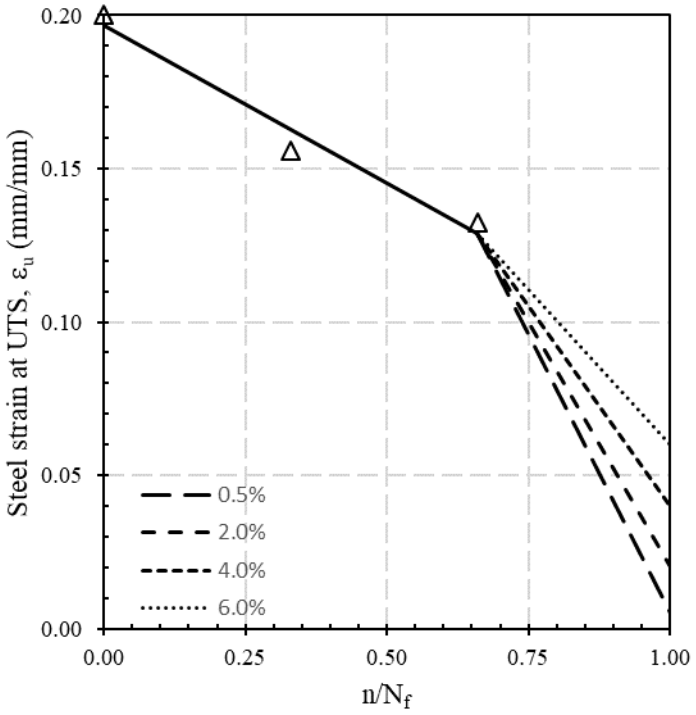

Figure 7-10. Preliminary proposed curves to account for the reduction of the ultimate strain capacity in unaged samples due to the cyclic effect. The solid line applies to all levels of cyclic strain during the pre-loading phase. The triangles represent the average strain values at n/N_f of 0%, 33% and 66%, respectively.

7.4 Conclusions

This chapter presented a literature review on fracture of reinforcing steel due to low-cycle fatigue, including recent research using steel manufactured per New Zealand standards. Experimental results describing the influence of the cyclic effect on the ultimate strain capacity of the steel were also discussed, and preliminary equations to account for that effect were proposed.

The main conclusions of the literature review and experimental investigation are as follow:

1. Fatigue life empirical equations relating the elastic and plastic cyclic strain with the number of fully reversed cycles to failure have been proposed by several researchers over the years. It appears that fatigue life is influenced by the diameter of the bar and the geometry of the rolled-on deformations.
2. Except for one research where the specimens were encased in steel thus preventing buckling, buckling of the rebars was always present. It is very well known that buckling reduces the fatigue life of the specimen when compared with a buckling restrained specimen tested at the same strain amplitude.
3. Previous research looking at the crack growth in smooth specimens fabricated using A533B (f_y of 480 MPa and f_u of 625 MPa) subjected to axial cyclic plastic deformation, where buckling of the specimens was prevented at all times, indicates that cracks in the specimens initiates at fractions of fatigue life, n/N_f, equal to or greater than 10%. It also indicates that there is no clear trend between the surface crack length and fatigue life with the strain level applied in the specimens.
4. Experimental results indicated that the cyclic loading on a reinforcing bar affects its strain capacity due to monotonic uniaxial loading. If buckling is not prevented, the reduction of the strain at the ultimate tensile strength due to cyclic loading, ε'_{UTS}, for n/N_f of 10%, 33%, and 66% is estimated to be 6%, 22%, and 34% of the ε_{UTS} obtained with a virgin sample.
5. At each fraction of fatigue life investigated, there was not a clear trend between the ε'_{UTS} with the strain level at which the specimens were pre-loaded cyclically.
6. An empirical equation and a series of curves have been proposed, which, if properly calibrated, can be used to estimate the reduction of the ultimate strain capacity in unaged steel reinforcing bar samples due to the cyclic effect. A more comprehensive experimental campaign, including buckling restrained tests, is required for such calibration.

7.5 References

Brown, J., Kunnath, S.K. (2004) "Low-cycle fatigue failure of reinforcing steel bars," *ACI Materials Journal,* Vol. 101(6): 457-466.

Coffin, L.F.Jr. (1954) "A study of the effects of cyclic thermal stresses on a ductile metal," *Transactions of the American Society of Mechanical Engineers,* New York, N. Y., Vol. 76: 931-950.

Dowling, N.E. (1977) "Crack growth during low-cycle fatigue of smooth axial specimens," *Cyclic Stress-Strain Aspects of Fatigue Crack Growth, ASTM STP 637,* American Society for Testing and Materials, 97-121.

El-Bahy, A., Kunnath, S.K, Stone, W.C., Taylor, A.W. (1999) "Cumulative seismic damage of circular bridge columns: benchmark and low-cycle fatigue tests," *ACI Structural Journal,* Vol. 96(4): 633-641.

Hawileh, R., Rahman, A., Tabatabai, H. (2010) "Evaluation of the low-cycle fatigue life in ASTM A706 and A615 grade 60 steel reinforcing bars," *Journal of Materials in Civil Engineering,* Vol. 22: 65-76.

Kam, W. Y., Pampanin, S., Elwood, K. (2011) "Seismic performance of reinforced concrete buildings in the 22 February Christchurch (Lyttelton) Earthquake," *Bulletin of the New Zealand Society for Earthquake Engineering,* Vol. 44(4): 239-278.

Kunnath, S.K., El-Bahy, A., Taylor, A.W., Stone, W.C. (1997) *Cumulative seismic damage of reinforced concrete bridge piers,* National Institute of Standards and Technology, NISTIR 6075.

Loporcaro, G. (2017) *A least invasive method to estimate the residual strain capacity of steel reinforcement in earthquake-damaged buildings,* (Doctoral thesis embargoed until 9 October 2019), University of Canterbury, Christchurch, New Zealand.

Mander, J.B., Panthaki, F.D., Kasalanati, A. (1994) "Low-cycle fatigue behaviour of reinforcing steel," *Journal of Materials in Civil Engineering,* Vol. 6(4): 453-468.

Manson, S. S., Halford, G. R. (1981) *"*Practical implementation of the double linear damage rule and damage curve approach for treating cumulative fatigue damage*," International Journal of Fracture,* Vol. 17(2): 169-192.

Miner, M.A. (1945) "Cumulative Damage in Fatigue," *Journal of Applied Mechanics,* Vol. 12(1): A-159.

8 ASSESSING THE RESIDUAL CAPACITY OF REINFORCED CONCRETE FRAMES

8.1 Introduction

Current seismic assessment and rehabilitation guidelines are mainly focused on the evaluation of pre-damaged existing buildings. Very little information is instead available for assessing the residual capacity of damaged buildings, even when considering relatively modern structures designed according to capacity design principles and thus relying upon the development of plastic hinges in the beams. When available, although they account for the damaged state of the elements (Polese et al, 2012; FEMA 306) or residual crack widths (Maeda et al., 2012), provide an incomplete assessment from a fatigue life standpoint.
The latter is particularly important for assessing the ability of a standing building to resist aftershocks once a big portion of their initial capacity has been consumed during the mainshock, and thus support the complex decision-making process of how and whether or not to make safe (i.e., repair and/or retrofit) or demolish.
One of the most controversial issues highlighted by the 2010-2011 Canterbury earthquake sequence is the complexity and lack of knowledge and guidelines for an adequate evaluation of the reduced capacity of a damaged building when compared to its pre-earthquake condition. As a more important corollary, the absolute term of the post-earthquake capacity, referred to as residual capacity is of critical importance to: a) determine the new vulnerability of the building; and b) evaluate its capacity to sustain subsequent aftershocks and/or other design level event during the remaining life-time of the building. In turns this would allow the evaluation of the new seismic risk of the building and suggest appropriate performance-based repairing/strengthening strategies. Arguably, partly but not exclusively as a result of such lack of knowledge and guidelines on the evaluation of the residual capacity and on the selection of

appropriate repairing techniques, many modern buildings, in a number somehow exceeding common expectation, have ended up being demolished.

As described in Chapter 7, when considering residual capacity within the context of fatigue life, past research has been done on low-cycle fatigue of the longitudinal reinforcement only. Nevertheless, there are other factors such as bond between steel and concrete, amount of longitudinal reinforcement, strength characteristics of steel and concrete, as well as strain-rate effects that strongly influences the plastic hinge cumulative cyclic behaviour and therefore, its residual capacity. In addition, when looking at the member level, research on low-cycle fatigue seems to have been focused mainly on bridge columns (Mander and Cheng, 1999; El-Bahy et al, 1999).

This Chapter presents a review of the current know-how on seismic residual capacity, describes the various factors affecting the residual fatigue life at a component level (i.e., plastic hinge), and how they can be quantified and incorporated into a full displacement-based seismic assessment procedure.

8.2 Residual capacity: Current practice

8.2.1 Bridges

Mander and Cheng (1999) investigated the low cycle fatigue failure as part of a study on replaceable (i.e., specially-detailed reinforcing fuse-bars) plastic hinges in bridge columns. They stated that failure in a concrete bridge column might be due to either: 1) fatigue of the longitudinal reinforcing steel; 2) failure of the concrete due to lack of confinement or fracture of the transverse reinforcement; and/or 3) compression buckling of the longitudinal reinforcement. Since potential plastic hinge zones are properly designed and detailed with adequate transverse reinforcement, they assumed the fatigue of the steel was the main failure mode, supporting the need of replaceable plastic hinges as an alternative repairing technique. Based on the dependable plastic strain and fatigue life relationship proposed by Mander et al (1994) assuming a linear strain profile across the concrete column, they obtained the following plastic curvature and fatigue life relationship.

$$\theta_p \cdot D = \frac{0.113}{1 - 2 \cdot d'/D} \cdot \left(N_f\right)^{-0.5} \tag{8-1}$$

where $\phi_p D$ = dimensionless plastic curvature amplitude; *d'* = depth from the outermost concrete fibre to the centre of reinforcement; *D* = overall column diameter. The plastic curvature experimentally determined is estimated as

$$\emptyset_p \cdot D = \frac{\theta_p}{L_p/D} \tag{8-2}$$

where $\theta_p = \theta_u - \theta_y$ (maximum experimentally observed drift minus experimentally observed yield drift); L_p = equivalent plastic hinge length (value typically assumed by the engineer based on literature).

In order to apply the theoretical model to a variable amplitude displacement history, they combined a dependable total strain and fatigue life relationship (Mander et al, 1994) with the well-known Miner's rule (Miner, 1945)

$$N_{f,eff} = \sum_i \left(\frac{\theta_{ui}}{\theta_{eff}}\right)^3 \tag{8-3}$$

where $N_{f,eff}$ = effective number of cycles at a constant drift amplitude, θ_{eff}.

Column specimens were tested under constant and variable drift amplitude. They observed that, except for one specimen, low-cycle fatigue of the longitudinal reinforcement was the dominant failure mode. The predicted number of cycles were compared with the experimentally observed effective number of cycles at first fatigue crack, finding the theoretical prediction a little conservative, especially for high-cycle fatigue (i.e., $N_f \sim 100$ or more), attributed to the conservatism in the assessment of the effective plastic hinge length.

Later, El-Bahy et al (1999) investigated the cumulative damage in reinforced concrete circular bridge columns, aiming at determining their low cycle fatigue characteristics while addressing issues related to damageability and reserve capacity. The investigation was based on the premise that structural damage is related to the fatigue behaviour of concrete and steel.

They observed three failure modes: 1) global buckling of the longitudinal bars; 2) confinement failure following the rupture of the confining spirals; and 3) low-cycle fatigue of the longitudinal reinforcement. Only flexural failure members were considered in this study, and based on the results of constant amplitude tests, they developed the following drift-based

fatigue-life expression for damaged-based seismic design of circular flexural dominated bridge columns.

$$\delta = 10.6 \cdot \left(N_f\right)^{-0.285} \tag{8-4}$$

where δ = lateral drift, in percent.

8.2.2 Fema 306

FEMA 306 proposed a quantitative procedure to assess earthquake damaged reinforced concrete and masonry wall buildings. It applies nonlinear static techniques to estimate the performance of the building in future events in both its pre-event and damaged states. The method has been used to investigate the effectiveness of potential performance restoration measures (i.e., it is performance based).

The basic steps involve: 1) formulation of a capacity curve (with undamaged properties); 2) estimation of the displacement capacity, d_c, for a given performance level; 3) estimation of the hypothetical displacement demand, d_d ; 4) modification of the component force-deformation relationships required to reformulate the capacity curve and repetition of 2) and 3) to determine d'_c and d'_d (see Figure 8-1).

Structural performance levels and damage are defined for each element (see Table 8-1), and the user is referred to FEMA 273[1] to determine the displacement (pre-event) capacities at the component level. For the damaged component, modification factors are proposed depending on the behaviour mode and the severity of damage (e.g., Figure 8-2 and Figure 8-3), or alternatively they can be obtained by laboratory testing.

8.2.3 Polese et al (2013)

Polese et al (2013) proposed a method to assess the residual capacity of non-confirming reinforced concrete columns typical of the Mediterranean region. A database of 36 cyclic tests, 23 with deformed bars and 13 with round bars were used for the calibration of the method. The specimens consisted of rectangular columns with constant normalized axial load $\nu = \frac{N}{A_c f_{cm}}$ of 0.5, "nonconforming" confinement (i.e., stirrups spacing $s > {}^{d}/_{3}$), and either flexural or combined flexure-shear failure modes.

[1]The document FEMA 273 has been superseded by the ASCE 41-17.

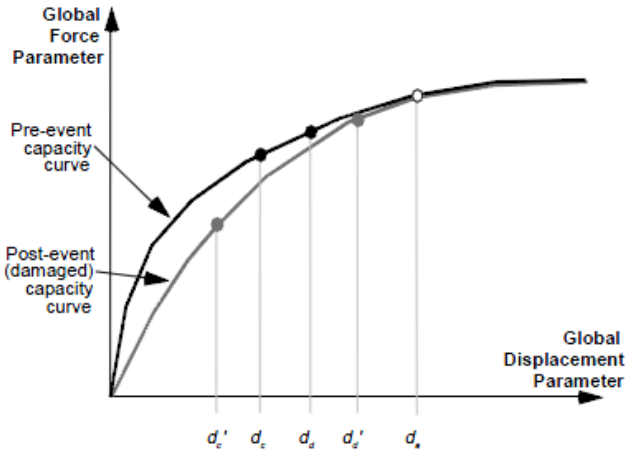

d_e = Estimate of maximum global displacement caused by damaging earthquake

d_c = Global displacement capacity for pre-event structure for specified performance level

d_c' = Global displacement capacity for damaged structure for specified performance level

d_d = Global displacement demand for pre-event structure for specified seismic hazard

d_d' = Global displacement demand for damaged structure for specified seismic hazard

Figure 8-1. Displacement parameters for damage evaluation (FEMA 306).

Table 8-1. Structural Performance levels and Damage – vertical elements (FEMA 306).

Elements	Type	Structural Performance Levels		
		Collapse Prevention S-5	**Life Safety S-3**	**Immediate Occupancy S-1**
Concrete Frames	Primary	Extensive cracking and hinge formation in ductile elements. Limited cracking and/or splice failure in some nonductile columns. Severe damage in short columns.	Extensive damage to beams. Spalling of cover and shear cracking (< 1/8" width) for ductile columns. Minor spalling in nonductile columns. Joint cracks < 1/8" wide.	Minor hairline cracking. Limited yielding possible at a few locations. No crushing (strains below 0.003).
	Secondary	Extensive spalling in columns (limited shortening) and beams. Severe joint damage. Some reinforcing buckled.	Extensive cracking and hinge formation in ductile elements. Limited cracking and/or splice failure in some nonductile columns. Severe damage in short columns.	Minor spalling in a few places in ductile columns and beams. Flexural cracking in beams and columns. Shear cracking in joints < 1/16" width.
	Drift[2]	4% transient or permanent	2% transient; 1% permanent	1% transient; negligible permanent

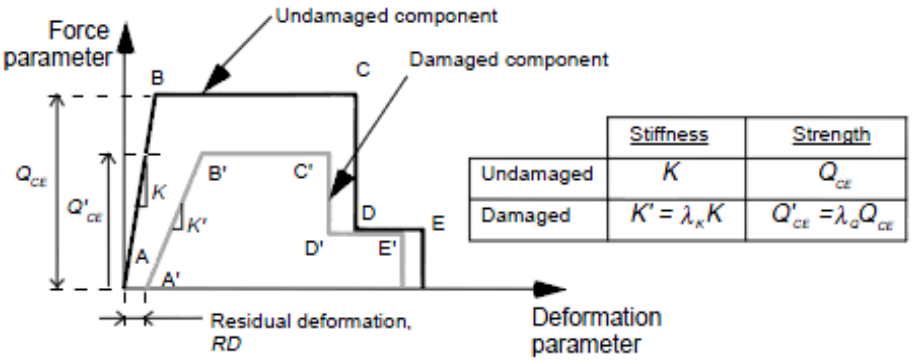

Figure 8-2. Component modelling criteria (FEMA 306).

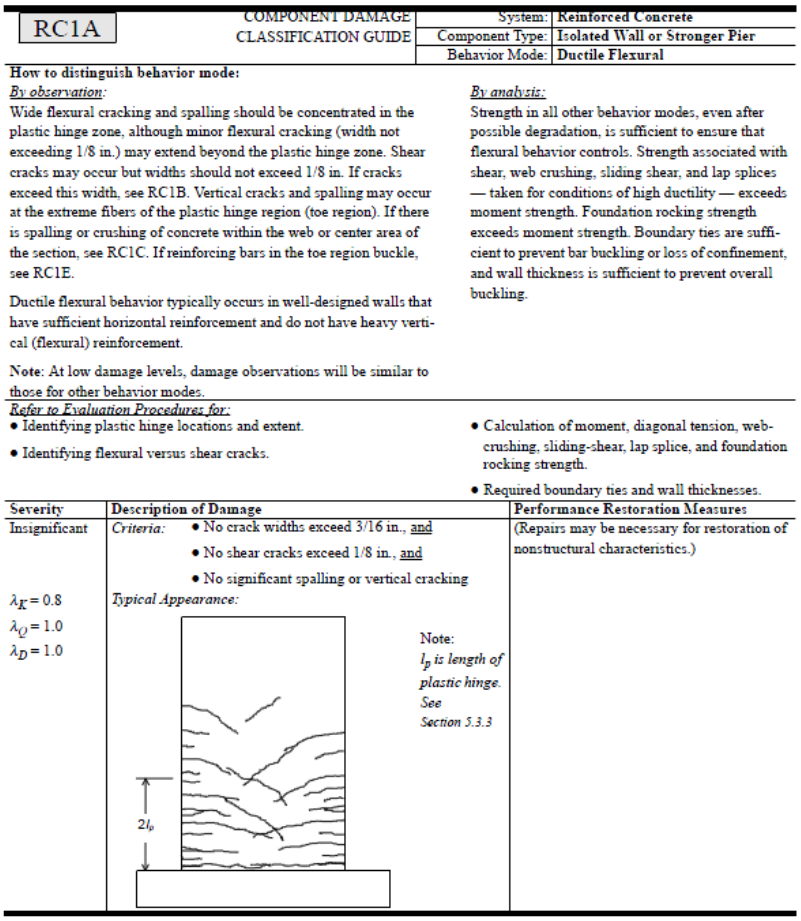

RC1A — COMPONENT DAMAGE CLASSIFICATION GUIDE

System:	Reinforced Concrete
Component Type:	Isolated Wall or Stronger Pier
Behavior Mode:	Ductile Flexural

How to distinguish behavior mode:

By observation:

Wide flexural cracking and spalling should be concentrated in the plastic hinge zone, although minor flexural cracking (width not exceeding 1/8 in.) may extend beyond the plastic hinge zone. Shear cracks may occur but widths should not exceed 1/8 in. If cracks exceed this width, see RC1B. Vertical cracks and spalling may occur at the extreme fibers of the plastic hinge region (toe region). If there is spalling or crushing of concrete within the web or center area of the section, see RC1C. If reinforcing bars in the toe region buckle, see RC1E.

Ductile flexural behavior typically occurs in well-designed walls that have sufficient horizontal reinforcement and do not have heavy vertical (flexural) reinforcement.

Note: At low damage levels, damage observations will be similar to those for other behavior modes.

By analysis:

Strength in all other behavior modes, even after possible degradation, is sufficient to ensure that flexural behavior controls. Strength associated with shear, web crushing, sliding shear, and lap splices — taken for conditions of high ductility — exceeds moment strength. Foundation rocking strength exceeds moment strength. Boundary ties are sufficient to prevent bar buckling or loss of confinement, and wall thickness is sufficient to prevent overall buckling.

Refer to Evaluation Procedures for:

- Identifying plastic hinge locations and extent.
- Identifying flexural versus shear cracks.
- Calculation of moment, diagonal tension, web-crushing, sliding-shear, lap splice, and foundation rocking strength.
- Required boundary ties and wall thicknesses.

Severity	Description of Damage	Performance Restoration Measures
Insignificant $\lambda_K = 0.8$ $\lambda_Q = 1.0$ $\lambda_D = 1.0$	*Criteria:* • No crack widths exceed 3/16 in., and • No shear cracks exceed 1/8 in., and • No significant spalling or vertical cracking *Typical Appearance:* Note: *l_p is length of plastic hinge. See Section 5.3.3*	(Repairs may be necessary for restoration of nonstructural characteristics.)

Figure 8-3. Example of damage in reinforced concrete walls and modification factors (FEMA 306).

The capacity (backbone) curves at the component level are first derived following the recommendations of ASCE 41-06 (it has been superseded by ASCE 41-17), with updated limit values as suggested in ACI 369R-11 (see Figure 8-4, where $a' = a - \left[\theta_y \left(\frac{\lambda_Q}{\lambda_k} - 1\right) - RD\right]$). Modification factors are then applied to account for stiffness, strength and plastic rotation degradation (see Table 8-2). They also proposed a (preliminary) relationship between observed damage and expected level of ductility demand.

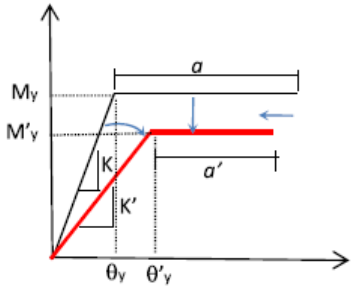

	stiffness	strength	Plastic rotation
intact	K	M_y	a
damaged	$K'=\lambda_K K$	$M_y'=\lambda_Q M_y$	$a'=a-a_d$

Figure 8-4. Modelling criteria for the damaged plastic hinges (Di Ludovico and Polese, 2013).

Table 8-2. Stiffness, strength and residual drift modification factors (Di Ludovico and Polese, 2013).

For deformed bars:	$\lambda_k = 1.0 \quad \text{for} \quad \theta/\theta_y^{th} \leqslant 1.0$
	$\lambda_k = 1 - [1.01 - 0.96 \cdot (\theta/\theta_y)^{-1.10}] \quad \text{for} \quad 1.0 < \theta/\theta_y^{th} \leqslant \theta_u/\theta_y^{th}$
	$\lambda_Q = 1.0 \quad \text{for} \quad \theta/\theta_y^{th} \leqslant 3.9$
	$\lambda_Q = 1.0 - 0.05 \cdot (\theta/\theta_y^{th} - 3.9) \quad \text{for} \quad 3.9 < \theta/\theta_y^{th} \leqslant \theta_u/\theta_y^{th}$
	$RD/\theta_y^{th} = 0.0 \quad \text{for} \quad \theta/\theta_y^{th} \leqslant 2.9$
	$RD/\theta_y^{th} = 0.05(\theta/\theta_y^{th} - 2.9)^2 + 0.40(\theta/\theta_y^{th} - 2.9) \quad \text{for} \quad 2.9 < \theta/\theta_y^{th} \leqslant \theta_u^{th}/\theta_y^{th}$
For round bars:	$\lambda_k = 1.0 \quad \text{for} \quad \theta/\theta_y^{th} \leqslant 0.9$
	$\lambda_k = 1 - [1.07 - 0.98 \cdot (\theta/\theta_y)^{-0.80}] \quad \text{for} \quad 0.9 < \theta/\theta_y^{th} \leqslant \theta_u/\theta_y^{th}$
	$\lambda_Q = 1.0 \quad \text{for} \quad \theta/\theta_y^{th} \leqslant 4.0$
	$\lambda_Q = 1.0 - 0.03 \cdot (\lvert\theta\rvert/\theta_y^{th} - 4.0) \quad \text{for} \quad 4.0 < \theta/\theta_y^{th} \leqslant \theta_u/\theta_y^{th}$
	$RD/\theta_y^{th} = 0.0 \quad \text{for} \quad \theta/\theta_y^{th} \leqslant 2.0$
	$RD/\theta_y^{th} = 0.007(\theta/\theta_y^{th} - 2.0)^2 + 0.30(\theta/\theta_y^{th} - 2.0) \quad \text{for} \quad 2.0 < \theta/\theta_y^{th} \leqslant \theta_u^{th}/\theta_y^{th}$
with:	$\theta_y^{th} = \frac{M_P L_S}{3EI_{eff}} \qquad k_{eff}^{th} = \frac{3EI_{eff}}{L_S}$

8.2.4 Maeda et al (2017)

Maeda et al (2017) presented an outline and basic concept for damage evaluation of reinforced concrete buildings based on residual capacity. The approach is based on a residual capacity index consistent with the Japanese Standard for Seismic Evaluation of Existing RC buildings. The seismic residual capacity *R* is defined as

$$R = \frac{{}_D Is}{Is} x100 \tag{8-5}$$

, where ${}_D Is$ is the original seismic performance index, and Is is the post-earthquake seismic performance index.

The original seismic performance index is calculated based on the lateral resistance and deformation ductility of the structural elements. The main component of ${}_DIs$ as described in the Seismic Evaluation Standard is the E_0 index, defined as the product of the strength index C (index of story lateral strength, calculated from the ultimate story shear in terms of story shear coefficient) and the ductility index F (assumed to vary between 1.27 and 3.2 for ductile columns, 1.0 for brittle columns, and 0.8 for extremely brittle short columns as per the Seismic Evaluation Standard). The seismic capacity deterioration is estimated by the energy dissipation capacity at a component level. A seismic reduction factor is then defined as follows.

$$\eta = \frac{E_r}{E_t} \tag{8-6}$$

, where E_r is the dissipated energy, and E_t is the total absorbable energy (see Figure 8-5). The authors proposed the seismic reduction factors of Table 8-3 to be used for both ductile and brittle members, which were obtained experimentally and analytically. The damage classes are defined in Table 8-4, and Figure 8-6 shows the idealized lateral force-displacement relationships for ductile structures and the corresponding damage class.

Table 8-3. Seismic capacity reduction factor η (Maeda et al, 2017).

Damage Class	Column			Beam		Shear wall	
	Ductile	Quasi-ductile	Brittle	Ductile	Brittle	Ductile	Brittle
I	0.95	0.95	0.95	0.95	0.95	0.95	0.95
II	0.75	0.7	0.6	0.75	0.7	0.7	0.6
III	0.5	0.4	0.3	0.5	0.4	0.4	0.3
IV	0.2	0.1	0.0	0.2	0.1	0.1	0.0
V	0.0	0.0	0.0	0.0	0.0	0.0	0.0

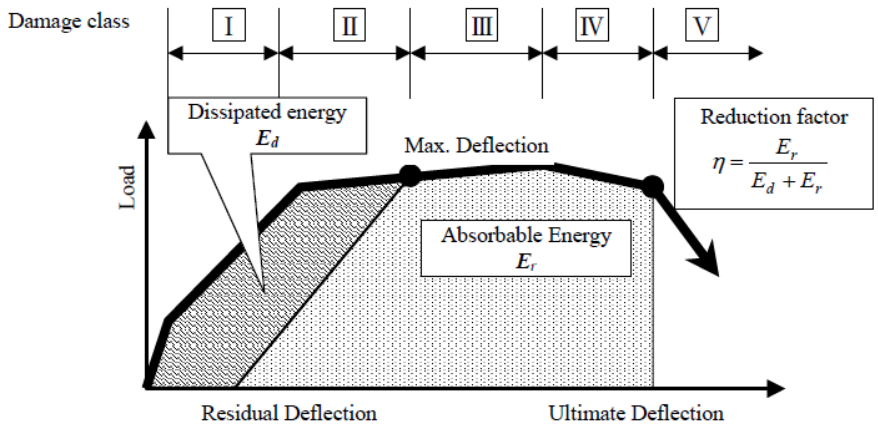

Figure 8-5. Seismic capacity reduction factor η (Maeda et al, 2017).

Table 8-4. Damage classes for reinforced concrete structural members (Maeda et al, 2017)

Damage class	Observed damage on structural members
I	Some cracks less than 0.2 mm are observed.
II	Cracks 0.2 to 1 mm wide are observed.
III	Heavy cracks 1 to 2 mm wide are observed. Some spalling of concrete is observed.
IV	Many heavy cracks greater than 2 mm wide are observed. Reinforcing bars are exposed due to spalling of the cover concrete.
V	Buckling of reinforcement, concrete crushing and vertical deformation of columns and/or shear walls are observed. Side-sway, subsidence of upper floors, and/or fracture of reinforcing bars are observed in some cases.

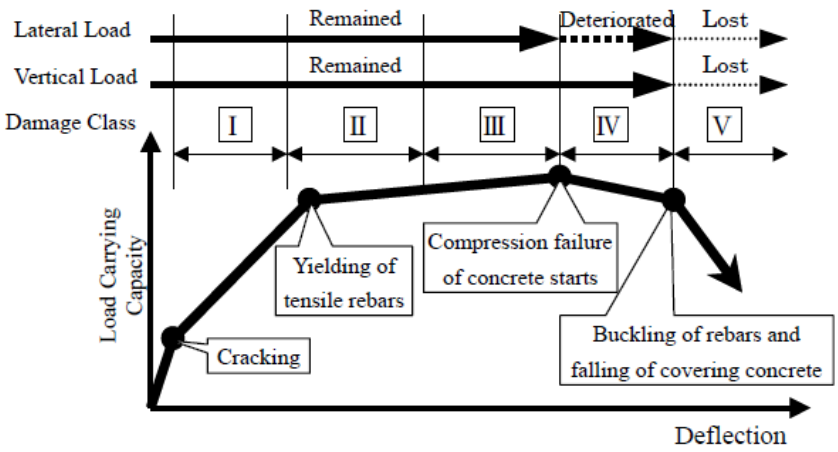

Figure 8-6. Idealized lateral force-displacement relationships for ductile structures and the corresponding damage class (Maeda et al, 2017).

It is interesting to note that recently Mukai et al (2017) applied the Japanese methodology to a full scale five-storey reinforced concrete modern building and concluded that "*the damage rating method turned out to give overly conservative results… the method gives a conservative result for ductile buildings designed after 1981. In order to apply the method for new buildings, the damage evaluation method for structural elements should be advanced more in the future*".

8.3 Factors affecting the residual fatigue life at a component level

This Section provides with a description of the various factors affecting the residual fatigue life at a component (i.e., plastic hinge) level. Although these concepts can be extended to a more general situation, it has been specifically developed for well detailed beams failing in flexure with a stable hysteretic behaviour. These factors are conceptually expressed in terms of coefficients and sketched in figures, and where applicable, equations to quantify them are also included.

Figure 8-7 shows a typical reinforced concrete beam cross-section and its moment-curvature relationships obtained through section analysis, a comparison between the original and damaged moment-curvature relationships, a comparison between unaged and aged steel stress-strain curves, and conceptual factors to account for stiffness deterioration, reduction in ductility, the increase in strength due to ageing, as well as cyclic and bond deterioration.

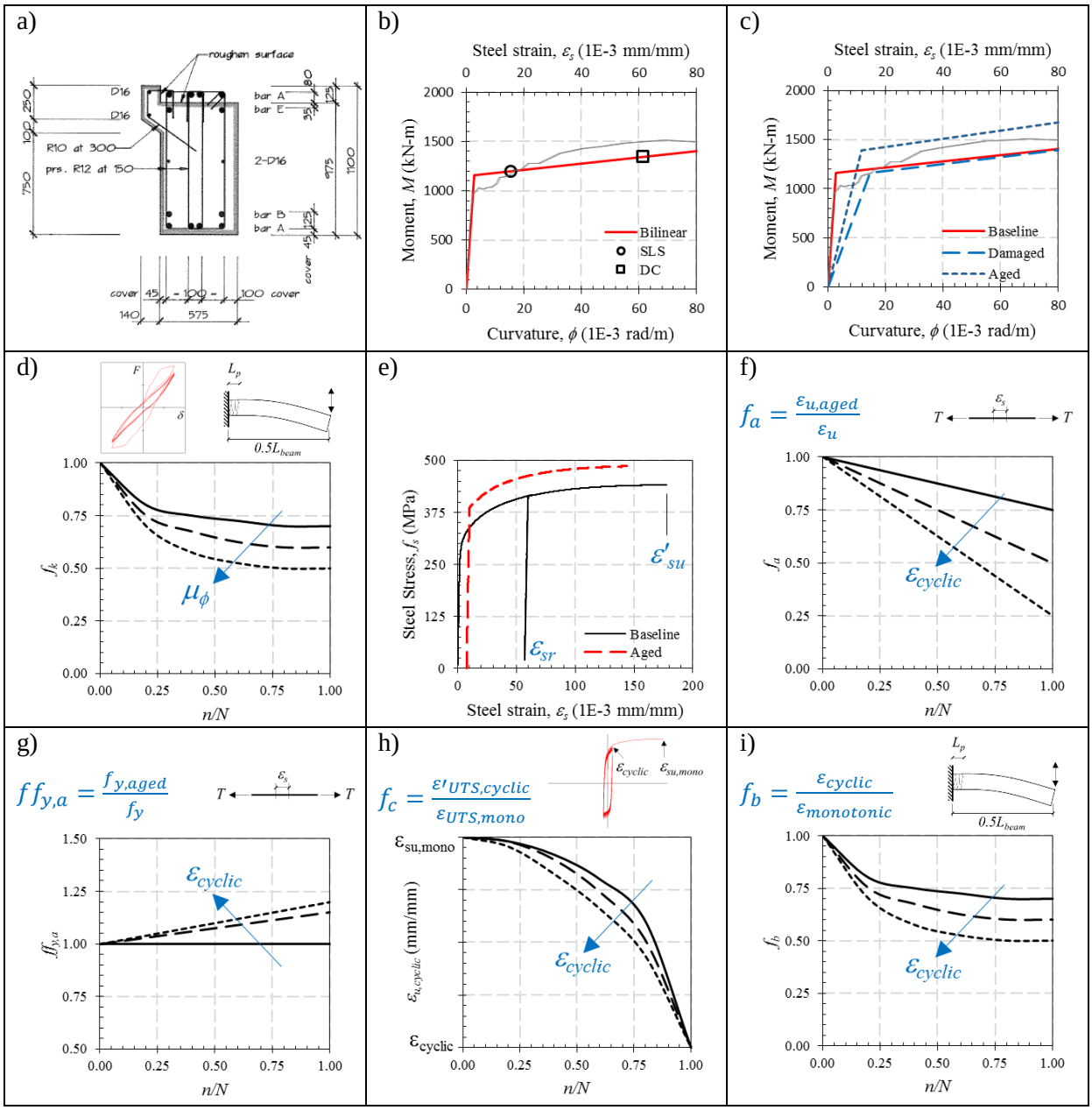

Figure 8-7. a) Reinforced concrete beam cross-section; b) its moment-curvature; c) comparison between original and damaged moment-curvatures; d) conceptual factor to account for stiffness deterioration; e) comparison between unaged and aged steel stress-strain curves; f) conceptual factors to account for reduction in ductility; g) increase in strength due to ageing; h) cyclic deterioration; and i) bond deterioration.

8.3.1 Fatigue life

As stated in Mander et al. (1994), fracture of longitudinal reinforcement due to low-cycle fatigue might be one of the most typical failure modes that can occur in flexural members during an earthquake, especially for structures located in mid-to-high seismic zones when one-to-five fully reversed cycles of large strain equi-amplitudes up to ε_s= 0.06 mm/mm or 6% may be expected. There are several plastic-strain equi-amplitude with fatigue life relationships currently available in the literature (e.g., Mander et al., 1994; Kunnath et al., 1997; Brown and Kunnath, 2004; Hawileh et al., 2010; Loporcaro, 2017, among others) which can be used to estimate the total number of cycles to rupture, N_f, for a given plastic strain, ε_p. Unfortunately, most of the relationships have been calibrated with tests in which buckling was always present thus reducing the fatigue life of the rebars when compared with a buckling restrained specimen tested at the same strain amplitude. As an example, Mander et al (1994) proposed the following empirical equation to be universally applicable to all reinforcing steels.

$$\varepsilon_p = 0.08 \cdot \left(2 \cdot N_f\right)^{-0.5} \tag{8-7}$$

More empirical equations can be obtained from Chapter 7.

8.3.2 Energy dissipation and stiffness deterioration

Based on available information such as original calculations, drawings (see Figure 8-7a) and intrusive and non-intrusive investigations, moment-curvature relationships (Figure 8-7b) can be computed for those sections or members showing inelastic deformation. For these envelope (capacity) curves, design limits states can also be estimated as shown in the figure. Before assessing a damaged building, however, these relationships should be modified to account for stiffness deterioration and curvature ductility demand (factor conceptually expressed as f_k in Figure 8-7d), as well as for the reduced ability of the reinforced concrete element to dissipate energy after it has been cyclically degraded (factor conceptually expressed as f_E, not schematically shown in the figures). Figure 8-7c shows what the original (baseline) capacity curve would look like when compared with the damaged one, with or without strain-ageing.

The loss of the initial (elastic) stiffness is addressed later in this Chapter (see Section 8.6). Factors to account for stiffness deterioration are also proposed.

Regarding the energy dissipation characteristics, Peckan et al. (1999) provide guidance (for unrepaired structures) to estimate the energy dissipation of the structure (in terms of equivalent viscous damping) based on displacement ductility, material, and structure type. However, it is noteworthy that as described in Chapters 2 and 4, damaged specimens, when properly repaired, are still able to dissipate a significant amount of energy which compares very well with the "as when new" energy dissipation characteristics. Therefore, for structures repaired per Chapter 2 it is assumed that the energy dissipation characteristics have been fully restored (i.e., f_E equal to 1.0).

8.3.3 Strain ageing

As explained by Loporcaro (2017), some carbon steels display, after it has been submitted to plastic strain, a time and temperature dependent strain ageing effect, which modifies the steel material properties. The process can be explained by the diffusion of the interstitial nitrogen and carbon atoms, which restrict the motion of the dislocations in their new position after the steel was strained. This restraint effect becomes stronger as the ageing time increases, as well as with higher interstitial nitrogen and carbon content, thus increasing the steel strength and reducing the ductility. Research suggests that small additions of Titanium or Vanadium minimise the strain ageing effects.

The strain ageing effect at ambient temperature is a slow process, however, it can be artificially accelerated at high temperatures. As explained by Loporcaro, the strain ageing effect after one year at 15 °C, are the same as if the steel was aged in boiling water (at 100 °C at sea level) during four hours.

Figure 8-7e shows a stress-strain profile of a rebar made of steel not affected by ageing (black curve) such as steel manufactured with the addition of vanadium (Loporcaro et al., 2016). In this case, the bar was strained to a certain level and then unloaded, leading to residual strains. If the bar is aged and loaded again, it will approximately follow the same unaged stress-strain curve. If, however, the steel material is strain-ageing sensitive such as the NZ Grade 300 steel (red curve), when the bar is unloaded, aged and loaded again, there is an increase in the yield and ultimate stresses. In addition, it has been experimentally demonstrated that strain-ageing reduces the ductility (i.e., the strain at rupture) of the bars. The reduction seems to be proportional to the pre-strain level reached prior to ageing (factor conceptually expressed as f_a in Figure 8-7f). Regarding the yield and ultimate stresses, they seem to increase with the increase of the pre-strain level (factors conceptually expressed as $ff_{y,a}$ in Figure 8-7g and $ff_{u,a}$).

This increase is more pronounced for the yield stress. Loporcaro (2017) report the following changes in the lower yield and ultimate strengths due to strain-ageing obtained with NZ Grade 300 steel samples, after being pre-loaded to a certain strain, ε_{peak}.

Table 8-5. Change in the lower yield and ultimate tensile strengths due to strain ageing for NZ Grade 300 steel (Loporcaro, 2017).

Pre-strain, ε_{peak} (mm/mm)	Lower yield strength (MPa)			Ultimate tensile strength (MPa)		
	Unaged	Aged	Difference	Unaged	Aged	Difference
0.015	307	388	81	492	499	7
0.030	379	453	74	497	531	34
0.060	432	476	44	489	518	29
0.120	475	527	52	489	546	57
0.180	500	574	74	503	574	71

Based on these results, the following factors to account for the increase in the yield and ultimate tensile strengths can be obtained. This increase is important because it can modify the hierarchy of failure thus invalidating the capacity design philosophy.

$$ff_{y,a} = 1.16 \text{ (with a standard deviation of 0.07)} \quad (8\text{-}8)$$

$$ff_{u,a} = 1.08 \text{ (with a standard deviation of 0.05)} \quad (8\text{-}9)$$

Loporcaro (2017) also report the following strains at the ultimate tensile strength for aged samples obtained with NZ Grade 300 steel after being pre-loaded to a certain strain, ε_{peak}.

Table 8-6. Summary of the mechanical properties of pre-strained and aged Grade 300 steel samples (Loporcaro, 2017).

Pre-strain, ε_{peak} (mm/mm)	Vickers hardness (HV_{30})		Lower yield strength (MPa)		Tensile strength, UTS (MPa)		Strain at UTS $\varepsilon_{u,aged}$ (mm/mm)	
	Average	S.D.	Average	S.D.	Average	S.D.	Average	S.D.
0	150	3.0	322	8.4	507	10.5	0.203	0.002
0.02	168	4.90	388	11.3	501	5.7	0.142	0.020
0.04	180	2.5	436	3.2	521	3.2	0.103	0.005
0.06	191	4.9	490	2.0	533	1.7	0.081	0.002
0.08	198	3.9	512	3.3	536	3.3	0.067	0.002

Based on Table 8-6 the following equation can be obtained.

$$\varepsilon_{u,aged} = 19.821 \cdot \varepsilon_{peak}^2 - 3.2507 \cdot \varepsilon_{peak} + 0.2017 \quad (8\text{-}10)$$

In the previous equation, the coefficients of determination, R^2, is 0.9983, therefore, the model fits the data reasonably well. Since the ultimate strain of NZ Grade 300 steel is typically 0.200 mm/mm (see Chapter 7), then the following factor to account for the reduction of the strain at the ultimate tensile strength can be obtained.

$$f_a = 99.1 \cdot \varepsilon_{peak}^2 - 16.25 \cdot \varepsilon_{peak} + 1.0 \tag{8-11}$$

8.3.4 Cyclic deterioration effect of steel strain-life

In Chapter 7 it was demonstrated that if a reinforcing bar is cyclically strained during *n* cycles at ε_{cyclic} for $n < N_f$ cycles, unloaded and then tested monotonically, it will fracture at a strain ε'_{UTS}, where $\varepsilon_{cyclic} \leq \varepsilon'_{UTS} < \varepsilon_{UTS}$. It is believed that this effect is caused by the crack growth phenomena (Dowling, 1977). Thus, the ε'_{UTS} can be estimated as the ε_{UTS} multiplied by the factor f_c conceptually expressed in Figure 8-7h. A linear trend for n/N_f between 0 and 66% was preliminary proposed for cases where buckling of the rebar occurs.

$$\varepsilon'_{UTS} = -0.109 \cdot \left(\frac{n}{N_f}\right) + 0.20, for\ unaged\ samples \tag{8-12}$$

Since the ultimate strain of NZ Grade 300 steel is typically 0.200 mm/mm (see Chapter 7), then the following factor to account for the reduction of the strain at the ultimate tensile strength due to the cyclic effect can be obtained. Chapter 7 provides guidance on how to estimate f_c for n/N_f greater than 66%.

$$f_c = -0.545 \cdot \left(\frac{n}{N_f}\right) + 1.0, for\ unaged\ samples \tag{8-13}$$

Although no test results are available for cases where buckling is prevented, it appears that for n/N_f equal to or less than 10%, the reduction in the ε'_{UTS} due to the cyclic effect is insignificant (see Chapter 7).

8.3.5 Bond deterioration effect

When a reinforced concrete element is cyclically loaded, the bond between steel and concrete deteriorates. As it deteriorates, the length over which the strains spread out increases, thus reducing the strain for the same curvature ductility demand (factor conceptually expressed as

f_b in Figure 8-7i). The reinforcement ratio and concrete tensile strength plays an important role on this effect. There is evidence (e.g., SESOC, 2011) suggesting that low reinforcement ratios and high tensile values tend to induce single crack formations instead of a well distributed cracking pattern.

This factor was implicitly accounted when the relationships between maximum crack widths and peak steel strain were derived (see Section 7.5). These relationships will be later applied in this chapter to estimate the seismic residual capacity of a plastic hinge.

8.3.6 Limit-states for damaged components

Since the limit states are usually strain-based (e.g., Priestley et al., 2007), it is sensible to adjust them to account for the damaged material characteristics. For steel, the strains associated to a certain limit state can be estimated by applying coefficients accounting for the damage, as previously described. For concrete, experimental and numerical investigations on the cyclic deterioration of concrete at low strain levels are required because the onset of nonlinear behaviour (i.e., damage) occurs at strain levels lower than the ones that are typically used to define damage in macro-terms (e.g., concrete crushing). These experiments are out of the scope of this research; therefore, no recommendations are provided on this aspect.

8.4 Seismic residual capacity of a plastic hinge: Worked example

The proposed procedure to account for the seismic residual capacity of a plastic hinge is explained by a worked example. Reference is made to previous concepts described above, as well as to equations developed in previous chapters. As previously stated, although the procedure can be extended to a more general situation, it has been specifically developed for buildings designed following capacity design principles, where well detailed beams fail in flexure with a stable hysteretic behaviour.

8.4.1 Beam section analysis

The first step of the process is to gather all available information such as original calculations, drawings, and intrusive (e.g., concrete and steel material properties, “as-built” dimensions of the structural components, verification of reinforcement content) and non-intrusive investigations (e.g., residual drifts, damage to non-structural components, crack widths and their location, orientation, amount and distribution). For those beams showing inelastic deformation and/or that are part of the lateral force resisting system, moment-curvature (i.e.,

capacity curve) relationships are computed. If required, the capacity curves can be combined with design limits states (see Section 6.2.2 for a reference of design limit states).
Figure 8-8 shows beam cross section with indications of amount and location of reinforcement, as well as the steel and concrete material properties. Section analysis was performed on this beam and the moment-curvature shown in Figure 8-9 was obtained. The MATLAB code Cumbia (Montejo and Kowalsky, 2007) was used for such purpose.

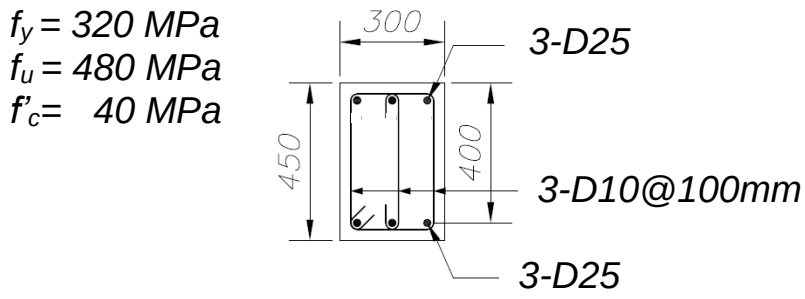

Figure 8-8. Material properties and beam section details (longitudinal reinforcement ratio ρ_s of 1.23%) used for the section analysis.

The section analysis provides relationships between beam curvature with applied moment and steel and concrete strains, which are key parameters for assessing the residual capacity of plastic hinges. For this case (i.e., a beam reinforced with NZ Grade 300E steel), it is assumed that the strain at ultimate tensile stress, ε_{UTS}, is equal to 0.20 mm/mm, or 20%.

8.4.2 Mean strain estimation between consecutive flexural cracks

As explained in Section 6.5, the use of maximum strain at peak displacement to estimate the maximum crack width may lead to overestimations of the crack width, in particular at low strain levels. Therefore, it is more appropriate to account for the strain gradient within the crack spacing. In Chapter 6, several equations to estimate the mean strain between two consecutive cracks were proposed for elements reinforced with NZ Grade 300E steel. The mean strain between cracks can be obtained as follows.

$$\kappa \cdot \varepsilon_{mean} = -324.4 \cdot \varepsilon_{peak}^3 + 37.23 \cdot \varepsilon_{peak}^2 + 1.187 \cdot \varepsilon_{peak} \quad \text{(for } \rho_s \geq 0.58\%\text{)} \qquad (8\text{-}14)$$

$$\kappa \cdot \varepsilon_{mean} = -219.2 \cdot \varepsilon_{peak}^3 + 32.36 \cdot \varepsilon_{peak}^2 + 1.023 \cdot \varepsilon_{peak} \quad \text{(for } \rho_s = \rho_{min}\text{)} \qquad (8\text{-}15)$$

, where

$$\kappa = \frac{53.33 \cdot S_{crack} \cdot f_R^{0.8} \cdot \sqrt{f'_c}}{d_b \cdot f_y} \quad (8\text{-}16)$$

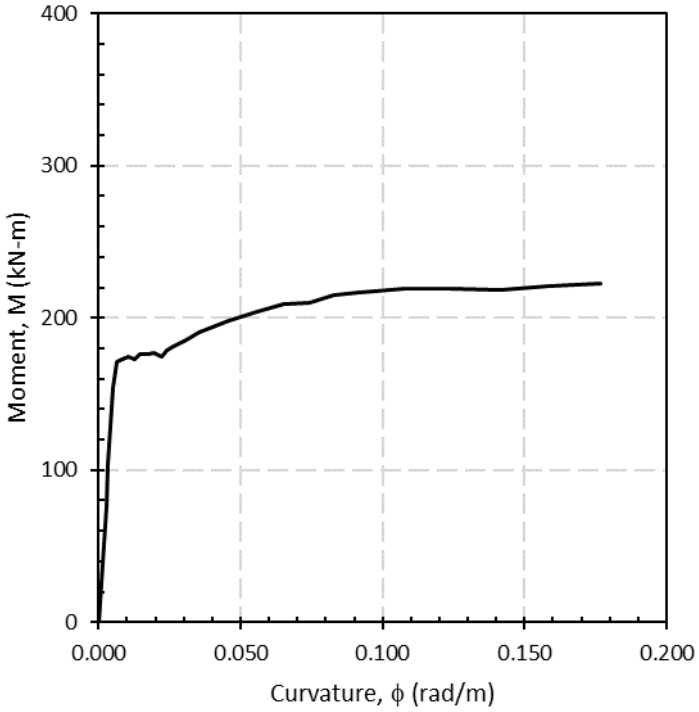

Figure 8-9. Moment-curvature relationship obtained for the beam section shown in Figure 8-8.

It is evident that, in order to estimate the mean strain, the crack spacing, S_{crack}, must be known. Lettow (2006) proposed values for the related rib area factor, f_R, which depends on the bar diameter, d_b. (see Table 8-7).

Table 8-7. Related rib area factors, f_R (Lettow, 2006).

Bar diameter, d_b (mm)	Related rib area factor, f_R
6	0.050
10	0.060
12	0.070
16	0.080
20	0.085
25	0.090
32	0.094

It is noteworthy that when estimating the mean steel strain, the following condition must be satisfied.

$$0.60 \leq \frac{\varepsilon_{mean}}{\varepsilon_{peak}} \leq 1.0 \quad (8\text{-}17)$$

The above equations are valid for beams with $P_u/f'_c \cdot A_g \leq 0.10$, which is believed to apply for most situations.

8.4.3 Maximum crack widths estimation

Once the mean strain has been estimated, the maximum crack width, w_{max}, can be obtained with the following equation (see Section 6.6).

$$w_{max} = S_{crack} \cdot \varepsilon_{mean} \cdot \left(\frac{h - kd}{d - kd}\right) \quad (8\text{-}18)$$

In the previous equation, S_{crack}= crack spacing (assumed to be 150 mm); ε_{mean}= mean steel strain over S_{crack}, estimated with equations 8-14 and 815; h= overall depth of the section; kd= neutral axis depth (based on section analysis); h= section depth; and d= effective depth.

8.4.4 Residual crack widths estimation

The maximum crack widths estimated with equation 8-18 can be converted to residual crack widths using the equations derived in Section 6-3.

For beams with $P_u/f'_c \cdot A_g = 0$ (assumed in this example):

$$\frac{w_r}{w_m} = 39.9 \cdot \varepsilon_{peak} + 0.075, \quad (for\ \varepsilon_y \leq \varepsilon_{peak} \leq 10 \cdot \varepsilon_y) \quad (8\text{-}19)$$

$$\frac{w_r}{w_m} = 5.09 \cdot \varepsilon_{peak} + 0.637, \quad (for\ 10 \cdot \varepsilon_y \leq \varepsilon_{peak} \leq 0.05) \quad (8\text{-}20)$$

For beams with $P_u/f'_c \cdot A_g = 0.10$:

$$\frac{w_r}{w_m} = 47.1 \cdot \varepsilon_{peak} - 0.254, \quad (for\ 3 \cdot \varepsilon_y \leq \varepsilon_{peak} \leq 10 \cdot \varepsilon_y) \quad (8\text{-}21)$$

$$\frac{w_r}{w_m} = 12.68 \cdot \varepsilon_{peak} + 0.319, \quad (for\ 10 \cdot \varepsilon_y \leq \varepsilon_{peak} \leq 0.035) \quad (8\text{-}22)$$

For beams with $P_u/f'_c \cdot A_g = 0.20$:

$$\frac{w_r}{w_m} = 48.4 \cdot \varepsilon_{peak} - 0.537, \quad (for\ 6 \cdot \varepsilon_y \leq \varepsilon_{peak} \leq \sim 10 \cdot \varepsilon_y) \quad (8\text{-}23)$$

8.4.5 Residual strain capacity and curvature ductility

The residual strain (or remaining strain) capacity, ε_{res}, can be computed as the strain at the ultimate tensile stress, ε_{UTS}, minus the strain at peak displacement, ε_{peak}, plus the strain recovery once the induced load has been removed (see Figure 8-10). It is noteworthy that some assessment guidelines assume the ultimate strain to be much less than the ε_{UTS}. For instance, in the NZSEE (2017) guidelines the ultimate steel strain is considered to be 0.05-0.06 mm/mm, or 5-6%.

The above can be expressed as follows.

$$\varepsilon_{res} = \varepsilon'_{UTS} - \varepsilon_{peak} + \frac{f_s}{E_s} \tag{8-24}$$

For cases where there is no strain-ageing (e.g, NZ Grade 500E steel) or cyclic (e.g., preliminary for bars where buckling did not occur and n/N_f is equal to or less than 10%, see Chapter 7) effects, the strain at ultimate tensile stress, ε'_{UTS} in Equation (8-24) is equal to ε_{UTS}. The residual strain capacity, *RSC*, is calculated as follows.

$$RSC = \frac{\varepsilon_{res}}{\varepsilon_{UTS}} \tag{8-25}$$

Another parameter shown in the figure is the peak curvature ductility, μ_ϕ, which can be estimated as the curvature at peak displacement upon the yield curvature.

$$\mu_\varphi = \frac{\varphi_{peak}}{\varphi_y} \tag{8-26}$$

8.4.6 Graphic representation of the seismic residual capacity of a plastic hinge

Figure 8-12*a* and *b* show a graphic representation of the seismic residual capacity of a plastic hinge where strain ageing and the cyclic effect are not of concern. In Figure 8-12*a* the residual crack width, w_{res}, is related with the strain at peak displacement, ε_{peak}, and the residual strain capacity, *RSC*. On the other hand, Figure 8-12*b* relates the residual crack width with the residual strain, ε_{res}, and the curvature ductility at peak displacement, μ_ϕ.

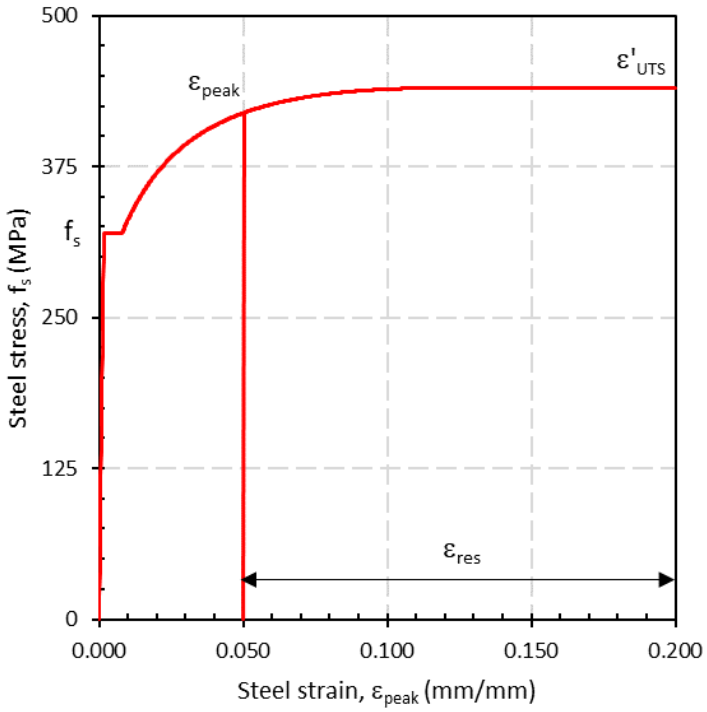

Figure 8-10: Steel stress-strain curve with a loading-unloading-loading sequence.

As an example, a residual crack 4 mm wide measured on site in this beam, spaced 150 mm crs., corresponds approximately to the strains, curvature ductility and residual strain capacity of Table 8-8 (see blue arrows in Figure 8-12*a* and *b*).

At this stage, judgement is required in order to determine whether the above values are deemed acceptable, or if strengthening/stiffening are required as part of a rehabilitation project of the building.

Table 8-8. Residual strain capacity for a residual crack 4 mm wide.

Parameter	Value
ε_{peak} (mm/mm)	0.03
ε_{res} (mm/mm)	0.17
μ_ϕ (-)	14.5
RSC (%)	85.0

As a reference, the NZS 3101:2006 states that for well-detailed plastic hinges where the concrete is properly confined by stirrups curvature ductility values of at least 20 can be reached during a design earthquake level.

Regarding the residual strain capacity, The Engineering Advisory Group (2013) consider that a strain hardening value (defined as the strain at peak displacement upon the strain at the ultimate tensile stress of the bar) of 15% (i.e., a residual strain capacity equal to or greater

than approximately 85%) in flexural dominated walls as a threshold to determine whether strengthening/stiffening is required in addition to epoxy injection techniques. Strain hardening of 30% or greater (i.e., a residual strain capacity equal to or less than approximately 70%) require demolish and rebuild the affected area.

8.4.7 Strain-ageing and cyclic effect

When strain-ageing and/or the cyclic effect are of concern, the factors described in Sections 8.3.3 and 8.3.4 can be considered to reduce the strain at ultimate tensile stress, ε'_{UTS}. Figure 8-12*c* and *d* consider the strain-ageing effect; Figure 8-12*e* and *f* consider the cyclic effect for n/N_f of 10% assuming that buckling of the reinforcement may be an issue; and Figure 8-12*g* and *h* consider both the strain-ageing and cyclic effects.

For the case where strain-ageing is of concern, (see Figure 8-12*c* and *d*), a residual crack 4 mm wide corresponds to a residual strain capacity of approximately 50%. Residual crack widths in the order of 0.6 mm correspond to a residual strain capacity of 85%. Thus, the reduction of the residual strain capacity for a given crack width highlights the importance of strain-ageing when assessing damaged buildings.

8.4.8 Additional comments on the seismic residual capacity of plastic hinges

1. When assessing the seismic residual capacity of plastic hinges, it is important to bear in mind that the effect of strain hardening is very localized. The fact that strain hardening has occurred over a finite length of bar, it means that this bar segment is now stronger than the adjacent bar segment that has reached a lower strain level. Similar to the Tom Paulay's capacity design analogy of a chain with one of its links being weaker and (in a new design, targeted to be) more ductile than the others (see Figure 8-11), and assuming that the moment gradient (i.e., the slope of the bending moment diagram) within the plastic hinge allows for such behaviour, the strains developed during a subsequent load excursion within the bar segment that reached lower levels of strain (i.e., the ductile link in the chain) may be greater than the strains developed within the bar segment that suffered strain hardening (i.e., the brittle but stronger links in the chain). In other words, the bar is somehow self-protecting from experiencing a tensile failure. Not surprisingly, Kunnath et al (1997) observed that their specimens experienced other types of failure prior to reaching a low-cycle fatigue failure.

Similarly, the PWC beam specimens described in Chapters 3 and 4, although they sustained the 2010-2011 Canterbury Earthquake Sequence, were further subjected to cyclic loading until developing residual crack widths of up to 6.0 mm, epoxy repaired and subjected again to cyclic loading, did not experience fracture of the rebar; the failure was due to excessive damage in the concrete. In addition, most of the previous research reviewed in Chapter 2 did not report fracture of the longitudinal reinforcement.

Therefore, in order to assess the residual capacity of a plastic hinge, importance must be given to the moment gradient within the plastic hinge. Strain demands must be estimated not only at the point where strain hardening is expected have occurred, but also at adjacent locations where strain hardening is not expected to have occurred, or it has occurred at a smaller scale.

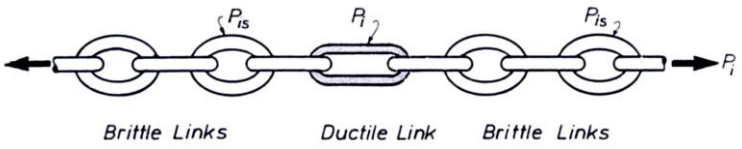

Figure 8-11. Capacity design analogy of a chain with one of its links weaker and more ductile than the others (Reitherman, 2006).

2. As it was preliminary concluded in Chapter 5, strain-rate effects do not seem to play an important role on the cracking pattern. However, they may be important for beams with reinforcement content approaching to the minimum required as per NZS 3101:2006.
3. There is great uncertainty on how to quantify the dynamic (i.e., earthquake) effect on the residual crack widths. This effect can be more critical in long duration earthquakes where the peak demand occurs at an earlier stage, when the subsequent seismic demand is able to restore, totally or partially, the structure's original position. The dynamic effect has not been accounted for in the procedure previously discussed (i.e., the residual crack widths from a real earthquake can be much smaller than those predicted with the proposed equations), therefore it can provide unconservative estimates of the residual strain capacity of the damaged bar section.

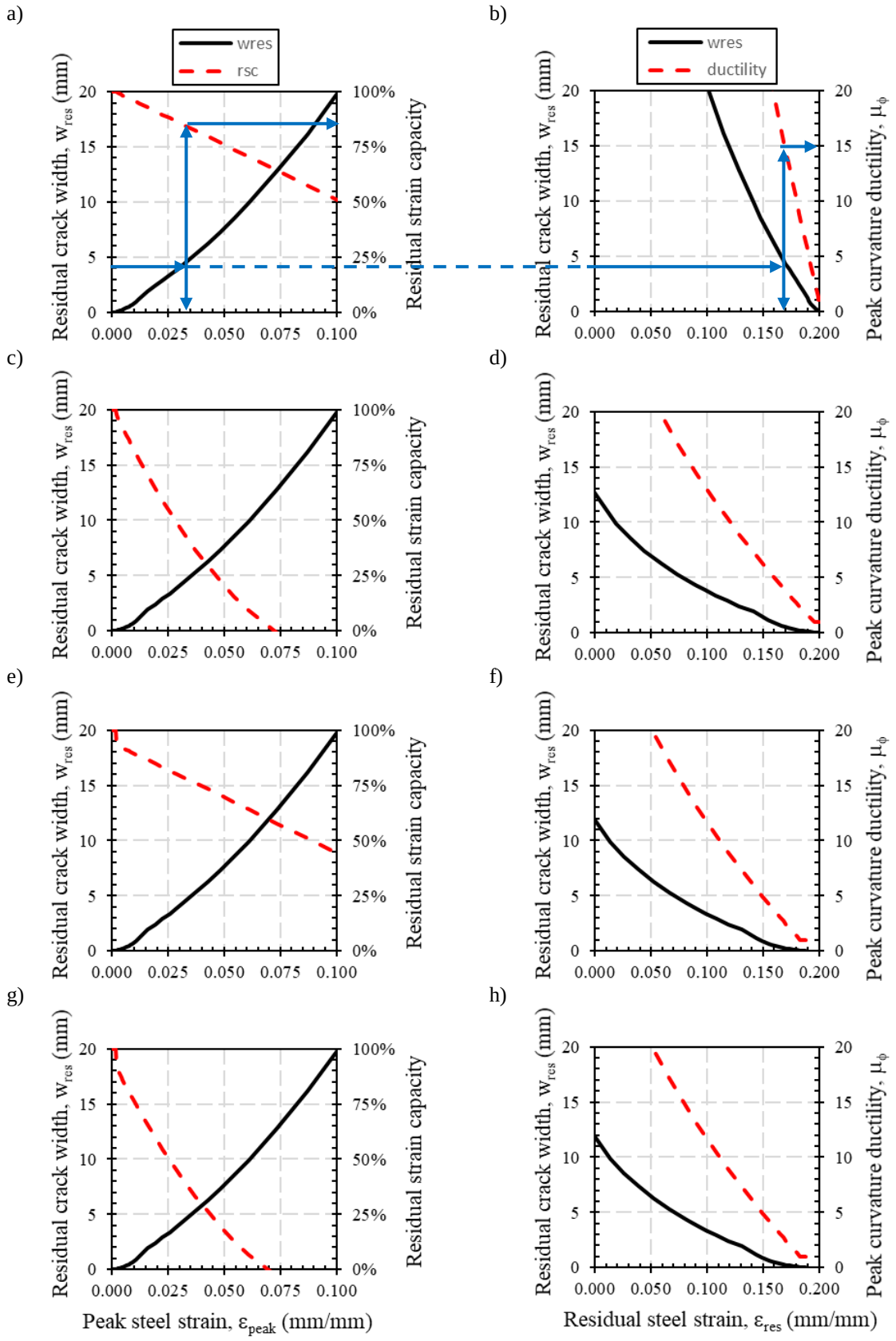

Figure 8-12. a) and b) Graphic representation of the residual strain capacity of a plastic hinge where strain ageing and the cyclic effect are not of concern; c) and d) considering strain-ageing effects; e) and f) considering the cyclic effect; and g) and h) considering strain-ageing and cyclic effects.

4. However, the procedure developed in Chapter 6 for the residual crack width estimation (used for the seismic residual capacity estimation) is based on the steel strain at the first peak. In Section 6.2.4 it was observed that, because of cyclic bond deterioration, the peak strains decrease as the number of cycles increase, reaching in some cases a constant strain value. Therefore, assuming a constant steel strain equal to the strain measured in the first cycle is a conservative measure.
5. Lastly, it is very important to observe the damage to non-structural components, not only to make sure that the building experienced displacements in excess of the yield displacement (as explained in Chapter 6, the residual crack widths formulation is based on the assumption that the beams have yielded), but also to confirm that the "probable" peak displacement (estimated based on the damage to the non-structural components) correlates with the expected peak displacement based on the final state of the building (i.e., the residual drifts and cracks).

8.5 Implementation of the Proposed Model at a MDOF System Level

8.5.1 Overview

The following figures show flowcharts of the proposed framework for seismic assessment of reinforced concrete frames accounting for seismic residual capacity and fatigue life of plastic hinges. The analytical procedure can be used to estimate the potential residual capacity of a building prior to an earthquake (for pre-earthquake strengthening campaigns), or after the earthquake (for rapid earthquake response assessments) to assess the ability of the building to sustain future code-based aftershocks.

For post-earthquake evaluations, the element properties should be first calibrated based on actual observations (e.g., crack patterns, plastic hinge length, etc) per the equations proposed in this Chapter (or per FEMA 306 for reinforced concrete shear wall buildings) to account for the reductions in the seismic capacity of damaged components due to the mainshock. Figure 8-13 describes how to account for such effect.

As shown in the figure, moment-curvature analyses are performed for critical members and the undamaged building's capacity curve is estimated. The mainshock displacement demand, Δ_{SD}, can be estimated based on crack widths, residual drifts, or damage to non-structural components, for instance. The fatigue life of each critical member is estimated and compared with the cyclic fatigue demand. If it is satisfactory (i.e., $n/N_f < 1.0$ or to a certain predetermined value), then the structural displacement capacity, Δ_{SC}, is estimated and

compared with the mainshock displacement demand. If either the fatigue life and/or the displacement capacity of the building have been exceeded during the mainshock, then a decision can be made on whether remediation actions, immediately after the earthquake, are required.

Following the mainshock, the residual strain capacity of each plastic hinge is estimated as described in Section 8.4 based on actual observations (e.g., crack widths, "observed" or "real" plastic hinge length, residual drifts, damage to non-structural components), and the damaged building is assessed for an aftershock(s).

Note that the procedure described in Figure 8-13 is also applicable to pre-earthquake evaluations, with the difference that the displacement and fatigue demands need to be based on the design earthquake level, instead of being based on actual observations.

As shown in Figure 8-14, the fatigue life assessment for a code-based aftershock proceeds in a similar manner, with the difference that the elements are, as previously mentioned, updated to account for the residual strain capacity, stiffness and energy dissipation deterioration. The fatigue life check for each critical member is a combination of cyclic demand vs capacity ratios during the mainshock and code-based aftershock. If either the fatigue life or the displacement capacity is smaller than the demand values, an iterative process is followed reducing the code-based demand spectrum (it reduces the drift demands that are to be sustained, and consequently reduces also the plastic strain demands, increasing the fatigue life) until the capacity is at least equal to the demand. Lastly, depending on the reduction of the code-based demand spectrum, a decision-making process is performed to decide whether repair/strengthening or demolition/rebuild must be implemented.

One aspect to consider when assessing the fatigue life of plastic hinges is that, as described in Chapter 7, investigations on low-cycle fatigue for reinforcing steel have historically been carried out (maybe with the exception of one previous research) with a test setup in which buckling of the bar specimen was not prevented, thus reducing the fatigue life of the rebars when compared with a buckling restrained specimen tested at the same strain amplitude. Therefore, for cases where buckling of the rebar was not observed during the damage reconnaissance, empirical equations other than the one shown in Section 8.3.1 (i.e., Mander et al, 1994), for instance, must be used.

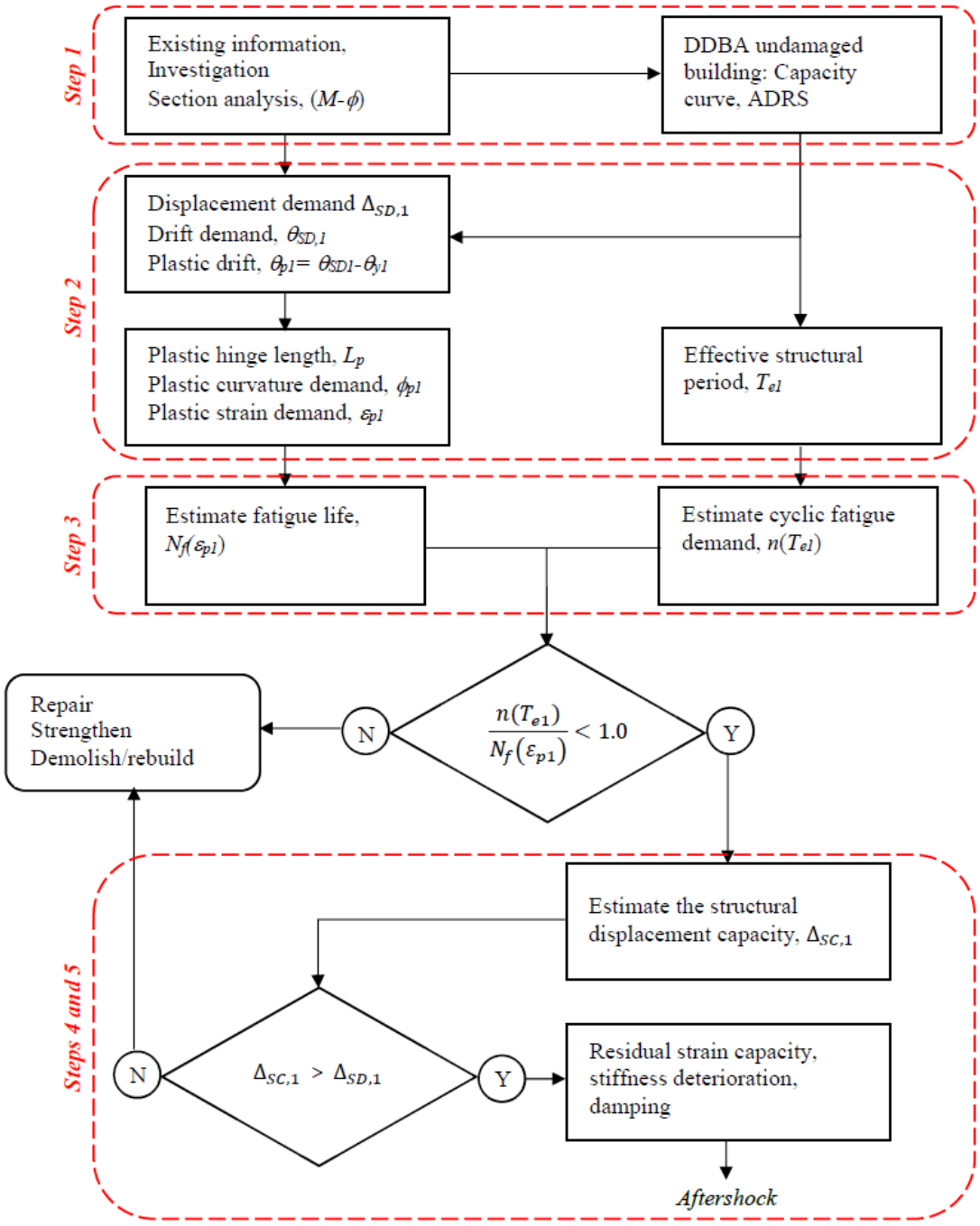

Figure 8-13. Flow chart for seismic assessment accounting for residual fatigue life: Mainshock.

8.5.2 Step-by-Step Procedure

Referring to Figure 8-15, the above procedure can be exemplified by using the Acceleration-Displacement-Response-Spectrum (ADRS) procedure. For sake of simplicity, this example assumes that the mainshock is equivalent to a design earthquake level (as for pre-earthquake assessments), therefore the displacement demand is described in terms of the performance point (i.e., the point at which the capacity curve intersects the demand spectrum). As mentioned before, for post-earthquake assessments the displacement demand should be

estimated based on actual observations (e.g., crack widths, "observed" or "real" plastic hinge length, residual drifts, damage to non-structural components).

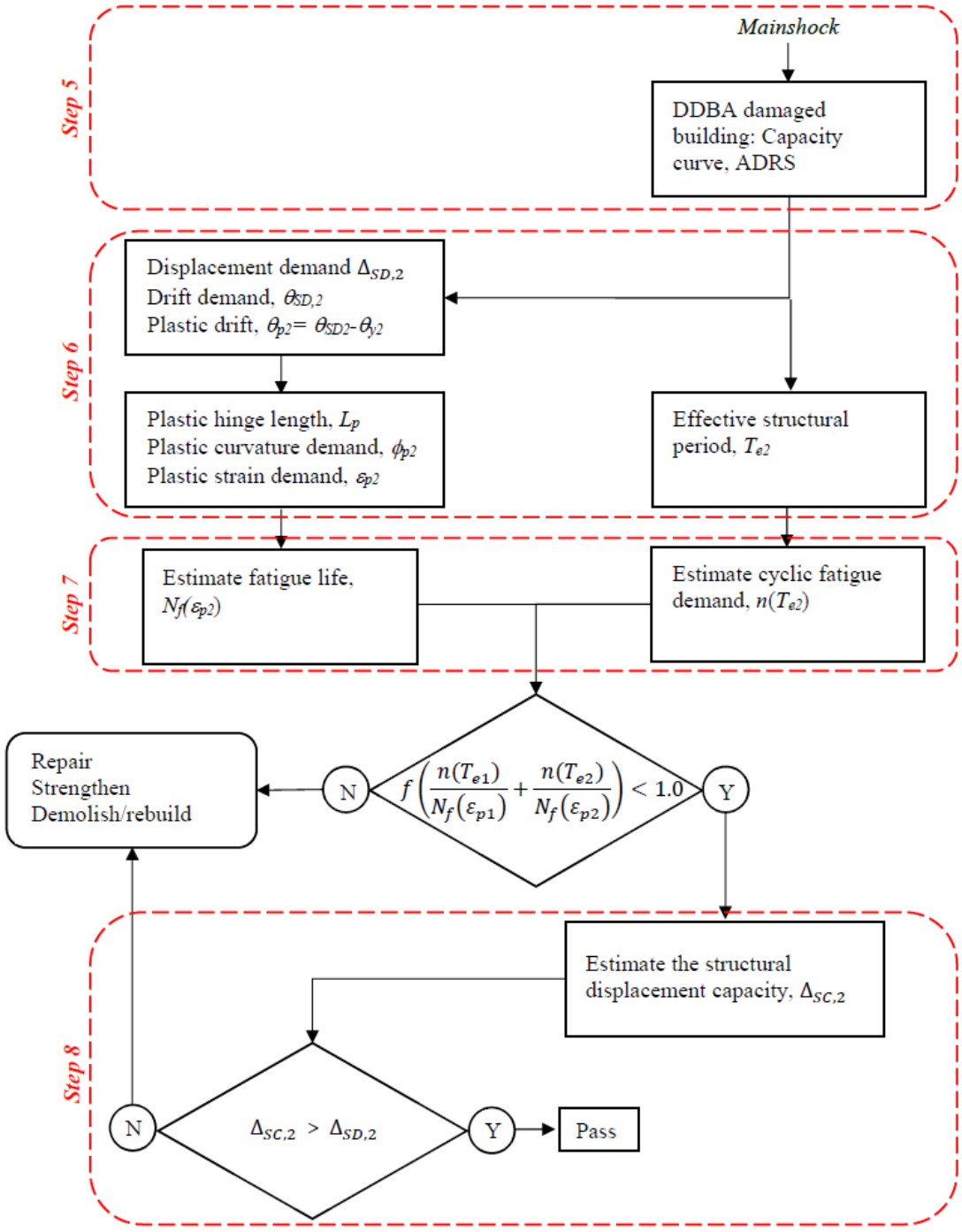

Figure 8-14. Flow chart for seismic assessment accounting for residual fatigue life: Aftershock.

Step 1. Based on existing information and basic (moment-curvature) principles, the capacity curve of the undamaged original structure is computed and plotted against the code-based ADRS (Figure 8-15*a*). Here, both "exact" and the bilinear approximation are shown.

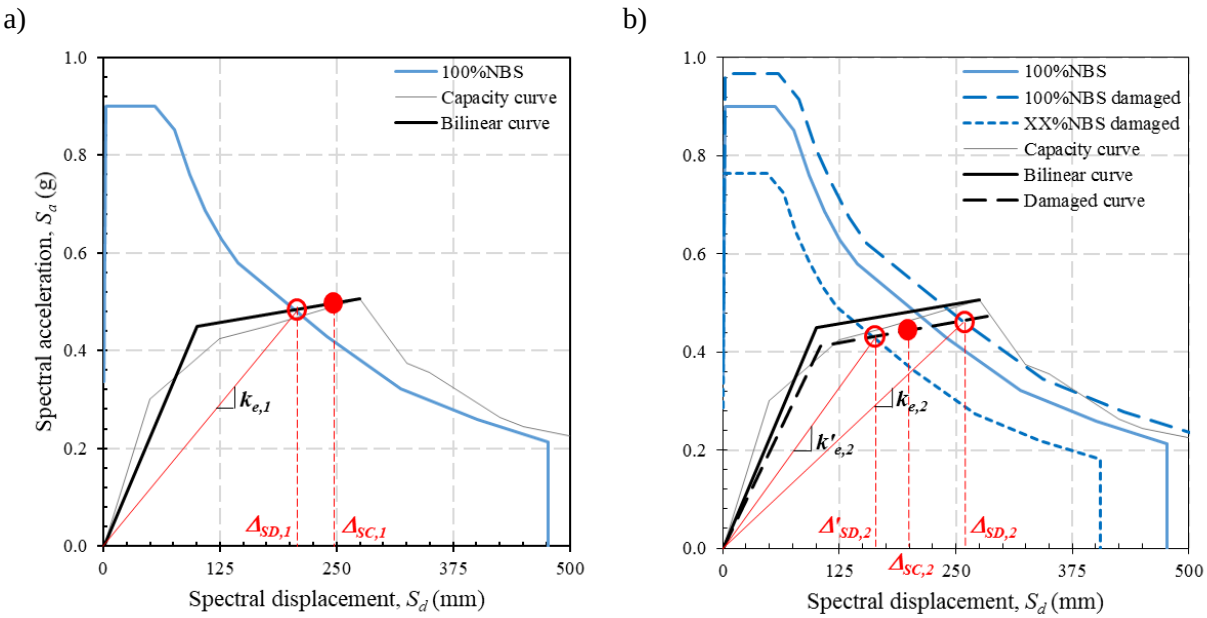

Figure 8-15. ADRS procedure accounting for seismic residual fatigue life: a) original undamaged structure, and b) damaged structure. (Note: to be compatible with the ADRS format, the secant stiffness is normalized by the effective seismic weight of the structure).

Step 2. The structure displacement demand $\Delta_{SD,1}$ (empty red circle in Figure 8-15*a*) corresponding to the performance point at 100%NBS (for pre-earthquake assessments) is obtained or estimated based on actual observations (for post-earthquake assessments). Following DDBA principles, plastic strain demands ε_{p1} (for an assumed plastic hinge length, L_p, in the case of pre-earthquake assessments, or for an "observed" or "real" plastic hinge length in the case of post-earthquake assessments), as well as effective structural vibration period T_{e1} (for an effective mass and the corresponding secant stiffness) are estimated.

Step 3. With the above information, the fatigue life $N_f(\varepsilon_{p1})$ (i.e., number of cycles to failure) and cyclic fatigue demand $n(T_{E1})$ (i.e., number of equi-amplitude cycles experienced during the mainshock) are estimated, and the cyclic demand vs capacity ratio $f(n_1/N_1)$ checked. In this example it is considered that the ratio is smaller than 1.0 (or to a certain predetermined value), therefore, no demolish/retrofit action would be required.

The reader is referred to previous research such as Malhotra (2002), Hancock and Bommer (2005), Stafford and Bommer (2009), and Mander and Rodgers (2013), among others, for the estimation of the cyclic fatigue demand. For instance, Mander and Rodgers (2013) normalized time history responses to an equivalent number of cycles at a code-based seismic displacement amplitude (based on NZS 4203:1984 and NZS1170.5:2004), using fatigue

exponents C of 1, 2 and 3, for concrete-critical fatigue, reinforcing-steel critical fatigue, and structural-steel fatigue (see Figure 8-17).

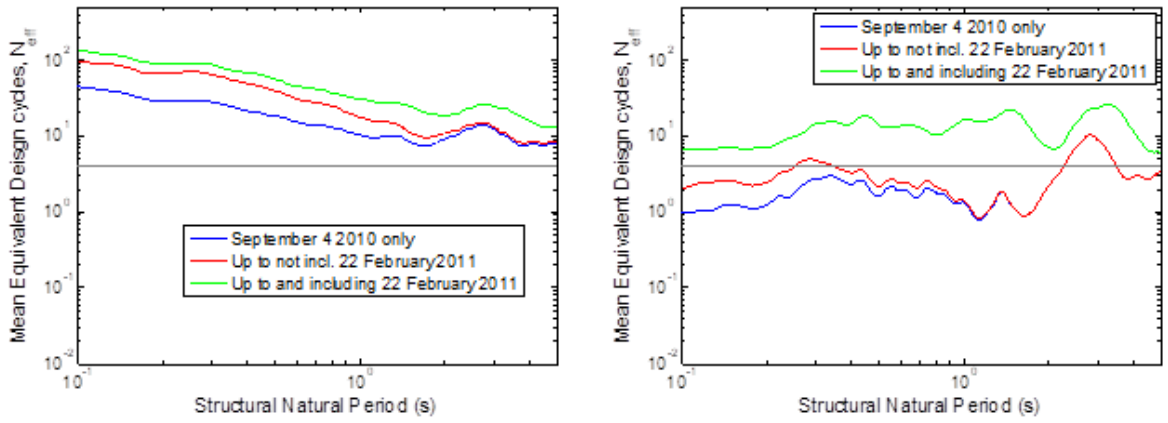

Figure 8-16. Total number of equivalent design code cycles for fatigue exponent C= 1 (left) and C= 2 (right), based on NZS1170.5 (Mander and Rodgers, 2013). Courtesy of G. W. Rodgers.

Step 4. The structural displacement capacity, $\Delta_{SC,1}$ is estimated (solid red circle). In this example it is considered that $\Delta_{SC,1}$ is larger than $\Delta_{SD,1}$, therefore the building's seismic performance is satisfactory, and no demolish/retrofit action would be required.

Step 5. Before assessing the damaged building for a future code-level aftershocks, the capacity curve is updated accounting for (at a component level) stiffness deterioration due to cyclic response and the residual strain capacity. If required, the aftershock demand spectrum can also be increased to account for the reduction in the energy absorption capabilities after a portion of it has been exhausted during the mainshock (see "100%NBS damaged" curve in Figure 8-15*b*). Steps 4 and 5 implicitly mean that after the mainshock building's displacement capacity has been reduced, and possibly its strength as well (e.g., some plastic hinges have failed).

Step 6. Similar to step 2, the structure displacement demand $\Delta_{SD,2}$ (empty red circle in Figure 8-15*b*) is obtained, and plastic strain demands ε_{p2}, as well as the effective structural vibration period T_{e2} are estimated.

Step 7. With the above information, the fatigue life $N_f(\varepsilon_{p2})$ and cyclic fatigue demand $n(T_{E2})$ are estimated, and the combination of cyclic demand vs capacity ratios during the mainshock and aftershock $f(n_1/N_1+n_2/N_2)$ is checked. In this example it is considered that some structural elements fail (i.e., the ratio is larger than 1.0), therefore, an iterative process is followed by reducing the %NBS until $f(n_1/N_1+n_2/N_2)$= 1.0 (or to a certain predetermined value), and consequently, $\Delta'_{SD,2}$, the updated structural displacement demand is obtained.

Step 8. The new structural displacement capacity, $\Delta_{SC,2}$ is estimated (solid red circle). Here it is considered that $\Delta_{SC,2}$ is greater than $\Delta'_{SD,2}$ (if it was found to be smaller, then a new iterative process would be required). With the XX%NBS achieved (e.g., 50%NBS), a decision-making process is performed to decide how and whether to make safe the damaged structure (i.e., repair, strengthen) or demolish/rebuild.

8.6 Loss of initial (elastic) stiffness

As described in Section 8.2.2 and Section 8.2.3, Fema 306 and Polese et al (2013) proposed modification factors to account for stiffness deterioration in damaged reinforced concrete shear walls and non-conforming columns, respectively, depending on the severity of the damage. However, very little information has been provided to account for the loss of initial stiffness in damaged beam plastic hinges.

Additional *FE* simulations were performed on the experimental model described in Section 6.1 in order to investigate such effect. As in Chapter 6, the effect of the reinforcement content was also studied. For each model, an initial monotonic load was applied until reaching a certain displacement level, then the load was completely removed and applied again. The initial stiffness in the second loading phase was determined and associated to the peak curvature ductility demand reached in the first loading phase. Figure 8-17 shows an example of the force-displacement regime. Table 8-9 to Table 8-11 show the results obtained for three different reinforcement contents.

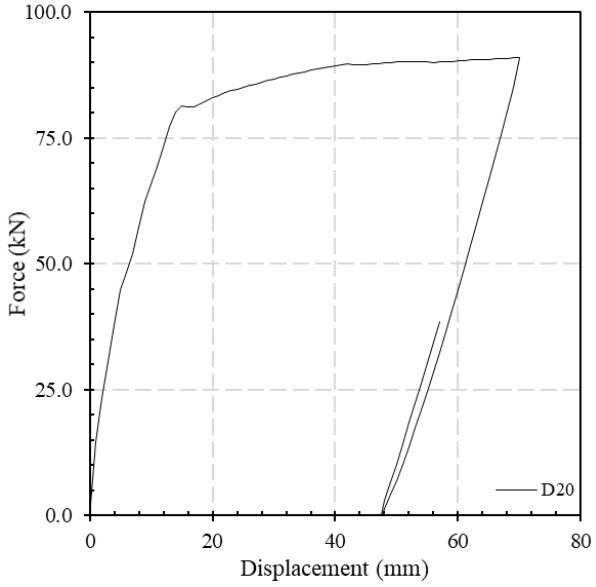

Figure 8-17. Force-displacement curve with unloading-reloading phase following a displacement ductility of 4.5, for a specimen reinforced with D20 bars.

The yield curvature was estimated as recommended by Priestley et al (2007).

$$\varphi_y = 2 \cdot \frac{\varepsilon_y}{h_{beam}} \tag{8-27}$$

It is interesting to note that the upper-bound value of I_{eff}/I_{gross} = 0.50 recommended by Paulay & Priestley (1992) appears to apply to highly reinforced members (ρ_s > 1.61%) and low ductility demands, typically μ_ϕ < 5.0 (see Table 8-11). On the other hand, the lower bound value of I_{eff}/I_{gross} = 0.30 appears to apply to members with ρ_s > 1.03%, and ductility demands μ_ϕ > 10 (see Table 8-10 and Table 8-11).

Table 8-9. Displacement, peak curvature, peak curvature ductility demand, and effective moment of inertia in the reloading phase obtained numerically for a beam reinforced with D10 bars (ρ_s = 0.40%).

Beam rotation	Displacement (mm)	Curvature, ϕ (rad/m)	ϕ/ϕ_y	I_{eff}/I_{gross}
Cracking	1	0.000544	0.06	0.216
1st yield	6	0.006819	0.72	0.230
0.01	16	0.034248	3.63	0.351
0.015	24	0.047134	5.00	0.145
0.02	31	0.060664	6.43	0.128
0.025	39	0.078579	8.33	0.130
0.03	47	0.095463	10.12	0.133
0.035	55	0.111350	11.81	0.135
0.04	63	0.125509	13.31	0.140

Table 8-10. Displacement, peak curvature, peak curvature ductility demand, and effective moment of inertia in the reloading phase obtained numerically for a beam reinforced with D16 bars (ρ_s = 1.03%).

Beam rotation	Displacement (mm)	Curvature, ϕ (rad/m)	ϕ/ϕ_y	I_{eff}/I_{gross}
Cracking	1	0.000544	0.06	0.359
1st yield	10	0.00758	0.80	0.422
0.01	16	0.021935	2.33	0.343
0.015	24	0.037095	3.93	0.348
0.02	31	0.049253	5.22	0.370
0.025	39	0.056694	6.01	0.330
0.03	47	0.067476	7.16	0.379
0.035	55	0.078745	8.35	0.333
0.04	63	0.093474	9.91	0.315

Table 8-11. Displacement, peak curvature, peak curvature ductility demand, and effective moment of inertia in the reloading phase obtained numerically for a beam reinforced with D20 bars (ρ_s = 1.61%).

Beam rotation	Displacement (mm)	Curvature, ϕ (rad/m)	ϕ/ϕ_y	I_{eff}/I_{gross}
Cracking	1	0.000544	0.06	0.523
0.01	16	0.016296	1.73	0.498
0.015	24	0.030138	3.20	0.571
0.02	31	0.040458	4.29	0.552
0.025	39	0.052102	5.53	0.587
0.03	47	0.061324	6.50	0.517
0.035	55	0.072781	7.72	0.392
0.04	63	0.089683	9.51	0.327
0.045	70	0.105299	11.17	0.308

Figure 8-18 shows the effective member moment of inertia values for different reinforcement content, and the limits recommended by Paulay and Priestley (1992). It is evident that even at curvature demands slightly exceeding the curvature at cracking, there is an abrupt drop in the elastic stiffness in the reloading phase.

Table 8-12 shows the effective member moment of inertia values recommended by the NZS 3101:2006 (incorporating amendment No. 1, 2 and 3, issued August 2017). Based on Figure 8-18, it is evident that for nominally ductile structures (μ = 1.25), unless the *SLS* event is such that the cracking moment is not exceeded, the effective moment of inertia will never be equal to the gross moment of inertia as recommended by the NZS 3101:2006, it will be equal to 0.50 at the most for highly reinforced beams.

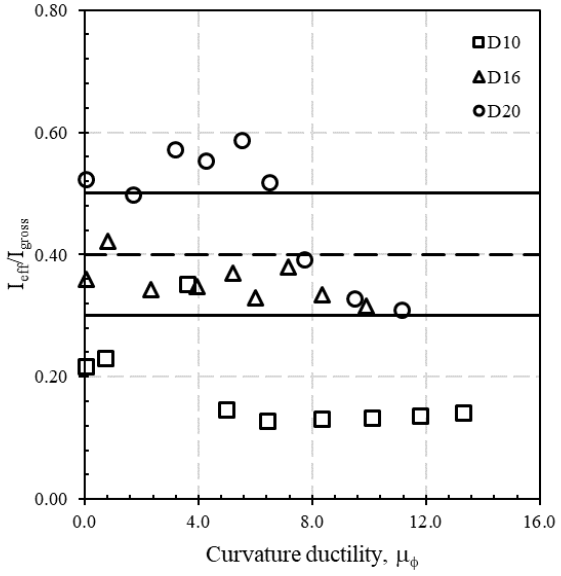

Figure 8-18. Effective member moment of inertia values for different reinforcement content. The solid lines and dash line represent the range and average values recommended by Paulay & Priestley (1992).

Table 8-12. Effective section properties as a proportion of gross section properties (NZS 3101:Part 2:2006).

Ultimate Limit State		Serviceability Limit State		
f_y = 300MPa	f_y = 500MPa	μ = 1.25	μ = 3	μ = 6
0.43 I_{gross} 0.5% ≤ ρ_s ≤ 1.75%	0.32 I_{gross} 0.3% ≤ ρ_s ≤ 1.4%	I_{gross}	0.70 I_{gross}	0.50 I_{gross}

Figure 8-19 shows, according to the NZS 3101:2006, how the effective stiffness at first yield varies with different concrete strengths and reinforcement proportions. The code states that "*with low reinforcement contents the stiffness is high…with increasing reinforcement proportions the effective stiffness first decreases rapidly before increasing gradually with higher reinforcement contents…while concrete strength has relatively little influence on stiffness the reinforcement grade has a significant effect*". Firstly, as previously stated, unless the cracking moment is not exceeded, the effective stiffness will never be as high as the gross stiffness, regardless of the amount of reinforcement. Secondly, the statement regarding the stiffness reduction with increasing reinforcement proportions clearly violates the fact that the stiffness is proportional to the strength (Priestley et al, 2007). Thirdly, although the reinforcement grade influences the effective stiffness, the shift in the moment inertia ratios appears to be more related to the fact that steel Grade 500 is equivalent to 5/3 streel Grade 300. For instance, the low point in Figure 8-19*b* occurs at about ρ_s= 0.8%, whereas in Figure 8-19*a* it occurs at about ρ_s= 0.5% (which is approximately 3/5 or 60% of ρ_s= 0.8%).

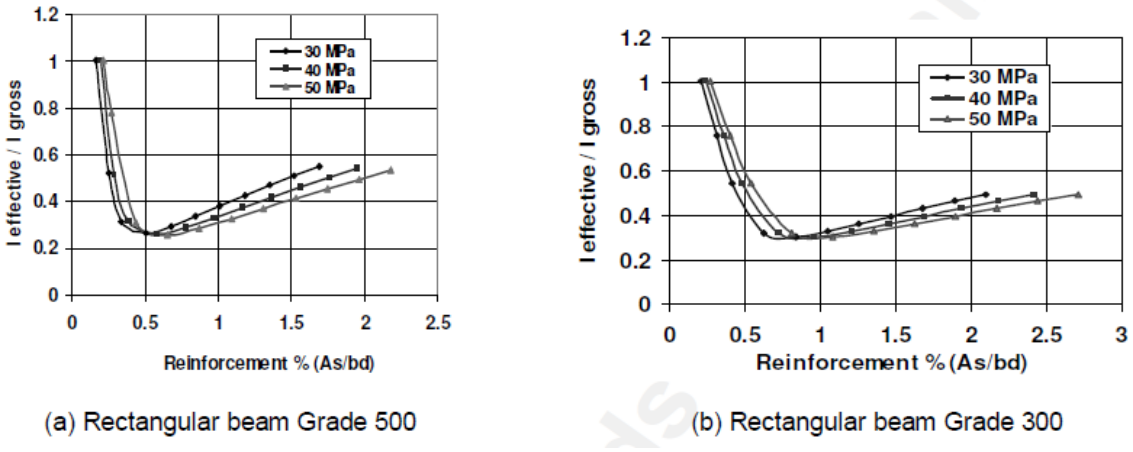

Figure 8-19. Effective stiffness of beams (NZS 3101:2006)

Thus, instead of limiting the effective moment of inertia to the grade of steel used and the displacement ductility, it appears more appropriate to define the effective moment of inertia based on the amount of reinforcement and curvature ductility demands.

For beams with reinforced with steel Grade 300, and steel reinforcement ρ_s greater than 1.0% (or greater than 0.6% for Grade 500) and for high curvature ductility levels ($\mu_\phi > 10$), the effective moment of inertia can be considered as $0.30I_{gross}$, regardless of the amount (or type) of steel.

On the other hand, for beams with steel reinforcement ρ_s greater than 1.0% (or greater than 0.6% for Grade 500) and for low curvature ductility levels ($\mu_\phi < 10$), the effective moment of inertia can be considered as $0.35I_{gross}$ for ρ_s= 1.0%, and $0.50I_{gross}$ for ρ_s= 1.6%.

For lightly reinforced beams with ρ_s = 0.4% (or 0.24% for Grade 500), the effective moment of inertia can be as low as $0.15I_{gross}$ to $0.20I_{gross}$, regardless of the curvature ductility demand.

As a general comment, it is noteworthy that repair techniques such as the ones described in Chapter 2, if performed properly, can partially restore the initial stiffness of damaged elements. In this case, the values suggested in this Section can be considered conservative values.

8.7 Conclusions

This Chapter presented a literature review on the current practice to assess the seismic residual capacity of structures. It also described the various factors affecting the residual fatigue life at a component level (i.e., plastic hinge) of well-designed reinforced concrete frames, which, if not properly considered during the assessment process, can lead to unconservative estimations of the residual capacity of the structure. Equations to quantify each of the factors were proposed, and a methodology to incorporate them into a full displacement-based procedure for pre-earthquake and post-earthquake seismic assessment was also presented.

For post-earthquake seismic assessments, special attention must be given to the observed damage (e.g., crack widths and patterns, “real” plastic hinge lengths, residual drifts, damage to non-structural components) so that the proposed procedure can be calibrated and/or validated.

Non-linear finite elements simulations were used to quantify the loss of initial stiffness. The numerical model was based on a specimen tested in the laboratory and validated by comparing the analytical results with the experimental observations. Based on the results, effective moments of inertia are proposed. The main conclusions of the parametric investigation are as follows:

1. The upper-bound value of I_{eff}/I_{gross} = 0.50 recommended by Paulay & Priestley (1992) appears to apply to highly reinforced members (ρ_s > 1.6%) and low ductility demands, typically μ_ϕ < 5.0, whereas the lower bound value of I_{eff}/I_{gross} = 0.30 appears to apply to members with ρ_s > 1.0%, and ductility demands μ_ϕ > 10.
2. Even at curvature demands slightly exceeding the curvature at cracking, there is an abrupt drop in the elastic stiffness.
3. Unlike the NZS3101 that defines the effective moment of inertia based on the grade of steel used and the displacement ductility, it appears more appropriate to define the effective moment of inertia based on the amount of reinforcement and curvature ductility demand.

8.8 References

Applied Technology Council, ATC (1998) *FEMA 306 – Evaluation of earthquake damaged concrete and masonry wall buildings: Basic procedures manual*, Federal Emergency Management Agency, Washington.

Brown, J., Kunnath, S.K. (2004) "Low-cycle fatigue failure of reinforcing steel bars," *ACI Materials Journal*, Vol. 101(6): 457-466.

Dowling, N.E. (1977) "Crack growth during low-cycle fatigue of smooth axial specimens," Cyclic Stress-Strain and Plastic Deformation Aspects of Fatigue Crack Growth, ASTM STP 637, *American Society for Testing and Materials*, pp. 97-121.

Engineering Advisory Group, EAG (2013) *Guidance on detailed engineering evaluation of earthquake affected non-residential buildings, Part 3 – Technical guidance, Section 9 – Reinforced concrete buildings*, Revision 6.

Hancock, J., Bommer, J.J. (2005) "The effective number of cycles of earthquake ground motion," *Earthquake Engineering and Structural Dynamics*, Vol. 34: 637-664.

Hawileh, R., Rahman, A., Tabatabai, H. (2010) "Evaluation of the low-cycle fatigue life in ASTM A706 and A615 grade 60 steel reinforcing bars," *Journal of Materials in Civil Engineering*, Vol. 22: 65-76.

Kunnath, S.K., El-Bahy, A., Taylor, A.W., Stone, W.C. (1997) *Cumulative seismic damage of reinforced concrete bridge piers*, National Institute of Standards and Technology, NISTIR 6075.

Lettow, S. (2006) *Ein Verbundelement für nichtlineare Finite Elemente Analysen – Anwendung auf Übergreifungsstöße (A bond element for nonlinear finite element analysis – Applied on splices)*, PhD Dissertation, IWB, Universität Stuttgart, Germany (in German).

Loporcaro, G., Pampanin, S., Kral, M.V. (2016) "Effect of strain-rate and material characteristics on the seismic residual capacity of reinforced concrete plastic hinges: numerical investigation," *2016 New Zealand Society of Earthquake Engineering Conference*, Christchurch, New Zealand.

Maeda, M., Nishida, T., Matsukawa, K., Murakami, M. (2017) "Revision of guideline for post-earthquake damage evaluation of reinforced concrete buildings in Japan," *16th World Conference on Earthquake Engineering*, Santiago, Chile.

Maeda, Nishida, T., Matsukawa, K., Murakami, M. (2017) "Revision of guideline for post-earthquake damage evaluation of reinforced concrete buildings in Japan," *Proceedings of the 16th World Conference on Earthquake Engineering*, Santiago, Chile.

Malhotra, P.K. (2002) "Cyclic-demand spectrum," *Earthquake Engineering and Structural Dynamics*, Vol. 31: 1441-1457.

Mander, J.B., Panthaki, F.D., Kasalanati, A. (1994) "Low-cycle fatigue behaviour of reinforcing steel," *Journal of Materials in Civil Engineering*, Vol. 6(4): 453-468.

Mander, J.B., Rodgers, G.W. (2013) "Cyclic fatigue demands on structures subjected to the 2010-2011 Canterbury earthquake sequence," *2013 New Zealand Society of Earthquake Engineering Conference*, Wellington, New Zealand.

Montejo, L.A., Kowalsky, M.J. (2007) *CUMBIA, set of codes for the analysis of reinforced concrete members*, North Carolina State University, Technical Report No. IS-07-01.

Mukai, T., Kabeyasawa, T., Tani, M., Suwada, H., Fukuyama, H. (2017) "Residual seismic capacity of ductile rc frame with wing walls based on full-scale loading test," *Bulletin of the New Zealand Society for Earthquake Engineering*, Vol. 50(44): 565-573.

Paulay, T., Priestley, M.N.J. (1992) *Seismic design of reinforced concrete and masonry buildings*, John Wiley & Sons, USA.

Pekcan, G., Mander, J.B., Chen, S.S. (1999) "Fundamental considerations for the design of non-linear viscous dampers," *Earthquake Engineering Structural Dynamics*, Vol. (28): 1405-1425.

Polese, M., Di Ludovico, M., Prota, A., Manfredi, G. (2013) "Damage-dependent vulnerability curves for existing buildings," *Earthquake Engineering and Structural Dynamics*, Vol. 42: 853-870.

Priestley, M.N.J., Calvi, G.M., Kowalsky, M.J. (2007) *Displacement-based seismic design of structures*, IUSS Press, Pavia, Italy.

Reitherman, R (2006) *Connections: Robert Park, Tom Paulay*, The EERI Oral History Series, Oakland, CA.

SESOC (2011) *Preliminary observations from Christchurch earthquakes*, Structural Engineering Society, New Zealand.

Stafford, P.J., Bommer, J.J. (2009) "Empirical equations for the prediction of the equivalent number of cycles of earthquake ground motion," *Soil Dynamics and Earthquake Engineering*, Vol. 29(11): 1425-1436.

9 CONCLUDING REMARKS AND FUTURE RESEARCH

9.1 Concluding remarks

In Chapter 2, a literature review on previous research about the effectiveness of epoxy injection repairs for seismic applications has been presented. The focus of this literature review was repairs of damaged beam-column joints and structures designed according to modern codes, in which a stable inelastic behaviour is expected to occur.

It was observed that the repaired specimens had a reduced initial stiffness compared with the prototype (or undamaged) specimen with no apparent reduction in their strength and exhibited higher displacement ductility capacities. Although the bond between the steel and concrete was partially restored, it allowed the repaired specimen to dissipate at least the same amount of hysteretic energy. The cracking pattern between the prototype and epoxy-repaired specimens was very similar, with new cracks formed adjacent to the epoxy injected cracks; the repaired cracks did not open-up. Thus, even when the specimens had failed or suffered severe damage, evidenced by wide cracks, concrete crushing and spalling, and buckling of longitudinal reinforcement, the strength and ductility exhibited by the repaired specimens was similar or in some cases, better than the prototype specimen.

Experimental tests on buildings subjected to earthquake loading demonstrated that even though the damage level was severe, the ability of the epoxy injection and repairs in general to restore the initial stiffness of the structure is significant.

In terms of damage assessment and repair guidelines, although there is some discrepancies between the assessment criteria and repair recommendations, it appears that there is consensus within the international community that concrete elements with cracks less than 0.2 mm wide only require cosmetic repairs; epoxy injection repairs of cracks less and 2.0 mm wide and concrete patching of spalled cover concrete (i.e., minor to moderate damage) is an appropiate repair strategy; and for severe damaged components (e.g., cracks greater than 2.0 mm wide,

crushing of the concrete core, buckling of the longitudinal reinforcement) local replacement of steel and/or concrete in addition to epoxy crack injection is more appropriate.

Chapters 3 and 4 described the experimental program and test results on three modern designed beam-column joints extracted from a 1980s 22-storey reinforced concrete frame building in the Christchurch's Central Business District (CBD), damaged after the 2010-2011 Christchurch earthquakes sequence (CES). Two of the specimens were tested under quasi-static cyclic loading to a level of cracking pattern consistent with what can be considered a moderate level of damage, repaired with an epoxy injection technique, and subsequently retested until reaching failure.

All the specimens failed in a flexure-shear mechanism, with severe diagonal cracking induced by the hooked bars details within the plastic hinge relocation detail (PHRD), although the epoxy injection allowed for some damage relocation outside the plastic hinge relocation detail.

A reasonable level of energy dissipation at both low (i.e., serviceability limit state) and high (i.e., ultimate limit state) rotation levels was achieved in the repaired specimens. The computed values are comparable to the ones from the unrepaired specimens. A secant stiffness reduction was observed in the repaired specimens at low rotation levels (below to the onset of nonlinearity, approximately). However, this stiffness reduction does not seem to be equally affected at high rotation levels.

Non-linear finite element (FE) simulation on a beam-column joint with similar characteristics showed that the flexure-shear failure mechanism within the PHRD could have been avoided by either increasing the shear reinforcement within the PHRD, increasing the shear span of the beam, or a combination of both.

Chapter 5 presented the results of experimental and numerical investigations on well-designed reinforced concrete beam-to-column joints, targeting at identifying and understanding qualitatively and quantitatively the effect of parameters such as bond deterioration, steel and concrete material properties, as well as the amount of longitudinal reinforcement, on the cracking pattern and nonlinear behaviour of reinforced concrete plastic hinges.

It was observed that lower number of cracks but with wider openings are expected to occur for larger f'_c and smaller ρ_s values. Moreover, it was observed that f_t strongly affects the expected cracking pattern in the beam-column joints, the latter being more uniformly distributed (i.e., more cracks and smaller crack widths) for lower f_t values.

Strain rate effects do not seem to play an important role on the cracking pattern. However, small variations in the cracking pattern were observed for low reinforcement content as it approaches to the minimum required as per NZS 3101:2006.

The numerical simulations also showed large plastic deformations at few locations (one-to-two major cracks) in plastic hinges, even though the longitudinal reinforcement content was above the minimum required as per NZS3101.

Chapter 6 presented a numerical parametric study on reinforced concrete beams with the aim to investigate the maximum and residual crack widths. Simple equations were developed in order to relate the maximum and residual crack widths with the steel strain at peak displacement.

The steel strain at the most critical location reduces cyclically due to the cyclic bond deterioration. Therefore, assuming a constant steel strain equal to the strain measured in the first cycle when the bond has not been lost, is a conservative approach.

It seems possible to develop a single relationship between residual crack width ratios and steel strain at peak displacement regardless of the amount of longitudinal reinforcement, for flexural dominated members.

Beam elongation is able to develop axial loads in beams of up to $0.10 f'_c \cdot A_g$. The axial load tends to reduce the residual crack width ratios. It was observed that axial load ratios $P_u / f'_c \cdot A_g$ of 0.30 are capable of closing the crack completely (because of the re-centring effect of the axial load) regardless the level of strain at peak displacement.

The mean steel strain between two adjacent cracks depends on the bar diameter and more precisely, on the bond.

Chapter 7 presented a literature review on fracture of reinforcing steel due to low-cycle fatigue, including recent research using steel manufactured per New Zealand standards. Except for one research where the specimens were encased in steel thus preventing buckling, buckling of the rebars was always present.

It appears that fatigue life is influenced by the diameter of the bar and the geometry of the rolled-on deformations.

Experimental results describing the influence of the cyclic effect on the ultimate strain capacity of the steel were also discussed, and preliminary equations to account for that effect were proposed.

Based on previous research on smooth specimens fabricated using A533B steel, it appears that, when buckling is prevented, cracks initiates at fractions of fatigue life, n/N_f, equal to or greater than 10%.

If buckling is not prevented, experimental tests on a limited number of samples indicate that the reduction of the strain at the ultimate tensile strength due to cyclic loading for fatigue lives n/N_f of 10%, 33%, and 66% is estimated to be 6%, 22%, and 34% of the that obtained with a virgin sample.

Chapter 9, presented a literature review on the current practice to assess the seismic residual capacity of structures. It also described the various factors affecting the residual fatigue life at a component level (i.e., plastic hinge) of well-designed reinforced concrete frames, which, if not properly considered during the assessment process, can lead to unconservative estimations of the residual capacity of the structure. Equations to quantify each of the factors were proposed, and a methodology to incorporate them into a full displacement-based procedure for pre-earthquake and post-earthquake seismic assessment was also presented.

For post-earthquake seismic assessments, special attention must be given to the observed damage (e.g., crack widths and patterns, “real” plastic hinge lengths, residual drifts, damage to non-structural components) so that the proposed procedure can be calibrated and/or validated.

Non-linear finite elements simulations were used to quantify the loss of initial stiffness. It was observed that, even at curvature demands slightly exceeding the curvature at cracking, there is an abrupt drop in the elastic stiffness. The upper-bound value of $I_{eff}/I_{gross} = 0.50$ recommended by Paulay & Priestley (1992) appears to apply to highly reinforced members ($\rho_s > 1.6\%$) and low ductility demands, typically $\mu_\phi < 5.0$, whereas the lower bound value of $I_{eff}/I_{gross} = 0.30$ appears to apply to members with $\rho_s > 1.0\%$, and ductility demands $\mu_\phi > 10$.

Unlike the NZS3101 that defines the effective moment of inertia based on the grade of steel used and the displacement ductility, it appears more appropriate to define the effective moment of inertia based on the amount of reinforcement and curvature ductility demand.

9.2 Limitations

It is important to mention that this research project is deterministic in nature, complemented with some parametric analysis. Although there are a number of practical cases where earthquake design and assessment are performed based on a deterministic approach, this research project has to be further developed from a probabilistic standpoint.

The effect of strain rate and material characteristics (Chapter 5), and the crack widths analytical investigation (Chapter 6) are based on a limited amount of experimental and numerical simulations. In the case of Chapter 6, the empirical equations were developed for specific material properties (NZ steel Grade 300, and concrete strength f'_c of 30 MPa).
The fatigue life empirical equations described in Chapter 7 were mostly calibrated for cases where buckling of the longitudinal reinforcement is not prevented. Also, their results can vary depending on the type of steel, bar diameter and rib geometry. Regarding the cyclic effect on ultimate strain capacity, the empirical equation was calibrated on a limited amount of experimental tests, using D12 NZ steel Grade 300 samples. A more comprehensive experimental campaign is needed in order to validate or calibrate the equation and expand its applicability to other types of steel and bar diameters.
Regarding the methodology developed to assess the residual capacity of reinforced concrete frames (Chapter 8), it does not account for the dynamic (i.e., earthquake) effect on the residual crack widths, therefore the residual crack widths after a real earthquake can be much smaller than those predicted with the proposed equations. It is noteworthy that this effect was somehow mitigated in the proposed methodology through the estimation of the residual crack widths based on the steel strain at the first peak. As discussed in Chapter 6, it was observed that peak strains decrease as the number of cycles increase due to cyclic bond deterioration, reaching in some cases a constant strain value.

9.3 Future research

Regarding Chapter 2, more literature review on effectiveness of epoxy repairs is needed as new experimental research becomes available within the engineering community.
In particular, more experimental campaigns such as the one described in Chapters 3 and 4, where real specimens are subjected to earthquake loading and the effectiveness of the epoxy injection techniques, is needed. The campaigns should also be extended to shear wall elements subjected to damage levels line with what is typically observed during moderate earthquakes, where epoxy injection techniques appear to be an adequate repair strategy.
Chapter 5 introduced how the cracking pattern can be affected by the amount of longitudinal reinforcement. However, more numerical investigations are needed to determine whether the minimum steel per NZS3101 has to increase in order to enforce a well distributed cracking pattern within the plastic hinges. More investigation is also needed to ascertain that strain rate effects do not seem to play an important role on the cracking pattern, and to define the

relationship between key parameters and strain rates which could determine a change in the cracking pattern.

Additional parametric analyses such as those introduced in Chapter 6 are needed. Parameters such as beam width-to-depth ratios, tensile and compressive concrete strength, and steel grade have to be considered. The dynamic effect on reducing the Res/Max crack width ratios deserves also attention.

As describer in Chapter 7, except for one research where the specimens were encased in steel thus preventing buckling, buckling of the rebars was always present. It is very well known that buckling reduces the fatigue life of the specimen when compared with a buckling restrained specimen tested at the same strain amplitude. Therefore, more low-cycle fatigue tests in which buckling of the rebar is prevented, are required.

A more comprehensive experimental campaign, including buckling restrained tests, is also required in order to validate and/or calibrate the empirical equation proposed to estimate the reduction of the ultimate strain capacity in unaged steel reinforcing bar samples due to the cyclic effect.

The methodology proposed in Chapter 8 should be updated as more investigation becomes available. It would also interesting to expand the methodology from a probabilistic stand point, incorporating the variability of the material properties and of the various factors that form the basis of the proposed method. The effect of the moment gradient on the strain distribution within the plastic hinge during future earthquakes, once strain hardening over a finite length of bar has occurred as a result of a previous earthquake, thus becoming stronger than the adjacent bar segment that has reached a lower strain level, has to be studied.

Additional parametric analyses to investigate the effect of width-to-depth ratios, tensile and compressive concrete strength, and steel grade on the loss of the initial stiffness have also to be performed.

APPENDIX A

Table A- 1. Energy dissipation (E) and secant stiffness (K) characteristics.

	Total rotation	Avg. displacement	Average rotation	Total E	Avg. E	Avg. K
	(%)	(mm)	(%)	(kN-mm)	(kN-mm)	kN/mm
Test 1	0.10	1.680	0.07	342.0	114.0	76.9
	0.20	3.165	0.13	747.2	249.1	61.5
	0.50	6.543	0.26	2367.8	789.3	49.0
	0.75	9.549	0.38	3381.8	1127.3	44.0
	1.00	14.485	0.58	13976.9	4659.0	30.5
	1.50	26.353	1.05	47861.9	15954.0	17.1
	2.00	38.355	1.53	74931.3	24977.1	11.8
	2.50	50.825	2.03	93689.9	31230.0	8.9
Test 2.1	0.10	1.832	0.07	595.4	198.5	56.0
	0.20	3.284	0.13	1905.4	635.1	46.5
	0.50	7.007	0.28	7764.5	2588.2	40.2
	0.75	10.679	0.43	13039.5	4346.5	36.0
	1.00	15.663	0.63	24355.9	8118.6	27.0
Test 2.2	0.10	1.857	0.07	623.9	208.0	55.7
	0.20	3.292	0.13	2143.2	714.4	45.1
	0.50	7.158	0.29	8476.6	2825.6	39.5
	0.75	10.964	0.44	13880.0	4626.7	36.4
	1.00	16.122	0.64	23887.6	7962.5	27.3
	1.50	28.156	1.12	58859.0	19619.7	15.8
	2.00	40.185	1.60	87935.9	29312.0	11.1
	2.50	52.885	2.11	111464.4	37154.8	8.3
	3.50	78.621	3.14	151648.2	50549.4	5.3
	4.50	105.786	4.22	126631.7	42210.6	2.9
Test 3.1	0.10	1.741	0.07	819.1	273.0	53.0
	0.20	2.996	0.12	2288.4	762.8	43.6
	0.50	6.735	0.27	7536.0	2512.0	37.7
	0.75	10.122	0.40	11680.6	3893.5	35.9
	1.00	14.665	0.59	19350.8	6450.3	29.3
	1.50	26.213	1.05	52488.7	17496.2	17.1
Test 3.2	0.10	2.023	0.08	519.4	173.1	33.6
	0.20	3.316	0.13	1693.1	564.4	31.9
	0.50	7.032	0.28	6463.9	2154.6	31.0
	0.75	9.842	0.39	11850.7	3950.2	29.8
	1.00	13.147	0.52	15761.5	5253.8	29.8
	1.50	22.922	0.92	38790.2	12930.1	21.5
	2.00	35.378	1.41	74087.6	24695.9	13.9
	2.50	47.895	1.91	108739.4	36246.5	10.3
	3.50	72.900	2.91	178322.8	59440.9	6.7
	4.50	99.579	3.98	183726.9	61242.3	4.2

Table A- 2. Energy dissipation (E) and secant stiffness (K) characteristics at first cycle.

	Avg. displacement	Average rotation	E	E	K
	(mm)	(%)	(kN-mm)	(kN-m)	(kN/mm)
Test 1	1.687	0.07	111.8	0.112	77.3
	3.111	0.12	242.0	0.242	63.2
	6.443	0.26	871.9	0.872	50.3
	9.470	0.38	1263.4	1.263	44.9
	14.334	0.57	5370.6	5.371	31.6
	26.149	1.04	16878.6	16.879	17.8
	38.060	1.52	25656.2	25.656	12.1
	50.608	2.02	32758.2	32.758	9.1
Test 2.1	1.837	0.07	211.4	0.211	55.9
	3.263	0.13	613.1	0.613	47.4
	7.044	0.28	2449.4	2.449	40.6
	10.684	0.43	4511.9	4.512	36.6
	15.616	0.62	8266.7	8.267	27.8
Test 2.2	1.828	0.07	237.0	0.237	56.8
	3.107	0.12	742.7	0.743	46.0
	7.162	0.29	2894.0	2.894	39.7
	10.891	0.43	4839.5	4.840	36.9
	16.009	0.64	7937.1	7.937	28.2
	27.994	1.12	19678.7	19.679	16.3
	39.404	1.57	29815.9	29.816	11.5
	52.848	2.11	37291.9	37.292	8.5
	77.880	3.11	56870.5	56.870	5.8
	104.632	4.18	50839.5	50.840	3.6
Test 3.1	1.755	0.07	288.2	0.288	52.8
	2.939	0.12	765.4	0.765	44.8
	6.718	0.27	2643.0	2.643	38.7
	10.101	0.40	3908.8	3.909	36.5
	14.594	0.58	7010.7	7.011	30.0
	26.146	1.04	18477.3	18.477	17.6
Test 3.2	2.057	0.08	182.9	0.183	34.4
	3.326	0.13	564.4	0.564	32.5
	6.989	0.28	2191.3	2.191	31.3
	9.377	0.37	4258.8	4.259	31.3
	13.130	0.52	5205.3	5.205	30.1
	22.678	0.91	13476.1	13.476	22.3
	35.037	1.40	24704.0	24.704	14.5
	47.609	1.90	36107.2	36.107	10.6
	72.443	2.89	61929.1	61.929	7.0
	98.255	3.92	70775.0	70.775	4.7

Table A- 3. Energy dissipation (E) and secant stiffness (K) characteristics at second cycle.

	Avg. displacement	Average rotation	E	E	K
	(mm)	(%)	(kN-mm)	(kN-m)	(kN/mm)
Test 1	1.692	0.07	109.2	0.109	76.3
	3.175	0.13	232.9	0.233	61.3
	6.552	0.26	722.9	0.723	48.9
	9.594	0.38	1060.9	1.061	43.8
	14.531	0.58	4315.6	4.316	30.1
	26.416	1.05	16182.1	16.182	16.9
	38.447	1.53	26606.8	26.607	11.8
	50.848	2.03	31926.5	31.927	8.9
Test 2.1	1.805	0.07	197.2	0.197	56.5
	3.317	0.13	655.6	0.656	45.6
	7.005	0.28	2694.0	2.694	40.5
	10.676	0.43	4213.6	4.214	36.0
	15.748	0.63	8035.5	8.036	26.8
Test 2.2	1.871	0.07	194.1	0.194	54.5
	3.372	0.13	711.5	0.712	44.5
	7.134	0.28	2784.3	2.784	39.6
	10.944	0.44	4436.4	4.436	36.4
	16.165	0.65	7845.4	7.845	27.1
	28.131	1.12	19869.8	19.870	15.8
	40.545	1.62	30065.9	30.066	10.9
	53.069	2.12	38559.9	38.560	8.3
	78.550	3.14	52953.5	52.953	5.3
	105.737	4.22	43552.2	43.552	2.8
Test 3.1	1.739	0.07	255.0	0.255	53.7
	3.056	0.12	732.7	0.733	43.9
	6.753	0.27	2444.0	2.444	37.3
	10.124	0.40	3822.2	3.822	35.8
	14.695	0.59	6210.8	6.211	29.2
	26.493	1.06	17851.8	17.852	16.8
Test 3.2	2.029	0.08	172.1	0.172	32.6
	3.297	0.13	563.2	0.563	31.6
	7.064	0.28	2139.3	2.139	31.1
	10.114	0.40	3820.3	3.820	29.2
	13.173	0.53	5208.4	5.208	29.7
	22.974	0.92	12512.1	12.512	21.2
	35.507	1.42	24978.6	24.979	13.8
	47.945	1.91	36693.8	36.694	10.3
	72.827	2.91	61429.0	61.429	6.8
	99.679	3.98	62423.5	62.423	4.1

Table A- 4. Energy dissipation (E) and secant stiffness (K) characteristics at third cycle.

	Avg. displacement	Average rotation	E	E	K
	(mm)	(%)	(kN-mm)	(kN-m)	(kN/mm)
Test 1	1.662	0.07	121.1	0.121	77.2
	3.210	0.13	272.3	0.272	60.1
	6.636	0.26	773.1	0.773	47.9
	9.583	0.38	1057.5	1.058	43.2
	14.590	0.58	4290.7	4.291	29.7
	26.495	1.06	14801.2	14.801	16.7
	38.558	1.54	22668.3	22.668	11.6
	51.019	2.04	29005.2	29.005	8.7
Test 2.1	1.854	0.07	186.8	0.187	55.6
	3.271	0.13	636.7	0.637	46.3
	6.972	0.28	2621.1	2.621	39.3
	10.678	0.43	4314.0	4.314	35.5
	15.627	0.62	8053.7	8.054	26.5
Test 2.2	1.871	0.07	192.7	0.193	55.7
	3.396	0.14	689.1	0.689	44.8
	7.179	0.29	2798.3	2.798	39.3
	11.058	0.44	4604.1	4.604	35.8
	16.193	0.65	8105.1	8.105	26.7
	28.342	1.13	19310.5	19.310	15.3
	40.604	1.62	28054.1	28.054	10.8
	52.740	2.11	35612.5	35.613	8.2
	79.433	3.17	41824.3	41.824	4.7
	106.987	4.27	32240.0	32.240	2.1
Test 3.1	1.727	0.07	276.0	0.276	52.6
	2.992	0.12	790.4	0.790	42.2
	6.735	0.27	2449.1	2.449	37.1
	10.140	0.40	3949.6	3.950	35.3
	14.707	0.59	6129.3	6.129	28.8
	26.000	1.04	16159.6	16.160	16.9
Test 3.2	1.984	0.08	164.5	0.164	33.7
	3.325	0.13	565.4	0.565	31.7
	7.044	0.28	2133.2	2.133	30.7
	10.035	0.40	3771.7	3.772	29.0
	13.137	0.52	5347.8	5.348	29.5
	23.116	0.92	12802.1	12.802	20.8
	35.591	1.42	24405.0	24.405	13.6
	48.131	1.92	35938.4	35.938	10.1
	73.430	2.93	54964.7	54.965	6.4
	100.802	4.02	50528.4	50.528	3.7

Table A- 5. Crack width measurements for cracks due to flexure-shear interaction (NM: Not Measured).

	Max. crack width, w_{max}		**Residual crack width, w_{res}**		**Crack width ratio, w_{max}/w_{res}**	
	+ve (mm)	-ve (mm)	+ve (mm)	-ve (mm)	+ve (-)	(-ve) (-)
Test 1	0	0	NM	NM	-	-
	0.1	0.1	NM	NM	-	-
	0.1	0.1	NM	NM	-	-
	0.2	0.2	NM	NM	-	-
	1.6	1.6	NM	NM	-	-
	4	8	NM	NM	-	-
	5	15	NM	NM	-	-
	NM	NM	NM	NM	-	-
Test 2.1	0	0	0	0	0.00	0.00
	0.1	0.1	0.1	0.08	1.00	0.80
	0.4	0.4	0.1	0.08	0.25	0.20
	1.2	0.5	0.3	0.08	0.25	0.16
	3	0.5	2	0.4	0.67	0.80
Test 2.2	0.15	0.15	0.08	0.08	0.53	0.53
	0.1	0.25	0.08	0.1	0.80	0.40
	0.3	0.45	0.1	0.1	0.33	0.22
	0.55	1.5	0.1	0.5	0.18	0.33
	1.5	3	1	1.5	0.67	0.50
	4.5	14.5	4	10.5	0.89	0.72
	6	15	6	14	1.00	0.93
	9	18	8	14.5	0.89	0.81
	NM	NM	NM	NM	-	-
	NM	NM	NM	NM	-	-
Test 3.1	0	0.125	0	0.08	0.00	0.64
	0.1	0.175	0	0.08	0.00	0.46
	0.175	0.3	0	0.08	0.00	0.27
	0.3	0.5	0.08	0.1	0.27	0.20
	1.3	2	0.6	1	0.46	0.50
	8.5	7	7.5	6	0.88	0.86
Test 3.2	0	0.1	0	0	0.00	0.00
	0.08	0.2	0.08	0.08	1.00	0.40
	0.15	0.2	0.08	0.1	0.53	0.50
	0.2	0.6	0.1	0.15	0.50	0.25
	0.25	0.8	0.1	0.175	0.40	0.22
	2	4	1	2.5	0.50	0.63
	4	7	2.5	5	0.63	0.71
	7	10	5	9	0.71	0.90
	NM	NM	NM	NM	-	-
	NM	NM	NM	NM	-	-

Table A- 6. Crack width measurements for cracks due to flexure.

	Max. crack width, w_{max}		**Residual crack width, w_{res}**		**Crack width ratio, w_{max}/w_{res}**	
	+ve (mm)	-ve (mm)	+ve (mm)	-ve (mm)	+ve (-)	(-ve) (-)
Test 3.2	0	0.1	0	0	0.00	0.00
	0.08	0.2	0.08	0.08	1.00	0.40
	0.15	0.2	0.08	0.1	0.53	0.50
	0.2	0.6	0.1	0.15	0.50	0.25
	0.25	0.8	0.1	0.175	0.40	0.22
	2	4	1	2.5	0.50	0.63
	4	7	2.5	5	0.63	0.71
	7	10	5	9	0.71	0.90
	NM	NM	NM	NM	-	-
	NM	NM	NM	NM	-	-

APPENDIX B

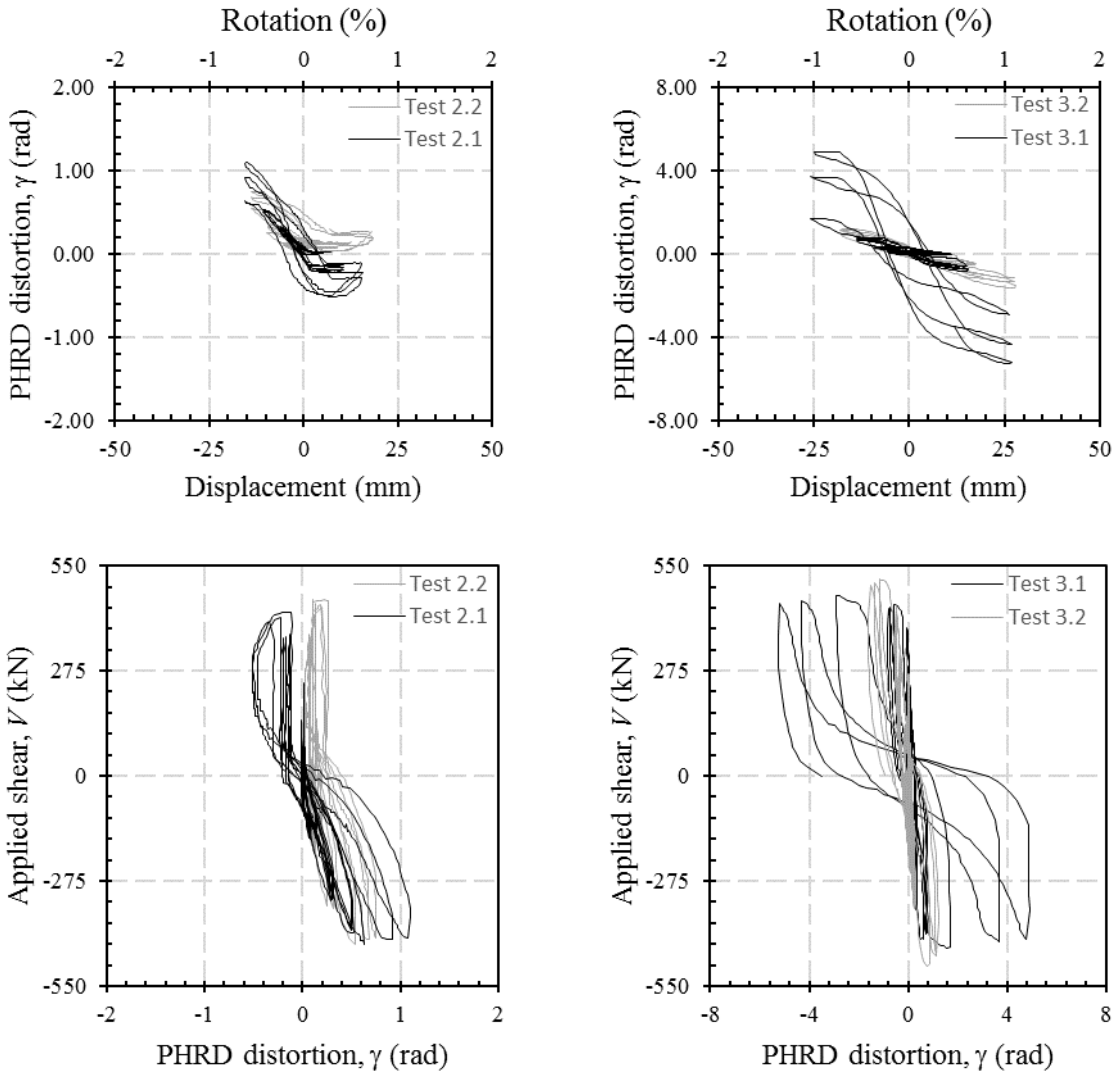

Figure B- 1. Shear distortion at the PHRD measured during Tests 2 (left) and Tests 3 (right).

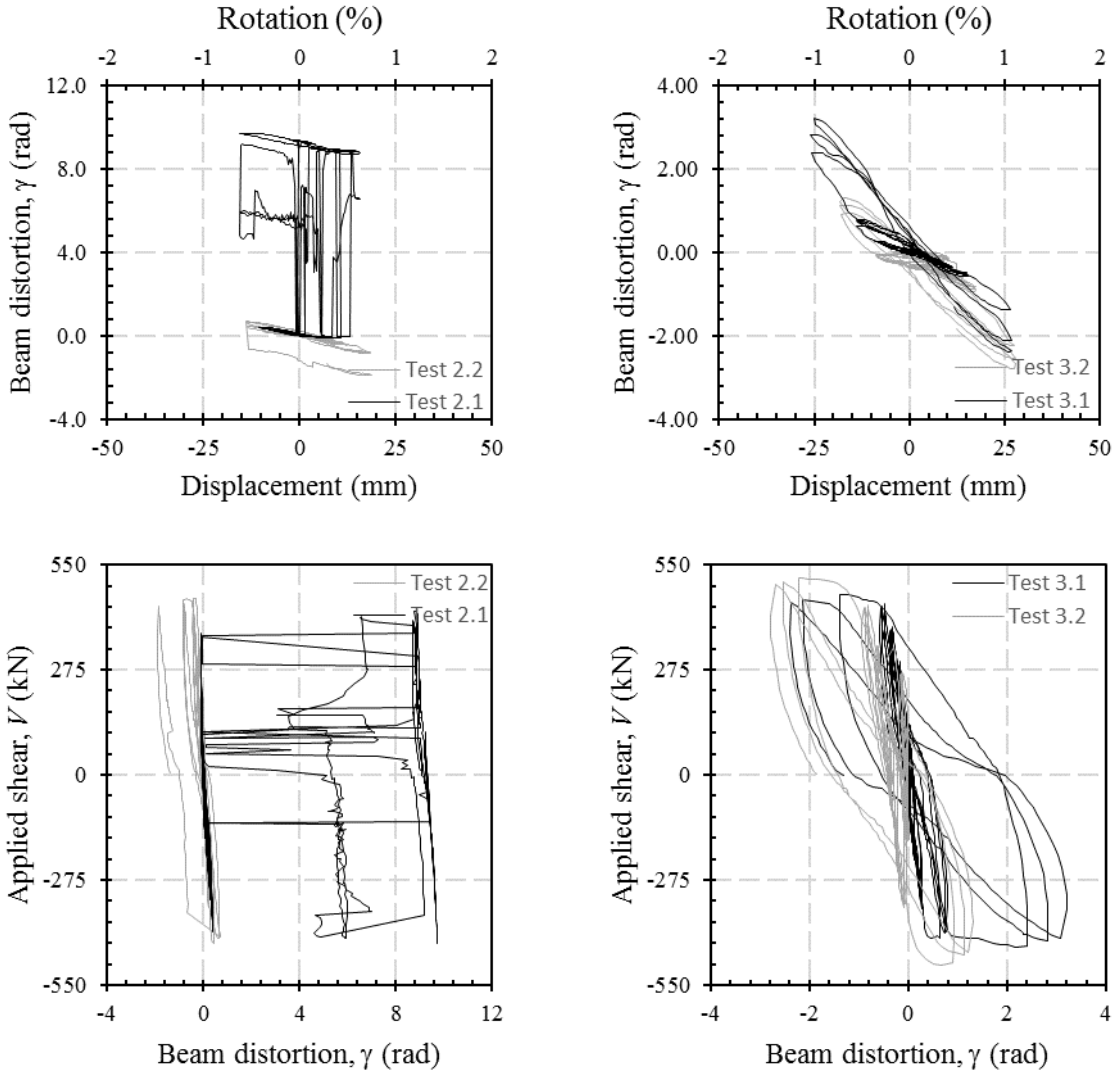

Figure B- 2. Shear distortion outside the PHRD measured during Tests 2 (left) and Tests 3 (right).

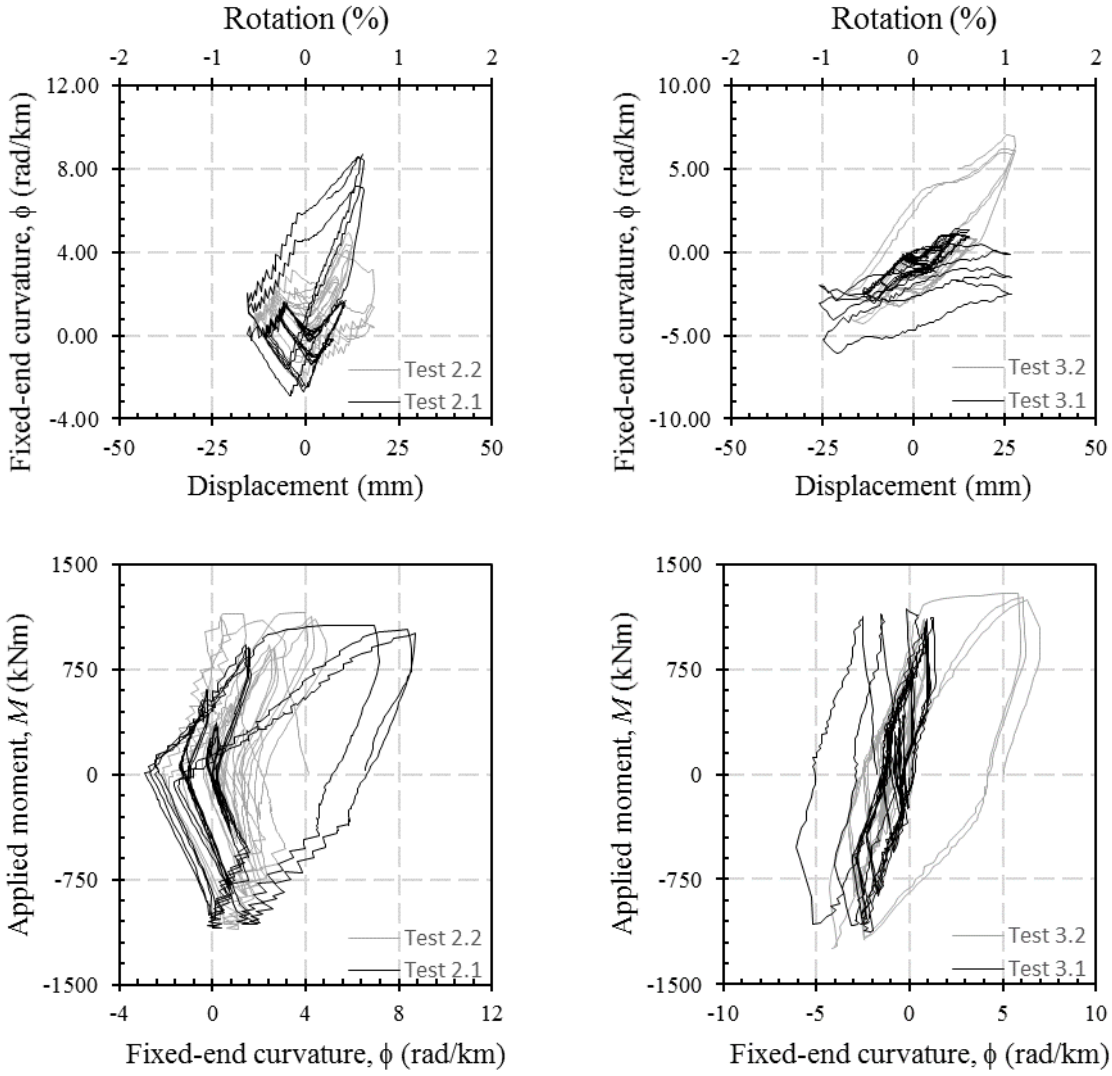

Figure B- 3. Curvature at beam-end measured during Tests 2 (left) and Tests 3 (right).

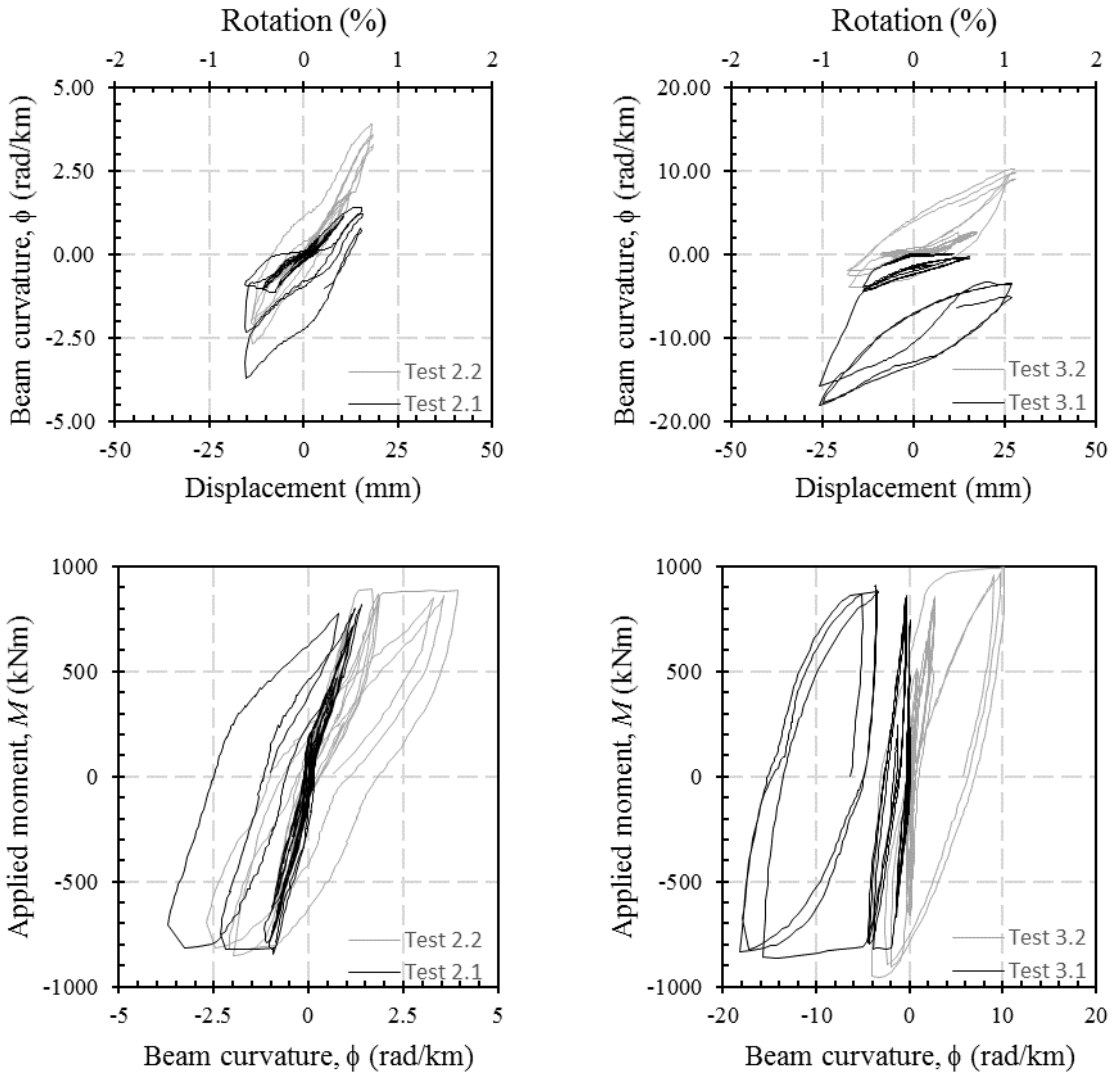

Figure B- 4. Curvature outside the PHRD measured during Tests 2 (left) and Tests 3 (right).

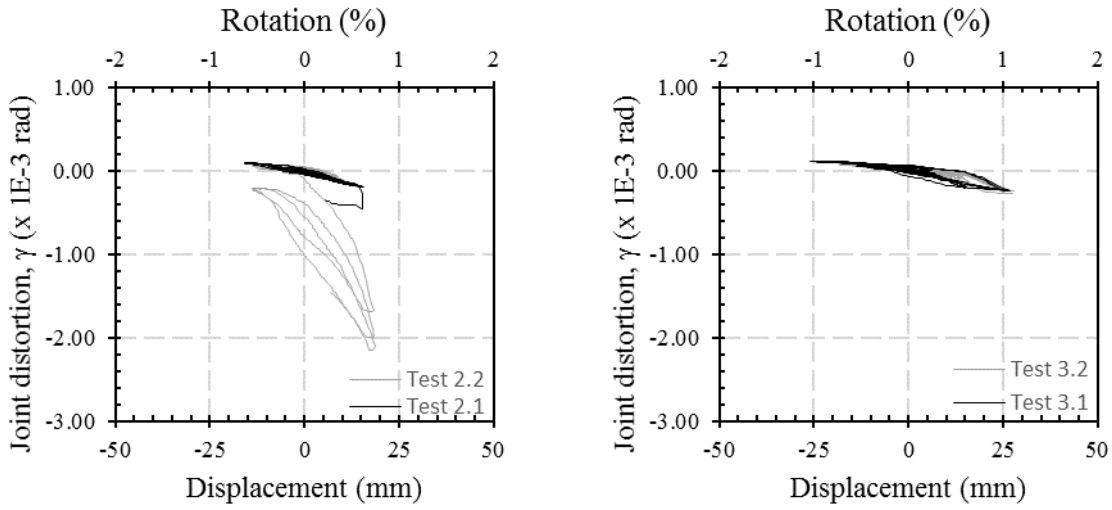

Figure B- 5. Joint shear distortion measured during Tests 2 (left) and Tests 3 (right).

APPENDIX C

Figure C- 1. Sealing of the cracks before the epoxy injection, Test 2.

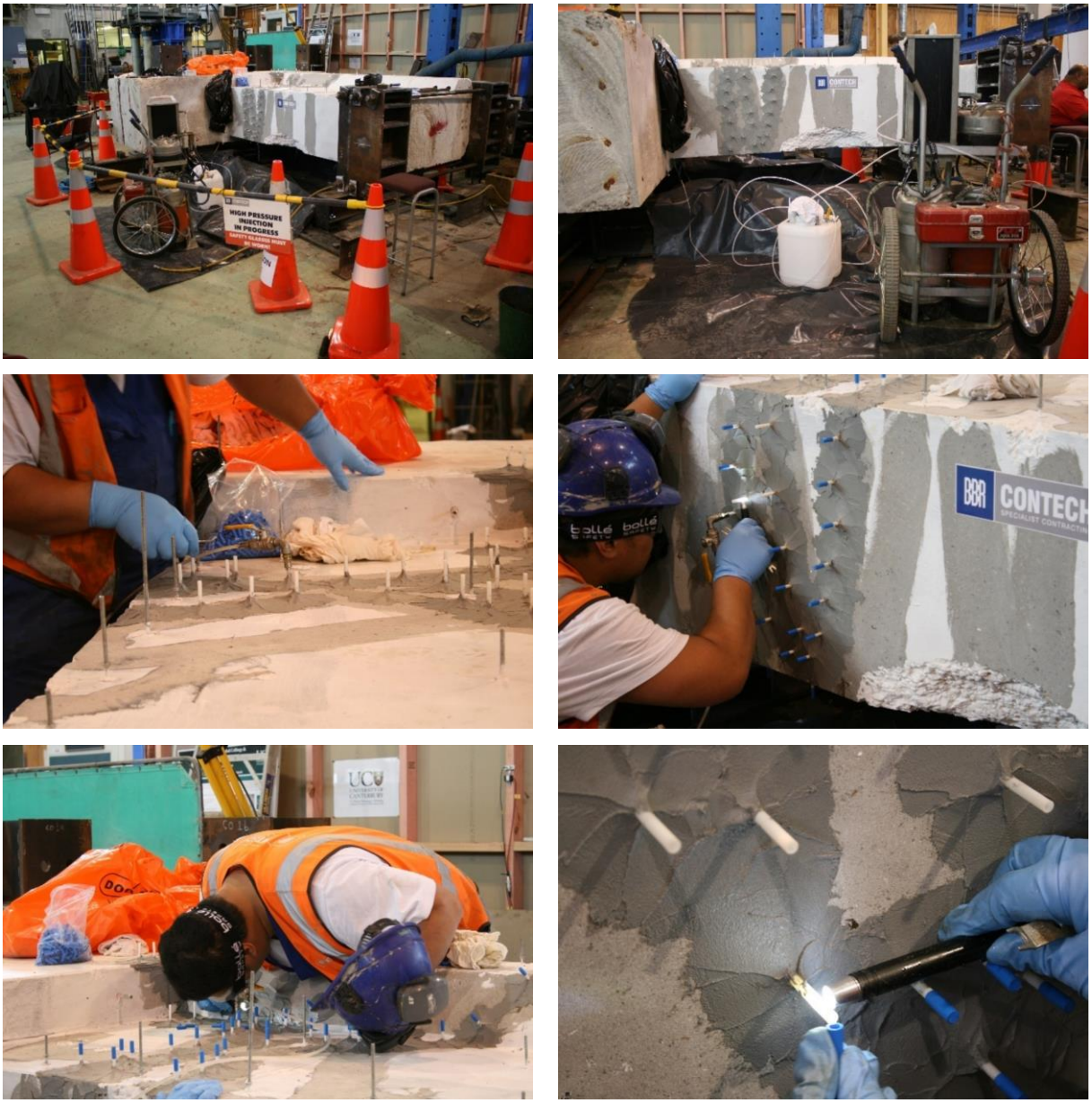

Figure C- 2. Epoxy crack injection process, Test 2.

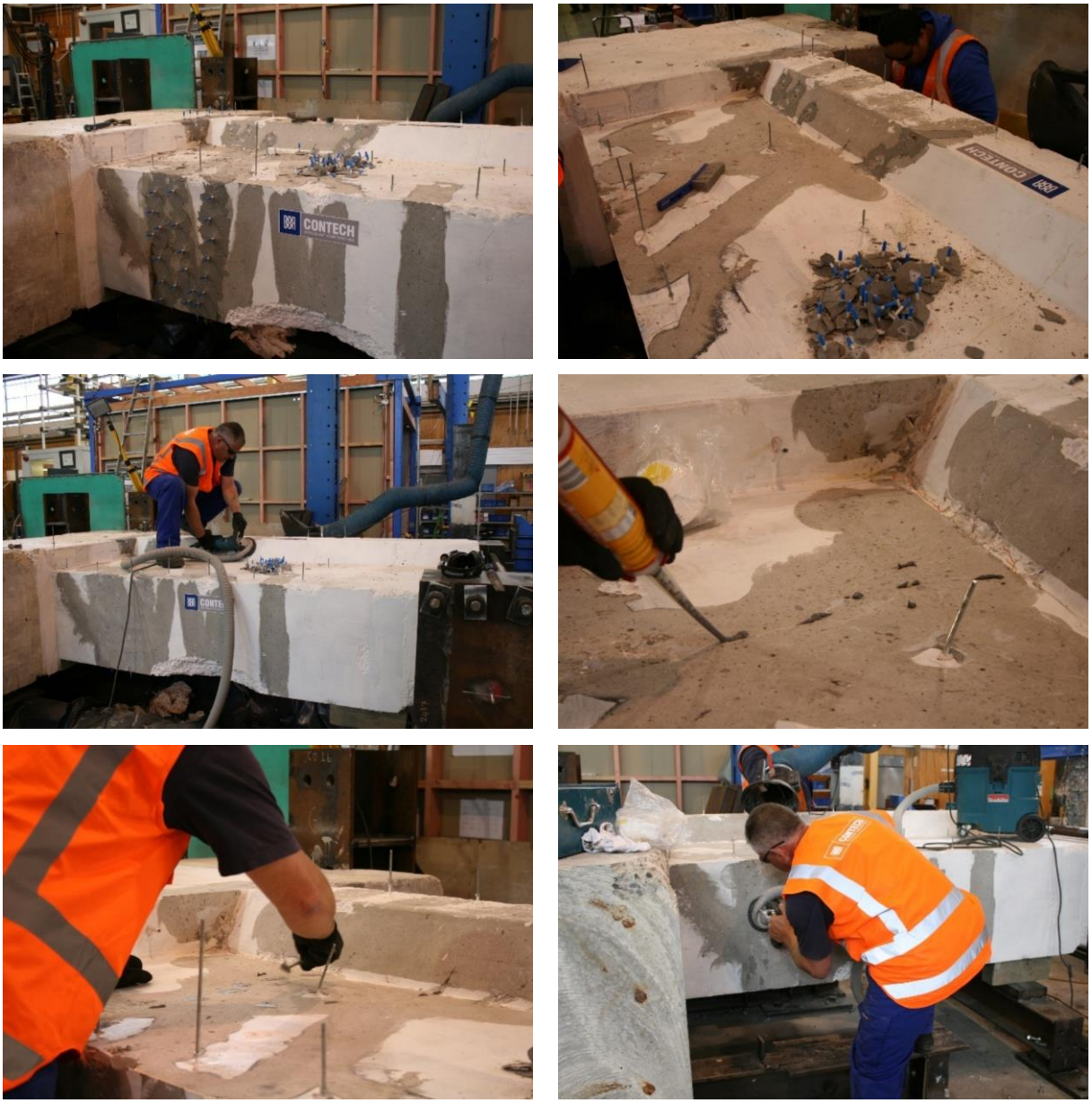

Figure C- 3. Cleaning process after the epoxy has cured, Test 2.

APPENDIX D

Figure D- 1. Sealing of the cracks before the epoxy injection, Test 3.

Figure D- 2. Epoxy crack injection process, Test 3.

Figure D- 3. Cleaning process after the epoxy has cured, Test 3.